



THE SWEDISH SCHOOL
OF TEXTILES
UNIVERSITY OF BORÅS

Graphene: a vision to the future of smart E-Textile application

Doctoral dissertation by
Milad Asadi Miankafshe

Year 2022

‘There is no power nor strength except by Allah’.

Graphene: a vision to the future of smart E-textile application

Faculty of Textiles, Engineering, and Business (the Swedish School of Textiles)
Department of Textile Technology
University of Borås
SE-501 90, Borås, Sweden

Copyright © Milad Asadi Miankafshe, 2022

Printed in Sweden by Arkitektkopia AB

ISBN 978-91-89271-64-7 (printed)
ISBN 978-91-89271-65-4 (pdf)
ISSN 0280-381X, Skrifter från Högskolan i Borås, nr. 128
Electronic version: <http://urn.kb.se/resolve?urn=urn:nbn:se:hb:diva-27721>



Abstract

Smart textile is a term referring to the textiles that could interact with their environment, receiving input and giving output based on their applications. Among smart textiles, electrically driven smart textiles (E-textiles) are being produced by various methods and materials integrated with textile substances. Graphene is one of these compounds that could be integrated into the polymer or integrated into the textile materials such as fibres. Therefore, other elements could be doped or immobilised on the graphene nanosheets for a wider range of applications, such as catalytic and electrocatalytic systems.

However, finding the most applicable and efficient method to integrate graphene into the textile fibres and further establishing a method for catalyst immobilisation are challenging and require focused research.

Therefore, this doctoral thesis focused on the innovative concept of integration of graphene and immobilisation of iron nanoparticles on it. Evidence from the systematic experiments was gathered for the case of dip-coating of polyester textiles with graphene oxide dispersion and enhancing the electrostatic bonding between fibres and graphene oxide nanosheets. In the second step, systematic experiments were gathered for the case of immobilisation of an inorganic catalyst (zerovalent iron) on textile supports. The goal of this thesis is to establish the feasibility of a mild and applicable method for textile material supports, which requires low temperature and mild pH, and further fabrication of heterogeneous catalytic and electrocatalytic systems for wastewater treatment. Polyester was chosen as the textile support material for graphene oxide coating and catalyst immobilisation due to its availability and cost-effectiveness.

The thesis has four distinct parts related to (a) Pre-surface-charge modification of the polyester for strong electrostatic bonding between polyester and graphene, (b) Design a continuous yarn coating system for mass production of graphene-coated conductive yarns, (c) Immobilisation of Fe^0 on graphene-coated polyester textiles and optimising their feasibility in catalytic systems and (d) Design and prove the feasibility of knitting a fully textile-based reactor having two anodic and cathodic sections by using rGO- Fe^0 yarns and stainless-steel multifilament yarns, respectively as a concept of electro-Fenton wastewater treatment.

Diverse analytical and instrumental techniques were used to monitor the surface modification of the polyester textiles and conductivity of the resulting textiles; moreover, the electromechanical and electrothermal properties of the graphene-modified textiles were examined. Further, the efficiency of catalyst immobilisation, physio-chemical properties of the immobilised catalyst, and their catalytical activities in dye removal from the water was studied. Results showed that surface charge modification of polyester fabric with both chitosan and hexadecylpyridinium chloride (HDPC) gives the most homogeneous graphene coating, resulting in high conductivity and very good fastness. Furthermore, results from scanning electron microscope (SEM), Differential scanning calorimetry (DSC), and UV/Visible spectrophotometry prove the success of immobilisation of zerovalent iron on the graphene-modified textiles.

The novelty of the research presented in this doctoral thesis is primarily attributed to the novelty of a hybrid graphene-catalyst immobilisation-grafting on polyester textile supports for wastewater treatment applications. The final concept of the thesis is to introduce the potential for assembling a fully textile-based reactor for Electro-Fenton wastewater treatments.

Keywords: graphene; graphene-coated e-textiles; catalyst immobilisation; hybrid graphene-catalyst multifunctional textiles; dye removal; e-textile; electro-Fenton; Fenton; wastewater treatment

Acknowledgments

I would like to express my gratitude to Professor Nawar Kadi, who has always been supportive and helpful during my study. This thesis would not be completed without his help. My appreciation also goes to my dear friend, Dr Mohammad Neaz Morshed, for his contribution to this thesis work. In addition, I am thankful to Vijar Kumar for his kind co-supervision. I would also like to thank the knitting lab technicians (Kristian Rödbý, Stefan Gustafsson, and Lars Brandin).

I am so grateful to my love, Parandis; without her support, I would not have been able to finish this doctoral study. And finally, I would like to express my gratitude to my family for their support during my study.

June 2022

Milad Asadi Miankafshe

List of appended publications

Peer-reviewed journal publications

Publication I

Miankafshe, Milad Asadi, Tariq Bashir, and Nils-Krister Persson. "The role and importance of surface modification of polyester fabrics by chitosan and hexadecylpyridinium chloride for the electrical and electro-thermal performance of graphene-modified smart textiles." *New Journal of Chemistry* 43.17 (2019): 6643-6658.

Publication II

Miankafshe, Milad Asadi, Tariq Bashir, and Nils-Krister Persson. "Electrostatic grafting of graphene onto polyamide 6, 6 yarns for use as conductive elements in smart textile applications." *New Journal of Chemistry* 44.18 (2020): 7591-7601.

Publication III

Morshed, M. N., Miankafshe, M. A., Persson, N. K., Behary, N., & Nierstrasz, V. A. (2020). Development of a multifunctional graphene/Fe-loaded polyester textile: robust electrical and catalytic properties. *Dalton Transactions*, 49(47), 17281-17300.

Publication IV

Miankafshe Milad Asadi, Vijay Kumar, Nawar Kadi. (2022)

Development of an industrial graphene/stainless steel, fully textile-based reactor for electrocatalysis: robust electrical and catalytic properties. (under editing)

Conference publications

Publication I

Miankafshe, Milad Asadi, Tariq Bashir, and Nils-Krister Persson. "The role and optimization of cationic agents for adhesion and electrical conductivity of graphene/coated textiles; Nanotexnology conference (ISFOE18), 2-5 July 2018, Thessaloniki, Greece.

Publication II

Milad Asadi Miankafshe, Tariq Bashir, Nils-Krister Persson. Grafen i Textilier, SIO Grafens resultatworkshop Svenskt Grafenforum, 16-17 October, Lund, Sweden

Table of Contents

Introduction	2
1. Background on E-textiles and use of graphene	2
1.2 Background on graphene oxide	3
Research gap	5
Research purposes	5
Research questions	6
1.2.1 Methods for reduction of graphene oxide to graphene	7
Alcohol reducing agent reduction	7
Thermal reduction	7
Chemical vapour deposition	7
Chemical reduction by a reducing agent	7
1.2.2 Element doping of graphene	8
1.2.3 Graphene incorporation with textile	8
1.2.4 Iron doping of graphene-coated textile	9
1.3 Strategy chosen for this thesis	9
1.3.1 Dip-coating	9
1.3.2 The role of reducing agent in electrical properties of reduced graphene oxide	11
1.3.3 Thesis framework and outline	12
1.4 Scope and limitation of the thesis	14
State-of-the-art	15
2.1 Surface charge modification of fabrics and yarns and graphene grafting	15
2.1.1 Preparation of textile surface for graphene grafting and iron immobilisation	15
2.1.2 Surface charge modification	15
2.1.3 Methods of grafting functional polymers on polyester fibres for surface charge modification	16
Grafting of hyperbranched poly-(amidoamine) dendrimer (ethylenediamine core and tertiary amine branches dendrimer) on polyester non-woven	17
Grafting of Chitosan on polyester yarns	17
Grafting of polyethyleneimine (PEI) on polyester yarns	18
Grafting of poly-(diallyldimethylammonium) chloride (PDDAC) on polyester yarns	19
Grafting of hexadecylpyridinium chloride monohydrate (HDPC) on polyester yarns	19

2.2 State-of-the-art in graphene-modified textiles for the heating element and tactile sensors	20
2.3 State-of-the-art in Graphene-modified textile support for catalyst immobilisation	21
2.3.1 Inorganic catalyst immobilisation	21
2.3.2 Technique of catalyst immobilisation on textiles	21
2.3.3 Main factors affecting the immobilisation of inorganic catalysts on textiles	21
2.3.4 Challenges of inorganic immobilisation on textiles.....	22
2.3.5 Catalytic system for wastewater treatment	22
2.3.6 Inorganic catalyst zerovalent iron particles (Fe ⁰)	23
2.4 State-of-the-art in wastewater treatment.....	24
2.5 State-of-the-art in advanced catalytic systems for wastewater treatment	24
2.5.1 Electrocatalysts	24
2.5.2 Electrocatalytic system for wastewater treatment	25
2.5.3 Advanced oxidation process through Fenton's and electro-Fenton reaction.....	25
2.6 Main Factors affecting the electro-Fenton process.....	27
Presence of H ₂ O ₂	27
The concentration of ferrous ions	27
Temperature	27
The pH of the solution	28
Power density	28
Mass transfer	28
Electrode distance.....	28
Electrode arrangements	29
2.6.1 Advantages and disadvantages of Electro-Fenton over convention Fenton reaction	29
2.7 Strategies for thesis design	30
Material and methods	31
3.1 Materials	31
3.1.1 Chemicals	31
3.1.2 Yarns.....	31
3.1.3 Polyester non-woven fabric.....	31
3.1.4 Polyester knitted fabric.....	32
3.2 Methods of material preparation	32
3.2.1 Preparation of polyester yarns	32
3.2.2 Preparation of knitted polyester fabrics.....	32

3.2.3 Preparation of polyester non-woven fabric for the Fenton process.....	32
3.3 Method of graphene grafting	34
3.3.1 Continuous yarn coating with graphene oxide.....	34
3.4 Method of catalysts immobilisation	34
In situ immobilisation of zerovalent iron on polyester non-woven	34
3.5 Reactor designed in the electro-Fenton process.....	37
3.6 Methods for analysis and material characterisation	38
Sessile-drop goniometry	38
Colour measurements.....	38
Chemical Compositions.....	38
Microscopic measurement	39
Thermogravimetric analysis (TGA).....	39
Differential scanning calorimetry (DSC).....	39
Electrokinetic measurement.....	39
Electrical performance measurement	40
Electro-mechanical performance of knitted graphene-modified fabrics.....	41
Electro-thermal performance of knitted graphene-modified fabrics	41
3.6.1 Methods for assessing catalytic pollutant removal.....	41
Uv-visible (UV-VIS) spectroscopy.....	41
Chemical oxygen demand (COD) analysis.....	42
Reusability.....	42
Particle size measurement.....	42
Cyclic voltammetry (CV).....	42
Results and Discussion	44
4.1 The effect of cationic agents on performance of graphene-modified knitted polyester fabrics.....	44
X-ray photoelectron spectroscopy (XPS)	45
ATR-FTIR spectroscopy.....	47
Streaming potential measurements	47
Sessile-drop goniometry	49
Surface Morphology.....	50
The colour strength and estimation of dye concentration.....	52
Manufacturing-based quality of modified fabrics	52
Electrical Conductivity.....	53

The electrothermal activity of the graphene-modified polyester knitted fabrics.....	54
4.2 Characterisation of the coated yarn for tactile sensor applications	59
Surface Morphology.....	59
Tensile properties of the yarns	59
Electrical performance of the yarn	61
4.3 Non-woven polyester fabric and its catalytic properties	63
Sessile droplet goniometry analysis.....	63
Particle size distribution.....	64
Electrokinetic measurements (Zeta potential analysis)	64
The colour strength and the coating evenness analysis.....	65
ATR-FTIR spectroscopy analysis	66
Thermal analysis and decomposition of materials	68
X-ray photoelectron spectroscopy (XPS) analysis.....	69
4.3.2 Analysis of catalytic property of polyester non-woven fabrics	70
Colour removal.....	70
Kinetics of colour removal using PET-rGO-Fe ⁰ and PET-PAM-rGO-Fe ⁰	72
Toxicity reduction analysis.....	73
Analysis of recyclability-reusability.....	74
Effect of concentration of PET-rGO-Fe ⁰ and PET-PAM-rGO-Fe ⁰ on dye removal.....	75
4.4 Fully textile-based reactor and its electro-Fenton performance	76
4.4.1 Colour removal.....	76
4.4.2 Kinetic colour removal using the fully textile-based reactor.....	76
Summary	78
General conclusion and future perspectives	78

List of Tables

Table 1. Comparison of the reduction methods for GO production.	7
Table 2. Comparison of the effect of reducing agents on surface resistance of cotton fabrics.	11
Table 3. Publications and the focus in each manuscript.	12
Table 4. Physical characteristics of polyester non-woven membranes	31
Table 5. The composition of polyester yarn samples.	34
Table 6. Modification steps for the polyester non-woven fabric	35
Table 7. The composition of samples.	44
Table 8. Atomic ratio of the surface chemical composition of samples.....	46
Table 9. Reflectance (R), colour strength (K/S), and relative percentage difference (RPD) of colour strength for GO-modified and rGO-modified fabrics.	52
Table 10. CIELab coordinates of GO-modified and rGO-modified fabrics. Colour differences (ΔE) of a control and pre-treated samples in both CIE and CMC systems. L* is the coordinate response to brightness and darkness of the surface, a* coordinate response to green-red shade of colour, and b* coordinate response to yellow-blue shade of colour.	53
Table 11. Sheet resistance (R_{sh}) and maximum current (I) at a voltage of 30 V for control and rGO-modified samples.	54
Table 12. The composition of polyester yarn samples.	59
Table 13. Tensile properties of the pristine, surface modified and functionalised polyester yarns.....	60
Table 14. Contact angle data from sessile droplet analysis.....	63
Table 15. CIELAB colour strength and the coating evenness measurement.....	66
Table 16. DSC data from the second heating scan and cooling scan of the samples.....	69
Table 17. Atomic proportion (a.t%) of the surface chemical composition of the samples.....	70
Table 18. A comparison of the reaction kinetics for the removal of crystal violet dyes using PET-GO, PET-rGO-Fe ⁰ and PET-PAM-rGO-Fe ⁰	73

List of figures

Figure 1. Schematic representation of Hummer's method for oxidising (a) graphene to (b) graphene oxide.	4
Figure 2 A general scheme of the textile production processes from fibre to final product as smart textile in which graphene could be applied through the processes.	10
Figure 3. Schematic representation of reduction of (a) graphene oxide (GO) to (b) reduced graphene oxide (rGO) by $\text{Na}_2\text{S}_2\text{O}_4$ as a reductant.	11
Figure 4. General theme of the thesis.	13
Figure 5. Hydrolysis of polyester via sodium hydroxide 12%.	15
Figure 6. (a) Denier reduction (alkalisation), (b) cationisation, (c) surface charge modification, and (d) chemical reduction of the GO coated fibre to rGO coated fibres. (e) schematic representation of the repulsion between non-treated polyester yarn and GO nano-sheets. (f) zeta potential of polyester, chitosan, and graphene oxide in different pH values.	16
Figure 7. Chemical structure of hyperbranched poly-(amidoamine) dendrimer consists of ethylenediamine core and tertiary amine branches (PAMAM).	17
Figure 8. Chemical structure of protonated chitosan.	18
Figure 9. Molecular structure of cationised branched polyethyleneimine (PEI).	18
Figure 10. Molecular structure of poly-(diallyldimethylammonium) chloride (PDDAC).	19
Figure 11. Molecular structure of hexadecylpyridinium chloride monohydrate (HDPC).	19
Figure 12. Electro-Fenton reaction set-up.	26
Figure 13. Illustration of the functionalisation process. (a) Alkalisiation of the yarn, (b) surface charge modification, (c) coating with graphene oxide (GO), (d) thermal curing and (e) chemical reduction of GO-modified yarn to generate electrical conductivity.	32
Figure 14. Schematic illustration of the modification process; (a) alkaline hydrolysis of PET membranes; (b) chemical grafting of hyperbranched poly-(amidoamine) (PAMAM) dendrimer.	33
Figure 15. Schematic representation of continuous yarn coating line. And a digital image of the in-house made set-up for yarn modification.	34
Figure 16. Time-temperature scheme for the process of (a) alkalisiation (denier reduction) of polyester yarns; (b) PAM-grafting; (c) incorporation of GO; (d) incorporation of Fe^{3+} (e) in situ immobilisation of rGO and Fe^0	35
Figure 17. Digital Images of the samples (a) PET, (b) PET-PAM-GO, (c) PET-PAM-rGO, (d) PET-PAM-rGO- Fe^0	36
Figure 18. (a) the fully textile-based reactor for electro-Fenton water treatment, (b) the knitting pattern designed by the CMS 330 software, and (c) the needle arrangement of the reactor.	37
Figure 19. A 4-probe measurement of the electrical sheet resistance (R_{sh}) of the fabric.	40
Figure 20. Build-up strain gauge powered by software for electromechanical measurements.	41
Figure 21 3-electrode set-up for electro-Fenton process.	43
Figure 22. the colloidal dyes segregated from the fabric into the solution during chemical reduction of a control sample (a), PDDAC-treated (b), HDPC-treated (c), PE-treated (d), and CS-treated sample (e).	45

Figure 23. (a) graphene oxide coated and (b) reduced graphene oxide coated knitted polyester fabric.	45
Figure 24. Wide scan XPS spectra of (a) pristine polyester (PET), PET-PEI, PET-CS, PET-HDPC, and PET-PDDAC. (b) PET-GO and PET-rGO.	46
Figure 25. ATR-FTIR spectra of a pristine fabric (PET), chitosan (8 g.L-1) treated fabric (PET-CS), graphene-coated fabric (PET-CS-GO), and reduced graphene-coated fabric (PET-CS-rGO).	48
Figure 26. Zeta potential (ζ) values determined for (a) PET-CS, PET-PDDAC, PET-PE, and PET-HDPC fabrics and (b) pristine PET fabric, PET fabric modified by graphene oxide (PET-GO), and a PET fabric modified by reduced graphene oxide (PET-rGO) in dependence on pH of an aqueous 10-3 mol/L KCL solution.	49
Figure 27. Image sequences of placing a deionised water droplet on (a) an unmodified polyester (PET), and (b) HDPC-modified polyester fabric (PET-HDPC) over time.	50
Figure 28. Water contact angle of (a) pristine PET, (b) graphene oxide-modified polyester (PET-GO), (c) reduced graphene oxide-modified polyester fabric (PET-rGO), (d) reduced graphene oxide-HDPC modified polyester fabric (PET-HDPC-rGO), (e) reduced graphene oxide-PDDAC modified polyester fabric (PET-PDDAC-rGO), (f) reduced graphene oxide-PE modified polyester fabric (PET-PE-rGO), and (g) reduced graphene oxide-CS modified polyester fabric (PET-CS-rGO).	50
Figure 29. SEM images of (a) PET-GO sample (4.5kx Mag.), (b) PET-GO sample (20kx Mag.), (c) PET-CS-GO sample (4.5kx Mag.), (d) PET-CS-GO sample (20kx Mag.), (e) PET-HDPC-GO sample (20kx Mag.), (f) PET-HDPC-GO sample (150x.), (g) PET-PDDAC-GO sample (20kx Mag.), (h) PET-PDDAC-GO sample (800x Mag.).	51
Figure 30. SEM images of (a) PET-rGO sample (20kx Mag.), (b) PET-CS-rGO sample (20kx Mag.), (c) PET-HDPC-rGO sample (20kx Mag.), and (d) PET-PDDAC-rGO sample (20kx Mag.).	51
Figure 31. The steady-state temperature vs applied voltages profile of the samples.	54
Figure 32. Temperature and current versus time profile of the (a) PET-HDPC-rGO by having a steady-state temperature of 115°C at a constant voltage of 30V, (b) PET-CS-rGO with a steady-state temperature of 55°C at a constant voltage of 25V, response times for both fabrics are less than 120 s. The current vs temperature profile of (c) PET-HDPC-rGO and (d) PET-CS-rGO during the electro-thermal activity with a function of $I(T) = 6.7401 \ln(T) + 37.899$ and $I(T) = 2.4788 \ln(T) + 6.5443$, respectively.	56
Figure 33. The measured resistance changes vs temperature profiles of (a) PET-HDPC-rGO with a function of $R = -0.0004T + 0.5083$, and (b) PET-CS-rGO with a function of $R = -0.0078T + 2.3658$	57
Figure 34. Infrared images at a steady-state temperature of (a) PET-CS-rGO, and (b) PET-HDPC-rGO at an applied voltage of 30 V., reaching 63.9 and 110°C for PET-CS-rGO and PET-HDPC-rGO correspondingly while having almost a homogeneous thermal expansion through the fabric surface.	57
Figure 35 (a). DSC photographs of PET-HDPC-rGO, with a glass transition (T_g) of 76.49°C. (b) DSC photographs of a control polyester fabric (PET), a pre-alkalised polyester fabric coated by reduced graphene oxide (PET-ALK-rGO), and an HDPC surface-modified polyester fabric coated by reduced graphene oxide. Heat capacity profile of PET-HDPC-rGO. Melting temperature (T_m) of the polyester fabric with a value of 200°C increases to 213°C for a PET-	

HDPC-rGO fabric. Heat capacity at constant pressure (C_p) of the same sample at 120°C is 1.261 J.(g.°C) ⁻¹	58
Figure 36. SEM images of (a) PET-GO, (b) PET-CS-GO (c) PET-HDPC-GO, (d) PET-rGO, (e) PET-CS-rGO, (f) PET-HDPC-rGO with 20kx magnification.	60
Figure 37. Stress-strain curves of a pristine polyester (PET), chitosan modified (PET-CS), graphene oxide modified (PET-CS-GO), and reduced graphene oxide modified (PET-CS-rGO) yarn.	61
Figure 38 (a). Electrical resistance ($k\Omega.10cm^{-1}$) of the CS and HDPC modified polyester yarns. (b) 2-probe set up for electrical measurement.	62
Figure 39. Particle size distribution of zerovalent iron nanoparticles; (a) PET-rGO- Fe ⁰ and (b) PET-PAM-rGO- Fe ⁰	64
Figure 40. Zeta-potential (ζ) values of non-wovens as a function of the pH values of the electrolyte solution (0.001M KCl). (PET refers to alkalisated polyester)	65
Figure 41. The colour differences (ΔE) of CIE and CMC systems (Values less than 1 are the smallest colour differences than the human eye can detect)	67
Figure 42. ATR-FTIR spectra of PET, PET-GO, PET-rGO-Fe ⁰ , PET-PAM, PET-PAM-rGO and PET-PAM-rGO-Fe ⁰	67
Figure 43. TGA and DTG curves of (a) PET-GO, (b) PET-rGO-Fe ⁰ , (c) PET-PAM-rGO, and (d) PET-PAM-rGO-Fe ⁰	68
Figure 44. Wide scan XPS spectra of (a) pristine PET, PET-PAM, PET-PAM-GO, and PET-PAM-rGO-Fe ⁰ samples.....	70
Figure 45. UV-visible spectroscopy of catalytic removal of crystal violet dyes using (a) PET-GO, (b) PET-PAM-GO, (c) PET-rGO-Fe ⁰ , and (d) PET-PAM-rGO-Fe ⁰ [Conditions: Crystal violet = 50 mg. L ⁻¹ , non-woven fabric = 700 mg. L ⁻¹ , NaBH ₄ = 0.1 M, pH=5].	71
Figure 46. Evolution of (a) C/C ₀ , (b) Ln(C/C ₀) and (c) the conversion (%) yield in time at room temperature for removal of crystal violet dyes using PET-GO (▲), PET- rGO-Fe ⁰ (■) and PET-PAM-rGO-Fe ⁰ (●) [Conditions: Crystal violet = 50 mg.L ⁻¹ , nonwoven fabric = 700 mg.L ⁻¹ , NaBH ₄ = 0.1 M, pH=5].	72
Figure 47. Recyclability and reusability of (a) PET-rGO-Fe ⁰ , (b) PET-PAM-rGO-Fe ⁰ on catalytic removal of crystal violet dye [Conditions: Crystal violet = 50 mg.L ⁻¹ , non-woven fabric = 700 mg.L ⁻¹ , NaBH ₄ = 0.1 M, pH=5].	74
Figure 48. Effect of catalyst concentration [0 mg.L ⁻¹ (◄), 50 mg.L ⁻¹ (◆), 100 mg.L ⁻¹ (▼), 300 mg.L ⁻¹ (▲), 500 mg.L ⁻¹ (●), 700 mg.L ⁻¹ (■), on the removal of crystal violet dyes (a) PET-rGO-Fe ⁰ and (b) PET-PAM-rGO-Fe ⁰ . [Conditions: Crystal violet = 50 mg.L ⁻¹ , NaBH ₄ = 0.1 M, pH=5].	75
Figure 49. UV-visible spectroscopy of catalytic removal of crystal violet dyes in electro-Fenton process.	76
Figure 50. Evolution of (a) C/C ₀ , (b) Ln(C/C ₀) and in time at room temperature for removal of crystal violet dyes using a GO-Fe ⁰ / stainless steel textile reactor.	77

Chapter 1

Introduction

Chapter outline

1. Background on E-textiles and use of graphene

Textile is exceptional as a class of fabricated materials, interacting in almost any human social activity. Over the last two decades, studies pertaining to textile electronics started from initial research explorations and going up to the industrial area. It began with investigating the integration of conductive wires and circuits into textiles [1, 2].

The term “smart textiles” refers to a wide field of studies that extend the functionality of common fabrics. Smart textiles are defined as textile products that could interact with the environment or the user. Not all smart textiles are electrically driven. When electronics and textiles converge, it can be named e-textile [3].

The combination of textiles and other technology, such as electronics, could have a tremendous impact on society [4, 5]. However, the development of e-textiles runs the risk of stagnation if the prevalent paradigm of assembling the enabling technology with textiles results in bulky, heavy, non-compliant products with low comfort. An alternative to the classic integration of electronics into textiles is producing intrinsically conductive yarns.

Electroconductive textile fibres are currently attracting much attention for a range of applications from electrostatic discharge [6], supercapacitors [7], health monitoring and diagnostic systems [8], energy harvesting [9], environmental remediation system [10], photonic, luminescence [11], UV blocking [12], antibacterial [13, 14], insect repellent [15], colour change [16], electro-thermal heating elements such as seat heaters in vehicles [17] and electrically heated garments, [18-20]. Most of the research is based on electrically conductive polymers or metallic conductive mechanisms. The resulting threads are not good for knitting or weaving when it comes to wearable smart textiles.

Recently, e-textiles have been prepared using different methods, such as:

- The spinning of Nano-metallic filaments, such as stainless steel microfilaments with conventional staple fibres [21],
- Melt-spinning of conductive nanoparticles and carbon products with polymers [22],
- Non-woven fabrics made of staple stainless steels, carbon fibres and polymers [23],
- Carbon allomorphs such as graphene incorporation. [24].

Carbon allomorphs could be integrated with textiles for their electrical conductivity [25]. Among them, graphene, a two-dimensional nanosheet, is the object of intensive study [26-29]. It is because the two-dimensional shape of the graphene, which has a thickness of one or a few atoms of sp^2 -bonded carbon atoms, could have the minimum impact on the strength,

softness and comfortability of the resulting textiles. Graphene has the potential to create highly valuable electrically conductive textile systems with maintained pliability and psychological comfort of the textile. However, there is still a lack of continuous integration methods for further developing knitted and woven smart textiles and garments.

Using graphene is the most cost-effective and high-performance alternative for different applications, from the thermal heater to electro-Fenton wastewater treatment. For that, in this study, graphene has been chosen as the main conductive element to convert conventional textiles into E-textiles.

1.2 Background on graphene oxide

Graphene is an interesting carbon allomorph for its electrical conductivity and mechanical and thermal properties. It has rich chemistry that can contribute to reactions as either a reducing agent as an electron donor or an oxidizer as an electron acceptor owing to its electronic structure, which results in both an electron affinity and an ionisation potential of 4.6 eV [30]. Another focus of studies on graphite is substitutional doping by replacing carbon with other elements. For instance, replacing carbon with boron and nitrogen results in p- and n-type graphite, respectively [31].

Extraordinary electronic properties in graphene are due to the high quality of its 2D crystal lattice [32, 33]. Specifically, small quantities are required to achieve electrical or electrothermal properties, and only a thin layer is required with potentially minimum impact on the thickness of the medium.

Graphene itself is known for its specific surface area ($2620 \text{ m}^2\text{g}^{-1}$), excellent mechanical properties (Young's modulus of 1 TPa), and high electrical conductivity (electron mobility of $2.5 \times 10^5 \text{ cm}^2\text{V}^{-1}\text{s}^{-1}$ at room temperature) and high thermal conductivity of (3000 W m K^{-1}). Graphene could be prepared by either mechanical exfoliation of graphite or epitaxial chemical vapour deposition [34, 35].

Graphene oxide (GO) caught the attention of the scientific community after the discovery of graphene in 2004, because of its potential for use in various technological applications such as photocatalysis [28], field-effect transistors [34], transparent electrodes [36], batteries [27, 37] bio sensors [38], and smart textiles [39].

In 2006, Ruoff's group was the first to establish a solution-based development for making single-layer graphene [40, 41]. The method is based on the chemical modification of graphite to produce a water-dispersible intermediary, graphite oxide (GO) [38].

The advantages of the GO method are its low-cost and large-scale production. The starting material is simple graphite, and by a simple Harsh oxidation Hummer's method [42-44], it can easily be scaled up to produce chemically derived graphene dispersed in a liquid. Ruoff's group has demonstrated free-standing films with extremely high tensile strength of up to $\sim 42 \text{ GPa}$ [45, 46].

With this method, GO is produced by exfoliating graphite, resulting in highly oxygenated graphene with hydroxyl and epoxide functional groups on the surface and carboxyl and

carbonyl groups at the edge of the sheets [47]. The Hummer's method is the oxidation of graphene in which KMnO_4 acts as an oxidation agent to introduce molecules of oxygen to the graphene surface.

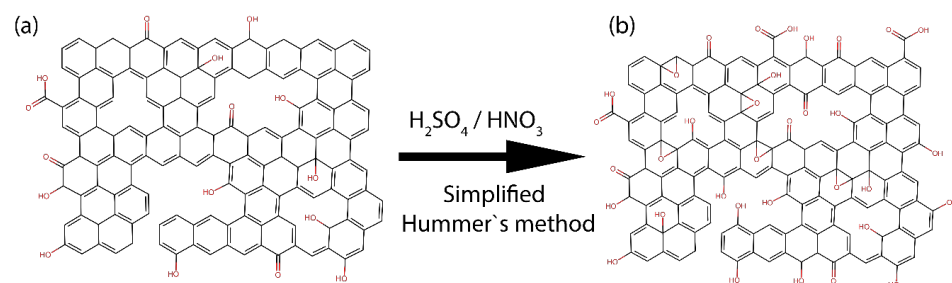


Figure 1. Schematic representation of Hummer's method for oxidising (a) graphene to (b) graphene oxide.

Unlike graphene, GO is not conductive and is hydrophobic. However, the graphitic network could be substantially restored by either thermal annealing or through a chemical reduction process.

When it comes to textile, strong bonding between graphene oxide flakes and textile yarns is required, as there is evidence that textile materials need to have a standard washing and friction fastness.

There is a paucity of studies on enhancing the interaction and bonding between fibres and graphene oxide flakes. Among the different methods of preparing graphene or graphene oxide, preparing a dispersion of GO and thereafter dip-coating the textile with it could be the most reasonable and applicable method for the textile industry. For instant thermal annealing of GO on textile, media is not possible, as textile materials are sensitive to temperature and can be decomposed.

Still, dip-coating of textile with graphene oxide does not give us a high conductivity and high quality/fastness of the product. Thus, in the first step of this thesis, the focus is on surface charge modification of the textile to bring electrostatic attraction and bonding between textile fibres and GO. As a result, the conductivity of the textile materials will increase, and the electro-thermal textile heater could be prepared for different applications, such as military customs for cold environments and aeroplane heating systems.

Further, graphene could be doped with other elements to bring a particular property to the textile for a specific application. However, the doping method and condition need more investigation. For instance, if graphene-coated textile is doped with iron properly, it could be used in catalysis applications for wastewater treatment and dye removal of textile wastewater.

If the conductivity of the GO/Fe is high enough, it could be used in electrocatalysis applications in combination with stainless steel fibres as well.

Nonetheless, the conductivity and fastness of the product are the main challenges and weaknesses of these textiles. Finding the most relevant process of incorporation of graphene and iron into textile is lacking. Thus, in this research, the focus is on designing an applicable process to produce high-quality GO-coated textile materials doped with iron for its catalytic and electrocatalytic applications.

Research gap

To the best of our knowledge, in previous studies conducted by other researchers, the electrostatic repulsion between fibres and graphene oxide (GO) has been neglected. Hence, it is essential to study the surface charge of the fibres and GO nanosheets and find an applicable method to improve the isoelectric point of the fibre and enhance the electrostatic attraction between fibres and GO. Moreover, it is essential to study the role of various cationic agents and their influence on the electrical conductivity of the fibre, the morphology of the coating and fastness of the resulting fibre.

Also, to the best of our knowledge, there is no research on producing a continuous graphene yarn coating system that provides conductive yarns which could be fed into knitting or weaving machines for further smart garment and device designing; this will result in having the same porosity and stretchability as a pristine fabric. Consequently, in this study, a continuous yarn coating system is designed to prepare graphene yarn bobbins for further knitting smart devices according to the needs, for instance, knitting a tactile sensor or a wastewater treatment reactor.

Graphene could be doped with other elements, such as iron to improve its performance or to add more functionality to the graphene. To the best of our knowledge, there is no applied research based on GO- Fe^0 integration on textiles. In this study, an applicable method for doped graphene oxide on coated fibres and fabrics with iron is investigated and introduced to the system. This led us to prepare a catalyst for wastewater treatment in both Fenton and electro-Fenton processes.

And at the end of the study, a fully textile-based reactor is designed based on a combination of GO- Fe^0 and stainless-steel yarns for further electrocatalyst wastewater treatment. In this research area, we focused on designing a reactor that could be produced on a large scale and be feasible in industrial wastewater treatment.

Research purposes

The first step of the study is to design an applicable method for dip-coating textiles with graphene oxide dispersion and previous improvements in the surface grafting of graphene through textiles, both in yarn and fabric medium. The plan was to apply various cationic agents to polyester yarns and fabrics and thereafter dip-coat these textiles with GO dispersion. Thus, it is essential to have the most effective coating conditions, including

temperature, time and pH. Further, the effect of each cationic agent on the surface morphology, fastness and electrical properties of the graphene layer is studied.

The second step of the study is to find an applicable method for doping graphene on textile mediums. There are various methods to dope graphene with other elements such as iron; however, when it comes to textiles, most available technologies are not applicable. This is mostly because they require high temperature or other harsh acidic or basic conditions that could deform or even decompose the textile materials. Hence, it is important to find and design an applicable procedure for doping the GO-modified textiles with iron zerovalent nanoparticles. The resulting Fe⁰-PET fabrics could be used in a wide range of applications. However, this study focuses on providing a catalyst and an electrocatalyst for wastewater treatment.

Research questions

rq1

- How would the methods of pre-surface modification of the polyester textiles affect the surface morphology, electrical, electrothermal, electromechanical and washing fastness of the resulting e-textile? What is the relevant reducing agent to reduce graphene oxide or immobilise iron zerovalent on GO-coated textile materials for electrical performances?

rq2

- How can you design a continuous process for homogeneous yarn coating with graphene for knitting machines for e-textile application, and what are the process parameters to ensure the mass production of graphene-modified yarn?
- How can the knitted fabric based on coated yarn be used for electrocatalysis applications in wastewater treatments?

rq3

- Which method is the most appropriate and applicable method of grafting graphene with iron-on textile, considering the condition of application, such as low temperature and pH, to avoid the decomposition of the textile material?

1.2.1 Methods for reduction of graphene oxide to graphene

Graphene oxide (GO) could be reduced to graphene through different methods, such as thermal annealing, chemical reduction, and chemical vapour deposition [48, 49].

Alcohol reducing agent reduction

A mild reduction of GO could occur with alcohol. Furthermore, this method does not damage the edge morphology of the GO, resulting in highly conductive rGO Nano-sheets; ethanol vapour reduction could be used to reduce graphene [50]. However, this method requires a high temperature (more than 900 °C), and it is not an applicable method for textile materials as the main substrate.

Thermal reduction

Thermal reduction of graphene could be prepared via the rapid heating of dry GO under inert gas and at high temperature [51, 52]. Like alcohol vapour reduction, thermal reduction requires a high temperature to reduce graphene into GO. Hence, this method is not usable in textile production.

Chemical vapour deposition

The growth of graphene on different metallic surfaces, such as copper, has been studied before [48, 53]. This method gives a large area of high-quality graphene Nanosheets; however, this method needs a high temperature (up to 1000°C), which is not applicable for textile materials.

Chemical reduction by a reducing agent

Numerous chemical reducing agents, such as SO₂, NaBH₄, NaOH, N₂H₄, C₆H₈O₄, KOH, Vitamin C and Na₂S₂O₄, have been used to chemically reduce GO [54]. Table 1 shows a different form of reduction that has been studied by others.

Table 1. Comparison of the reduction methods for GO production.

Ref. no	Reduction method	Form	C/O ratio	σ (S/cm)
[41]	Hydrazine hydrate	Powder	10.3	2
[55]	150 mM NaBH ₄ solution, 2h	TGF	8.6	0.045
[56]	Thermal annealing at 900°C	TGF	NA	~ 10 ³
[57]	Vitamin C	Film	12.5	77
	KOH	Film	NA	1.910 ⁻³

TGF: Transforming growth factor

When it comes to textiles, the most applicable method is chemical reduction. Among the named agents, Sodium dithionite Na₂S₂O₄ gives the highest electrical conductivity in textile applications [58]. Further, sodium borohydride NaBH₄ provides the highest immobilisation of iron particles [59]. Hence, these two strategic reducing agents have been used in this thesis.

1.2.2 Element doping of graphene

Element doping of graphene can result in various properties for different applications. Element doping is applied through annealing heat treatment, ion bombardment and plasma treatment, arc discharge, and other means to incorporate different elements such as iron into graphene, maintaining the intrinsic 2-dimensional structure of graphene. At the same time, the surface properties of the graphene change to give new properties and performances [49, 60-65].

There are different methods to dope graphene with iron particles, such as pyrolysis [65], the oxygen evolution reaction (OER) [66], hydrothermal synthesis [67] and chemical immobilisation [68]. Among the named methods, chemical immobilisation could be applied to textiles. Consequently, in this thesis, we used an in-situ chemical immobilisation of iron particles on the surface of the textile materials, using $\text{FeCl}_3 \cdot 6\text{H}_2\text{O}$ as a precursor [69, 70].

1.2.3 Graphene incorporation with textile

Graphene can be applied to textile in different ways and classified as *integrated into* or *integrated on* the textile materials, such as:

Chemical vapour deposition (CVD) growth of graphene along Cu wires or meshes [71, 72], dimension-confined hydrothermal method [73], Electrospinning [74], Melt spinning [75, 76], wet spinning of graphene oxide [77-79] (integration in) and dip-coating [80] or 3D printing (integration on). A schematic representation of the methods and steps in which graphene could be applied to the textile is illustrated in Figure 2.

In this thesis, I focused on dip-coating of both fibre and fabric to produce a large-scale industrial product that could be efficiently and cost-effectively produced. It has the potential to be used in knitting and weaving machines that could be programmed to design a specific e-textile based on the required properties and needs of the applications. Accordingly, the final application is a fully textile-based electrocatalytic reactor.

Dip-coating: A single two-dimensional exfoliated GO sheet has a thickness of one or a few atoms of sp^2 -bonded carbon atoms and could be used as a colloidal dye in the textile dyeing industry [24], offering interesting optical, electrical, and thermal properties [81, 82].

Graphene could be grafted into the positively charged polymers and make a covalent and electrostatic bond with the surface-modified fibre. The most reliable method for graphene textile yarn and fabric production is the dip-coating method. Hence, in this thesis, dip-coating is a priority for the whole research.

3D printing: Graphene could be 3D printed on various surfaces, such as textiles for various applications from antennas to supercapacitors [83-85]. However, this method has its drawbacks of not being able to be produced on a large scale and used in the textile industry.

Chemical vapour deposition: Chemical vapour deposition (CVD) is widely used to grow graphene on various surfaces; however, this method has its temperature limitation in textile cases. Some studies show that nanofibres could be grown on metallic surfaces, but this

method is not feasible for continuous textile yarn and fabric production [86]. This method is also limited to the chamber volume, which is unsuitable for the textile industry.

1.2.4 Iron doping of graphene-coated textile

Further, the combination of graphene with the functional nanoparticles gives added functionality in textiles, which can be termed multifunctional textiles, to each constituent and opens up new opportunities to enhance wider applications. The addition of metal nanoparticles such as zerovalent iron nanoparticles in graphene-coated polyester textiles will show not only significant improvements in electrochemical activity but also exhibit high catalytic and electro-catalytic activity due to their unique surface properties [67, 87].

1.3 Strategy chosen for this thesis

As mentioned before, there are several methods to prepare graphene fibres; however, most of these fibres could not be used in short-spinning machines to produce conductive staple or filament yarns. In other methods, if the yarn is produced, the strength and the flexibility of the yarn are not enough to overcome the tensions in the yarn during the knitting process.

So, the focus of this study is to find the most relevant dip-coating method from surface charge modification of the yarns up to graphene coating and iron doping. This means to convert conventional textile yarns to multifunctional graphene/iron yarns.

1.3.1 Dip-coating

As presented before, graphene oxide is produced by oxidation of the graphene. The availability of oxygen functional groups on the surface of graphene oxide (GO) gives excellent hydrophobic behaviour. Thus, an aqueous dispersion of GO could be prepared with a solubility as high as 2.0 wt% and applied as a dye to the textile. Exfoliated GO has electrical insulation properties owing to the attached oxygen functional groups [88]. Therefore, reduction of exfoliated GO to graphene (rGO) is required to obtain electrical conductivity [24, 58], resulting in the production of graphene-coated e-textiles [41, 89, 90].

The main weakness of this dyeing process in accomplishing an industrial product is that the GO Nano-sheets do not adhere properly to most textiles at any pH values, probably because of the electrostatic repulsion between GO and the textile substrate. This is because most textiles, such as polyester [91], have a negative surface potential (ζ) in an aqueous solution [92-94], and absorption of GO into the textile is strongly related to the charge modification of the fibers's surface

It has been reported that modification of polyester fabrics with cationic agents enhances the uptake of anionic dyes by changing the surface charge of the polyester fabric [95, 96]. Thus, GO sheets could easily and uniformly aggregate in a fibre with a positively charged polyelectrolyte. When alkalisied polyester fibre or fabric is impregnated with a cationic agent, the surface charge of the fibre becomes positive. Further, GO Nano-sheets form hydrogen bonds and possibly undergo ionic interaction with positively charged groups on the surface of the fibres [92].

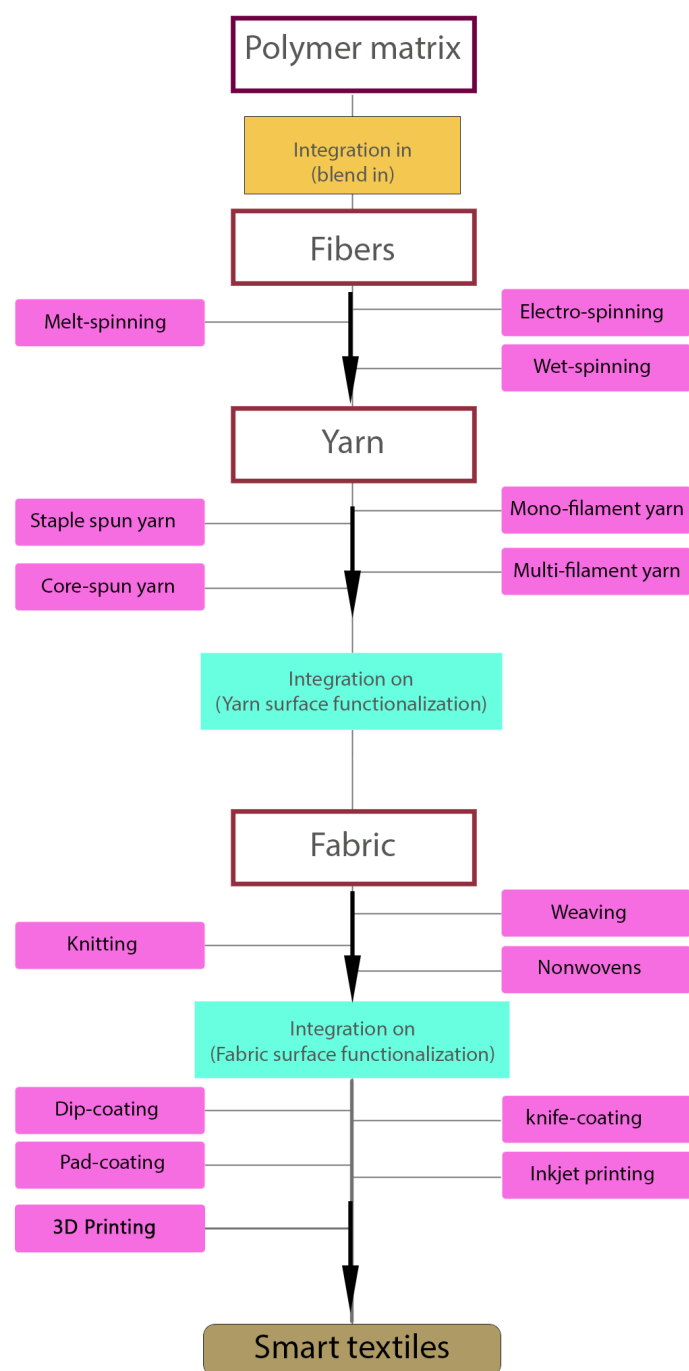


Figure 2 A general scheme of the textile production processes from fibre to final product as smart textile in which graphene could be applied through the processes.

To better understand the role of cationic agents in adsorption and their associated electrical properties, it is essential to determine the degree of uptake of GO by polyester through various cationic agents and their electrical, electro-mechanical, and electro-thermal properties.

1.3.2 The role of reducing agent in electrical properties of reduced graphene oxide

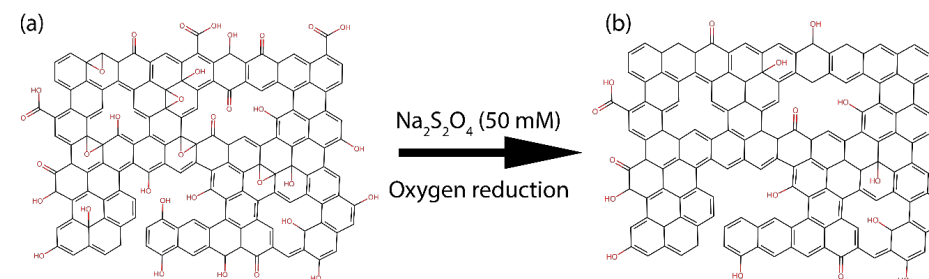


Figure 3. Schematic representation of reduction of (a) graphene oxide (GO) to (b) reduced graphene oxide (rGO) by Na₂S₂O₄ as a reductant.

Various reducing agents have been used by other researchers for better electrical performance of the reduced graphene oxide, either on film or textiles, such as cotton fabrics [58]. Their results are shown in Table 2.

Table 2. Comparison of the effect of reducing agents on surface resistance of cotton fabrics.

Ref no	Reducing agent	Surface resistance(kΩcm ⁻¹)
[58]	NaBH ₄ -GO-cotton	34,600
	NaOH-GO-cotton	23,300
	N ₂ H ₄ -go-cotton	62.7
	C ₆ H ₈ O ₄ -GO-cotton	31.2
	Na ₂ S ₂ O ₄ -GO-cotton	19.4

Sodium dithionite Na₂S₂O₄ (for electrical and electrothermal applications) and sodium borohydride NaBH₄ (for catalyst and electro-catalyst applications) are used in this thesis as reducing agents for both polyester yarn and fabrics.

1.3.3 Thesis framework and outline

This thesis could be separated into four thread lines, and each publication focuses on one aspect of it.

Table 3. Publications and the focus in each manuscript.

Paper	Focus	Publisher
1) The role and importance of surface modification of polyester fabrics by chitosan and hexadecylpyridinium chloride for the electrical and electro-thermal performance of graphene-modified smart textiles	Improvement of the electrostatic bonding among textile fabrics and graphene, increasing its electrical properties and producing a thermal heater e-textile.	New Journal of Chemistry 43.17 (2019): 6643-6658.
2) Electrostatic grafting of graphene onto polyamide 6, 6 yarns for use as conductive elements in smart textile applications	Improvement of the previous method, designing and building up a continuous yarn coating system.	New Journal of Chemistry 44.18 (2020): 7591-7601.
3) Development of a multifunctional graphene/Fe-loaded polyester textile: robust electrical and catalytic properties	Iron grafting of the resulting graphene-coated yarns for wider applications such as wastewater treatment.	Dalton Transactions, 49(47), (2020): 17281-17300.
4) Development of an industrial graphene/stainless steel-based, fully textile-based reactor for electrocatalysis: robust electrical and electrocatalytic properties. (under publication)	Design a fully textile-based reactor made of GO/Fe ⁰ yarns as anode section and stainless-steel yarns as cathode section for electrocatalysis of wastewater.	Under editing

Polyester-knitted fabrics are used in this thesis to determine the most appropriate cationic agent for surface charge modification of the fabric. This knitted fabric was treated with Chitosan (CS), Poly(diallyldimethylammonium) chloride (PDDAC), hexadecylpyridinium chloride (HDPC), branched polyethylenimine (PEI) solutions separately; thereafter, their electrical, electrothermal, electromechanical performances were recorded.

Polyester non-woven fabrics were used for the catalytic application, and PAMAM was used as a cationic agent for non-woven fabrics [59].

A yarn coating line was designed and assembled for continuous yarn coating and then to use those yarns in the knitting machine (as the anode) among stainless steel fibres (as the cathode) and polyamide fibre (as the main body of the fully textile-based reactor). A simplified schematic of the various branches of this thesis is shown in Figure 4.

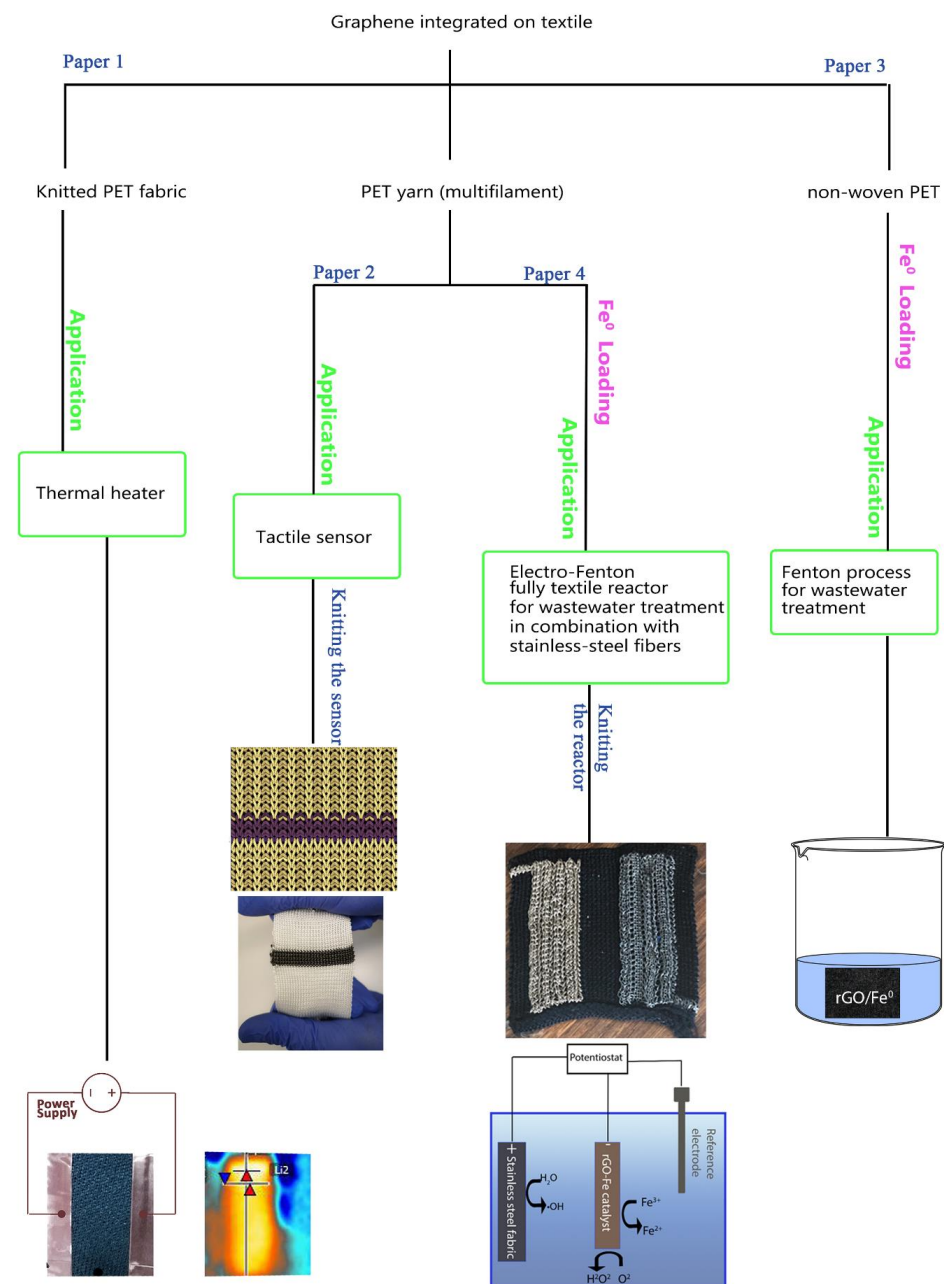


Figure 4. General theme of the thesis.

1.4 Scope and limitation of the thesis

The modification of conventional textiles with graphene and further immobilisation of catalysts fall under the scope of a multidisciplinary field, requiring scientific and technical competencies in textile technology, material science, surface chemistry, electrochemistry, among others. The context of this thesis is on the scope of material science, surface chemistry and electrochemistry, with applications in smart garments (tactile sensor and heating garments) as well as environmental remediation.

The research perspective and conclusions are based on laboratory-based experimental data gathering and their respective analysis. The necessary interpretation of the scope and limitation of this thesis highlight the following matters: 1. Surface charge modification of conventional textiles for further graphene oxide coating and iron immobilisation falls under the scope of textile chemistry, material science and inorganic chemistry to some extent. 2. The study of electrocatalytic wastewater treatment falls under electrochemistry and surface chemistry to some extent. The related field of multifunctional or smart textiles in other applications is beyond the scope of this thesis.

All the results presented here are collected in laboratory-scale trials. Large-scale (industrial) production of such multifunctional smart textiles is outside the scope of this thesis. They require further development and optimisation.

Chapter 2

State-of-the-art

Chapter outline

2.1. Surface charge modification of fabrics and yarns and graphene grafting

2.1.1 Preparation of textile surface for graphene grafting and iron immobilisation

Polyester fibres are hydrophobic; thus, to bring some hydrophilic properties to the fibres, fibres could be treated with a basic solution that would break branches off the polyester chain and give extra oxygen functional groups to the fibre. This will result in a hydrophilic fibre.

Alkalisiation (Hydrolysis): Alkaline treatment is one of the simplest and most effective chemical treatments to remove impurities on the fibre surface and break the polymer chain. In the hydrolysis of polyester, esters are easily hydrolysed by reaction with dilute alkalis, such as sodium hydroxide. Polyesters are attacked by alkalis, and ester linkages are broken; furthermore, ethane-1,2-diol is formed together with the salt of the carboxylic acid.

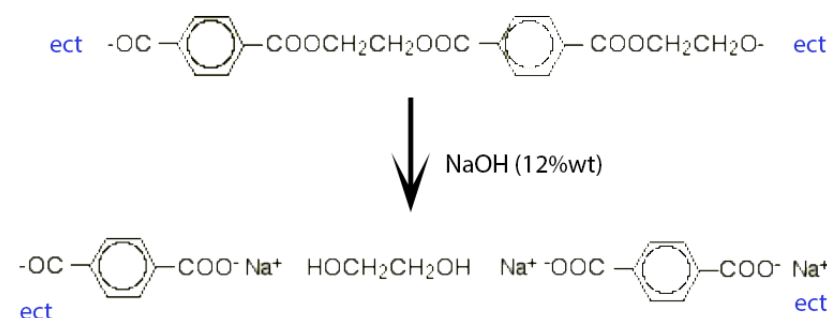


Figure 5. Hydrolysis of polyester via sodium hydroxide 12%.

2.1.2 Surface charge modification

As mentioned before, graphene oxide has a negative surface charge in dispersion; further, to have a strong electrostatic bonding between the fibre and GO nanosheets, it is important to change the surface charge of the polyester (naturally negative) to positive. There are different methods for surface charge modification.

Wet chemical surface charge modification: One method is textile treatment with cationic agents to produce positively charged functional groups on the surface of the textile as a part of this procedure to alter the surface charge of the polymer. Organic and inorganic agents could be used to modify the surface charge of the fibre.

Plasma treatment: Another method is textile treatment with a gas that has been electrified charged with freely moving electrons in both negative and positive states. The gas is partially ionised, and it could be a mix of neutral and atomic ions and electrons. The charged particles present in plasma interact with the fabric surface; consequently, it will temporarily change the surface charge of the fabric.

In this thesis, we worked on traditional wet chemical surface modification. Plasma treatment could be considered as a future work of this thesis in which both denier reduction and surface charge modification of the fibre would be done through nitrogen plasma treatment. The advantage of this method is the elimination of chemicals used and chemical waste.

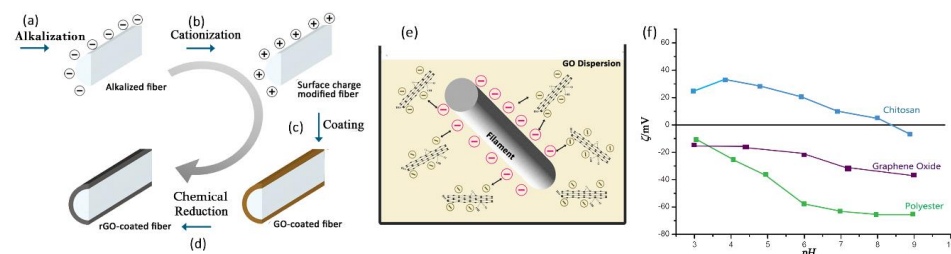


Figure 6. (a) Denier reduction (alkalisation), (b) cationisation, (c) surface charge modification, and (d) chemical reduction of the GO coated fibre to rGO coated fibres. (e) schematic representation of the repulsion between non-treated polyester yarn and GO nano-sheets. (f) zeta potential of polyester, chitosan, and graphene oxide in different pH values.

However, even though the plasma treatment is a more eco-friendly and sustainable method for surface charge modification of the fibre, in this thesis fibres are modified through wet chemical modification. This is due to the research limitations. Otherwise, plasma treatment is a preferable method for surface charge modification.

2.1.3 Methods of grafting functional polymers on polyester fibres for surface charge modification

To better understand the role of cationic agents in adsorption and their accompanying electrical properties, it is important to determine the degree of uptake of GO by polyester through various cationic agents and their electrical, electro-mechanical, and electro-thermal properties.

Grafting of hyperbranched poly-(amidoamine) dendrimer (ethylenediamine core and tertiary amine branches dendrimer) on polyester non-woven

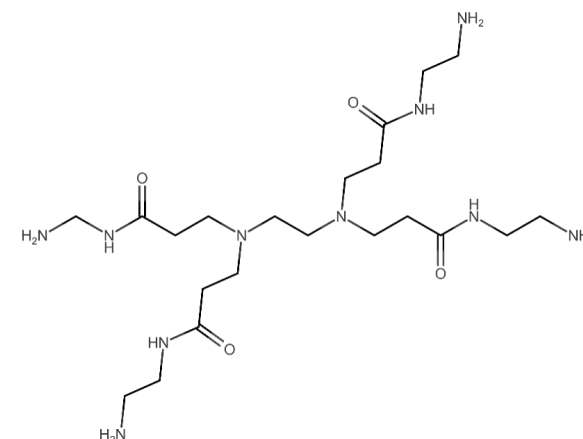


Figure 7. Chemical structure of hyperbranched poly-(amidoamine) dendrimer consists of ethylenediamine core and tertiary amine branches (PAMAM).

Poly(amidoamine) (PAMAM) dendrimer is an eco-friendly hyperbranched cationic polymer with explicit surface functional groups capable of forming complexes between textiles and GO/rGO via molecular encapsulation, covalent and non-covalent interactions [97]. Various studies reported the effectiveness of PAMAM in binding functional materials on a support matrix [98-103].

It has been reported [104] that strong interactions occur between GO/rGO and PAMAM in NH₂rGO-PAMAM nanocomposite when using PAMAM as the agent. However, to the best of our knowledge, PAMAM as a binder for GO coating on textiles has not been considered so far.

Grafting of Chitosan on polyester yarns

Chitosan (CS) has been used as a dispersant in GO dispersion [105], in addition to layer-by-layer self-assembly of GO and CS onto the textiles for UV-blocking applications [106]. Bio-composite membrane with a lamellar structure of reduced graphene oxide-chitosan (rGO-CS) [107] and also chitosan-graphene bio-composite nanofibres, have already been studied [108, 109]. However, chitosan could also be used as a cationic agent to modify the surface charge of the fabric. There are no reports where Chitosan has been used as the binder/cationic agent [96].

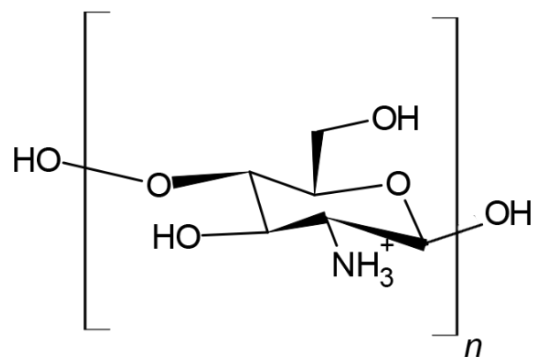


Figure 8. Chemical structure of protonated chitosan.

Grafting of polyethyleneimine (PEI) on polyester yarns

Branched polyethyleneimine (PEI) $H(NHCH_2CH_2)_nNH_2$ [93] has an extremely high cationic charge-to-density ratio, and each amino nitrogen can be protonated since the total cationic charge of PEI increases with the acidity of the solution [110]. These properties make it an excellent candidate for examination as a cationic agent.

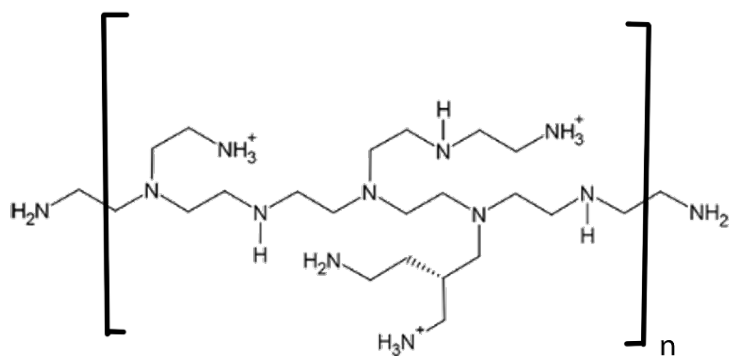


Figure 9. Molecular structure of cationised branched polyethyleneimine (PEI).

Grafting of poly-(diallyldimethylammonium) chloride (PDDAC) on polyester yarns

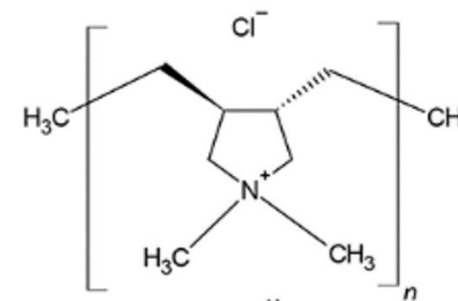


Figure 10. Molecular structure of poly-(diallyldimethylammonium) chloride (PDDAC).

Poly(diallyldimethylammonium) chloride (PDDAC), $(C_8H_{16}ClN)_n$, is an important water-soluble, cationic, functional commercial polymer that is used as a cationic agent to modify the surface of polyester fabric in the textile dyeing industry [95, 96] and also in the production of antibacterial fibre [111, 112].

Grafting of hexadecylpyridinium chloride monohydrate (HDPC) on polyester yarns

The effect of hexadecylpyridinium chloride (HDPC) $(C_{21}H_{38}ClN)$ on the surface charge of polyester fabrics and the absorbency of GO has already been studied [92]; thus, we consider it as a binder to compare with other agents.

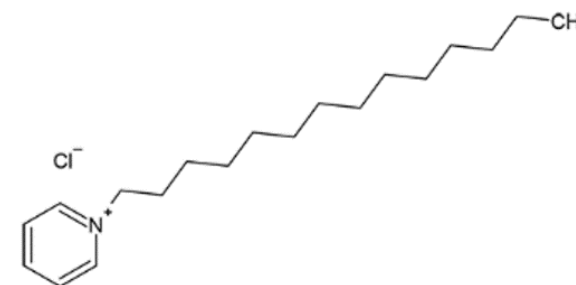


Figure 11. Molecular structure of hexadecylpyridinium chloride monohydrate (HDPC).

2.2 State-of-the-art in graphene-modified textiles for the heating element and tactile sensors

Flexible heating elements are used for a wide range of applications, including seat heaters in vehicles [17]; thermal de-icing in aircraft and ice-prevention of the structural membrane, such as in wings [113, 114]; heated floor panels in aircraft for cabin temperature controlling [115]; and electrically heated garments [18-20].

Graphene has been used as a heating element in ink before, as in the case of conventional heating systems made from alloy or copper [116]. It has been reported that the film-like heater made from strips of a Fe–Cr–Al-based alloy, which is available in the market, has many disadvantages, including a complicated fabrication process, heavyweight, rigidity and low heating efficiency [116-119]. Graphene ink also has been used to replace the conventional heating elements, and printing graphene on textile is already reported [83, 84]. However, this method has its challenges and limitations. Using graphene dispersion as a dye and coating the fabric or fibre with graphene seems to be the most cost-effective, scalable and reliable method to focus on due to its various properties, including thermal, conductivity, lightweight and flexibility, among others [80].

Graphene can be used as continuous temperature sensing systems in constructions and industrial applications [120, 121] because of its negative temperature coefficient (NTC) properties [122].

Further, a textile-rGO coated sample could be used as a tactile sensor for both pressure sensing [123] and strain sensing applications [124-127]; in this thesis, we benefit from both graphene properties and knitted fabric stretchability to create a tactile sensor that could be used in different applications.

2.3 State-of-the-art in Graphene-modified textile support for catalyst immobilisation

2.3.1 Inorganic catalyst immobilisation

The immobilisation of inorganic catalysts has been studied and well-established by other researchers. Accordingly, the catalyst could be separated more easily from the resulting products, and it could be reused several times; this will lead to a decrease in the process cost. A variety of inorganic catalysts by immobilisation of different metals, such as palladium, tungsten, nickel, platinum, cobalt and carbon, have been well studied [128]. The tendency of metal particles to agglomerate during the synthesis and their thermodynamic instability are serious drawbacks [129]. Further, the difficulty of catalyst separation and its high cost and the remaining waste forced researchers to overcome these problems by immobilisation of the catalyst on a support medium. Designing a support medium for the conventional catalysts systems could be more expensive than the catalyst itself. Hence, a low-cost, scalable system is highly required.

Immobilisation of catalysts on textile supports is a common and cheap way compared to conventional systems [130]. Considering textile as the main support, large-scale and cheap catalytical systems could be produced and reused in wastewater treatment systems.

2.3.2 Technique of catalyst immobilisation on textiles

Immobilisation of inorganic catalysts on textiles could take place through physical or chemical adsorption and encapsulation [131, 132]. The methods could be classified as:

1. Solvent-based or chemical-based dip-coating of textile. In this method, an aqueous solution of the inorganic catalysts is used to immobilise the inorganic catalyst on the surface of the textiles via an interaction (covalent, electrostatic bonding) between the catalysts and the fibres [133, 134].
2. Physical coating through padding, printing or encapsulation. In these methods, inorganic catalysts are forced to confine inside the textile support materials such as non-woven fabrics.

2.3.3 Main factors affecting the immobilisation of inorganic catalysts on textiles

There are many key factors affecting the immobilisation process. Apart from environmental conditions, such as temperature, pH, and concentration of the catalysts, there are other major aspects, such as:

1. Diffusion of the catalyst into the textile support
2. Interaction and stability of the immobilised catalyst
3. Method of immobilisation

To have an optimal diffusion, the functional groups present on the textile surface, namely its isoelectric point of the material, play an important key for better binding between the textile and the catalysis. Many approaches have adopted the surface modification of the textile for further ionic exchange and crosslinking or covalent bonding among the textile medium and the catalysts.

2.3.4 Challenges of inorganic immobilisation on textiles

Catalytic and electrocatalytic systems are gradually becoming important for sustainable and green systems. Recyclability and reusability of the catalyst are essential parts of the immobilisation process; it could ensure the decrease in catalyst consumption, the final cost, and improve the sustainability of the system.

The catalytic immobilisation on textile has its own significant challenges. Here are some examples of the challenges in the field:

1. Harsh condition of the immobilisation: normally, immobilisation requires harsh conditions, such as high temperature or special pH. When it comes to textiles, however, there are some limitations in terms of temperature and the pH of the system. Thus, optimisation of the process for such a medium is required.
2. Leach of catalyst: even though the catalysis is bonded to the textile, reports show that a large number of the catalysts leach out of the textile during the usage; thus, improvement in the bonding is highly demanded.
3. A problematic confrontation of the catalyst may occur, causing disorientation of the catalyst and, as a result, blocking of catalyst sites.
4. Interaction between textile and catalyst change in inherent properties of the textile, such as the strength of the fibres.

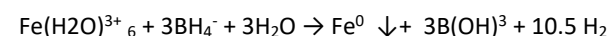
2.3.5 Catalytic system for wastewater treatment

Numerous advanced and efficient technologies are being replaced with traditional ways of wastewater treatment, such as coagulation and flocculation. These methods include Fenton and Fenton like processes applying various sources of iron ions and hydrogen peroxide [135], ozonation of the wastewater by infusion of ozone into the water [136], wet air oxidation [137], catalytic reduction [138], enzyme [139] and sonochemical degradation [140] systems.

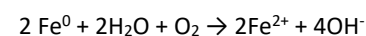
Among the named technologies, Fenton and Fenton-like systems as well as enzymatic systems, are the most promising processes for large-scale production and sustainability of the system.

2.3.6 Inorganic catalyst zerovalent iron particles (Fe^0)

Iron is the 4th most common element on the earth (6.3%) and the most common and cost-effective transition metal [141]. Zerovalent iron particles (Fe^0) are sub-micrometre particles of Fe metal [142]. The most common way to produce Fe^0 is a chemical reduction of an iron precursor using sodium borohydride (NaBH_4) as a reductant, as shown in the relation below:



Fe^0 tends to donate electrons due to its negative, reductive potential [143] ($E_V^0 = -0.44 \text{ V}$), and it rapidly oxidised in the presence of water and oxygen.



Fe^0 could produce reactive radicals, such as sulfate and hydroxyl radicals, by competently catalysing common oxidants, such as H_2O_2 , SO_5^{2-} , $\text{S}_2\text{O}_8^{2-}$ and O_2 [144]. These radicals could be used in wastewater treatment to recalcitrant organic pollutants [145].

2.4 State-of-the-art in wastewater treatment

In recent years, due to the fast industrialisation and growth of the textile dyeing industry, different contaminants such as pathogenic bacteria, heavy metal ions, and other organic toxicants are released into water streams, causing serious threats to nature as well as human health. These toxins could be highly toxic, chemically stable, bio-accumulators and resist decomposing [146]. Among all industrial wastewater, colourants produced in the textile industry share a big part of pollutants that need to be considered [147]. Colourants which are widely used in industries, such as textile industry, printing, packaging and clinical purposes, could be highly toxic [148]. When these dyes are released into nature, they can increase the biochemical and chemical oxygen demand (BOD & COD), inhibit plant growth and photosynthesis and finally, enter the food chain.

These types of pollutants are typically named emerging contaminants (ECs). They are most likely resistant to conventional wastewater treatments, for example, physical, chemical and biological wastewater treatment such as flocculation, coagulation, adsorption aerobic and anaerobic biological systems and filtration, or a combination of both physical and chemical treatments [149, 150].

As an alternative, novel generation treatment methods based on catalytic mechanisms as well as advanced oxidation processes (AOPs) are introduced for pollutant removal in wastewater systems [151]. AOPs are defined by the generation of hydroxyl radicals ($\bullet\text{OH}$) which are highly reactive ($E^0 = 2.8 \text{ V}$), and they are not the best option to remove pollutants from a medium such as water, soil and air [152].

2.5 State-of-the-art in advanced catalytic systems for wastewater treatment

To replace traditional wastewater treatments such as flocculation, coagulation and so on, an advanced system is required. Numerous new technologies based on both catalytic and non-catalytic systems are introduced for a better sustainable green removal of complex Nano-pollutants and hazardous compounds. For instance, supercritical water oxidation above the mixture's thermodynamic critical point [153], photocatalytic degradation by photocatalysts [154, 155], ozonation by infusion of ozone into the water [156], wet air oxidation [157], microwave degradation of wastewater through electromagnetic irradiation catalytic reduction [158], enzyme reduction systems [159], catalytic reduction [160], and the Fenton and Fenton-like systems using various sources of iron ions and H_2O_2 [135, 161], and electro-Fenton systems [162, 163].

2.5.1 Electrocatalysts

Catalytic reduction involves the usage of a solid catalyst and a reductant to degrade the wastewater pollutant through an electron-transfer reaction [164]. Numerous metallic

nanoparticles, such as gold, copper, nickel, cobalt and silver, are used for catalytic reduction of pollutants including phenols [165], pharmaceutical [166], pathogenic bacteria [167], and colourants [168] in wastewater.

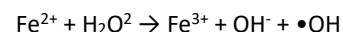
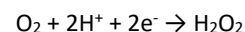
Immobilisation of these elements on a solid support is a conventional way for it to be used in catalytic systems. It ensures better stability of the catalyst and easy recovery and replacement; it could produce by-products that are non-toxic or substantially less toxic compared to those traditional technologies.

Several factors affect the performance of a catalytic system (as they are described in section 2).

- Stability of the catalyst in the reduction system.
- The concentration and ratio of the catalyst, reducing agent and pollutant.
- The temperature of the solution, a gradual increase of the removal reaction to a certain temperature point, has already been studied [169, 170].
- the pH of the system: as already reported [171], for a reduction to occur, the medium should not be alkaline. However, the reduction increases significantly by reducing the pH and having a more acidic medium.

2.5.2 Electrocatalytic system for wastewater treatment

Among the AOPs, the electrochemical advanced oxidation processes (EAOPs) are a promising alternative to the traditional AOP processes, as they are environmentally clean and could continuously produce a large number of hydroxyl radicals ($\bullet\text{OH}$) under the control of the applied potential [172, 173]. Hydroxyl radicals are produced in solution bulk through electrochemically assisted Fenton's reaction, where hydrogen peroxide is produced in situ from a 2-electrode reduction of O_2 on cathodes such as graphite-felt [174], following the reaction below:



2.5.3 Advanced oxidation process through Fenton's and electro-Fenton reaction

One of the most reliable systems used in wastewater treatment is Fenton-like treatments. Fenton chemical reaction is one of the most efficient advanced oxidations processed (AOPs). Fenton reaction is a reaction between ferrous ions (Fe^{2+} , Fe^{3+}) and hydrogen peroxide (H_2O_2) that results in the formation of hydroxyl radicals, which is a strong oxidant ($E^0 = 2.8 \text{ V}$). This oxidant is capable of degrading organic pollutants in water [152, 175-177].

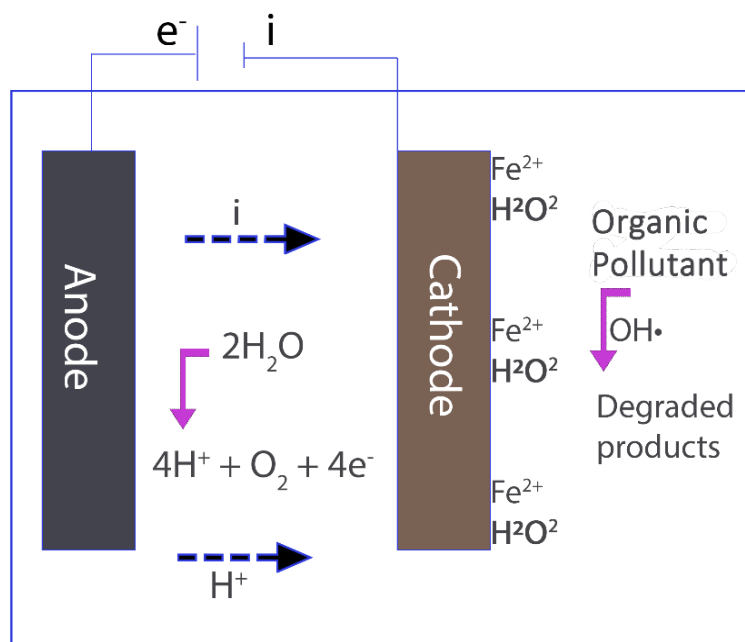
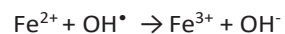


Figure 12. Electro-Fenton reaction set-up.



The produced hydroxyl radicals should degrade organic substances in wastewater. However, in the Fenton chain reaction, the rate constant of the first reaction is between 53 and 76 $\text{M}^{-1}\text{s}^{-1}$ [178, 179]. While that for the second reaction is 0.01 $\text{M}^{-1}\text{s}^{-1}$ [180]. This shows that ferrous ions are consumed more rapidly than what is produced in the Fenton system. In addition, ferrous ions can also be rapidly destroyed by H_2O_2 with the range of $3.2 - 4.3 \times 10^8 \text{ M}^{-1}\text{s}^{-1}$ [181].



Therefore, a more ferrous ion dosage is required to keep the moderate hydroxyl radical's production. Moreover, there is an issue of iron sludge formation. Recently, electrochemical methods in the Fenton process called electro-Fenton have been used in many applications, as well as wastewater treatment.

Electro-Fenton systems could be categorised into four systems:

Ferrous ions are externally applied, and both hydrogen peroxides are simultaneously generated at the cathode, focused on hydrogen peroxide production on carbon felt [182], graphite [183], and activated carbon fibre [184, 185], or carbon-PTFE [186] cathodes.

Hydrogen peroxide is externally applied, and ferrous ions are electrogenerated via the reduction of ferric ion or ferric hydroxide sludge [187].

Both hydrogen peroxide and ferrous ions are electrogenerated at a specific anode and cathode via 2-electroreduction of sparged oxygen [188].

In the electro-Fenton system, an electrical generator is used to simplify the reduction of dissolved oxygen in the water at the surface of the cathode and form hydrogen peroxide to participate in the Fenton reaction. At the same time, water is oxidised at the surface of the anode (Figure 12) [189-191].

The disadvantages with electro-Fenton are corrosion of the electrodes used in the system as well as power consumption ($\sim 5-70 \text{ A.m}^{-1}$) [192]. The goal of this thesis is to design a textile-based reactor that could be produced on a large-scale for wastewater treatment in the industry.

2.6 Main Factors affecting the electro-Fenton process

Presence of H_2O_2

Hydrogen peroxide concentration affects the radical $\bullet\text{OH}$ generation; therefore, keeping the right concentration of hydrogen peroxide at its optimal performance level is a key factor affecting the degradation efficiency of organic pollutants. Increasing the concentration of hydrogen peroxide could increase the efficiency of the degradation. However, if it exceeds the optimal concentration, it would increase the scavenging effect of radical $\bullet\text{OH}$, which occurs by hydrogen peroxide.

The concentration of ferrous ions

Fe^{2+} works as a catalyst and catalyses the decomposition of hydrogen peroxide to produce highly oxidative radical $\bullet\text{OH}$ that could degrade stubborn organic pollutants in the wastewater. Hence, the concentration of Fe^{2+} is an essential factor affecting degradation efficiency.

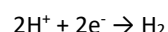
Temperature

The activation energy of Fenton's reaction is low; hence, it could be performed at room temperature. An increase to 35–40 $^\circ\text{C}$ was found to slightly increase the mineralisation efficiency, and ions and electrons are more flexible, having lower resistance (R) to the

solution. However, the high temperature could decrease the decomposition of H₂O₂. The suitable temperature for the electro-Fenton process was found to be between 20 to 30 °C.

The pH of the solution

The pH is a critical control factor. The degradation of organic pollutants is very sensitive to the pH value of the wastewater. At low pH values (≤ 2), the scavenging effect of radical •OH gets stronger; moreover, it leads to the formation of peroxonium ion (H₃O₂⁺) from the protonation of hydrogen peroxide and reducing the formation of H₂O₂. As it enhances the H₂ evolution at the cathode, as indicated by the following reaction,



The optimal pH range for a good performance is $2.5 \leq \text{pH} \leq 3.5$. A very high pH value would provoke catalyst loss by hydrolysis of Fe³⁺, resulting in a decrease in decomposition efficiency.

Power density

Usually, increasing the current density results in the dissolution rate of the anode and H₂O₂ generation on the cathode. The current (I) and the voltage between the electrodes (U) have a substantial impact on the release of H₂O₂ and Fe²⁺ concentration in the system during the electro Fenton process. Cathode enhances through Faraday's law [193, 194]:

$$C \text{ (gFe/m}^3\text{)} = \frac{I \cdot t \cdot M}{z \cdot F \cdot V} \times 10^3$$

where F is Faraday's constant (96,485 coulomb/mol), t is operation time (s), M is the molecular weight of Fe (56 g/mol), z is the number of an electron transfer ($Z\text{Fe} = 2$), V is the volume (L) and I is the electric current (A).

The greater energy consumption leads to an increase in temperature and the cost of treatment. Apart from pH, the most important factor of the electro-Fenton process is the applied potential in 3-electrode cells or the applied current in 2-electrode cells. In a 3-electrode cell, the potential of the cathode will be set to a constant value corresponding to a 2-electron reduction wave of O₂ to form H₂O₂ optimally. Furthermore, it depends also on the nature of the cathode.

Mass transfer

Mass transfer limitation is considered an important drawback of catalytical systems [195]. The catalytic reaction occurs after the diffusion step toward the catalyst particles (irons) and through the pore within the particles, which is called internal diffusion. Introducing a heterogeneous catalyst could reduce the mass transfer limitations [196, 197].

Electrode distance

Usually, the greater the distance between the electrodes, the greater the decrease in voltage or current during the electro Fenton process.

Electrode arrangements

The electrode arrangements could affect removal efficiency and energy consumption. Finding the best arrangement could improve the efficiency of the system.

2.6.1 Advantages and disadvantages of Electro-Fenton over convention Fenton reaction

The advantages of Electro-Fenton over convention Fenton reaction are:

- ✓ In situ generation of reaction: reagents remove the necessity to have storage and dosage facilities for those chemicals such as hydrogen peroxide.
- ✓ Anodic dissolution of Fe electrode is possible in a manner at neutral pH; however, the issue of unnecessary ferric hydroxide sludge generation will still exist.
- ✓ Ease of operation and automation.
- ✓ Continuous cathodic regeneration of Fe³⁺ to Fe²⁺.
- ✓ It has higher mineralisation rates of organic compounds compared to the conventional Fenton reaction process. This is due to additional OH• radical electrocatalytic generation at the anode.

The disadvantages of Electro-Fenton over convention Fenton reaction are:

- ✗ The system requires corrosion-resistant electrodes because of the corrosive acidic environment of the process. Acidic media is a superior condition for electro generation of H₂O₂ because, in basic media, the reduction of O₂ occurs over the following reactions:

$$\text{O}_2 + \text{H}_2\text{O} + 2\text{e}^- \rightarrow \text{HO}_2 + \text{OH}^-$$

$$\text{O}_2 + 2\text{H}_2\text{O} + 4\text{e}^- \rightarrow 4\text{OH}^-$$
- ✗ Formation of iron (III) oxide-hydroxide sludge. (For that, in situ reductions of Fe(III) to Fe(II) would be the most preferable for avoiding excessive sludge production). Nevertheless, the reaction rates are only reasonable at pH below 2.5. Another approach to reducing sludge generation is using the solid iron catalyst in the form of sieves, particles, and iron oxides, which can later simply be removed from the treated solution.
- ✗ Relatively low rates of electrochemical generation of H₂O₂, which can be enhanced by some types of electrodes.
- ✗ The high acidity of the treated water should be neutralised and needs additional chemicals use.

2.7 Strategies for thesis design

The design and strategy of this thesis were chosen based on the state-of-the-art technology, research gaps, and potential research perspective. The purpose of the study is to optimise the coating of textile with graphene oxide and further immobilise zerovalent iron particles as inorganic catalysts on the graphene-coated textile support materials.

The reason behind choosing these two materials is the potential of graphene oxide for grafting and the intended applications of iron particles in wastewater treatment. Zerovalent iron particles were selected for this thesis based on their efficiency in catalysing heterogeneous Fenton and electro-Fenton reactions.

The overall purpose of the study was extended into three main objectives:

1. Surface modification (pre-modification of the textile's surface charge) of the textile (polyester and polyamide yarns as well as polyester knitted fabrics) for further electrostatic bonding among the fibres and graphene oxide and to increase their electrical properties. The resulting graphene-coated textiles are conductive enough to prepare a textile heating system.
2. Immobilisation of zerovalent iron particles on graphene oxide coated polyester non-woven fabrics.
3. Immobilisation of zerovalent iron particles on graphene oxide coated polyester yarns (as the cathode) for use in an electro-Fenton system in combination with stainless steel fibres (as the anode).

Chapter 3

Material and methods

Chapter outline

3.1 Materials

3.1.1 Chemicals

Sodium hydroxide (NaOH) solution (Sigma-Aldrich Co., USA) was used for the alkalisation of the fabrics. Chitosan (CS) (Sigma-Aldrich) solution was prepared by dissolving it in acetic acid solvent (0.1 M) [198]. Poly-(diallyldimethylammonium) chloride (PDDAC), (Sigma-Aldrich), branched polyethylenimine (PEI) (Sigma-Aldrich) and hexadecylpyridinium chloride monohydrate (HDPC) (Sigma-Aldrich) aqueous solutions were prepared by dissolving them in ultrapure water [199]. A commercial aqueous dispersion of graphene oxide (4 g.L⁻¹) (Graphenea S.A., Spain) was used in experiments. Later, sodium hydrosulfite (Na₂S₂O₄) (Sigma-Aldrich), Hyperbranched poly-(amidoamine) (PAMAM) dendrimer, petroleum ether, ethanol (C₂H₆O), hydrogen peroxide (H₂O₂), FeCl₃·6H₂O and sodium tetrahydroborate (NaBH₄), ethanol (Et-OH) and crystal violet dyes (CAS No. 548-62-9) were purchased from Sigma-Aldrich Ltd. All purchased chemicals used in this study were of analytical grade and used as received.

3.1.2 Yarns

An air-jet textured polyester multifilament yarn (167dtex144) was selected for the experiment. A multifilament stainless steel yarn (14/1 x 90/200z, Bekinox®) was used for knitting the fully textile-based reactor.

3.1.3 Polyester non-woven fabric

The polyester non-woven fabric used in the catalyst system was fabricated at the University of Borås based on polyethylene terephthalate (PET) fibres (average diameter 12 µm). The non-woven fabric was produced using a needle punching process. The physical characteristics of the fabricated non-wovens are shown in Table 4. Non-woven fabric was pre-modified with poly-(amidoamine) dendrimer (ethylenediamine core and tertiary amine branches dendrimer) (PAMAM).

Table 4. Physical characteristics of polyester non-woven membranes

Physical characteristics	Values
Mass per unit area (g/m ²)	98.00
Thicknesses (mm)	0.94
Fibre density	0.80
Porosity (%)	99.91
Air permeability (mm/s)	854.20

3.1.4 Polyester knitted fabric

A rib-knitted polyester fabric (gauge 20; air-jet textured filament; dtex 167/144/1; produced in house by an OVJA 0.8 E knitting machine, Mayer & Cie CO., Germany) was prepared for the experiment. The weight of the fabric was 176.5 g.m⁻². Fabrics were cut into 3×9 cm² specimens.

Polyester fabrics were pre-modified with CS, HDPC, PDAA, and PEI and further dip-coated with GO dispersion to identify the most relevant candidate for use in different applications.

3.2 Methods of material preparation

3.2.1 Preparation of polyester yarns

Polyester fibres were treated with an aqueous solution of sodium hydroxide (12%wt) at 60°C for 90 min; further, yarns were washed and dried in the oven at 80°C for 10 min [200, 201]. Afterwards, yarns were treated in a solution of Chitosan (4 g.L⁻¹) and HDPC (4 g.L⁻¹) at 6°C for 60 min, separately [202]. A schematic picture of the procedure is shown in Figure 13.

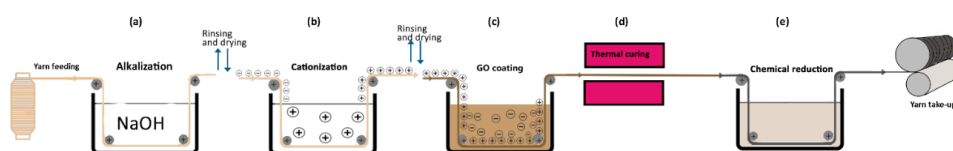


Figure 13. Illustration of the functionalisation process. (a) Alkalisation of the yarn, (b) surface charge modification, (c) coating with graphene oxide (GO), (d) thermal curing and (e) chemical reduction of GO-modified yarn to generate electrical conductivity.

3.2.2 Preparation of knitted polyester fabrics

To increase the wettability and dyeability of the fibres and fabrics, samples were alkalisied with an aqueous solution of sodium hydroxide (12%wt) with a liquor ratio of (1:50) at 60°C for 90 min. Further samples were selectively modified with an agent-based on the textile type and the application. The results display the adsorption of GO into Chitosan and HDPC-modified yarns seem promising for use in industrial applications. The use of these agents as mordants not only advances the qualitative and quantitative adhesion of GO to textiles but also significantly increases the conductivity of the yarn.

3.2.3 Preparation of polyester non-woven fabric for the Fenton process

Polyester non-woven fabrics were prepared in two steps for further immobilisation of catalysis [161, 203-205].

First, the smooth hydrophobic fibre surface of the polyester non-woven fabric was modified by the dissolution of amorphous regions and surface oxidation through the alkalisation process [80]. The non-woven fabric was continuously stirred in an alkaline bath containing 12%wt sodium hydroxide and distilled water (1:50) at 60°C for 90 min. Here, PET fibre undergoes a nucleophilic substitution reaction where chain scission of PET occurs, resulting in the formation of hydroxyl and carboxylate end groups, which introduces the hydrophilic properties to the fibre surface. The resulting non-woven fabric was then rinsed with distilled water, filtered and dried at 90°C.

The resulting hydrophilic polyester non-woven fabrics were modified by hyperbranched polyamidoamine (PAMAM) dendrimer consisting of ethylenediamine core and tertiary amine branches for constructive surface chemical properties during the integration of zerovalent iron nanoparticles (Fe⁰) and graphene oxide through chemical grafting method as described elsewhere [69, 168, 206]. Further, the PET non-wovens were immersed in an ethanol/water (3:1 v/v) bath for 4h at 70°C in the atmospheric air chamber. The resultant material denoted as PET-PAM was then rinsed, filtered and dried at 60°C for 24 h. The preparation of the polyester fibres for further catalyst immobilisation is illustrated in Figure 14.

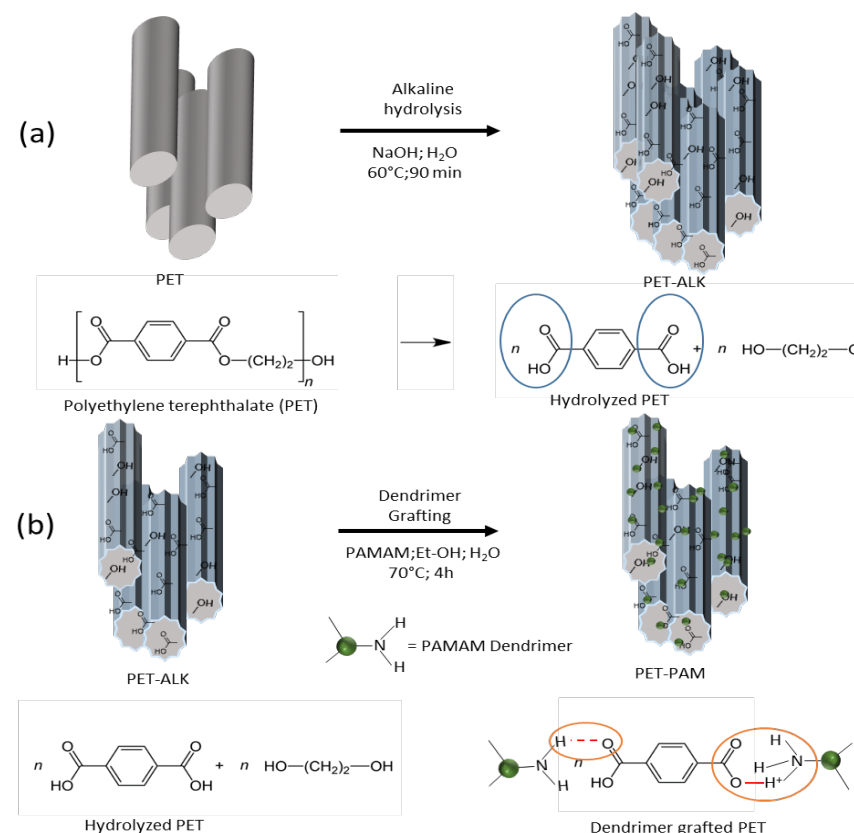


Figure 14. Schematic illustration of the modification process; (a) alkaline hydrolysis of PET membranes; (b) chemical grafting of hyperbranched poly-(amidoamine) (PAMAM) dendrimer.

3.3 Method of graphene grafting

3.3.1 Continuous yarn coating with graphene oxide

Surface charge modified yarns were coated with GO in an in house made continuous system (Figure 15) and further reduced with an aqueous solution of $\text{Na}_2\text{S}_2\text{O}_4$ [58] (50 mM) and a liquor ratio of 1:100 for 30 min at 95°C. Figure 15 shows a schematic and digital image of the coating line.

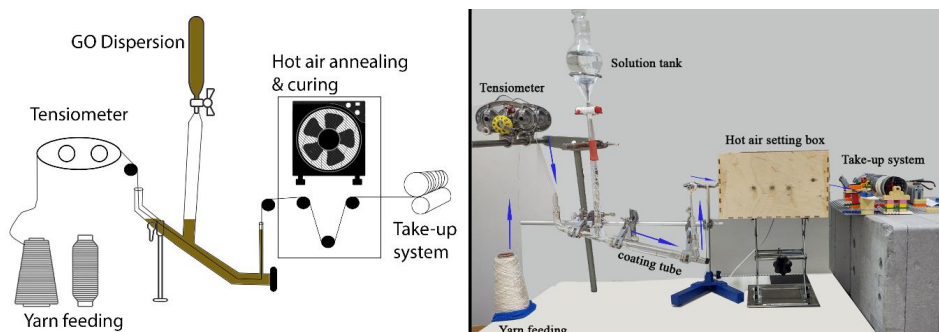


Figure 15. Schematic representation of continuous yarn coating line. And a digital image of the in-house made set-up for yarn modification.

A cationised yarn could easily adsorb negatively charged GO and further air dry in a curing system.

Table 5. The composition of polyester yarn samples.

Sample	Yarn	Surface modification agent	Coating layer
PET	Alkalised polyester	-	-
PET-GO	Alkalised Polyester	-	graphene oxide
PET-CS-GO	Alkalised polyester	chitosan	graphene oxide
PET-HDPC-GO	Alkalised polyester	hexadecylpyridinium chloride	graphene oxide
PET-rGO	Alkalised polyester	-	reduced graphene oxide
PET-CS-rGO	Alkalised polyester	chitosan	reduced graphene oxide
PET-HDPC-rGO	Alkalised polyester	hexadecylpyridinium chloride	reduced graphene oxide

3.4 Method of catalysts immobilisation

In situ immobilisation of zerovalent iron on polyester non-woven

Non-woven polyester fabrics were selected for immobilisation of zerovalent iron. Samples are named as shown in Table 6.

Table 6. Modification steps for the polyester non-woven fabric

Sample Name	Modification 1	Modification 2	Modification 3	Modification 4
Pristine PET	-	-	-	-
PET	Alkali hydrolysis	-	-	-
PET-GO	Alkali hydrolysis	-	GO incorporation	-
PET-rGO	Alkali hydrolysis	-	rGO incorporation	-
PET-rGO-Fe ⁰	Alkali hydrolysis	-	rGO incorporation	Fe ⁰ incorporation
PET-PAM	Alkali hydrolysis	PAMAM grafting	-	-
PET-PAM-GO	Alkali hydrolysis	PAMAM grafting	GO incorporation	-
PET-PAM-rGO	Alkali hydrolysis	PAMAM grafting	rGO incorporation	-
PET-PAM-rGO-Fe ⁰	Alkali hydrolysis	PAMAM grafting	rGO incorporation	Fe ⁰ incorporation

Coating of graphene oxide and immobilisation of zerovalent iron nanoparticles on the polyester fabric were achieved through dip-coating and the in-situ reduction-immobilisation method (Figure 16). First, PET fabric was dipped in ultra-sonicated (for 30 min) aqueous dispersion of GO (0.4 wt.%; pH=3; L: R 1:100) at 45°C for 30 min under mild stirring. The resultant PET-GO and PET-PAM-GO were oven-dried at 90°C for 90 min. Later, iron particles were loaded and stabilised in GO-coated polyester yarns by using $\text{FeCl}_3 \cdot 6\text{H}_2\text{O}$ as a precursor [69, 70]. Hence, GO modified samples were dipped in a solution containing iron precursor (0.6 wt.%), water (75%) and ethanol (25%), L/R 1:100 for 4 h under stirring at room temperature. The resultant PET-GO-Fe³⁺ and PET-PAM-GO-Fe³⁺ were immediately reduced into PET-rGO-Fe⁰ and PET-PAM-rGO-Fe⁰, respectively, by using NaBH_4 aqueous solution (5 mM, L/R 1: 50) at 95°C for 45 min under stirring. The resultant fabrics were then rinsed with warm ultrapure water, dried at 70°C for 90 min, and stored in an O_2 -free desiccator.

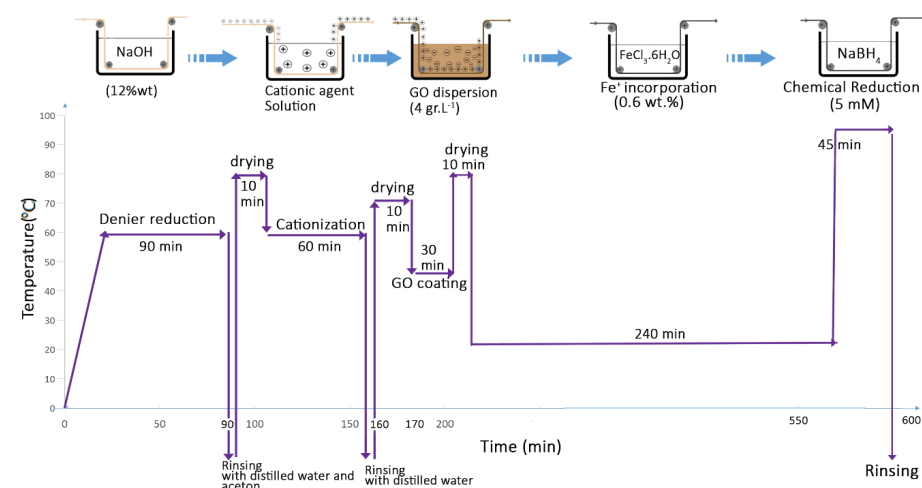
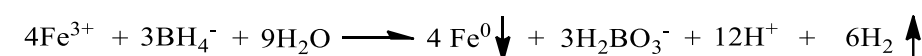


Figure 16. Time-temperature scheme for the process of (a) alkalisation (denier reduction) of polyester yarns; (b) PAM-grafting; (c) incorporation of GO; (d) incorporation of Fe^{3+} (e) in situ immobilisation of rGO and Fe^0 .

Digital images of PET non-woven, GO-coated PET, rGO-coated PET and finally, iron-immobilised rGO-coated PET are shown in Figure 17.



Figure 17. Digital Images of the samples (a) PET, (b) PET-PAM-GO, (c) PET-PAM-rGO, (d) PET-PAM-rGO-Fe⁰.

3.5 Reactor designed in the electro-Fenton process

A fully textile-based reactor was knitted on the CMS 330 TC with a 12-gauge. The fabric structure was full rib, with tubular sections over the conductive yarn. The tubular sections had tuck stitches to ensure that the fabric did not 'bubble' too much. Density wise, it would be measured from the fabric you have, counting the number of stitches and rows over 1cm. It would vary over the full rib fabric and the tubular. The reactor is made out of three different sections:

1. Non-conductive polyamide base fibres
2. Stainless steel fibres for the cathode section
3. Graphene/Fe⁰ fibres for the anode section

The structure pattern and the sample image are shown in Figure 18.

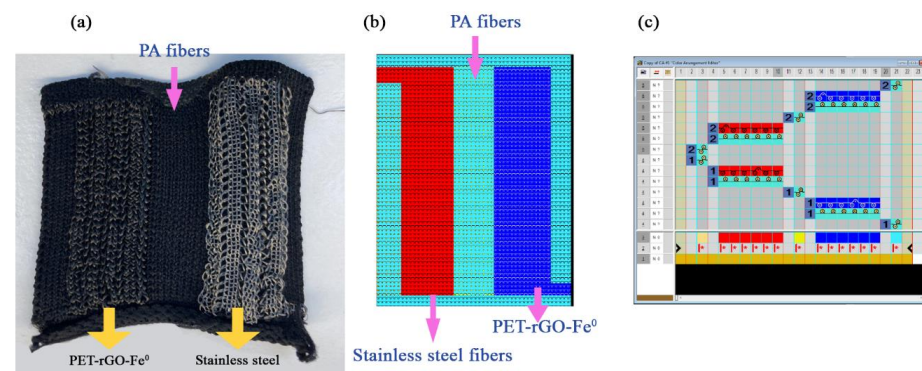


Figure 18. (a) the fully textile-based reactor for electro-Fenton water treatment, (b) the knitting pattern designed by the CMS 330 software, and (c) the needle arrangement of the reactor.

After the preparation of the reactor, the graphene oxide yarn section was iron immobilised according to the procedure explained in section 3.4.

3.6 Methods for analysis and material characterisation

Sessile-drop goniometry

Surface tension characterisation of the modified textiles was measured through the contact angle measurement by an optical tensiometer (Attension theta, Biolin Scientific Co., Sweden). Typically, the sample was placed on the sample stage of the instrument. The height of the stage was adjusted with the camera, and the mounting syringe contained distilled water. 5 μ l of the size of the water droplet dropped on the surface of the sample, and it was recorded for 10 sec. Data collection panel of the Theta Optical Tensiometer records the analysis of the drop by using One Attension software and the Young-Laplace equation [207]. All the experiments were triplicated, and the mean contact angle has been considered.

Colour measurements

The reflectance spectra of samples in the visible spectral range ($\lambda=400$ -700 nm) were recorded with a Datacolor Check Pro spectrum (Datacolor Co., USA), and the colour strength of the wavelength with maximum absorbency (400 and 410 nm for GO-modified and rGO-modified samples) was calculated according to Kubelka-Munk Theory [208, 209]:

$$\frac{K}{S} - \frac{K_0}{S_0} = \frac{(1-R)^2}{2R} - \frac{(1-R_0)^2}{2R_0}$$

where K_0 and S_0 are the absorption coefficient and scattering coefficient of the control samples. K and S are the absorption and scattering coefficients of the modified samples. R and R_0 are reflectance of the modified sample and control sample, respectively.

The colour strength is proportional to the concentration of colloidal dye uptake by the fabric. It could be written as below, where C is dye concentration and k is a constant:

$$\Delta \frac{K}{S} = k\Delta C$$

The samples' colour properties were expressed in terms of CIELab values, and the total colour change (ΔE) of each sample was investigated exclusively. ΔE in the CIE system is obtained by the following equation [210, 211]:

$$\Delta E_{ab}^* = \sqrt{(L_2^* - L_1^*)^2 + (a_2^* - a_1^*)^2 + (b_2^* - b_1^*)^2}$$

where a^* is the coordinate responses in the green to the red colour range, b^* is the coordinate responses in the blue to the yellow colour range, and L^* is responding to the brightness and darkness of the colour.

Chemical Compositions

An FTIR spectrometer (Nicolet iS10, Thermo Fisher Scientific Co., USA) was used to record Fourier transform infrared (FTIR) spectra to investigate the chemical compositions of the materials. The spectra were taken between wavenumber 400 cm^{-1} to 4000 cm^{-1} . The samples were drilled before IR analysis, and background spectra were recorded on air.

A spectrophotometer (PHI 5500 ESCA, Physical Electronics Inc., USA) equipped with monochromatic aluminium (Al) source (photon energy = 1486.6 eV) was used to study the X-ray photoelectron spectroscopy (XPS) of the samples. The binding energy (BE) positions were related to an adventitious carbon peak ($\text{C1s} = 285.0$ eV) before data analysis due to the insufficient conductivity; an electron neutraliser was used to compensate for the charge. A narrow scan for the chemical state analysis with a selected range for individual elements and step size of 0.1 eV/step and a survey scan for the compositional evaluation (Energy range of 0 to 1100 eV; step size of 0.4 eV/step), was performed [212-215].

Microscopic measurement

The surface morphology of the samples was recorded by scanning electron microscope (SEM) using ZEISS EVO15, MEB HR ZEISS Sigma 300 electron microscope, and digital optical microscope (OM) from Dino-Lite. Before SEM imaging, all samples were metalised by conductive materials (gold) using the Biorad E5200 device. Average fibre diameter and particle size of materials were investigated from HR-SEM images using image analysis software ImageJ1.40G [69] and obtained standard deviation and corresponding size distribution histograms. For OM, samples were placed firmly in the sample stand as it is. Images were captured by using DinoCapture 2.0 software.

Thermogravimetric analysis (TGA)

Thermogravimetric analysis (TGA) demonstrates the thermal degradation of the studied sample by measuring the change in the mass of the sample. Thermogravimetric curves are plotted in integral (relative mass in % of initial mass; TG) and differential (a derivative of TG curve over time; DTG curves) forms. The peak at the DTG curve represents the T_{max} of the composition, and the temperature corresponding to 5 wt.% degradations in the TG curve is noted as T_{onset} . Approximately 10 mg of the sample was placed in a platinum crucible, and TG and DTG curves were recorded (TGA Q500, TA Instruments Co., UK) under nitrogen flow (40 $\text{cm}^3 \text{min}^{-1}$) from 25°C to 600°C at a linear heating rate of 20°C min^{-1} .

Differential scanning calorimetry (DSC)

DSC is a key technique to associate temperatures with specific physical properties of the substances and direct determination of the enthalpy related to the process of interest [216]. DSC measurement (DSC Q2000, TA Instruments Co., UK) was performed in a nitrogen atmosphere on approximately 5 mg of each sample. Samples were heated from 25 to 200°C in aluminum pans at a heating rate of 10°C min^{-1} , held in isothermal condition for 2 min to destroy its anisotropy and cooled down at a cooling rate of 10°C min^{-1} to 25°C. Then, it was heated up to 200°C with the same heating rate. All the thermal parameters were calculated on the second heating scan.

Electrokinetic measurement

Zeta-potential (ζ) values of fabrics as a function of the pH values of the electrolyte solution (0.001 M KCl) was measured for all samples. The measurement was carried out using the

streaming potential method, in which a liquid is forced to flow through two parallel plates containing samples, and streaming potential is generated (Surpass, Anton Paar AB., Sweden). To adjust the pH values of the electrolyte solution, 0.01 M HCl and 0.01 M NaOH were used. The zeta potential values were calculated using the Helmholtz-Smoluchowski equation [217].

Electrical performance measurement

The electric conductivity of the knitted and non-woven polyester fabric was measured by a 4-probe method using tungsten probes and 34401A Digital Multimeter, 6½ Digit (Keysight Technologies Inc.). Typically, the samples were placed firmly under the probes, a DC is applied between the outer two probes, and a voltage drop is measured between the inner two probes (Figure 19). Sheet resistance (R_{sh}) of samples was calculated from direct current (DC) electrical resistance measurement, based on the equation below. However, it should be noted that the most accurate measurements are taken from the centre of the sample.

$$R_{sh} = \frac{\pi}{\ln(2)} \frac{\Delta V}{I}$$

Here, R_{sh} is the sheet resistance, ΔV is the change in voltage measured between the inner probes, and I is the current applied between the outer probes. The sheet resistance is expressed with the units of Ω/sq to differentiate it from bulk resistance. Using the thickness of the measured material, the sheet resistance has been used to calculate its resistivity according to the equation below:

$$\rho = R_{sh} \cdot t$$

Where ρ is resistivity, and t is the sheet thickness.

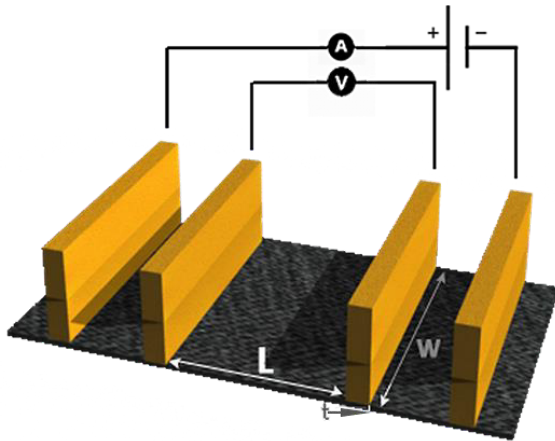


Figure 19. A 4-probe measurement of the electrical sheet resistance (R_{sh}) of the fabric.

Electro-mechanical performance of knitted graphene-modified fabrics

The relative changes in electrical resistance of knitted polyester fabrics in both wale and course directions at various strain levels (0–35%) were recorded by using a self-made fabric dynamic resistance machine, programmed with ACT controller software (SMC Co., USA) (Figure 20).

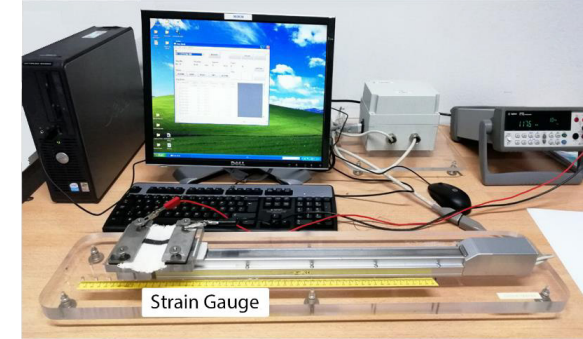


Figure 20. Build-up strain gauge powered by software for electromechanical measurements.

Electro-thermal performance of knitted graphene-modified fabrics

To investigate the electro-thermal performance of the samples, a range of voltages (5–30 V) was applied to the rGO-modified fabrics through a DC power supply. An infrared thermal camera (FLIR-E63900, FLIR System Co., Sweden) and a 3-channel thermal data logger (SD200 Extech, FLIR System Co., Sweden) were used to characterise the surface temperature distribution.

To better understand the thermal behaviour of the modified fabrics, thermal characterisation of samples was carried out with a differential scanning calorimeter (DSC Q2000, TA Instruments Co., UK) under a nitrogen atmosphere.

3.6.1 Methods for assessing catalytic pollutant removal

Uv-visible (UV-VIS) spectroscopy

A UV/Visible spectrophotometer (Thermo Scientific™ Evolution 201 UV-Vis spectrophotometer) was used to monitor the dye removal from the wastewater. The instant to initial absorbance ratio of dye concentration in the solution (C_t/C_0) was measured at various time intervals. The colour removal (conversion percentage) was calculated according to the concentration at pre-determined time intervals by using the equation below [218], referring to the absorbance calibration curve of the known standard solution.

$$\text{Colour removal \%} = \frac{C_0 - C}{C_0} \times 100$$

Here, C_0 = Initial concentration of colourants solution, C = Concentration of the colourants at different time intervals.

Chemical oxygen demand (COD) analysis

Chemical oxygen demand (COD) analysis was applied to measure the toxicity reduction of water after the removal of dyes (ASTM D1252-06 (B)) using COD vials provided by CHEMetrics, Inc. (USA) [59, 219]. The result is stated as parts per million (mg.L^{-1}) and calculated according to the following equation:

$$\text{COD (mg.L}^{-1}\text{)} = (23010 \times \Delta_{620}) \times 3$$

Here, Δ_{620} represents the absorption difference (at $\lambda_{620\text{nm}}$) of the vials after digestion of the water sample at 150°C for 2h.

Reusability

In both catalytical and electrocatalytic studies, after completion of removal of crystal violet dye, textiles were removed from the solution and washed with distilled water before reuse for another removal cycle. Samples were tested to evaluate their potential recyclability and reusability in a catalysis system under the same experimental conditions.

Particle size measurement

An image processing software was used to analyse SEM and TEM images of the samples to measure the average size of the particles.

Cyclic voltammetry (CV)

Electrochemistry is a powerful tool to investigate reactions involving electron transfers. Electrochemistry relates the flow of electrons to chemical changes, which could be measured through cyclic voltammetry. In inorganic chemistry, the resulting chemical change is often the oxidation or reduction of a metal complex (such as iron). An electrode is an electrical conductor, typically platinum, gold or carbon. Using an external power source (such as a potentiostat), a constant voltage can be applied to the electrode to modulate the energy of the electrons in the electrode. Once the electrons in the electrode are at higher energy than the LUMO of iron, an electron from the electrode is transferred to the iron.

Cyclic voltammetry (CV) is widely used to study electrochemical reactions. In a 3-electrode system, a constant potential or current could be applied through a working electrode (WE) (here GO/Fe⁰), while having a counter electrode (here stainless-steel fabric) and a standard reference electrode (Ag/AgCl) to keep the potential or current constant. A schematic representation of the 3-electrodes cell is shown in Figure. 21.

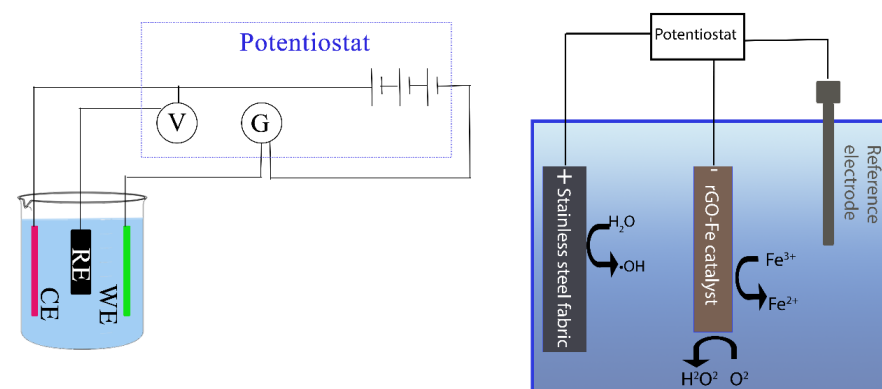


Figure. 21 3-electrode set-up for electro-Fenton process.

Changing the driving force of a chemical reduction requires altering the identity of the molecule used as the reductant [220].

The measurement was performed in X solution at pH X and room temperature; the scan range was between (x-y V). A reactor was designed with stainless steel as a counter electrode, and graphene-Fe⁰ loaded fibres were used as a working electrode. And both electrodes were knitted in a single designed reactor.

Chapter 4

Results and Discussion

4.1 The effect of cationic agents on performance of graphene-modified knitted polyester fabrics

To study the effect of the cationic agent on the textile, a knitted polyester (PET) fabric was used for the study. Before surface modification, each sample was alkalisied as described before. Once an alkalisied polyester (PET) is treated with a solution of cationic agent, hydroxyl and carboxyl groups of alkalisied fabric could make hydrogen or electrostatic bonding with the functional groups of the agent. For an instant, protonated amine present in CS or PE might form electrostatic bonds with PET.

After the surface modification of the yarns, fabrics were immersed in a GO dispersion, resulting in a quick attraction between GO nano-sheets and the fabric, in which oxygen functional groups of GO could form hydrogen or electrostatic bond with hydroxyl and amino groups of modified fabrics.

The influence of each modification on fabric properties was compared with a pristine fabric as a control sample. The composition of the samples is summarised in Table 7.

Table 7. The composition of samples.

Sample	Composition
PET-GO	Polyester, graphene oxide
PET-ALK-GO	Alkalisied polyester, graphene oxide
PET-CS-GO	Alkalisied polyester, chitosan, graphene oxide
PET-HDPC-GO	Alkalisied polyester, hexadecylpyridinium chloride, graphene oxide
PET-PE-GO	Alkalisied polyester, branched polyethylenimine, graphene oxide
PET-PDDAC-GO	Alkalisied polyester, poly(diallyl-dimethylammonium) chloride, graphene oxide
PET-rGO	Polyester, reduced graphene oxide
PET-ALK-rGO	Alkalisied polyester, reduced graphene oxide
PET-CS-rGO	Alkalisied polyester, chitosan, reduced graphene oxide
PET-HDPC-rGO	Alkalisied polyester, hexadecylpyridinium chloride, reduced graphene oxide
PET-PE-rGO	Alkalisied polyester, branched polyethylenimine, reduced graphene oxide
PET-PDDAC-rGO	Alkalisied polyester, poly(diallyl-dimethylammonium) chloride, reduced graphene oxide

Surface modification of the fabrics through CS and HDPC not only increases the up-taking of GO Nano-sheets by textile, but also due to the strong ionic bonds between graphene and fibre, the coating layer does not get damaged or wasted during the chemical reduction step. It is believed that this is an industry-relevant graphene impregnation method. Figure 22 shows $\text{Na}_2\text{S}_2\text{O}_4$ solution after the chemical reduction step.

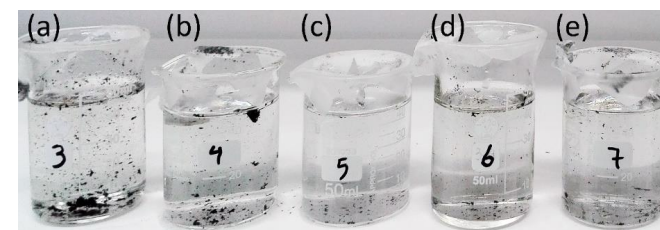


Figure 22. the colloidal dyes segregated from the fabric into the solution during chemical reduction of a control sample (a), PDDAC-treated (b), HDPC-treated (c), PE-treated (d), and CS-treated sample (e).

The control sample was processed in a beaker (a), PDDAC-treated in a beaker (b), HDPC-treated in a beaker (c) PE-treated in a beaker (d) and CS-treated in a beaker (e). The differences between segregated rGO flakes of control and pre-treated fabrics are significant enough to be detected by human eyes, and it can be seen that a control sample loses a considerable amount of rGO through the reducing step as well as rinsing step and it is not promising for large-scale production. As CS and HDPC modified fabrics have better fastness and lose lower amount of dye during the reduction procedure, those are good agents for use in industrial production. Figure 23 shows a graphene oxide coated polyester knitted fabric (a) and a reduced graphene oxide knitted fabric (b).

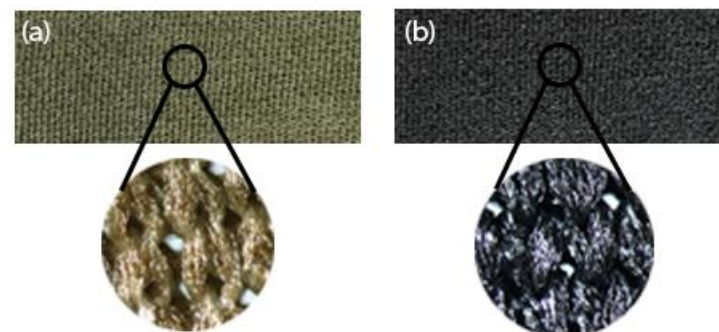


Figure 23. (a) graphene oxide coated and (b) reduced graphene oxide coated knitted polyester fabric.

X-ray photoelectron spectroscopy (XPS)

X-ray photoelectron spectroscopy (XPS) was used to record the atomic composition of an untreated PET, PET-CS, PET-PE, PET-HDPC, and PET-PDDAC as well as PET-GO and PET-rGO samples. The wide scan spectra of the samples are shown in Figure 24.

As demonstrated in Table 8, a control sample contains 75% carbon and 25% oxygen. Since both CS and PE are rich in amino groups, by a modification of the fabric with CS and PE, nitrogen was detected in the surface composition, having 67% carbon, 28% oxygen, and 5% nitrogen for PET-CS; and 74% carbon, 19% oxygen and 7% nitrogen for PET-PE.

Table 8. Atomic ratio of the surface chemical composition of samples.

Sample	C (%)	O (%)	N%
PET	75	25	0
PET-CS	67	28	5
PET-HDPC	77	23	0
PET-PDDAC	76	24	0
PET-PE	74	19	7
PET-GO	74	25	1
PET-rGO	80	20	0

To investigate the functional groups introduced to the polyester surface, high-resolution spectra of the C1s, O1s and N1s peaks were investigated in detail. In the N1s XPS spectrum of PET-CS (0.8 wt%), peaks at 398.5 eV ($-\text{C}\equiv\text{N}$) and at 399.0-400.5 eV ($-\text{NH}_2$) with a corresponding proportion of 38 and 62% were observed; moreover, in the N1s XPS spectrum of PET-PE (0.4 wt%), peaks at 397.6 eV ($-\text{C}\equiv\text{N}$), 399.0 eV ($-\text{NH}_2$), and 401.2 eV ($-\text{CONR}_2$) with a corresponding proportion of 27, 68 and 5% were observed. However, nitrogen was not detected in the composition of PET-PDDAC and PET-HADPC.

The C1s spectrum of a pristine PET can be fitted with four peaks at 283.8 eV, 285.0 eV, 286.5 eV and 289.0 eV attributed to C=C, C-C, C-O, and COO^- bonds, respectively. The concentration of all chemical groups on the PET surface before and after modification can be calculated from the high-resolution C1s peaks. The unmodified PET contains 19% C=C, 57% C-C, 15% C-O, and 9% COO^- groups. PET-CS contains 9% C=C, 49% C-C, 34% C-O, and 8% COO^- groups; PET-PDDAC contains 18% C=C, 51% C-C, 22% C-O, and 9% COO^- groups; PET-PE contains 32% C=C, 52% C-C, 11% C-O, and 5% COO^- groups. For PET-HDPC, the concentration of C=C increased to 39% and the concentration of C-C and COO^- decreased to 51 and 6%; moreover, a newly introduced C-OH group (287.0 eV) with a concentration of 7% was detected. The presence of -OH could increase the hydrophilicity of polyester by forming hydrogen bonds with water. XPS analysis for PET-GO and PET-rGO provides evidence of reduction of graphene oxide as

content of oxygen decreased to 20% for PET-rGO from 25% for PET-GO and content of carbon increased from 74% for PET-GO to 80% for PET-rGO. A wide scan range XPS spectrum of PET-GO and PET-rGO is shown in Figure 24.

The results from the high-resolution C1s spectrum prove that the intensity of oxygen functional groups was decreased after the chemical reduction of GO. C1s spectrum of PET-GO can be fitted with two peaks at 285.0 eV, and 287.0 eV, corresponding to C-C and C=O bonds having a concentration of 60 and 40%. While for PET-rGO, the concentration of C-C bonds increased to 72%, the concentration of C=O bonds decreased to 21%, and a new peak at 289.0 eV attributed to COO^- with a concentration of 7% was observed.

ATR-FTIR spectroscopy

ATR-FTIR analysis was performed on alkalis, surface-modified, GO-modified, and rGO-modified knitted polyester fabrics to record and analyse the chemical composition of the fabrics and their possible bonds.

All spectra were normalised by equalising the height of the adsorption peak at 1713 cm^{-1} , which represents C=O stretch (ester). The peak at 725 cm^{-1} represents the aromatic sp^2 C-H bend (Figure 25). The peak at 1017 cm^{-1} specifies a plane vibration of the benzene ring, the peaks at 1094 and 1240 cm^{-1} indicate C-O stretch (ester), and absorption at 2920 cm^{-1} is due to the asymmetric C-H stretching. All these peaks are identical to polyester.

Subsequently, modification of the knitted fabric with a solution of chitosan (8 $\text{g}\cdot\text{L}^{-1}$) (PET-CS) provides a small peak at 3425 cm^{-1} , representing N-H stretch. Still, once the fabric was modified by a solution (4 $\text{g}\cdot\text{L}^{-1}$) of chitosan, a very low intense peak around 3400 cm^{-1} was observed. The strong C=O peak at 1713 cm^{-1} may cover up the bending peaks between 1550 and 1700, such as the N-H bond at 1560 and 1650 cm^{-1} . Figure 25 shows the FTIR spectra of a fabric pre-modified with a solution (8 $\text{g}\cdot\text{L}^{-1}$) of chitosan.

PET-PE fabric has additional peaks at 1576 and 3427 cm^{-1} ; these peaks also represent N-H bonds. After absorption of GO on modified polyesters, the peak at 2920 cm^{-1} disappeared; it is comprehensible through the chemical composition of GO nano-sheets. For rGO-coated samples, due to the reduction of oxygen functional groups, peaks at 1094, 1172, and 1240 cm^{-1} almost disappeared.

Streaming potential measurements

The isoelectric point ($\text{iep} = \text{pH}|_{\zeta=0}$) observed by electrokinetics was measured as the streaming potential to determine the zeta-potential values. Polyester fabric has an isoelectric point of $\text{pH} = 3.9$, which indicates that the surface charge of polyester is negative for pH higher than 3.9. The negative surface charge of polyester is as a result of the dissociation of functional groups ($-\text{OH}$ and $-\text{COOH}$) of the polymer.

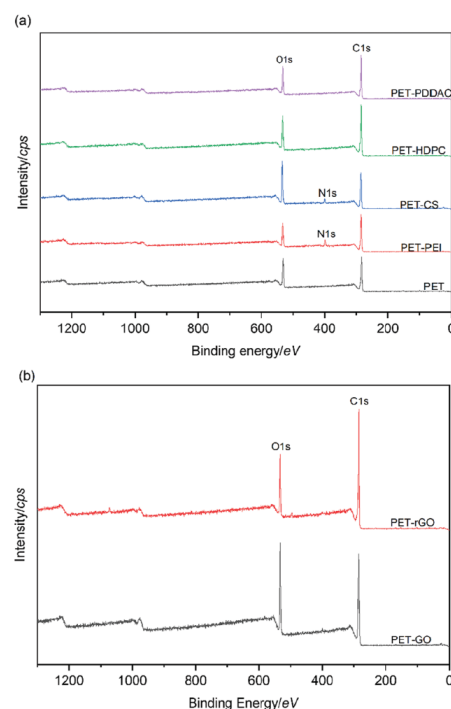


Figure 24. Wide scan XPS spectra of (a) pristine polyester (PET), PET-PEI, PET-CS, PET-HDPC, and PET-PDDAC. (b) PET-GO and PET-rGO.

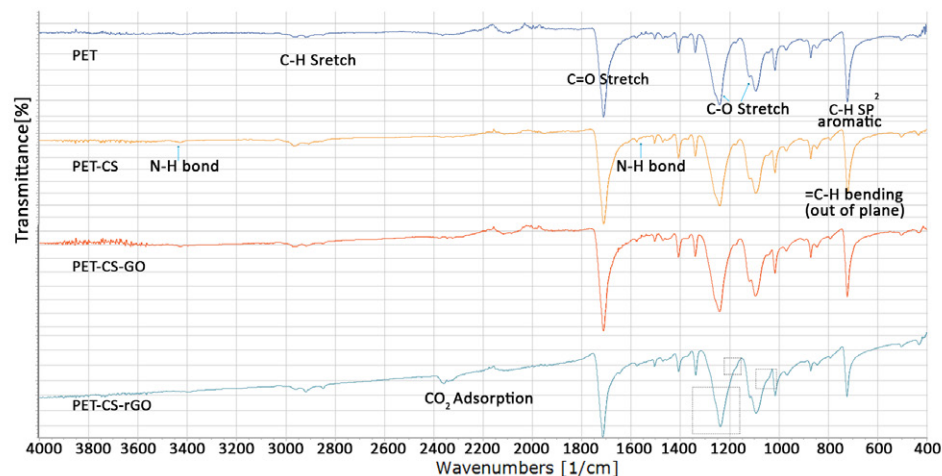


Figure 25. ATR-FTIR spectra of a pristine fabric (PET), chitosan (8 g.L-1) treated fabric (PET-CS), graphene-coated fabric (PET-CS-GO), and reduced graphene-coated fabric (PET-CS-rGO).

Graphene oxide carries a negative surface charge at any pH, due to the ionisation of oxygen-containing functional groups; moreover, it displays strong pH dependence, starting from -19 mV at pH 1.0 and increasing to -49 mV at pH 8.0 [221, 222]. A negative surface charge of GO may lead to hindrance in the attachment of the GO on the surface of pristine polyester yarn.

Treatment of the fabrics by cationic agents reduces the number of carboxylic groups and increases the positively charged functional groups present on the surface of the textile. This results in increasing the value of isoelectric points. PET-PE carries a positive surface charge for any range of pH. PET-PDDAC and PET-CS have an isoelectric point of 6.2 and 6.0, respectively. For PET-HDPC, the isoelectric point has not changed by having the same value as a pristine PET ($\text{pH}|_{\zeta=0} = 3.9$); this could be due to the increase in ($-\text{OH}$) groups of PET-HDPC samples. The zeta-potential values of surface-modified fabrics are shown in Figure 26 (a).

Thereafter, the surface charge of GO-modified and rGO-modified polyester knitted fabrics were recorded (Figure 26(b)). Due to the presence of functional groups on the surface of GO-modified fabrics, it carries a negative surface charge for any range of pH. However, the reduction of oxygen functional groups increases the zeta potential value, and it has a $\text{pH}|_{\zeta=0}$ of 5.

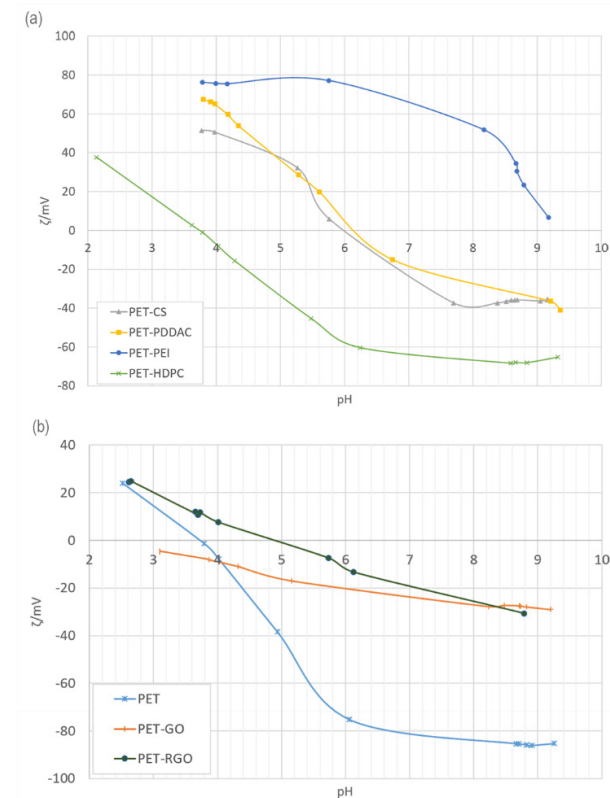


Figure 26. Zeta potential (ζ) values determined for (a) PET-CS, PET-PDDAC, PET-PE, and PET-HDPC fabrics and (b) pristine PET fabric, PET fabric modified by graphene oxide (PET-GO), and a PET fabric modified by reduced graphene oxide (PET-rGO) in dependence on pH of an aqueous 10-3 mol/L KCL solution.

Sessile-drop goniometry

Sessile-drop goniometry was performed to indicate the contact angle of the knitted fabrics. A deionised water droplet was placed on the front side of the fabrics, and a camera with a display performance of 60 frames per second (fps) was used to determine the initial contact angle and the absorption time. Sessile-drop goniometry measures the static contact angle. However, for a rough surface, such as that of textiles, the liquid moves around before it settles, and the wetting phenomenon is more complex than a static state.

The effect of surface modification with cationic agents and further functionalisation of fabric with GO and rGO on the surface wettability was evaluated by image processing. Pristine knitted polyester fabric has a contact angle of 91° and an adsorption time of 0.8 s. The wettability of the fabric increased by introducing HDPC as the adsorption time decreased to 0.2 s, and the contact angle decreased to 61° . Figure 27 shows the image sequences of water droplets placed on pristine knitted PET and knitted PET-HDPC fabrics.

The absorption time was increased to 13 s for PET-CS. Yet, the contact angle is lower (79°) compared to a pristine knitted fabric. The adsorption time for PET-PDDAC and PET-PE samples also increased to 3 and 6 s, having a contact angle of 77 and 62°, respectively.



Figure 27. Image sequences of placing a deionised water droplet on (a) an unmodified polyester (PET), and (b) HDPC-modified polyester fabric (PET-HDPC) over time.

After GO-modification of the knitted fabric, it turned out to be more hydrophobic, having an average contact angle of 137°. However, after the reduction of functional groups on the surface of GO nano-sheets, fabrics show different contact angles depending on the pre-treatment of the fabrics. For an instant, as shown in Figure 28 PET-rGO, PET-PDDAC-rGO and PET-HDPC-rGO have a contact angle of 138, 132, and 131°, which demonstrates that the hydrophobicity of the fabric decreases after treatment by PDDAC and HDPC. However, for PET-CS-rGO and PET-PE-rGO, the contact angle increased to 144 and 145°. The hydrophobicity of PET-rGO fabrics is beneficial for many outdoor applications by maintaining the electrical conductivity, antistatic, and heat generation properties.

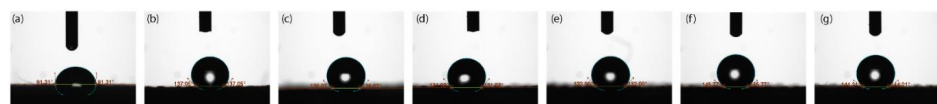


Figure 28. Water contact angle of (a) pristine PET, (b) graphene oxide-modified polyester (PET-GO), (c) reduced graphene oxide-modified polyester fabric (PET-rGO), (d) reduced graphene oxide-HDPC modified polyester fabric (PET-HDPC-rGO), (e) reduced graphene oxide-PDDAC modified polyester fabric (PET-PDDAC-rGO), (f) reduced graphene oxide-PE modified polyester fabric (PET-PE-rGO), and (g) reduced graphene oxide-CS modified polyester fabric (PET-CS-rGO).

Surface Morphology

Morphology of the coating layers was investigated by the means of a scanning electron microscope (SEM). SEM images of the control (GO-PET) and pre-modified GO-coated knitted fabrics are shown in Figure 29. For the control sample (Figure 29(a)), GO nanosheets are not absorbed properly to the surface of the fibres, and there is barely sufficient attachment between GO nanosheets and fibres. It can be seen from Figure 29(b) that for a control sample, coating layers are wrinkled, which might result in increasing the electrical resistivity. Figure 29(c) shows the surface of a chitosan-treated fabric (PET-CS-GO), and the red circle site in the image shows multi-layers of GO

attached to the surface of polyester yarns. There are some particles attached to aggregated GO nanosheets (blue arrows), which are possibly impurities from the environment. It can be seen from Figure 29(d) that a multilayer of GO nanosheets is appropriately attached to the surface of PET-CS-GO yarns, which is possibly due to the strong bonding of carboxyl and carbonyl groups of the GO nanosheets and hydroxyl and protonated amino groups of chitosan.

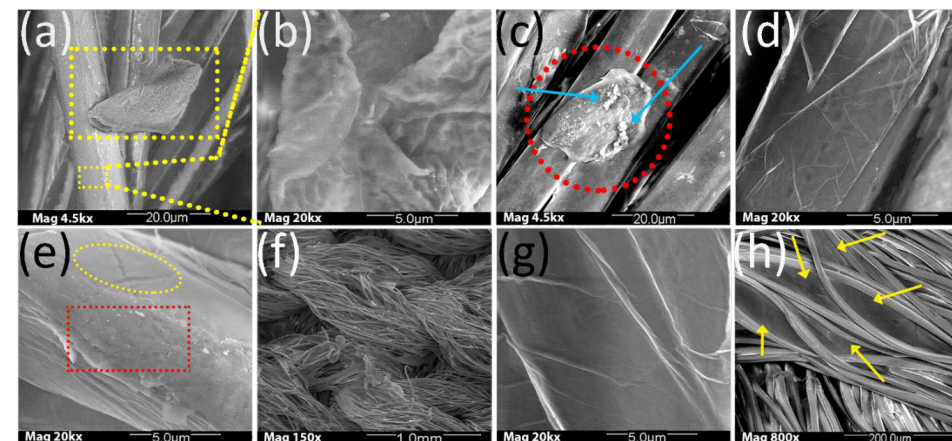


Figure 29. SEM images of (a) PET-GO sample (4.5kx Mag.), (b) PET-GO sample (20kx Mag.), (c) PET-CS-GO sample (4.5kx Mag.), (d) PET-CS-GO sample (20kx Mag.), (e) PET-HDPC-GO sample (20kx Mag.), (f) PET-HDPC-GO sample (150x Mag.), (g) PET-PDDAC-GO sample (20kx Mag.), (h) PET-PDDAC-GO sample (800x Mag.).

Figure 29(e, f) shows the surface of the HDPC-modified sample (PET-HDPC-GO). Multi-layers of GO nanosheets are formed on the fibre (red rectangle) as well as the single layers (yellow ellipse). In both cases, the coating layer is attached properly to the fibre. Smoother and even coating was formed on the surface of the PDDAC-modified sample (PET-PDDAC-GO) with minimum shrinkage of GO nanosheets (Figure 29(g)). In this case, GO sheets with a large surface area are formed among the mono-filaments of the fibre as well ((h)).

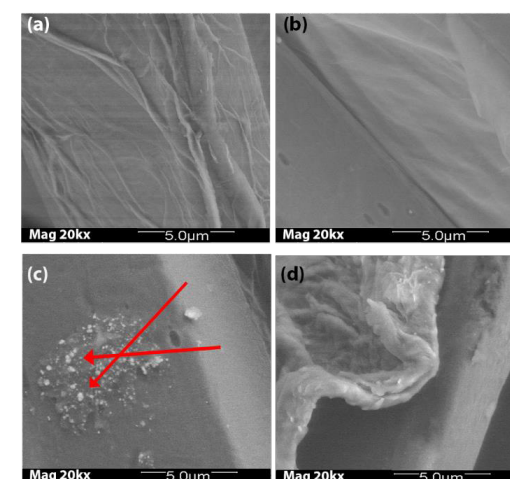


Figure 30. SEM images of (a) PET-rGO sample (20kx Mag.), (b) PET-CS-rGO sample (20kx Mag.), (c) PET-HDPC-rGO sample (20kx Mag.), and (d) PET-PDDAC-rGO sample (20kx Mag.).

SEM images of rGO-modified samples (Figure 30) were recorded to observe the influence of chemical reduction on the morphology of the samples. It was observed that shrinkages through the coating layers for the control sample (PET-rGO), shown in Figure 30(a), were successfully prevented by

pre-treating the fabric with chitosan (PET-CS-rGO) (Figure 30(b)) and HDPC (PET-HDPC-rGO) (Figure 30(c)). Aggregation of sodium was observed (red arrows) on some sites of PET-HDPC-rGO. This might be the impurities from the reduction process due to the interaction of sodium hydrosulfite ($\text{Na}_2\text{S}_2\text{O}_4$) with HDPC or GO. However, PDDAC-modified fabric (PET-PDDAC-rGO) does not show a uniform and smooth coating layer (Figure 30(d)).

The colour strength and estimation of dye concentration

Among all the modified knitted fabrics, PET-CS up-takes the highest concentration of colloidal dye, having a relative percentage difference (RPD) of colour strength of 40.52%. Yet, the up-taken dye was increased for all pre-modified samples, having an RPD of 31.78, 27.34 and 20.24% for PET-HDPC-GO, PET-PDDAC-GO and PET-PE-GO, respectively. As was expected, due to the higher repulsion between GO nanosheets and alkalis polyester yarns, the colour strength of alkalis fabric (PET-ALK-GO) was reduced (-6.46%). After chemical reduction of GO nanosheets, all pre-modified fabrics showed higher colour strength compared to a control sample. For example, PET-CS-rGO, PET-PE-rGO, PET-PDDAC-rGO, and PET-HDPC-rGO have an RPD of 33.61% and 33.43%, 36.97%, and 31.66%, respectively. Reflectance (R), colour strength (K/S), and relative percentage difference (RPD) of colour strength for GO-modified and rGO-modified knitted fabrics are shown in Table 9.

Table 9. Reflectance (R), colour strength (K/S), and relative percentage difference (RPD) of colour strength for GO-modified and rGO-modified fabrics.

Sample	R	K/S	RPD
GO-modified samples			
PET-GO	10.29	3.90	-
PET-ALK-GO	10.86	3.65	-6.46
PET-CS-GO	7.75	5.49	40.52
PET-PE-GO	8.84	4.70	20.24
PET-HDPC-GO	8.18	5.15	31.78
PET-PDDAC-GO	8.42	4.98	27.34
rGO-modified samples			
PET-rGO	7.67	5.65	-
PET-ALK-rGO	7.66	5.72	1.24
PET-CS-rGO	5.91	7.55	33.61
PET-PE-rGO	5.99	7.54	33.43
PET-HDPC-rGO	6.03	7.45	31.66
PET-PDDAC-rGO	5.78	7.75	36.97

Manufacturing-based quality of modified fabrics

To investigate the evenness of coating layers, the colour difference (ΔE) of each sample was measured according to CIE and CMC systems [223, 224]. CIELab coordinates and total colour differences (ΔE) according to CIELab and CMC (2:1) systems for GO-modified and rGO-modified fabrics are presented in Table 10. These fabrics have a lower value for the L^* coordinate, which stands for darkness-brightness of the colour.

A control sample has a high average ΔE of 1.66 ± 1.22 , and the sample does not have an adequate colour evenness. On the contrary, all surface-modified samples have an average ΔE of less than 1. According to the standards, a ΔE of 1.0 is the smallest colour difference that the human eye might detect. Hence, any ΔE less than 1.0 is imperceptible and acceptable for the textile industry [210].

PET-CS-rGO ($\Delta E = 0.21 \pm 0.07$) and PET-HDPC-rGO ($\Delta E = 0.3 \pm 0.16$) have the most even dye quality, which could be another reason for better performance in electrical activity. PET-PDDAC-rGO and PET-PE-rGO fabrics have an average ΔE of 0.55 ± 0.19 and 0.63 ± 0.25 .

Table 10. CIELab coordinates of GO-modified and rGO-modified fabrics. Colour differences (ΔE) of a control and pre-treated samples in both CIE and CMC systems. L^* is the coordinate response to brightness and darkness of the surface, a^* coordinate response to green-red shade of colour, and b^* coordinate response to yellow-blue shade of colour.

Sample	L^*	a^*	b^*	ΔE (CIE)	ΔE (CMC)	Sample	L^*	a^*	b^*	ΔE (CIE)	ΔE (CMC)
PET-GO	46.92	1.64	10.24			PET-rGO	36.86	0.96	4.49	-	-
PET-ALK-GO	47.53	1.66	9.75	0.78	0.51	PET-ALK-rGO	36.91	0.89	4.47	0.09	0.11
PET-CS-GO	40.58	2.16	8.97	6.49	3.34	PET-CS-rGO	31.43	0.71	2.84	5.69	3.49
PET-PE-GO	43.45	2.01	9.58	3.55	1.85	PET-PE-rGO	31.95	0.63	3.25	5.08	3.03
PET-HDPC-GO	43.57	2.83	11.61	3.81	2.42	PET-HDPC-rGO	32.40	0.82	3.72	4.54	2.58
PET-PDDAC-GO	42.73	2.10	9.75	4.24	2.16	PET-PDDAC-rGO	30.48	0.44	2.06	6.85	4.42

Electrical Conductivity

Functional groups present on the edges and surface of the GO sheets are the reason for electrically insulating properties. To bring electro-conductive properties to the fabrics, GO-modified samples were chemically reduced to rGO, and sheet resistance (R_{sh}) of reduced samples was recorded via a 4-probe method [2]. The current-voltage profile of the samples was recorded in a voltage range of 5–30 V. The sheet resistance and maximum current at a voltage of 30 V are summarised in Table 11. A control fabric, without any surface modification, shows a sheet resistance of $27.3 \pm 2.8 \text{ k}\Omega/\square$. As was expected, an alkalis fabric shows higher electrical resistance, having a sheet resistance of $122 \pm 9.8 \text{ k}\Omega/\square$. The sheet resistance of PET-HDPC-rGO, PET-CS-rGO, and PET-PE-rGO decreased to 0.59 ± 0.02 , 2.7 ± 0.09 , and $3.9 \pm 0.19 \text{ k}\Omega/\square$ compared to a control sample, having a value of $27.3 \pm 2.8 \text{ k}\Omega/\square$. While for PET-PDDAC-rGO, the value increased to $38.5 \pm 0.54 \text{ k}\Omega/\square$, which is possibly because of the morphology of the surface of the fabrics.

Table 11. Sheet resistance (R_{sh}) and maximum current (I) at a voltage of 30 V for control and rGO-modified samples.

Sample	R_{sh} ($k\Omega/\square$)	I (mA)
PET-rGO	27.3 ± 2.8	-
PET-ALK-rGO	122 ± 9.8	-
PET-CS-rGO	2.7 ± 0.09	15
PET-PE-rGO	3.9 ± 0.2	5.56
PET-HDPC-rGO	0.59 ± 0.02	61.50
PET-PDDAC-rGO	38.5 ± 0.5	-

The electrothermal activity of the graphene-modified polyester knitted fabrics

To characterise the electro-thermal properties of rGO-coated knitted fabrics, direct current (DC) power was applied (5–30 V) to the samples with a valid heating area of $2 \times 1.5 \text{ cm}^2$, and electro-thermal properties were investigated under ambient conditions via a thermal camera and a thermal data-logger sensor.

Since the resistance of a non-modified and PDDAC-treated knitted fabrics is high and no current passes through, there was not any heat exchange to the fabrics. In this case, the PE-treated sample also did not show any significant increase in temperature (38°C at 30 V). For CS-treated and HDPC-treated samples, after supplying electrical power to the fabric, the surface temperature increased monotonically over time until a steady-state temperature was reached (Figure 31).

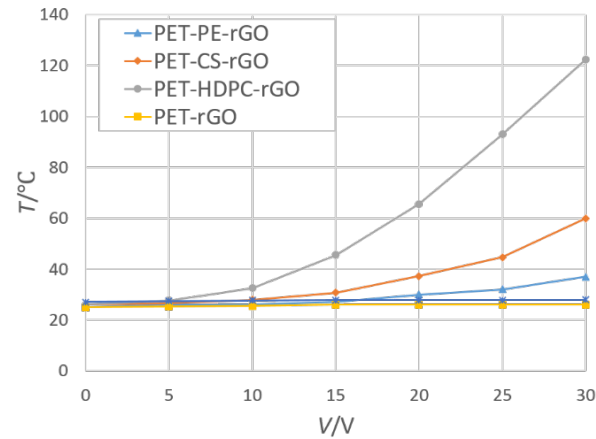


Figure 31. The steady-state temperature vs applied voltages profile of the samples.

It was observed that the steady-state temperature increased by increasing applied voltage with a quadratic correlation of input voltage and temperature. The results are consistent with Joule's law [118, 225]:

$$P = \frac{U^2}{R}$$

where P is power, U has applied voltage, and R is the resistance.

The HDPC-treated sample has a higher steady-state temperature at the same voltage as compared to the CS-treated sample. This might be attributed to the lower transduction of electrical energy into Joule heating. The heating rate curve of the HDPC-treated sample at 30 V is illustrated in Figure 32 (a). As can be seen, the HDPC-treated sample shows a steady-state temperature of 120°C with a maximum heating rate of 0.5°C s^{-1} at a driving voltage of 30 V. Lower steady-state temperature of 60°C with a maximum heating rate of 0.2°C s^{-1} at the same driving voltage of 25 V was observed for CS-treated sample (Figure 32 (b)), which has higher sheet resistance compared to the HDPC-treated fabric.

It has been reported that a thin film of graphene has a steady-state temperature of 139°C at a given voltage of 30 V [225]. Considering the sheet resistance of a thin film of graphene as $0.159 \text{ k}\Omega/\square$. Even though a coated fabric has a higher surface area than a film, still achieving $0.59 \text{ k}\Omega/\square$ sheet resistance and 120°C steady-state temperature is a fruitful outcome. To meet the comfort requirements of the human body for the heating garment regarding cold proof applications, such as outdoor service clothes, the cold storage working cloths, and submarine work clothes, the heating temperature is generally about 40°C . In medical applications, such as hot compress therapy, the temperature of the garment is usually around 55°C [226]. Both CS and HDPC pre-treated fabrics fulfil the temperature requirement for such applications.

By decreasing the applied voltage from 30 to 25 V, the steady-state temperature of the HDPC-treated and CS-treated samples decreased to 93 and 54°C , respectively. Additionally, the time required to reach 90% of the steady-state temperature called the response time is an important factor for heat performance evaluation and applications [225, 227]. Both samples show a response time of less than 120 s.

After reaching the steady-state temperature, the power supply was switched off, and the temperature started decreasing immediately with a logarithmic trend line of $T = -6.277 \ln(s) + 63.752$ for PET-HDPC-rGO and $T = -17.14 \ln(s) + 133.62$ for PET-CS-rGO samples. The time required to lose heat and decrease the temperature from 110°C to 30°C was 600 s for PET-HDPC-rGO, and 300 s for PET-CS-rGO sample to lose the temperature from 55°C to 30°C , which shows that both samples have a similar heat exchange behaviour via the environment.

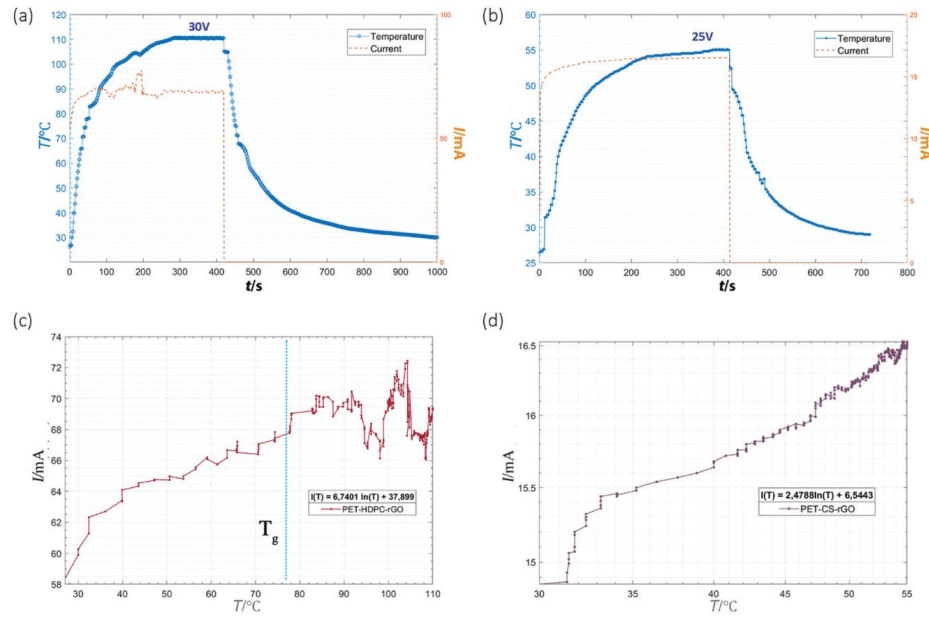


Figure 32. Temperature and current versus time profile of the (a) PET-HDPC-rGO by having a steady-state temperature of 115°C at a constant voltage of 30V, (b) PET-CS-rGO with a steady-state temperature of 55°C at a constant voltage of 25V, response times for both fabrics are less than 120 s. The current vs temperature profile of (c) PET-HDPC-rGO and (d) PET-CS-rGO during the electro-thermal activity with a function of $I(T) = 6.7401 \ln(T) + 37.899$ and $I(T) = 2.4788 \ln(T) + 6.5443$, respectively.

Carbon has a negative temperature coefficient (NTC) and by increasing the temperature, the resistance of graphene will decrease [122]. Based on Ohm's law, decreasing the resistance at the same voltage will increase the current.

It can be seen from Figure 32 (c) that as the temperature increases from room temperature to 110°C, the current increases from 58 to 69 mA with a logarithmic relationship; as a simplified linear relationship, a gradient of 0.09 is obtained. Resistance of fabric decreased to 0.46 Ω from 0.54 Ω (Figure 33 (a)) by increasing the temperature from 30 to 120°C. Further, in the CS-treated sample, the current increased from 14.8 to 16.5 mA (Figure 32 (d)), as the temperature increases to 55°C with a gradient of 0.06. As result, the resistance decreased to 1.94 from 2.3 Ω (Figure 33 (b)). Having NTC properties will make the graphene-coated fabric a good candidate for continuous temperature sensing applications.

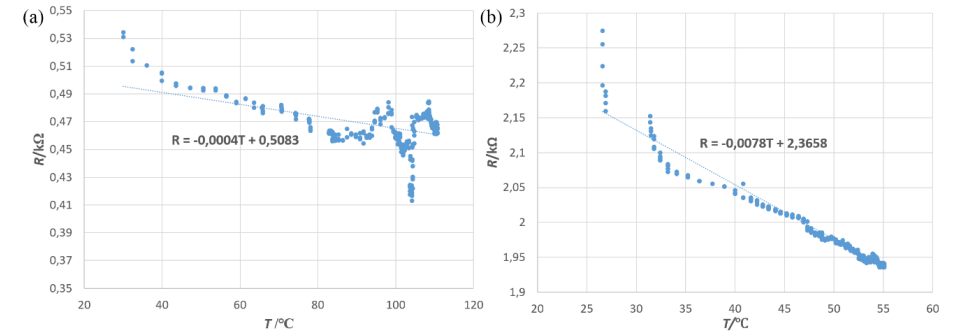


Figure 33. The measured resistance changes vs temperature profiles of (a) PET-HDPC-rGO with a function of $R = -0.0004T + 0.5083$, and (b) PET-CS-rGO with a function of $R = -0.0078T + 2.3658$.

Figure 34 shows the infrared thermal images of PET-HDPC-rGO and PET-CS-rGO samples at their steady-state temperature under an applied voltage of 30 V. This is because the temperature distribution through the surface of the samples at the applied voltage is rather homogeneous. Graphene has an excellent thermal and electrical conductivity and graphene films show an even heat distribution [118]. The evenness of heat distribution along a graphene-coated fabric might be due to the evenness of the coating and the inherent properties of the graphene.

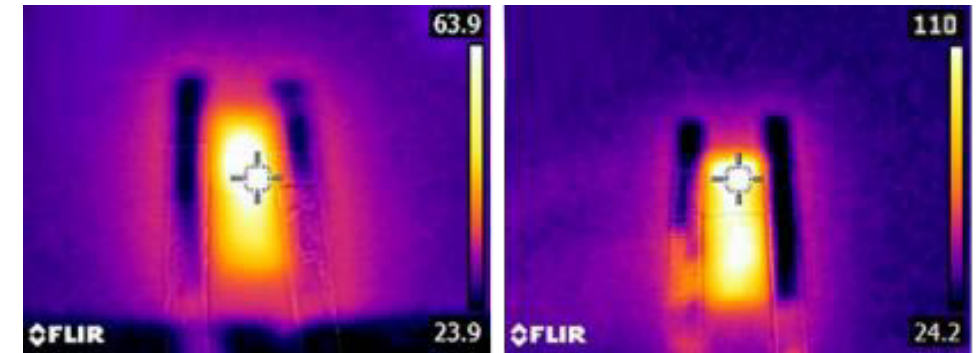


Figure 34. Infrared images at a steady-state temperature of (a) PET-CS-rGO, and (b) PET-HDPC-rGO at an applied voltage of 30 V., reaching 63.9 and 110°C for PET-CS-rGO and PET-HDPC-rGO correspondingly while having almost a homogeneous thermal expansion through the fabric surface.

The glass transition temperature (T_g) of PET-HDPC-rGO gained by DSC measurement (Figure 35) is 76.5°C; it is believed that the peaks in the PET-HDPC-rGO sample after around 80°C (Figure 32 (c)) are due to the change in the crystallinity of the fabric and its influence on the coating layer. Hence, there are large peaks at 90, 100, 110, and 115°C in respect of resistivity (Figure 33 (a)).

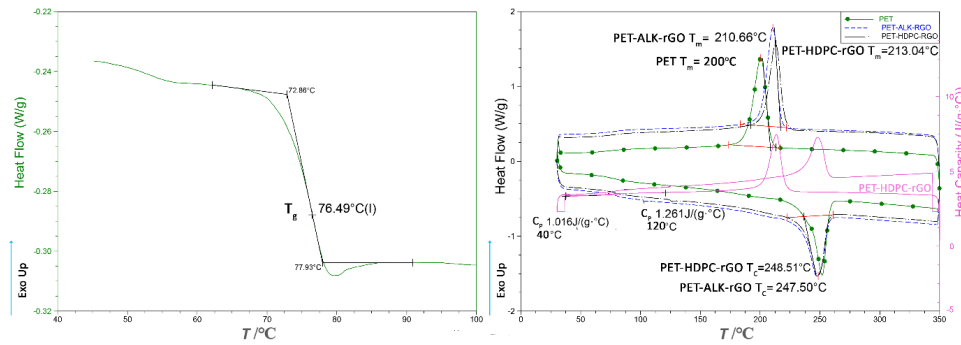


Figure 35 (a). DSC photographs of PET-HDPC-rGO, with a glass transition (T_g) of 76.49°C. (b) DSC photographs of a control polyester fabric (PET), a pre-alkalised polyester fabric coated by reduced graphene oxide (PET-ALK-rGO), and an HDPC surface-modified polyester fabric coated by reduced graphene oxide. Heat capacity profile of PET-HDPC-rGO. Melting temperature (T_m) of the polyester fabric with a value of 200°C increases to 213°C for a PET-HDPC-rGO fabric. Heat capacity at constant pressure (C_p) of the same sample at 120°C is 1.261 J.(g.°C)⁻¹.

Furthermore, to better understand the thermal behaviour of a graphene-coated fabric compared to a control fabric, DSC measurement was studied for a control polyester fabric (PET), a pre-alkalised polyester fabric coated by reduced graphene oxide (PET-ALK-rGO), as well as a PET-HDPC-rGO fabric. Melting temperatures (T_m) for samples were 200°C, 210°C, and 213°C for PET, PET-ALK-rGO, and PET-HDPC-rGO fabrics, respectively. The increase in T_m for both PET-ALK-rGO and PET-HDPC-rGO is noticeable.

4.2 Characterisation of the coated yarn for tactile sensor applications

To provide a yarn with electro-conductive properties, GO-coated Polyester yarns were chemically reduced, using an aqueous solution of $\text{Na}_2\text{S}_2\text{O}_4$ [58] with a concentration of 50 mM and a liquor ratio of 1:100 for 30 min at 95°C. Then, the yarns were rinsed several times in warm ultrapure water and dried at 70°C for 10 min.

A pristine yarn with no surface modification was prepared in the same manner as a control sample. It was observed that, for such a yarn, the coating was easily separated from the yarn during the rinsing process. The composition of the samples of polyester yarns is summarised in Table 12.

Table 12. The composition of polyester yarn samples.

Sample	yarn	Surface modification agent	Coating layer
PET	Alkalised polyester	-	-
PET-GO	Alkalised Polyester	-	graphene oxide
PET-CS-GO	Alkalised polyester	chitosan	graphene oxide
PET-HDPC-GO	Alkalised polyester	hexadecylpyridinium chloride	graphene oxide
PET-rGO	Alkalised polyester	-	reduced graphene oxide
PET-CS-rGO	Alkalised polyester	chitosan	reduced graphene oxide
PET-HDPC-rGO	Alkalised polyester	hexadecylpyridinium chloride	reduced graphene oxide

Surface Morphology

The morphology of the polyester yarns was investigated by employing a scanning electron microscope (SEM). As shown in Figure 36, for a non-treated polyester yarn (Figure 36(a)), GO Nanosheets have not been attached appropriately. Surface modification of the fibres will significantly improve the uniformity and adsorption of the coating, which will result in an even coating with very few wrinkled sites for both CS (Figure 36(b)) and HDPC (Figure 36(c)) modified polyester yarns. The chemical reduction of GO on the surface of a pristine yarn will noticeably reduce the smoothness and evenness of the coating layer (Figure 36(d)), while for both CS and HDPC modified yarns (Figure 36 (e,f)), an even coating is achieved.

Tensile properties of the yarns

In the tensile test, five clamped replicas of each sample were subjected to a constant rate of tensile loading forces to stretch and break the filament, while tensile strength (N), elongation at break (%), modulus (N.tex⁻¹), and tenacity (N.tex⁻¹) were recorded.

As shown in Table 13, a pristine polyester yarn has a force and elongating at break of 5.46 N and 28.91%, respectively, with a modulus of 1.655 N.tex⁻¹. When the yarn was modified with a diluted acetic solution of CS (PET-CS) or an aqueous solution of HDPC (PET-HDPC), the tensile strength of the composite did not seem to be impaired.

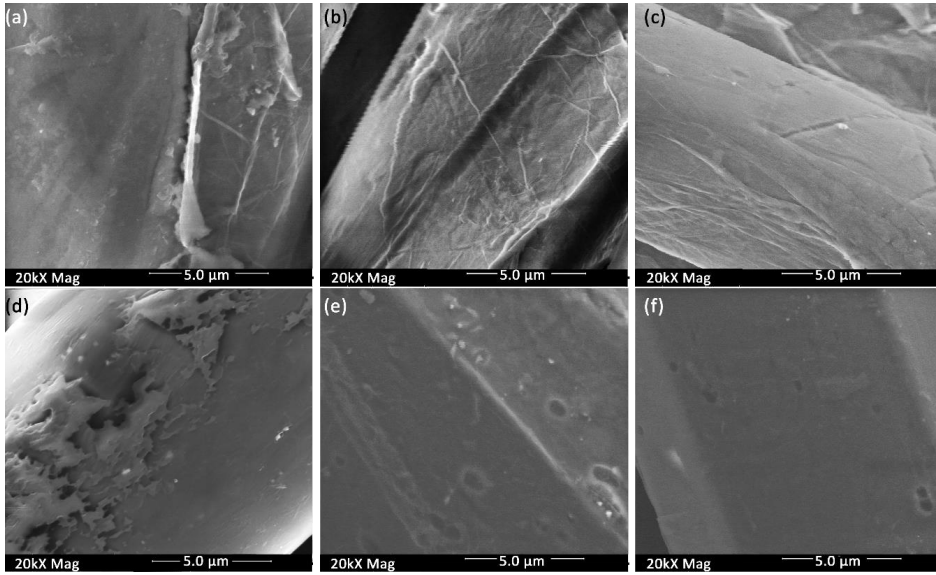


Figure 36. SEM images of (a) PET-GO, (b) PET-CS-GO (c) PET-HDPC-GO, (d) PET-rGO, (e) PET-CS-rGO, (f) PET-HDPC-rGO with 20kx magnification.

PET-CS and PET-HDPC yarns have a tensile strength of 5.11 and 5.25 N, and elongation at breaks of 26.63 and 26.64%, correspondingly. However, a minor increase in the modulus of the yarns was observed for both PET-CS (1.81 N.tex^{-1}) and PET-HDPC (1.76 N.tex^{-1}), with a slightly lower elastic deformation, which might be due to the change in the composition of the batch.

The impregnation process (PET-CS-GO and PET-HDPC-GO) causes a negligible downgrade in tensile strength and elongation at break with a tensile strength of 5.3 and 5.33 N, and elongation at breaks of 26.02 and 24.8%, correspondingly.

Additionally, it was detected that the chemical reduction process does not weaken the tensile properties of the CS-treated (PET-CS-RGO) yarn, as it has a marginally higher tensile strength (5.41 N) compared to a GO-coated yarn (PET-CS-GO). The modulus of the yarn decreases to 1.419 N.tex^{-1} compared to 1.792 N.tex^{-1} for PET-CS-GO yarn. This might be due to a slight change in the molecular chain of the yarn during the chemical reduction process.

Table 13. Tensile properties of the pristine, surface modified and functionalised polyester yarns.

Sample	Tensile strength (N)	Elongation at break (%)	Tenacity (N/tex)	Modulus (N/tex)
PET	5.5 ± 0.17	28.91 ± 2.64	0.329 ± 0.01	1.655 ± 0.14
PET-CS	5.36 ± 0.09	26.63 ± 2.04	0.320 ± 0.005	1.816 ± 0.11
PET-CS-GO	5.3 ± 0.26	26.02 ± 2.84	0.317 ± 0.015	1.792 ± 0.07
PET-CS-rGO	5.41 ± 0.10	30.32 ± 4.11	0.323 ± 0.006	1.419 ± 0.24
PET-HDPC	5.28 ± 0.21	26.64 ± 1.74	0.315 ± 0.013	1.769 ± 0.16
PET-HDPC-GO	5.33 ± 0.09	24.8 ± 1.55	0.319 ± 0.005	1.893 ± 0.10
PET-HDPC-rGO	5.19 ± 0.34	23.75 ± 2.58	0.31 ± 0.02	1.823 ± 0.13

The chemical reduction process slightly weakened the HDPC-treated yarn (PET-HDPC-RGO) by decreasing the tensile strength to 5.19 N. The changes in elongation at break (23.75%) and modulus (1.82 N.tex^{-1}) were negligible. The stress-strain curves of an alkalis polyester (PET), CS-modified (PET-CS), GO-modified (PET-CS-GO), and rGO-modified (PAETCS-rGO) yarns are shown in Figure 37.

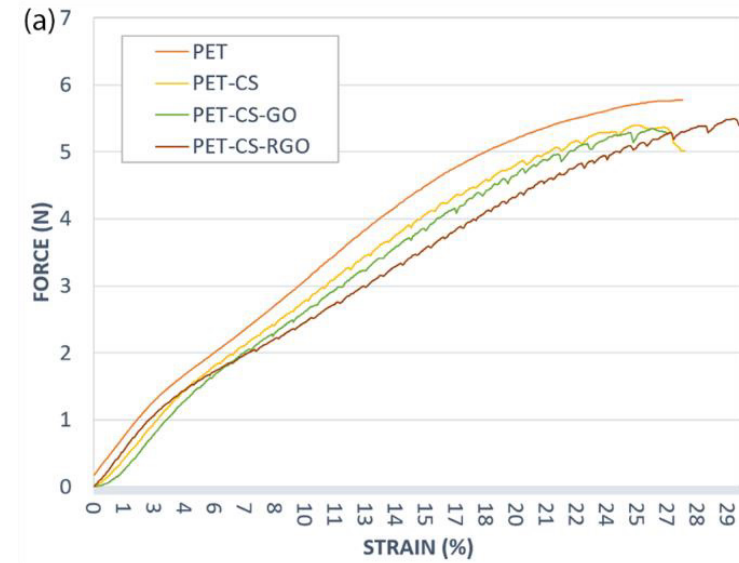


Figure 37. Stress-strain curves of a pristine polyester (PET), chitosan modified (PET-CS), graphene oxide modified (PET-CS-GO), and reduced graphene oxide modified (PET-CS-rGO) yarn.

Electrical performance of the yarn

Electrical resistance (R) of rGO-modified polyester yarns was measured via a two-probe method using direct current (DC) electrical resistance measurement (Figure 38 (b)). It was measured as the unit of $\text{k}\Omega$ for a length of 10 cm yarn. GO is electrically insulating because of the presence of functional groups on the edges and surface of GO nanosheets, and chemical reduction of GO is required to exhibit conductive properties. Still, rGO modified yarns without surface modification do not exhibit electrical conductivity, probably due to the weak interactions between GO nanosheets and fibres. Surface modification with CS on polyester (PET-CS-rGO) delivers electrical properties to the yarn, having an average resistance of 24.2 ± 3.1 .

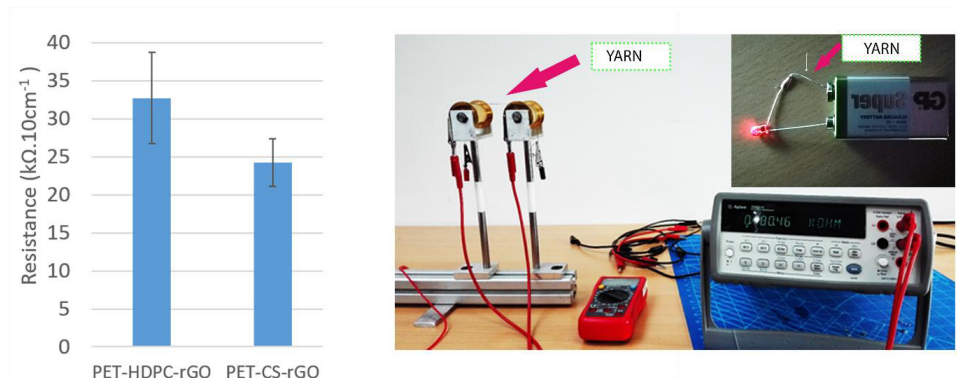


Figure 38 (a). Electrical resistance ($k\Omega \cdot 10cm^{-1}$) of the CS and HDPC modified polyester yarns. (b) 2-probe set up for electrical measurement.

Modification of the yarn with HDPC also provides electrical properties, and the average resistance of HDPC-modified polyester (PET-HDPC-rGO) is 32.7 ± 6 $k\Omega$. The electrical conductivity of the yarn was high enough to light a LED using a 9V battery.

4.3 Non-woven polyester fabric and its catalytic properties

Sessile droplet goniometry analysis

Sessile-drop goniometry was applied to measure the wettability of all non-woven samples, which henceforth reflects the surface chemical properties of the fabric and diffusion resistance before and after individual surface modifications. The water contact angle of the pristine polyester that was used in this study was as high as 138° , indicating the characteristic hydrophobic nature of the polyester fabric. The contact angle of all non-woven samples is mentioned in Table 14.

Table 14. Contact angle data from sessile droplet analysis

Sample	Contact angle ($^\circ$)
Pristine PET	138
PET	0
PET-PAM	126
PET-GO	36
PET-rGO-Fe ⁰	0
PET-PAM-GO	48
PET-PAM-rGO	126
PET-PAM-rGO-Fe ⁰	0
PET-rGO	122

Alkaline hydrolysis of the non-woven fabric results in a reduction of the water contact angle to $\theta_{H_2O} = 0^\circ$, indicating the formation of hydroxyl (-OH) and carboxylic (-COOH) end groups on the surface of the fabric, which introduces the hydrophilic properties of the surface due to the nucleophilic replacement reaction where chain scission of polyester polymers occurred. Nevertheless, hyperbranched polyamidoamine (PAMAM) dendrimer consists of ethylenediamine core, and tertiary amine branches tend to give a hydrophobic surface $\theta_{H_2O} = 126^\circ$, while providing favourable surface functional groups that are necessary for stable GO and Fe⁰ incorporation. The results show that graphene oxide (GO) provides a surface with a sufficient hydrophilic characteristic surface (θ_{H_2O} of PET-GO is 36° ; θ_{H_2O} of PET-PAM-GO is 48°). Further chemical reduction of GO makes it intensely hydrophobic (θ_{H_2O} of PET-rGO is 122° ; θ_{H_2O} of PET-PAM-rGO is 126°). However, hydrophilic characteristics were observed on Fe⁰ grafted on both reduced graphene (rGO) and PAMAM coated samples, which can be caused by the presence of iron particles within the metal or oxide form. Iron particles show well established hydrophobic properties, as explained in other studies in the literature [168, 228].

Particle size distribution

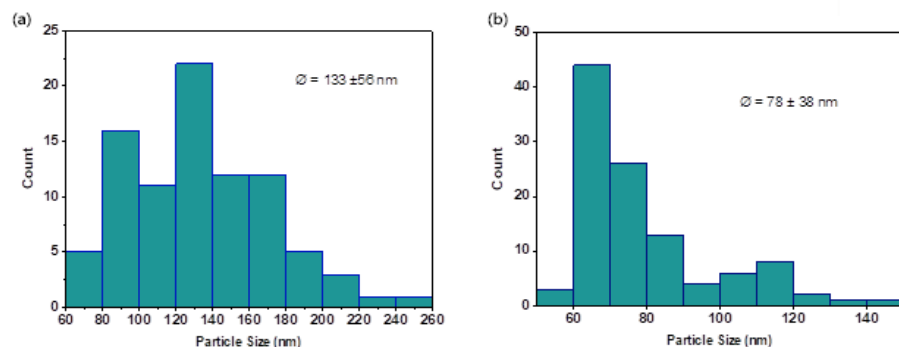


Figure 39. Particle size distribution of zerovalent iron nanoparticles; (a) PET-rGO- Fe⁰ and (b) PET-PAM-rGO- Fe⁰

In polyamidoamine dendrimer, grafted polyester with highly dispersed GO showed smoother external surface and more attenuated roughness and uniform particle distribution (Figure 39) at sizes $\bar{\phi} = 78 \pm 38$ nm compared to PET-GO-Fe⁰ (average particle size of Fe⁰, $\bar{\phi} = 133 \pm 56$ nm).

Electrokinetic measurements (Zeta potential analysis)

The isoelectric point ($\text{iep} = \text{pH}|\zeta = 0$) to determine the zeta potential values of the control sample and all modified polyester non-woven fabrics was observed by electrokinetics and measured as streaming potential. The zeta potential analysis of the samples is shown in Figure 40. It can be seen that the isoelectric point of pristine polyester fibres is $\text{pH} = 3.9$, which means that a positive surface charge will be observed for the polyester fibres with a pH lower than 3.9. Due to the introduction of $-\text{OH}$ and $-\text{COOH}$ groups, the surface charge and isoelectric point were also negative, starting from -6.89 mV at $\text{pH}=3.45$ to -49.23 mV at $\text{pH}=9.91$.

Upon grafting of PAMAM on PET, the surface charge increased to $+52.31$ mV at $\text{pH}=3.70$. The isoelectric point of PET-PAM was recorded at $\text{pH}= 8.15$. This might be since, after dendrimer grafting, the degree of $-\text{COOH}$ and $-\text{OH}$ groups decrease while increasing in $-\text{NH}_2$ surface functional groups. A positive surface charge of PAMAM grafted PET could facilitate the grafting of negatively charged graphene oxide compared to a pristine polyester non-woven. For the PET-PAM-GO sample, the mutual presence of PAMAM and graphene oxide on the surface showed a negative surface charge property with an isoelectric point at $\text{pH}= 4.85$. The zeta potential value was recorded starting $+10.35$ at $\text{pH}=3.25$, which reduces to -46.88 mV at $\text{pH}= 9.96$.

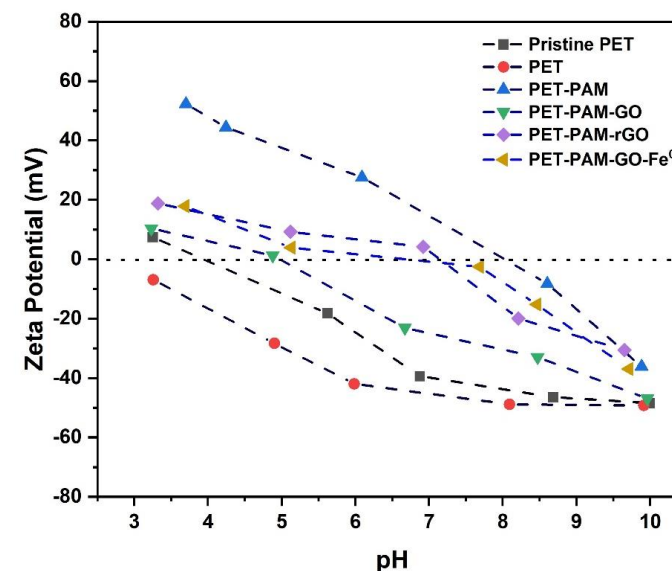


Figure 40. Zeta-potential (ζ) values of non-wovens as a function of the pH values of the electrolyte solution (0.001M KCl). (PET refers to alkalis polyester)

The negative surface containing PAMAM dendrimer and graphene oxide could pose an ideal environment for robust electrostatic incorporation of cationic iron particles (Fe³⁺) to improve the electro-catalytic properties of polyester non-woven membranes. After incorporation of Fe³⁺ and GO followed by reduction into Fe⁰ and rGO respectively, the isoelectric point of PET-PAM-rGO and PET-PAM-rGO-Fe⁰ shifted to $\text{pH}=7.15$ and $\text{pH}=7.05$, respectively.

The colour strength and the coating evenness analysis

The colour strength test was applied on PET-GO, PET-PAM-GO, PET-PAM-rGO, PET-PAM-rGO-Fe⁰, PET-rGO, PET-rGO-Fe⁰ samples in 10 different zones of the samples, and the mean values are provided in Table 15. It can be seen that the K/S value slightly increased from 3.94 to 4.42, compared to PET-GO and PET-PAM-GO samples. This is due to the higher absorbance of GO by the PET-PAM sample. As the reduction of GO to rGO changes the light brown colour of the fabric to carbon colour, the L^* , a^* , and b^* coordinates change from 45.44, 1.36, and 7.77 to 40.80, 1.55, and 5.75, respectively. When the fabric is incorporated with iron, the L^* , a^* , and b^* coordinates change to 41.91, 2.64, and 10.59, respectively.

Table 15. CIELAB colour strength and the coating evenness measurement.

Sample Name	%R at Wl. of Max (420nm)	K/S at Wl. of Abs. Max	L*	a*	b*	ΔE (CIE)	ΔE (CMC)
PET-GO	10.22	3.94	45.44	1.36	7.77	1.38±0.85	0.79±0.48
PET-rGO	7.73	5.51	33.6	0.36	1.05	0.59±0.4	0.36±0.23
PET-rGO-Fe ⁰	4.32	10.63	26.12	0.21	1.69	0.64±0.26	0.5±0.16
PET-PAM-GO	9.3	4.42	40.80	1.55	5.75	0.86±0.49	0.64±0.37
PET-PAM-rGO	8.34	5.05	36.42	0.47	1.42	0.84±0.63	0.49±0.33
PET-PAM-rGO-Fe ⁰	8.33	5.08	41.91	2.64	10.59	1.81±0.62	1.51±0.51

Here, (%R) = reflectance, K/S= colour strength, CIElab coordinates (L* is the coordinate response to brightness and darkness of the surface, a* coordinate response to the green-red shade of colour, and b* coordinates response to the yellow-blue shade of colour), ΔE (CIE) = Colour differences in CIE systems and ΔE (CMC)= Color differences in CMC systems.

The colour differences (ΔE) in both CIE and CMC systems (Figure 41) were measured by the mean of ten random colour measurements on each specimen. The values higher than 1 ($\Delta E > 1$) are visible to human eyes. Therefore, values higher than 1 ($\Delta E > 1$) are not acceptable in the textile dyeing industry for commercial production. Here, we can estimate the evenness of each incorporation step by recording ΔE of the specimen. PET-PAM-GO has a value of 0.86±0.49 and 0.64±0.37 in CIE and CMC systems, while PET-GO has a value of 1.38±0.85 and 0.79±0.48 in CIE and CMC systems, respectively. All samples except PET-PAM-rGO-Fe⁰ (1.81±0.62 (CIE), 1.51±0.51(CMC)) have a ΔE less than 1.

ATR-FTIR spectroscopy analysis

ATR-FTIR analysis was performed on non-woven samples to investigate the chemical composition and their possible bonds. All spectra were normalised by levelling the height of the adsorption peak at 1711 cm⁻¹, which indicates C=O stretch (ester) of polyester. Other identical peaks to polyester include the aromatic sp² C-H bend (723 cm⁻¹), a plane vibration of the benzene ring (1015 cm⁻¹), C-O stretch (ester) (1095 and 1240 cm⁻¹), and asymmetric C-H stretching (2965 cm⁻¹) were also observed in the FT-IR spectrum. After absorption of GO on

the polyester non-wovens (PET-GO), a peak at 3433 cm⁻¹ attributed to the O-H stretch appeared (Figure 42 (a)). Once the fabric was modified with iron (PET-rGO-Fe⁰), the intensity of the peak at 3433 cm⁻¹ increased and new peaks at 1054, 970, 684, 662, and 621 cm⁻¹ associated with C-O, O-H, and C-H stretch were detected. By modification of the fabric with PAMAM (PET-PAM) (Figure 42 (b)), a peak with low intensity was detected at 3285 cm⁻¹; this peak shows the presence of an N-H bond. Once the fabric is modified with rGO (PET-PAM-rGO), the intensity of some peaks, such as C=O and C-O stretches, decreases and the peak at 3285 cm⁻¹ disappears. Further, after the modification of the sample with iron (PET-PAM-rGO-Fe⁰), new peaks at 3361 cm⁻¹ (O-H stretch), 961 cm⁻¹ (C-H bend), 677 cm⁻¹ (C-H stretch), 547 cm⁻¹, and 492 cm⁻¹ (C-Br stretch) were detected. The intensity of peaks at 1905 cm⁻¹ and 1240 cm⁻¹ (C-O stretch) were altered.

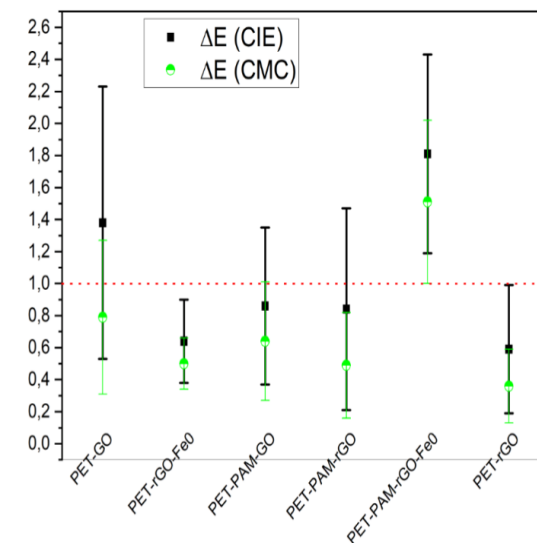


Figure 41. The colour differences (ΔE) of CIE and CMC systems (Values less than 1 are the smallest colour differences than the human eye can detect)

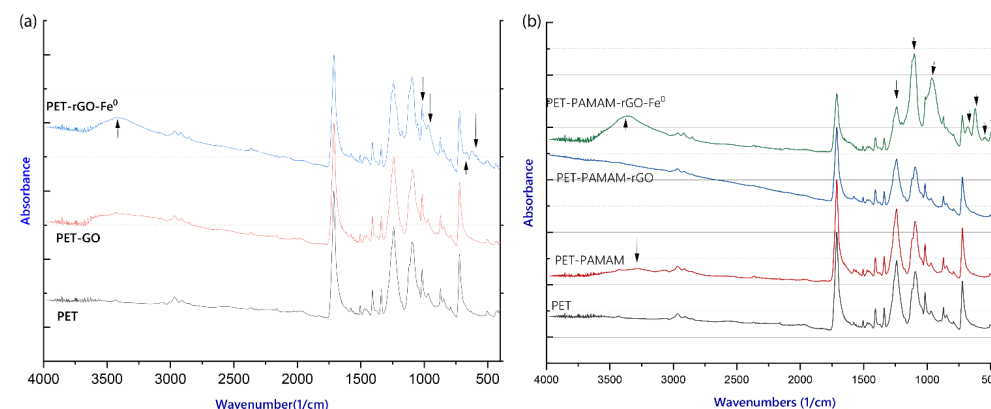


Figure 42. ATR-FTIR spectra of PET, PET-GO, PET-rGO-Fe⁰, PET-PAM, PET-PAM-rGO and PET-PAM-rGO-Fe⁰.

Thermal analysis and decomposition of materials

In a combustion process, materials undergo thermal degradation over burning, and TGA measurements are used as an indicator of polymer flammability [229]. The temperature at the maximum weight loss rate of the DTG curve is noted as T_{max} ; the temperatures corresponding to 5 wt% degradations at TGA cure are noted as T_{onset} , T_{max} , T_{onset} , residue (%) at T_{onset} , and residue (%) at 600°C of all samples from TG and DTG curves were calculated. It can be seen in Figure 43 that a pristine fabric (PET) has a T_{max} of 447°C. Once the functional materials are loaded, it increases to 463°C as the fabric is coated with GO (PET-GO). When the fabric is doped with iron (PET-rGO-Fe⁰), T_{max} decreases to 447°C, leaving 47.6% char residue at 600°C. Pristine PET and PET-GO samples show almost the same residue at 600°C of 17.44, and 17.52%, respectively. PET-PAM-rGO and PET-PAM-rGO-Fe⁰ have a T_{max} of 455, and 446, respectively.

The melting temperature (T_m) was measured from the maximum endothermic melting peak of the second heating cycle of DSC analysis. The crystallisation temperature (T_c) was recorded from the maximum exothermic crystallisation peak of the cooling cycle. Further, the heat of cold-crystallisation (ΔH_c) and the heat of fusion (ΔH_f) were calculated from the cooling and heating scan, respectively.

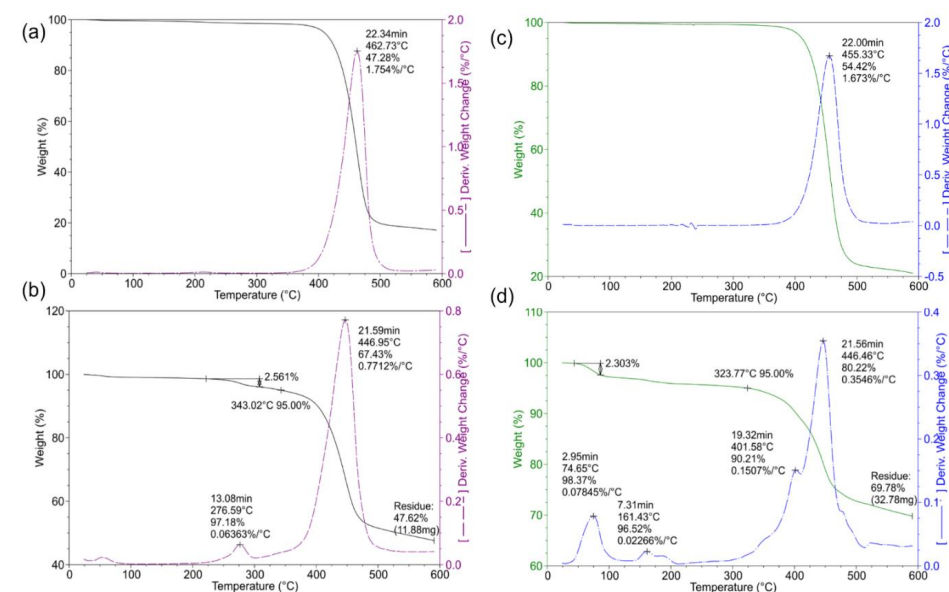


Figure 43. TGA and DTG curves of (a) PET-GO, (b) PET-rGO-Fe⁰, (c) PET-PAM-rGO, and (d) PET-PAM-rGO-Fe⁰.

Both iron-grafted samples have a small peak (PET-rGO-Fe⁰ at 276°C, 2.82% decomposition; and PET-PAM-rGO-Fe⁰ at 161°C, 1.85% decomposition). There is a peak at 75°C for PET-PAM-

rGO-Fe⁰ (1.63% reduction) which might be due to the moisture evaporation, as iron-containing functional groups tend to absorb moisture.

The melting temperature (T_m), the crystallisation temperature (T_c), and the heat of cold-crystallisation (ΔH_c) of the samples were obtained from DSC analyses (Table 16). It is evident from the DSC analyses that the melting temperature decreased from 255°C for PET to 240°C for PET-rGO-Fe⁰ and 243°C for PET-PAM-rGO-Fe⁰. ("Melting peak width" is correlated to the distribution of crystallinity of the polymer). T_{onset} is defined as the intersection of the tangents of the peak with the generalised baseline for polymeric materials. T_{onset} decreased from 243°C for PET to 218 and 226°C for PET-rGO-Fe⁰ and PET-PAM-rGO-Fe⁰, respectively. ΔH_f and ΔH_c of the sample decreased dramatically from 33.14 and 39.73 J g⁻¹ for PET to 12.17 and 12.64 J g⁻¹ for PET-rGO-Fe⁰, and it decreased to 7.32 and 7.69 J g⁻¹ for PET-PAM-rGO-Fe⁰. This might be due to the introduction of iron to the polymer that affects the melting and crystallisation process of the polymer.

Table 16. DSC data from the second heating scan and cooling scan of the samples.

Sample Name	Melting (from the heating scan)			Crystallisation (from the cooling scan)		
	T_{onset} (°C)	T_m peak (°C)	ΔH_f (J.g ⁻¹)	T_{onset} (°C)	T_c peak (°C)	ΔH_c (J.g ⁻¹)
Pristine PET	243	255	33.14	216	204	39.73
PET	241	254	33.67	214	201	38.44
PET-GO	232	245	28.39	207	198	34.65
PET-rGO-Fe ⁰	218	240	12.17	207	188	12.64
PET-PAM	242	255	39.33	216	201	41.92
PET-PAM-GO	234	245	27.82	209	200	32.91
PET-PAM-rGO	237	249	38.19	220	208	42.38
PET-PAM-rGO-Fe ⁰	226	243	7.321	211	194	7.69
PET-rGO	237	259	34.81	223	210	37.69

X-ray photoelectron spectroscopy (XPS) analysis

PAMAM dendrimer modified samples (PET-PAM, PET-PAM-GO, and PET-PAM-GO-Fe⁰) were analysed by XPS to identify the changes in element composition and the nature of the chemical bonding due to the subsequent surface modifications (Figure 44). As it can be seen from Table 17, a polyester itself contains 76.7 a.t% carbon and 21 a.t% oxygen. After modification of the fabric with PAMAM (PET-PAM), nitrogen was detected in the surface composition, having 74.5 a.t% carbon, 18 a.t% oxygen, and 7.45 a.t% nitrogen. PET-PAM-GO sample contains 70 a.t% oxygen, 1.3 a.t% nitrogen and 28 a.t% oxygen, and PET-PAM-rGO-Fe⁰ sample has 41.6 a.t% carbon, 42.6 a.t% nitrogen, 42.5 a.t% oxygen and 6 a.t% iron on its atomic weight per cent.

Table 17. Atomic proportion (a.t.%) of the surface chemical composition of the samples.

Sample Name	C1s (a.t %)	O1s (a.t %)	N1s (a.t %)	Fe2p (a.t %)
PET	76.7	21	0	0
PET-PAM	74.5	18	7.45	0
PET-PAM-GO	70	28	1.4	0
PET-PAM-rGO-Fe ⁰	41.6	42.6	1.3	6.08

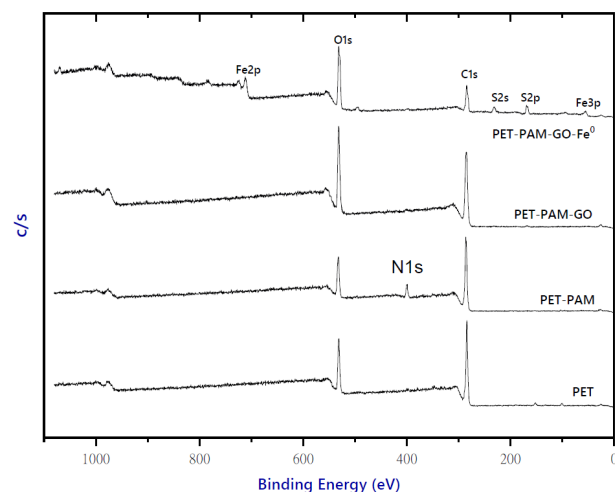


Figure 44. Wide scan XPS spectra of (a) pristine PET, PET-PAM, PET-PAM-GO, and PET-PAM-rGO-Fe⁰ samples.

4.3.2 Analysis of catalytic property of polyester non-woven fabrics

Colour removal

The catalytic performance of surface-modified polyester non-woven fabric containing iron nanoparticles on the graphene-coated fabrics was studied through their effectiveness in the removal of toxic colourants (crystal violet) from water. A cube cuvette was placed in a UV-vis spectrophotometre where the dye's solution and non-woven fabric were brought into contact in the presence of a reducing agent, as explained before. Degradation of the pollutants was started at once because of the formation of higher oxidation potential hydroxyl radicals ($\bullet\text{OH}$) due to the interaction between iron particles and NaBH_4 , besides adsorption of the pollutants by GO layers. The removal of crystal violet dyes concerning time has been recorded (real-time in situ) and plotted as shown in Figure 45. The characteristic absorption peak observed at $\lambda_{590\text{ nm}}$ is related to the intensity of crystal violet [230]. The removal reactions of crystal violet dyes using different non-woven fabrics (PET-GO, PET-rGO, PET-PAM-GO, PET-PAM-rGO, PET-rGO-Fe⁰ and PET-PAM-rGO-Fe⁰) were carried out under the same experimental conditions [Crystal violet = 50 mg.L⁻¹, non-woven fabric = 1cm² (700 mg), NaBH_4 = 0.1 M, pH=5]. As shown in

Figure 45 (a) and (b), there is no significant removal in the intensity of the dyes during 120 min exposure of the dyes in PET-GO and PET-PAM-GO containing solution, except for physisorption of the dyes due to the presence of GO. Yet, many studies reported higher catalytic behaviour of graphene oxide in a photocatalytic environment. The control polyester fabric does not pose any catalytic behaviour and has already been reported in various literature [205, 231, 232].

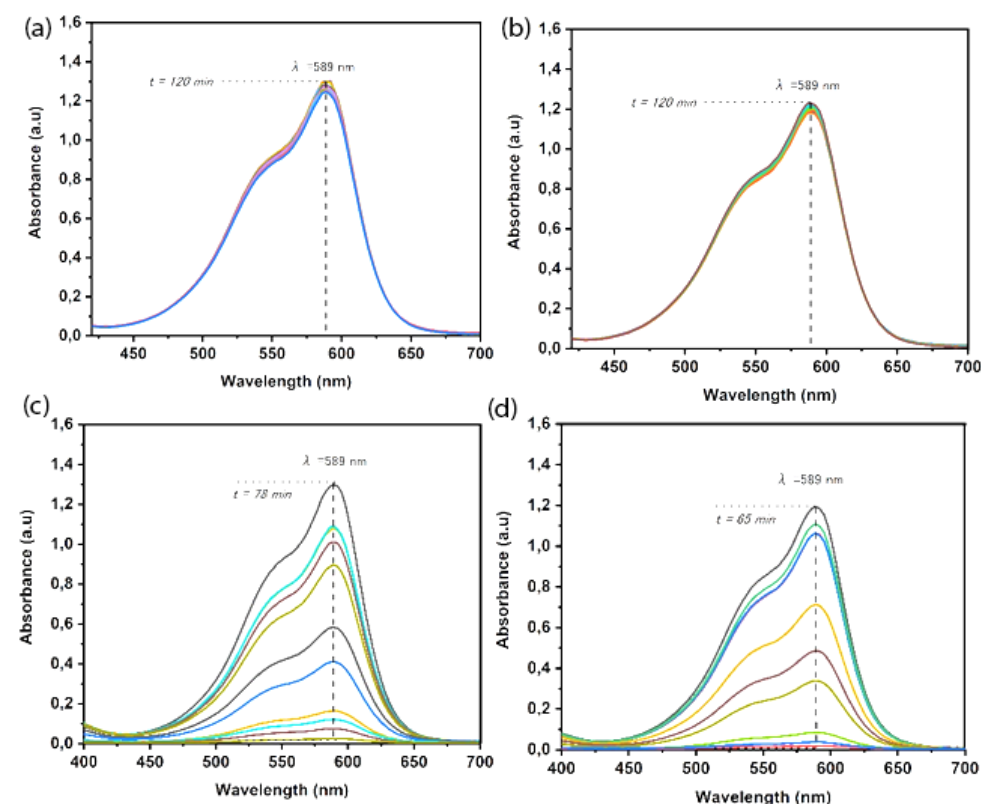


Figure 45. UV-visible spectroscopy of catalytic removal of crystal violet dyes using (a) PET-GO, (b) PET-PAM-GO, (c) PET-rGO-Fe⁰, and (d) PET-PAM-rGO-Fe⁰ [Conditions: Crystal violet = 50 mg. L⁻¹, non-woven fabric = 700 mg. L⁻¹, NaBH_4 = 0.1 M, pH=5].

Nevertheless, a significant reduction in the intensity of the absorbance at $\lambda_{590\text{ nm}}$ was observed once exposed to non-woven catalysts containing iron (PET-rGO-Fe⁰ and PET-PAM-rGO-Fe⁰), suggesting the discolouration of crystal violet. Both non-woven catalysts demonstrated a rapid removal performance (Figure 45(c), (d)). The removal rate reached 99.04% in 65 min, for PET-PAM-rGO-Fe⁰ and 97.68% in 78 min. Fast removal of crystal violet could be due to the stability and amount of functional material (Fe⁰) loaded on each non-woven fabric, ensuring the maximum exposure of the reagent and producing striking hydroxyl radicals for

discolouration. Even though results indicate graphene oxide has a fairly poor direct effect on the removal of dyes, the hexagonal microstructures of graphene oxide facilitated the incorporation of Fe⁰ on the polyester surface towards high precision of stability, a disparity which later contributed to the removal of the pollutant.

Kinetics of colour removal using PET-rGO-Fe⁰ and PET-PAM-rGO-Fe⁰

Among all samples, PET-rGO-Fe⁰ and PET-PAM-rGO-Fe⁰ demonstrated catalytic properties towards the removal of crystal violet dyes, so their kinetics were considered for further study in this section. For that, the initial absorbance ratio of the crystal violet dye at $\lambda_{590\text{ nm}}$ (A/A_0) during the reduction reaction was measured, which is the corresponding concentration ratio (C/C_0), making it possible to plot $\ln(C/C_0)$ as a function of time according to the Equation below as shown in Figure 46 (a,b).

$$\ln \frac{C}{C_0} = \ln \frac{A}{A_0} - k \cdot t$$

Linear evolution in time of $\ln(C/C_0)$ as supported by R^2 values is the model used for validation of first-order reaction kinetics for crystal violet colour removal with the non-woven fabric with 98.83 and 99.04 for PET-rGO-Fe⁰ and PET-PAM-rGO-Fe⁰, respectively (Table 18). The results deliver evidence of a decent linear relationship of $\ln(C/C_0)$ versus reaction time for both PET-rGO-Fe⁰ and PET-PAM-rGO-Fe⁰, following the first-order and pseudo-first-order reaction kinetics concerning crystal violet dye removal.

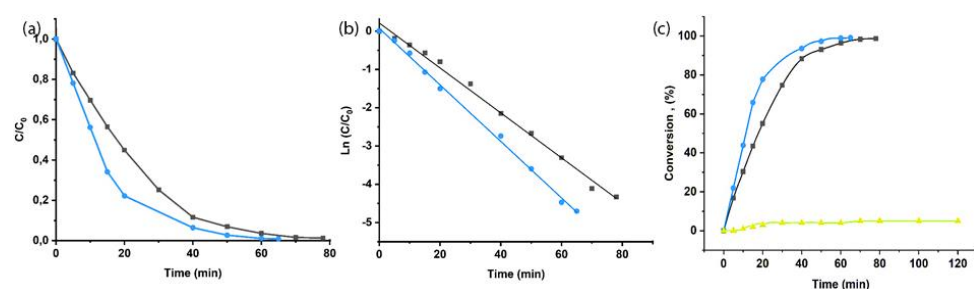


Figure 46. Evolution of (a) C/C_0 , (b) $\ln(C/C_0)$ and (c) the conversion (%) yield in time at room temperature for removal of crystal violet dyes using PET-GO (▲), PET-rGO-Fe⁰ (■) and PET-PAM-rGO-Fe⁰ (●) [Conditions: Crystal violet = 50 mg.L⁻¹, nonwoven fabric = 700 mg.L⁻¹, NaBH₄ = 0.1 M, pH=5].

PET-PAM-rGO-Fe⁰ exhibited faster (0.07384 min⁻¹) removal than that of PET-rGO-Fe⁰ (0.05873 min⁻¹), which might be due to the higher quantity of Fe⁰ and better stability of the catalysts on the PAMAM-modified sample as supported by TGA analysis.

In addition, the conversion percentage of PET-GO, PET-rGO-Fe⁰ and PET-PAM-rGO-Fe⁰ reaches 4.98% in 120 min, 98.83% in 78 min, and 99.04% in 65 min, respectively (Figure 46 (c)). High conversion and fast kinetics in catalytic degradation might be attributed to the good stabilisation of zerovalent iron particles and characteristic adsorption properties of GO nanosheets.

Table 18. A comparison of the reaction kinetics for the removal of crystal violet dyes using PET-GO, PET-rGO-Fe⁰ and PET-PAM-rGO-Fe⁰

Sample	Conc. of pollutants	^a Time (min)	^b Rate constant, k (min ⁻¹)	^c Correlation coefficient, R ²	Conversion, (%)
PET-GO	50 mg.L ⁻¹	120	0.00091	31.94	04.98
PET-rGO-Fe ⁰	50 mg.L ⁻¹	78	0.05873	99.33	98.83
PET-PAM-rGO-Fe ⁰	50 mg.L ⁻¹	65	0.07384	99.77	99.04

^a reaction time required for complete colour removal.

^b k: rate constant for the 1st order kinetics, and is expressed in min⁻¹.

^c R²: correlation coefficient of the linear regression.

Toxicity reduction analysis

To study the toxicity reduction, the relative evaluation of COD concentration of PET-GO, PET-rGO-Fe⁰ and PET-PAM-rGO-Fe⁰ treated solution, based on a control solution, were studied as per the method explained in Section 3.5.1. The COD of the control solution was considered 100%. Results indicate a relative reduction in COD after the treatment, from 100% to 62.08% and 46.37% for PET-rGO-Fe⁰ and PET-PAM-rGO-Fe⁰, respectively.

The key cause for this tendency might be the decreasing number of dye molecules and their intermediates, mostly with the process of oxidising crystal violet dyes mineralised into water and carbon dioxide. However, even though the COD reduction is more than 50%, higher detoxification efficiency is a precondition for the industrial prospects of this process. Complete reduction of COD can be proposed with further experiment design involving continued treatment of the wastewater after the complete colour removal, which will allow available reactive species to react with leuco-compounds as a subsequent step for complete detoxification.

Analysis of recyclability-reusability

Reusability of the products is an important factor when it comes to industrial applications. Accordingly, the recyclability of PET-rGO-Fe⁰ and PET-PAM-rGO-Fe⁰ was evaluated under the conditions explained in section 4.5.1. Results display that the non-woven fabric can be recycled up to five times with a slight reduction in the catalytic activity, as observed after the catalytic removal of crystal violet dye in constant time (Figure 47).

PET-PAM-rGO-Fe⁰ exhibited 91.5% of its activity in the fifth crystal violet removal attempt. However, the removal percentage of PET-rGO-Fe⁰ reduced to 81.3% after a five-cycle application. This may be explained by possible variation in Fe⁰ re-aggregation and contact surface decay between two catalysts, which remains to be elucidated through further investigations. These results provide an extensive ground for improvement in textile-based catalytic wastewater treatment systems over conventional solutions.

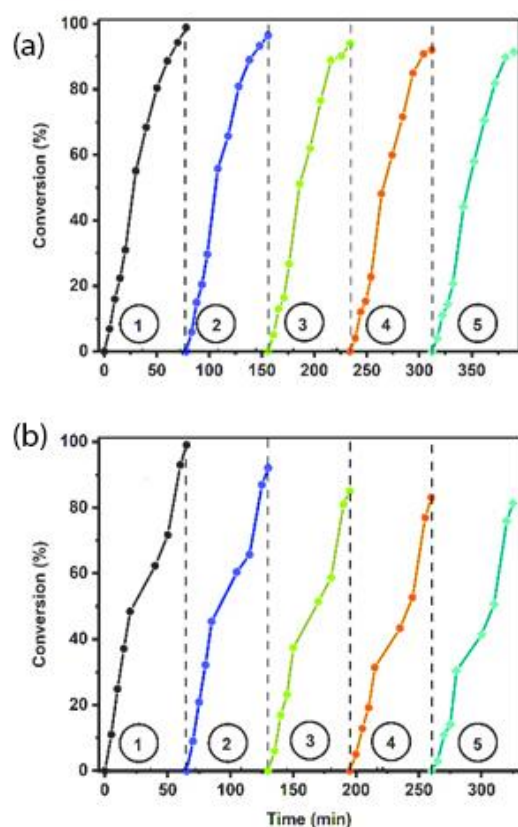


Figure 47. Recyclability and reusability of (a) PET-rGO-Fe⁰, (b) PET-PAM-rGO-Fe⁰ on catalytic removal of crystal violet dye [Conditions: Crystal violet = 50 mg.L⁻¹, non-woven fabric = 700 mg.L⁻¹, NaBH₄ = 0.1 M, pH=5].

Effect of concentration of PET-rGO-Fe⁰ and PET-PAM-rGO-Fe⁰ on dye removal

The concentration of catalysts on the adsorption medium is one of the most important parameters affecting the adsorption process [233]. Hence, the impact of the concentration of catalysts on the reduction and degradation activities was studied. For comparative purposes, the concentration of both catalysts was changed in the same manner, and the dye removal setup was identical. Results displayed the same trend for both catalysts in the removal of crystal violet dyes. The catalytic activity increased as the concentration of catalysts increased until the equilibrium concentration of the catalyst (Figure 48). It shows that in an increasing amount of the catalyst's concentration, the catalytic capacity was higher, which can be explained by the participation of a higher amount of Fe⁰ towards generating reactive species that stimulate the removal process. Nevertheless, at the equilibrium, although a number of the iron particle is present in the reaction, the reducing agent (NaBH₄) becomes saturated, which cannot produce further reactive species, so a plateau effect appears. The decrease in the catalyst's concentration from 700 mg.L⁻¹ to 300 mg.L⁻¹ do not significantly reduce the catalytic activity, indicating that even with a small quantity, the catalyst provides a good catalytic activity.

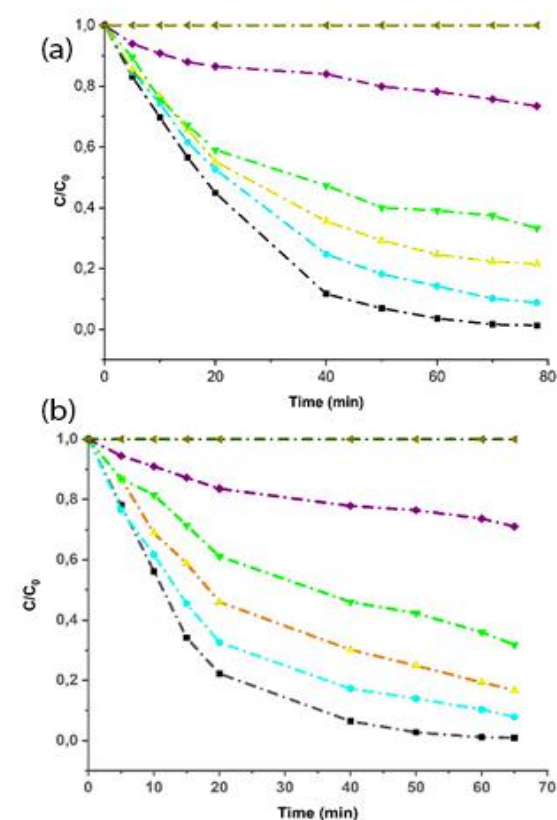


Figure 48. Effect of catalyst concentration [0 mg.L⁻¹ (●), 50 mg.L⁻¹ (◆), 100 mg.L⁻¹ (▼), 300 mg.L⁻¹ (▲), 500 mg.L⁻¹ (●), 700 mg.L⁻¹ (■), on the removal of crystal violet dyes (a) PET-rGO-Fe⁰ and (b) PET-PAM-rGO-Fe⁰. [Conditions: Crystal violet = 50 mg.L⁻¹, NaBH₄ = 0.1 M, pH=5].

4.4 Fully textile-based reactor and its electro-Fenton performance

4.4.1 Colour removal

The electrocatalytic performance of the reactor containing iron particles on the rGO-modified surface and stainless-steel yarns has been studied briefly by their efficiency in the removal of toxic colourants (here crystal violet-blue) from water. A 3-electrode setup in a dye solution was brought into contact, and a constant current of 0.02 A was applied to the working electrode (rGO-Fe⁰); every 10 minutes, a UV-vis spectrophotometer was used to measure the degradation of the dye. The degradation starts at once because of the formation of higher oxidation potential hydroxyl radicals ($\bullet\text{OH}$) due to the current applied to the system. The real-time in situ reductions were plotted as shown in Figure 49. The characteristic absorption peak observed at $\lambda_{590 \text{ nm}}$ is attributed to the intensity of the crystal violet [230]. (Experimental condition: crystal violet = 50 mg.L⁻¹, current = 0.02 A). A significant reduction in the intensity of the absorbance at $\lambda_{590 \text{ nm}}$ was observed when the dye solution was exposed to the reactor, suggesting the decolouration of crystal violet.

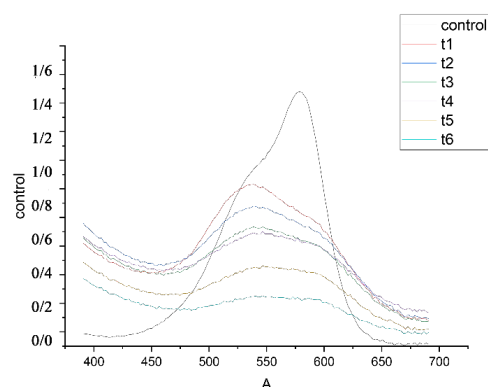


Figure 49. UV-visible spectroscopy of catalytic removal of crystal violet dyes in electro-Fenton process.

After 60 minutes of applying a constant current of 0.02, the conversion (%) of the colour dyes was calculated according to the equation explained in the previous chapter. The results show that 65.7% of the dye has been removed from the water after 60 minutes.

4.4.2 Kinetic colour removal using the fully textile-based reactor

To measure the kinetics of the removal, initial absorbance ratio of the crystal violet dye at $\lambda_{590 \text{ nm}}$ (A/A_0) during the reduction reaction was determined. It accounts for the corresponding concentration ratio (C/C_0) as a function of the time, according to the equation below:

$$\ln \frac{C}{C_0} = \ln \frac{A}{A_0} - k \cdot t$$

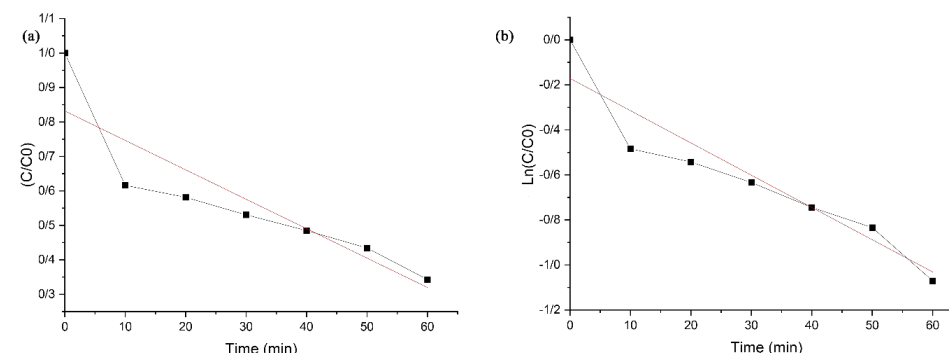


Figure 50. Evolution of (a) C/C_0 , (b) $\ln(C/C_0)$ and in time at room temperature for removal of crystal violet dyes using a GO-Fe⁰ / stainless steel textile reactor.

As can be seen from Figure 50, the conversion ratio is very high in the first 10 minutes and thereafter the ratio decreases. This could be due to the reduction of the concentration of zerovalent iron particles. The average removal ratio of the system is 0.01433 min⁻¹, which is considered rapid kinetics in catalytic degradation.

Chapter 5

Summary

The objective of this thesis was to investigate the use of different applicable technologies as strategies for coating conventional textiles with graphene and further immobilisation of other elements, such as iron on graphene-modified textiles for further use in sustainable Fenton and electro-Fenton wastewater treatment application.

As explained in chapter 1, modification of conventional textiles with graphene as well as element doping of graphene could give a wide range of properties to the textile from UV-blocking, energy harvesting, health monitoring, electrothermal and electrical properties. However, as explained in chapter 1, the main focus of this thesis is on the electrical, electrothermal, and catalytical properties of the modified textiles.

When it comes to textile, not all available methods apply to the textile mediums. The materials used in this study with the detailed methods and protocols for obtaining such modified textiles were described in chapters 2 and 3.

Chapter 4 includes the obtained results in this thesis. The first approach is surface charge modification of the conventional textiles for further graphene oxide coating. Improving the coating protocol and enhancing the fastness and conductivity of the resulting textile are included in the first approach.

The second approach involves designing a continuous yarn coating system for further knitting a specific device, such as a tactile sensor or a wastewater treatment reactor.

The third approach relates to designing an applicable method for further iron doping of graphene-modified textiles; the resulting textiles were used in catalytical wastewater treatment.

The fourth and last approach of this thesis had to do with knitting a fully textile-based reactor with two various anodic and cathodic blocks (rGO-Fe⁰; stainless steel yarns) for electrocatalytic dye removal.

General conclusion and future perspectives

The main finding in this study is the experimental evidence for a simple approach to graft graphene and inorganic catalysts on textiles. The study was done in textiles in yarn form, non-woven and knitted polyester fabrics. It has been conclusively shown that the method of surface charge modification of the polyester fibres before graphene oxide coating to produce conductive yarns, as well as the surface chemistry of the functionalised polyester textiles, has a synergistic effect on the success of GO coating and immobilisation of Fe⁰ on polyester fibres; moreover, it has been shown that this will highly improve electrical and catalytical properties of the textile.

The first section of the study was related to the activation and grafting of various cationic agents on polyester fibres and further coating with graphene oxide dispersion. Analysis based

on scanning electron microscopy (SEM), sessile droplet goniometry, Fourier transform infrared (FT-IR) and zeta potential measurement confirmed the successful surface charge modification of the polyester as well as even graphene oxide coating on the polyester surface. Results from electrical and electrothermal analysis prove that the resulting textiles are conductive enough to be used in heating element applications, such as military or cold environment garments. Electromechanical analysis of the resulting e-textiles proves that these yarns could be used for electromechanical applications, such as pressure or tension sensor.

The second section of the study confirms the successful continuous coating and immobilising line for coating single or twisted yarns. The results from the washing fastness and colour measurement prove that these yarns would have enough fastness to be used in automatic knitting machines among conventional yarns to knit a specific device, such as a strain sensor or wastewater treatment reactor.

The third section of the thesis focused on the immobilisation of iron on non-woven polyester fabrics. Analysis from UV-VIS spectroscopy with toxicity reduction proves the successful method of immobilisation of iron particles on graphene oxide coated fibres and yarns.

The last section of the thesis showed that these rGO-Fe⁰ yarns among stainless steel yarns could be knitted as a smart device that could be used for electro-Fenton wastewater treatment.

In this thesis work, different novel approaches have been introduced and investigated, which not only contribute to the literature in the related domains but also advance the area of surface charge modification, graphene oxide coating and further graphene grafting with other elements, such as iron, on a textile medium.

Some of the main contributions and highlights are as follows:

1. This thesis took a new approach to immobilisation of inorganic catalysts on graphene-modified polyester textiles as a new support material for the catalyst and electrocatalyst applications
2. Combining a textile with a conductive material and a catalytic system, this thesis has contributed to the domain of both multifunctional (main focus on electrical properties) textiles and heterogeneous catalysts. This is the first attempt to combine graphene and inorganic catalyst properties on a textile support material.
3. In general, these detailed studies of graphene-modified e-textiles and catalytic and electrocatalytic wastewater treatment contribute to the general knowledge of multifunctional graphene-catalytic systems, to the knowledge of the Fenton and electro Fenton process, but also the advancement and scaling up of sustainable wastewater treatment systems.

Although this study has extensively investigated the concept of converting conventional textile polyester supports to multifunctional (in this thesis, focus on electrical and catalytical properties) materials that could be used in Fenton and Electro-Fenton like processes, it fails to address several points, especially in electrocatalytic systems.

One of the most important plans is to replace both alkalisation and chemical surface charge modification with plasma technology, in which textiles could be nitrogen plasma treated before graphene oxide coating. This leads to a more sustainable and green method, as there is no need for chemicals, solvents and water consumption.

In this thesis, the study of toxicity reduction analysis for the electro-Fenton reactor is lacking. The reusability and recyclability of the resulting reactor also remain unanswered.

Further research in the field of electro-Fenton wastewater treatment using textile support, scaling it up and enhancing the concentration of the catalyst have endless ideas and possibilities that could be at the core of further studies.

REFERENCES

- Schneegass, S. and Amft, O. *Smart textiles*. 2017: Springer.
- Guo, L. et al. *Smart Textiles and their Applications*. 2016. Woodhead Publishing Limited, Cambridge.
- Stoppa, M. and Chiolerio, A. *Wearable electronics and smart textiles: A critical review*. *Sensors*, 2014. **14**(7): p. 11957-11992.
- Persson, N.K. et al. *Actuating Textiles: Next Generation of Smart Textiles*. *Advanced Materials Technologies*, 2018. **3**(10): p. 1700397.
- Schwarz, A. et al. *A roadmap on smart textiles*. *Textile Progress*, 2010. **42**(2): p. 99-180.
- Cheng, K.B., Ueng, T.H. and Dixon, G. *Electrostatic discharge properties of stainless steel/polyester woven fabrics*. *Textile Research Journal*, 2001. **71**(8): p. 732-738.
- Huang, Y. et al. *From industrially weavable and knittable highly conductive yarns to large wearable energy storage textiles*. *ACS Nano*, 2015. **9**(5): p. 4766-4775.
- Lymberis, A. and De Rossi, D.E. *Wearable ehealth systems for personalised health management: state of the art and future challenges*. Vol. 108. 2004: IOS Press.
- Chai, Z. et al. *Tailorable and wearable textile devices for solar energy harvesting and simultaneous storage*. *ACS Nano*, 2016. **10**(10): p. 9201-9207.
- Pervez, M.N. et al. *Low-temperature synthesis of novel polyvinylalcohol (PVA) nanofibrous membranes for catalytic dye degradation*. *Journal of Cleaner Production*, 2020. **262**: p. 121301.
- Iyer, S.N. et al. *Study of photoluminescence property on cellulosic fabric using multifunctional biomaterials riboflavin and its derivative Flavin mononucleotide*. *Scientific Reports*, 2019. **9**(1): p. 1-16.
- Morshed, M.N. et al. *Sonochemical fabrication of nanocrystalline titanium dioxide (TiO₂) in cotton fiber for durable ultraviolet resistance*. *Journal of Natural Fibers*, 2020. **17**(1): p. 41-54.
- Vieillard, J. et al. *CuO nanosheets modified with amine and thiol grafting for high catalytic and antibacterial activities*. *Industrial & Engineering Chemistry Research*, 2019. **58**(24): p. 10179-10189.
- Hebeish, A. et al. *Preparation of durable insect repellent cotton fabric: Limonene as insecticide*. *Carbohydrate Polymers*, 2008. **74**(2): p. 268-273.
- Agnihotri, A. et al. *Insect-repellent textiles using green and sustainable approaches*, in *The Impact and Prospects of Green Chemistry for Textile Technology*. 2019, Elsevier. p. 307-325.
- Sadi, M.S. et al. *Direct screen printing of single-faced conductive cotton fabrics for strain sensing, electrical heating and color changing*. *Cellulose*, 2019. **26**(10): p. 6179-6188.
- Wittkowski, T. *Electrically conductive textiles for occupant sensing and/or heating applications*. 2014, Google Patents.
- Craddick, J.E. *Electrothermal garment*. 1921, Google Patents.
- Park, S. and Jayaraman, S. *Smart textiles: Wearable electronic systems*. *MRS Bulletin*, 2003. **28**(8): p. 585-591.
- Li, L. et al. *Wearable electronic design: electrothermal properties of conductive knitted fabrics*. *Textile Research Journal*, 2014. **84**(5): p. 477-487.
- Hwang, P.-W. et al. *Electromagnetic shielding effectiveness and functions of stainless steel/bamboo charcoal conductive fabrics*. *Journal of Industrial Textiles*, 2014. **44**(3): p. 477-494.
- Kumar, S. et al. *Fibers from polypropylene/nano carbon fiber composites*. *Polymer*, 2002. **43**(5): p. 1701-1703.
- Ozen, M.S. et al. *Investigation of the Electromagnetic Shielding Effectiveness of Needle Punched Nonwoven Fabrics Produced from Stainless Steel and Carbon Fibres*. *Fibres & Textiles in Eastern Europe*, 2018.

24. Fugetsu, B. et al. *Graphene oxide as dyestuffs for the creation of electrically conductive fabrics*. Carbon, 2010. **48**(12): p. 3340-3345.
25. Morgan, P. *Carbon fibers and their composites*. 2005: CRC Press.
26. Zhou, Y. et al. *Polyurethane-based solid-solid phase change materials with in situ reduced graphene oxide for light-thermal energy conversion and storage*. Chemical Engineering Journal, 2018. **338**: p. 117-125.
27. Kucinskis, G., Bajars, G. and Kleperis, J. *Graphene in lithium ion battery cathode materials: A review*. Journal of Power Sources, 2013. **240**: p. 66-79.
28. Li, X. et al. *Graphene in photocatalysis: a review*. Small, 2016. **12**(48): p. 6640-6696.
29. Ke, Q. and Wang, J. *Graphene-based materials for supercapacitor electrodes—A review*. Journal of Materiomics, 2016. **2**(1): p. 37-54.
30. Enoki, T., Suzuki, M. and Endo, M. *Graphite intercalation compounds and applications*. 2003: Oxford University Press.
31. Kaner, R. et al. *Boron-carbon-nitrogen materials of graphite-like structure*. Materials Research Bulletin, 1987. **22**(3): p. 399-404.
32. Novoselov, K.S. et al. *Two-dimensional gas of massless Dirac fermions in graphene*. Nature, 2005. **438**(7065): p. 197-200.
33. Morozov, S. et al. *Giant intrinsic carrier mobilities in graphene and its bilayer*. Physical Review Letters, 2008. **100**(1): p. 016602.
34. Novoselov, K.S. et al. *Electric field effect in atomically thin carbon films*. Science, 2004. **306**(5696): p. 666-669.
35. Berger, C. et al. *Electronic confinement and coherence in patterned epitaxial graphene*. Science, 2006. **312**(5777): p. 1191-1196.
36. Kim, K.S. et al. *Large-scale pattern growth of graphene films for stretchable transparent electrodes*. Nature, 2009. **457**(7230): p. 706-710.
37. Li, X. et al. *Chemically derived, ultrasmooth graphene nanoribbon semiconductors*. Science, 2008. **319**(5867): p. 1229-1232.
38. Choi, W. et al. *Synthesis of graphene and its applications: a review*. Critical Reviews in Solid State and Materials Sciences, 2010. **35**(1): p. 52-71.
39. Geim, A.K. and Novoselov, K.S. *The rise of graphene*, in *Nanoscience and technology: a collection of reviews from nature journals*. 2010, World Scientific. p. 11-19.
40. Stankovich, S. et al. *Graphene-based composite materials*. Nature, 2006. **442**(7100): p. 282-286.
41. Stankovich, S. et al. *Synthesis of graphene-based nanosheets via chemical reduction of exfoliated graphite oxide*. Carbon, 2007. **45**(7): p. 1558-1565.
42. Hummers Jr, W.S. and Offeman, R.E. *Preparation of graphitic oxide*. Journal of the American Chemical Society, 1958. **80**(6): p. 1339-1339.
43. Hirata, M. et al. *Thin-film particles of graphite oxide 1:: High-yield synthesis and flexibility of the particles*. Carbon, 2004. **42**(14): p. 2929-2937.
44. Park, S. and Ruoff, R.S. *Chemical methods for the production of graphenes*. Nature Nanotechnology, 2009. **4**(4): p. 217.
45. Stankovich, S. et al. *Systematic post-assembly modification of graphene oxide paper with primary alkylamines*. Chemistry of Materials, 2010. **22**(14): p. 4153-4157.
46. Dikin, D.A. et al. *Preparation and characterization of graphene oxide paper*. Nature, 2007. **448**(7152): p. 457-460.
47. Lerf, A. et al. *Structure of graphite oxide revisited*. The Journal of Physical Chemistry B, 1998. **102**(23): p. 4477-4482.
48. Pei, S. and Cheng, H.-M. *The reduction of graphene oxide*. Carbon, 2012. **50**(9): p. 3210-3228.
49. Yu, W. et al. *Progress in the functional modification of graphene/graphene oxide: A review*. RSC Advances, 2020. **10**(26): p. 15328-15345.
50. Su, C.-Y. et al. *Highly efficient restoration of graphitic structure in graphene oxide using alcohol vapors*. ACS Nano, 2010. **4**(9): p. 5285-5292.
51. Kim, H., Abdala, A.A. and Macosko, C.W. *Graphene/polymer nanocomposites*. Macromolecules, 2010. **43**(16): p. 6515-6530.
52. Huh, S.H. *Thermal reduction of graphene oxide*. Physics and Applications of Graphene-Experiments, 2011. **19**: p. 73-90.
53. Chang, S.-J. et al. *Graphene growth from reduced graphene oxide by chemical vapour deposition: seeded growth accompanied by restoration*. Scientific Reports, 2016. **6**(1): p. 1-9.
54. Chua, C.K. and Pumera, M. *Chemical reduction of graphene oxide: a synthetic chemistry viewpoint*. Chemical Society Reviews, 2014. **43**(1): p. 291-312.
55. Shin, H.J. et al. *Efficient reduction of graphite oxide by sodium borohydride and its effect on electrical conductance*. Advanced Functional Materials, 2009. **19**(12): p. 1987-1992.
56. Becerril, H.A. et al. *Evaluation of solution-processed reduced graphene oxide films as transparent conductors*. ACS Nano, 2008. **2**(3): p. 463-470.
57. Fernández-Merino, M.J. et al. *Vitamin C is an ideal substitute for hydrazine in the reduction of graphene oxide suspensions*. The Journal of Physical Chemistry C, 2010. **114**(14): p. 6426-6432.
58. Shateri-Khalilabad, M. and Yazdanshenas, M.E. *Fabricating electroconductive cotton textiles using graphene*. Carbohydrate Polymers, 2013. **96**(1): p. 190-195.
59. Nabil, B. et al. *Development of new multifunctional filter based nonwovens for organics pollutants reduction and detoxification: High catalytic and antibacterial activities*. Chemical Engineering Journal, 2019. **356**: p. 702-716.
60. Bai, H. et al. *Non-covalent functionalization of graphene sheets by sulfonated polyaniline*. Chemical Communications, 2009(13): p. 1667-1669.
61. Wang, X. and Shi, G. *An introduction to the chemistry of graphene*. Physical Chemistry Chemical Physics, 2015. **17**(43): p. 28484-28504.
62. Duan, X. et al. *Effects of nitrogen-, boron-, and phosphorus-doping or codoping on metal-free graphene catalysis*. Catalysis Today, 2015. **249**: p. 184-191.
63. Song, Y. et al. *Iron (III) Chloride doping of CVD graphene*. Nanotechnology, 2014. **25**(39): p. 395701.
64. Zhou, T. et al. *Increased activity of nitrogen-doped graphene-like carbon sheets modified by iron doping for oxygen reduction*. Journal of Colloid and Interface Science, 2019. **536**: p. 42-52.
65. Sibul, R. et al. *Iron-and nitrogen-doped graphene-based catalysts for fuel cell applications*. ChemElectroChem, 2020. **7**(7): p. 1739-1747.
66. Li, J. et al. *Electronic modulation of nickel phosphide by iron doping and its assembly on a graphene framework for efficient electrocatalytic water oxidation*. Journal of Alloys and Compounds, 2020. **824**: p. 153913.
67. Liu, H. et al. *Easy one-step hydrothermal synthesis of nitrogen-doped reduced graphene oxide/iron oxide hybrid as efficient supercapacitor material*. Journal of Solid State Electrochemistry, 2015. **19**(1): p. 135-144.
68. Hsu, K.-I. et al. *Immobilization of iron hydroxide/oxide on reduced graphene oxide: peroxidase-like activity and selective detection of sulfide ions*. RSC Advances, 2014. **4**(71): p. 37705-37713.
69. Deb, H. et al. *Design and development of TiO₂-Fe₃O₄ nanoparticle-immobilized nanofibrous mat for photocatalytic degradation of hazardous water pollutants*. Journal of Materials Science: Materials in Electronics, 2019. **30**(5): p. 4842-4854.
70. Morshed, M.N. et al. *Stabilization of zero valent iron (Fe⁰) on plasma/dendrimer functionalized polyester fabrics for Fenton-like removal of hazardous water pollutants*. Chemical Engineering Journal, 2019. **374**: p. 658-673.
71. Hu, C. et al. *Spontaneous reduction and assembly of graphene oxide into three-dimensional graphene network on arbitrary conductive substrates*. Scientific Reports, 2013. **3**: p. 2065.

72. Li, X. et al. *Directly drawing self-assembled, porous, and monolithic graphene fiber from chemical vapor deposition grown graphene film and its electrochemical properties*. Langmuir, 2011. **27**(19): p. 12164-12171.
73. Dong, Z. et al. *Facile fabrication of light, flexible and multifunctional graphene fibers*. Advanced Materials, 2012. **24**(14): p. 1856-1861.
74. Mishra, R.K. et al. *Electrospinning of graphene-oxide onto screen printed electrodes for heavy metal biosensor*. Sensors and Actuators B: Chemical, 2017. **247**: p. 366-373.
75. Weise, B. et al. *Melt-and wet-spinning of graphene-polymer nano-composite fibres for multifunctional textile applications*. Materials Today: Proceedings, 2017. **4**: p. S135-S145.
76. Xu, Z. and Gao, C. *In situ polymerization approach to graphene-reinforced nylon-6 composites*. Macromolecules, 2010. **43**(16): p. 6716-6723.
77. Xu, Z. and Gao, C. *Graphene chiral liquid crystals and macroscopic assembled fibres*. Nature Communications, 2011. **2**: p. 571.
78. Xu, Z. et al. *Strong, conductive, lightweight, neat graphene aerogel fibers with aligned pores*. Acs Nano, 2012. **6**(8): p. 7103-7113.
79. Jalili, R. et al. *Scalable one-step wet-spinning of graphene fibers and yarns from liquid crystalline dispersions of graphene oxide: towards multifunctional textiles*. Advanced Functional Materials, 2013. **23**(43): p. 5345-5354.
80. Miankafshe, M.A., Bashir, T. and Persson, N.-K. *The role and importance of surface modification of polyester fabrics by chitosan and hexadecylpyridinium chloride for the electrical and electro-thermal performance of graphene-modified smart textiles*. New Journal of Chemistry, 2019. **43**(17): p. 6643-6658.
81. Stoller, M.D. et al. *Graphene-based ultracapacitors*. Nano letters, 2008. **8**(10): p. 3498-3502.
82. Suk, J.W. et al. *Mechanical properties of monolayer graphene oxide*. ACS Nano, 2010. **4**(11): p. 6557-6564.
83. He, H. et al. *3D-printed graphene antennas and interconnections for textile RFID tags: fabrication and reliability towards humidity*. International Journal of Antennas and Propagation, 2017. **2017**.
84. He, H. et al. *3D-printed graphene and stretchable antennas for wearable RFID applications*. in *2017 International Symposium on Antennas and Propagation (ISAP)*. 2017. IEEE.
85. Xu, X. et al. *Screen printed graphene electrodes on textile for wearable electrocardiogram monitoring*. Applied Physics A, 2019. **125**(10): p. 1-7.
86. Neves, A. et al. *Transparent conductive graphene textile fibers*. Scientific Reports, 2015. **5**(1): p. 1-7.
87. Ojha, K., Anjaneyulu, O. and Ganguli, A.K. *Graphene-based hybrid materials: synthetic approaches and properties*. Current Science, 2014: p. 397-418.
88. Stankovich, S. et al. *Stable aqueous dispersions of graphitic nanoplatelets via the reduction of exfoliated graphite oxide in the presence of poly (sodium 4-styrenesulfonate)*. Journal of Materials Chemistry, 2006. **16**(2): p. 155-158.
89. Bourlinos, A.B. et al. *Graphite oxide: chemical reduction to graphite and surface modification with primary aliphatic amines and amino acids*. Langmuir, 2003. **19**(15): p. 6050-6055.
90. Lotya, M. et al. *Liquid phase production of graphene by exfoliation of graphite in surfactant/water solutions*. Journal of the American Chemical Society, 2009. **131**(10): p. 3611-3620.
91. Grancaric, A.M., Tarbuk, A. and Pusic, T. *Electrokinetic properties of textile fabrics*. Coloration Technology, 2005. **121**(4): p. 221-227.
92. Moleon, J.A. et al. *Effect of N-cetylpyridinium chloride in adsorption of graphene oxide onto polyester*. Dyes and Pigments, 2015. **122**: p. 310-316.
93. Bao, H. et al. *Immobilization of trypsin in the layer-by-layer coating of graphene oxide and chitosan on in-channel glass fiber for microfluidic proteolysis*. Analyst, 2011. **136**(24): p. 5190-5196.
94. Sahito, I.A. et al. *Integrating high electrical conductivity and photocatalytic activity in cotton fabric by cationizing for enriched coating of negatively charged graphene oxide*. Carbohydrate Polymers, 2015. **130**: p. 299-306.
95. Salem, T. et al. *Modification of plasma pre-treated PET fabrics with poly-DADMAC and its surface activity towards acid dyes*. Progress in Organic Coatings, 2011. **72**(1-2): p. 168-174.
96. Oliveria, F.R. et al. *Dyeing of cotton and polyester blended fabric previously cationized with synthetic and natural polyelectrolytes*. Procedia Engineering, 2017. **200**: p. 309-316.
97. Perinotto, A.C. et al. *Dendrimer-assisted immobilization of alcohol dehydrogenase in nanostructured films for biosensing: Ethanol detection using electrical capacitance measurements*. Thin Solid Films, 2008. **516**(24): p. 9002-9005.
98. Xu, L. et al. *Biosensor Based on Self-Assembling Glucose Oxidase and Dendrimer-Encapsulated Pt Nanoparticles on Carbon Nanotubes for Glucose Detection*. Electroanalysis: An International Journal Devoted to Fundamental and Practical Aspects of Electroanalysis, 2007. **19**(6): p. 717-722.
99. Wang, S. et al. *Polyamidoamine dendrimer as a spacer for the immobilization of glucose oxidase in capillary enzyme microreactor*. Analytical biochemistry, 2010. **405**(2): p. 230-235.
100. Svobodova, L., Šnejdárková, M. and Hianik, T. *Properties of glucose biosensors based on dendrimer layers. Effect of enzyme immobilization*. Analytical and Bioanalytical Chemistry, 2002. **373**(8): p. 735-741.
101. Wan, D. et al. *A novel mesoporous nanocarrier: Integrating hollow magnetic fibrous silica with PAMAM into a single nanocomposite for enzyme immobilization*. Microporous and Mesoporous Materials, 2019. **280**: p. 46-56.
102. Jiang, J. et al. *Enzyme immobilized on polyamidoamine-coated magnetic microspheres for α -glucosidase inhibitors screening from Radix Paeoniae Rubra extracts accompanied with molecular modeling*. Talanta, 2019. **195**: p. 127-136.
103. Morshed, M.N. et al. *Stabilization of zero valent iron (Fe0) on plasma/dendrimer functionalized polyester fabrics for Fenton-like removal of hazardous water pollutant*. Chemical Engineering Journal, 2019.
104. Omar, N.A.S. et al. *Sensitive Detection of Dengue Virus Type 2 E-Proteins Signals Using Self-Assembled Monolayers/Reduced Graphene Oxide-PAMAM Dendrimer Thin Film-SPR Optical Sensor*. Scientific Reports, 2020. **10**(1): p. 1-15.
105. Tian, M. et al. *Robust ultraviolet blocking cotton fabric modified with chitosan/graphene nanocomposites*. Materials Letters, 2015. **145**: p. 340-343.
106. Tian, M. et al. *Ultraviolet protection cotton fabric achieved via layer-by-layer self-assembly of graphene oxide and chitosan*. Applied Surface Science, 2016. **377**: p. 141-148.
107. Hung, W.-S. et al. *Fabrication of hydrothermally reduced graphene oxide/chitosan composite membranes with a lamellar structure on methanol dehydration*. Carbon, 2017. **117**: p. 112-119.
108. Kuilla, T. et al. *Recent advances in graphene based polymer composites*. Progress in Polymer Science, 2010. **35**(11): p. 1350-1375.
109. Liu, Y. et al. *Facile preparation and characterization of poly (vinyl alcohol)/chitosan/graphene oxide biocomposite nanofibers*. Journal of Industrial and Engineering Chemistry, 2014. **20**(6): p. 4415-4420.
110. Boussif, O. et al. *A versatile vector for gene and oligonucleotide transfer into cells in culture and in vivo: polyethylenimine*. Proceedings of the National Academy of Sciences, 1995. **92**(16): p. 7297-7301.
111. Fischer, D. et al. *Poly (diallyldimethylammonium chlorides) and their N-methyl-N-vinylacetamide copolymer-based DNA-polyplexes: role of molecular weight and charge density in complex formation, stability, and in vitro activity*. International Journal of Pharmaceutics, 2004. **280**(1-2): p. 253-269.

112. Krajcik, R. et al. *Functionalization of carbon nanotubes enables non-covalent binding and intracellular delivery of small interfering RNA for efficient knock-down of genes*. Biochemical and Biophysical Research Communications, 2008. **369**(2): p. 595-602.
113. Giamati, M.J. *Variable power density heating using stranded resistance wire*. 1995, Google Patents.
114. Ely, R.S. and Ketcham, I.M. *Flexible electric heater for deicing airfoils*. 1950, Google Patents.
115. Schramm, K.C. *Aircraft heated floor panel*. 2004, Google Patents.
116. Kim, J.H. et al. *Heat generation properties of Ga doped ZnO thin films prepared by rf-magnetron sputtering for transparent heaters*. Thin Solid Films, 2008. **516**(7): p. 1330-1333.
117. Kang, T.J. et al. *Thickness-dependent thermal resistance of a transparent glass heater with a single-walled carbon nanotube coating*. Carbon, 2011. **49**(4): p. 1087-1093.
118. Sui, D. et al. *Flexible and transparent electrothermal film heaters based on graphene materials*. Small, 2011. **7**(22): p. 3186-3192.
119. Anagnostopoulos, G. et al. *An Evaluation of Graphene as a Multi-Functional Heating Element for Biomedical Applications*. Journal of Biomedical Nanotechnology, 2018. **14**(1): p. 86-97.
120. Kochman, E. and Kochman, D. *Textile heater with continuous temperature sensing and hot spot detection*. 2004, Google Patents.
121. Ohgushi, K., Hijiri, M. and Kitazawa, Z. *Fibrous heating element*. 1991, Google Patents.
122. Fang, X.-Y. et al. *Temperature-and thickness-dependent electrical conductivity of few-layer graphene and graphene nanosheets*. Physics Letters A, 2015. **379**(37): p. 2245-2251.
123. Lou, C. et al. *A graphene-based flexible pressure sensor with applications to plantar pressure measurement and gait analysis*. Materials, 2017. **10**(9): p. 1068.
124. Hu, X. et al. *Conductive graphene-based E-textile for highly sensitive, breathable, and water-resistant multimodal gesture-distinguishable sensors*. Journal of Materials Chemistry A, 2020. **8**(29): p. 14778-14787.
125. Wang, C. et al. *Tactile sensors for advanced intelligent systems*. Advanced Intelligent Systems, 2019. **1**(8): p. 1900090.
126. Xu, M. et al. *Transparent and flexible tactile sensors based on graphene films designed for smart panels*. Journal of Materials Science, 2018. **53**(13): p. 9589-9597.
127. Miao, P. et al. *Graphene nanostructure-based tactile sensors for electronic skin applications*. Nano-Micro Letters, 2019. **11**(1): p. 1-37.
128. Shi, F. and Cui, X. *Catalytic amination for N-alkyl amine synthesis*. 2018: Academic Press.
129. Fraile, J.M., García, J.I. and Mayoral, J.A. *Recent advances in the immobilization of chiral catalysts containing bis (oxazolines) and related ligands*. Coordination Chemistry Reviews, 2008. **252**(5-7): p. 624-646.
130. Zhang, H. and Zhu, H. *Preparation of Fe-doped TiO₂ nanoparticles immobilized on polyamide fabric*. Applied Surface Science, 2012. **258**(24): p. 10034-10041.
131. Zhao, X. et al. *Immobilizing catalysts on porous materials*. Materials Today, 2006. **9**(3): p. 32-39.
132. Fan, J. and Gao, Y. *Nanoparticle-supported catalysts and catalytic reactions—a mini-review*. Journal of Experimental Nanoscience, 2006. **1**(4): p. 457-475.
133. Xiao, S. et al. *Polyelectrolyte multilayer-assisted immobilization of zero-valent iron nanoparticles onto polymer nanofibers for potential environmental applications*. ACS Applied Materials & Interfaces, 2009. **1**(12): p. 2848-2855.
134. Crane, R.A. and Scott, T.B. *Nanoscale zero-valent iron: future prospects for an emerging water treatment technology*. Journal of Hazardous Materials, 2012. **211**: p. 112-125.
135. Jiang, C. et al. *A new insight into Fenton and Fenton-like processes for water treatment*. Journal of Hazardous Materials, 2010. **174**(1-3): p. 813-817.
136. Zhang, Z. et al. *Microwave degradation of methyl orange dye in aqueous solution in the presence of nano-TiO₂-supported activated carbon (supported-TiO₂/AC/MW)*. Journal of Hazardous Materials, 2012. **209**: p. 271-277.
137. Zhou, L. et al. *Phenolic compounds removal by wet air oxidation based processes*. Frontiers of Environmental Science & Engineering, 2018. **12**(1): p. 1-20.
138. Chang, Y.-C. and Chen, D.-H. *Catalytic reduction of 4-nitrophenol by magnetically recoverable Au nanocatalyst*. Journal of Hazardous Materials, 2009. **165**(1-3): p. 664-669.
139. Joshni, T.C. and Subramaniam, K. *Enzymatic degradation of azo dyes—a review*. International Journal of Environmental Sciences, 2011. **1**(6): p. 1250-1260.
140. Sanchez-Prado, L. et al. *Sonochemical degradation of triclosan in water and wastewater*. Ultrasonics Sonochemistry, 2008. **15**(5): p. 689-694.
141. Frey, P.A. and Reed, G.H. *The ubiquity of iron*. 2012, ACS Publications.
142. Xiang, W. et al. *An insight in magnetic field enhanced zero-valent iron/H₂O₂ Fenton-like systems: Critical role and evolution of the pristine iron oxides layer*. Scientific Reports, 2016. **6**(1): p. 1-11.
143. Zhang, Y. et al. *A new insight on the core-shell structure of zerovalent iron nanoparticles and its application for Pb (II) sequestration*. Journal of Hazardous Materials, 2013. **263**: p. 685-693.
144. Neyens, E. and Baeyens, J. *A review of classic Fenton's peroxidation as an advanced oxidation technique*. Journal of Hazardous Materials, 2003. **98**(1-3): p. 33-50.
145. Wu, Y., et al., *Zero-valent iron-based technologies for removal of heavy metal (loid) s and organic pollutants from the aquatic environment: recent advances and perspectives*. Journal of Cleaner Production, 2020: p. 123478.
146. Singh, C., Goyal, A. and Singhal, S. *Nickel-doped cobalt ferrite nanoparticles: efficient catalysts for the reduction of nitroaromatic compounds and photo-oxidative degradation of toxic dyes*. Nanoscale, 2014. **6**(14): p. 7959-7970.
147. Carvalho, R.N. et al. *Development of the first watch list under the environmental quality standards directive*. JRC Science Hub, 2015.
148. Wang, Z. et al. *Textile dyeing wastewater treatment*. Advances in treating textile effluent, 2011. **5**: p. 91-116.
149. Bernes, C. *Persistent organic pollutants*. 1998.
150. Gaur, N., Narasimhulu, K. and PydiSetty, Y. *Recent advances in the bio-remediation of persistent organic pollutants and its effect on environment*. Journal of Cleaner Production, 2018. **198**: p. 1602-1631.
151. Khurana, P., Thatai, S. and Kumar, D. *Destruction of recalcitrant nanomaterials contaminants in industrial wastewater*, in *Emerging and Nanomaterial Contaminants in Wastewater*. 2019, Elsevier. p. 137-158.
152. Cheng, M. et al. *Hydroxyl radicals based advanced oxidation processes (AOPs) for remediation of soils contaminated with organic compounds: a review*. Chemical Engineering Journal, 2016. **284**: p. 582-598.
153. Söğüt, O.Ö. and Akgün, M. *Treatment of dyehouse waste-water by supercritical water oxidation: a case study*. Journal of Chemical Technology & Biotechnology, 2010. **85**(5): p. 640-647.
154. Umar, M. and Aziz, H.A. *Photocatalytic degradation of organic pollutants in water*. Organic Pollutants-monitoring, Risk and Treatment, 2013. **8**: p. 196-197.
155. Devi, L.G. and Kavitha, R. *A review on non metal ion doped titania for the photocatalytic degradation of organic pollutants under UV/solar light: Role of photogenerated charge carrier dynamics in enhancing the activity*. Applied Catalysis B: Environmental, 2013. **140**: p. 559-587.
156. Wang, J. and Chen, H. *Catalytic ozonation for water and wastewater treatment: recent advances and perspective*. Science of the Total Environment, 2020. **704**: p. 135249.
157. Pruden, B. and Le, H. *Wet air oxidation of soluble components in waste water*. The Canadian Journal of Chemical Engineering, 1976. **54**(4): p. 319-325.
158. Xue, C. et al. *Current status of applying microwave-associated catalysis for the degradation of organics in aqueous phase—a review*. Journal of Environmental Sciences, 2019. **81**: p. 119-135.

159. Naghdi, M. et al. *Removal of pharmaceutical compounds in water and wastewater using fungal oxidoreductase enzymes*. Environmental Pollution, 2018. **234**: p. 190-213.
160. Ismail, M. et al. *Catalytic reduction of picric acid, nitrophenols and organic azo dyes via green synthesized plant supported Ag nanoparticles*. Journal of Molecular Liquids, 2018. **268**: p. 87-101.
161. Morshed, M.N. et al. *Development of a multifunctional graphene/Fe-loaded polyester textile: robust electrical and catalytic properties*. Dalton Transactions, 2020. **49**(47): p. 17281-17300.
162. Birjandi, N. et al. *Electricity generation through degradation of organic matters in medicinal herbs wastewater using bio-electro-Fenton system*. Journal of Environmental Management, 2016. **180**: p. 390-400.
163. Kahoush, M. et al. *Bio-Fenton and Bio-electro-Fenton as sustainable methods for degrading organic pollutants in wastewater*. Process Biochemistry, 2018. **64**: p. 237-247.
164. Hu, M. et al. *Catalytic reduction for water treatment*. Frontiers of Environmental Science & Engineering, 2018. **12**(1): p. 1-18.
165. Bouazizi, N. et al. *Copper oxide coated polyester fabrics with enhanced catalytic properties towards the reduction of 4-nitrophenol*. Journal of Materials Science: Materials in Electronics, 2018. **29**(13): p. 10802-10813.
166. Reddy, P.M. et al. *Catalytic reduction of pralidoxime in pharmaceuticals by macrocyclic Ni (II) compounds derived from orthophthalaldehyde*. Spectrochimica Acta Part A: Molecular and Biomolecular Spectroscopy, 2008. **70**(3): p. 704-712.
167. Nabil, B. et al. *Polyfunctional cotton fabrics with catalytic activity and antibacterial capacity*. Chemical Engineering Journal, 2018. **351**: p. 328-339.
168. Bouazizi, N. et al. *Entrapment and stabilization of iron nanoparticles within APTES modified graphene oxide sheets for catalytic activity improvement*. Journal of Alloys and Compounds, 2019. **771**: p. 1090-1102.
169. Gupta, V.K. et al. *A novel magnetic Fe@ Au core-shell nanoparticles anchored graphene oxide recyclable nanocatalyst for the reduction of nitrophenol compounds*. Water Research, 2014. **48**: p. 210-217.
170. Thawarkar, S.R. et al. *Kinetic investigation for the catalytic reduction of nitrophenol using ionic liquid stabilized gold nanoparticles*. RSC Advances, 2018. **8**(67): p. 38384-38390.
171. Liu, B. et al. *Insight into catalytic mechanisms for the reduction of nitrophenol via heterojunctions of gold nanoclusters on 2D boron nitride nanosheets*. ChemNanoMat, 2019. **5**(6): p. 784-791.
172. Brillas, E., Sirés, I. and Oturan, M.A. *Electro-Fenton process and related electrochemical technologies based on Fenton's reaction chemistry*. Chemical Reviews, 2009. **109**(12): p. 6570-6631.
173. Panizza, M. and G. Cerisola, *Direct and mediated anodic oxidation of organic pollutants*. Chemical Reviews, 2009. **109**(12): p. 6541-6569.
174. Sires, I. et al. *Electro-Fenton degradation of antimicrobials triclosan and triclocarban*. Electrochimica Acta, 2007. **52**(17): p. 5493-5503.
175. Fenton, H.J.H. *LXXIII.—Oxidation of tartaric acid in presence of iron*. Journal of the Chemical Society, Transactions, 1894. **65**: p. 899-910.
176. Vasquez-Medrano, R., Prato-Garcia, D. and Vedrenne, M. *Ferrioxalate-mediated processes, in Advanced Oxidation Processes for Waste Water Treatment*. 2018, Elsevier. p. 89-113.
177. Deng, Y. and Zhao, R. *Advanced oxidation processes (AOPs) in wastewater treatment*. Current Pollution Reports, 2015. **1**(3): p. 167-176.
178. Su, S. et al. *Degradation of amoxicillin in aqueous solution using sulphate radicals under ultrasound irradiation*. Ultrasonics Sonochemistry, 2012. **19**(3): p. 469-474.
179. Rastogi, A., Al-Abed, S.R. and Dionysiou, D.D. *Effect of inorganic, synthetic and naturally occurring chelating agents on Fe (II) mediated advanced oxidation of chlorophenols*. Water Research, 2009. **43**(3): p. 684-694.
180. Rastogi, A., Al-Abed, S.R. and Dionysiou, D.D. *Sulfate radical-based ferrous-peroxymonosulfate oxidative system for PCBs degradation in aqueous and sediment systems*. Applied catalysis B: environmental, 2009. **85**(3-4): p. 171-179.
181. Wu, J., Zhang, H. and Qiu, J. *Degradation of Acid Orange 7 in aqueous solution by a novel electro/Fe²⁺/peroxydisulfate process*. Journal of Hazardous Materials, 2012. **215**: p. 138-145.
182. Lin, H., Wu, J. and Zhang, H. *Degradation of clofibric acid in aqueous solution by an EC/Fe³⁺/PMS process*. Chemical Engineering Journal, 2014. **244**: p. 514-521.
183. Zhang, H., Wu, X. and Li, X. *Oxidation and coagulation removal of COD from landfill leachate by Fered-Fenton process*. Chemical Engineering Journal, 2012. **210**: p. 188-194.
184. Wahba, N., El Asmar, M. and El Sadr, M. *Iodometric method for determination of persulfates*. Analytical Chemistry, 1959. **31**(11): p. 1870-1871.
185. Chiu, K.-L. and Ng, D.H. *Synthesis and characterization of cotton-made activated carbon fiber and its adsorption of methylene blue in water treatment*. Biomass and Bioenergy, 2012. **46**: p. 102-110.
186. Zarei, M. et al. *Peroxi-coagulation degradation of CI Basic Yellow 2 based on carbon-PTFE and carbon nanotube-PTFE electrodes as cathode*. Electrochimica Acta, 2009. **54**(26): p. 6651-6660.
187. Wang, Y. and Chu, W. *Photo-assisted degradation of 2, 4, 5-trichlorophenol by Electro-Fe (II)/Oxone® process using a sacrificial iron anode: Performance optimization and reaction mechanism*. Chemical Engineering Journal, 2013. **215**: p. 643-650.
188. Zhang, H. et al. *Removal of COD from landfill leachate by an electro/Fe²⁺/peroxydisulfate process*. Chemical Engineering Journal, 2014. **250**: p. 76-82.
189. Lin, H. *Removal of organic pollutants from water by electro-Fenton and electro-Fenton like processes*. 2015, Université Paris-Est.
190. Jiang, C.-C. and Zhang, J.-F. *Progress and prospect in electro-Fenton process for wastewater treatment*. Journal of Zhejiang University-SCIENCE A, 2007. **8**(7): p. 1118-1125.
191. Nidheesh, P. and Gandhimathi, R. *Trends in electro-Fenton process for water and wastewater treatment: an overview*. Desalination, 2012. **299**: p. 1-15.
192. He, H. and Zhou, Z. *Electro-Fenton process for water and wastewater treatment*. Critical Reviews in Environmental Science and Technology, 2017. **47**(21): p. 2100-2131.
193. Martínez-Huitle, C.A., Rodrigo, M.A. and Scialdone, O. *Electrochemical water and wastewater treatment*. 2018: Butterworth-Heinemann.
194. Sillanpää, M. and Shestakova, M. *Electrochemical water treatment methods: Fundamentals, methods and full scale applications*. 2017: Butterworth-Heinemann.
195. Poza-Nogueiras, V. et al. *Current advances and trends in electro-Fenton process using heterogeneous catalysts—a review*. Chemosphere, 2018. **201**: p. 399-416.
196. Mohammadi, H., Bina, B. and Ebrahimi, A. *A novel three-dimensional electro-Fenton system and its application for degradation of anti-inflammatory pharmaceuticals: modeling and degradation pathways*. Process Safety and Environmental Protection, 2018. **117**: p. 200-213.
197. Meijide, J. et al. *Heterogeneous Electro-Fenton as "Green" Technology for Pharmaceutical Removal: A Review*. Catalysts, 2021. **11**(1): p. 85.
198. Rinaudo, M., Pavlov, G. and Desbrieres, J. *Influence of acetic acid concentration on the solubilization of chitosan*. Polymer, 1999. **40**(25): p. 7029-7032.
199. Jayakrishnan, A. and Shah, D.O. *Phase-transfer-catalyzed free-radical polymerization: Kinetics of polymerization of methyl methacrylate using ammonium peroxydisulfate/hexadecyl pyridinium chloride in ethyl acetate/water*. Journal of Polymer Science: Polymer Chemistry Edition, 1983. **21**(11): p. 3201-3208.
200. Sanders, E.M. and Zeronian, S.H. *An analysis of the moisture-related properties of hydrolyzed polyester*. Journal of Applied Polymer Science, 1982. **27**(11): p. 4477-4491.
201. Olson, L.M. and Wentz, M. *Moisture Related Properties of Hydrolyzed Polyester Fabrics*. Textile Chemist & Colorist, 1984. **16**(2).

202. Miankafshe, M.A., Bashir, T. and Persson, N.-K. *Electrostatic grafting of graphene onto polyamide 6, 6 yarns for use as conductive elements in smart textile applications*. New Journal of Chemistry, 2020. **44**(18): p. 7591-7601.
203. Takke, V. et al. *Studies on the atmospheric air-plasma treatment of PET (polyethylene terephthalate) woven fabrics: effect of process parameters and of aging*. Journal of Applied Polymer Science, 2009. **114**(1): p. 348-357.
204. Morshed, M.N. et al. *Iron-loaded amine/thiol functionalized polyester fibers with high catalytic activities: Comparative study*. Dalton Transactions, 2019. **48**: p. 8384-8399.
205. Morshed, M.N. et al. *Iron-loaded amine/thiol functionalized polyester fibers with high catalytic activities: a comparative study*. Dalton Transactions, 2019. **48**(23): p. 8384-8399.
206. Xiao, S. et al. *Excellent copper (II) removal using zero-valent iron nanoparticle-immobilized hybrid electrospun polymer nanofibrous mats*. Colloids and Surfaces A: Physicochemical and Engineering Aspects, 2011. **381**(1-3): p. 48-54.
207. Wege, H.A. et al. *Dynamic contact angle and spreading rate measurements for the characterization of the effect of dentin surface treatments*. Journal of Colloid and Interface Science, 2003. **263**(1): p. 162-169.
208. Trotman, E.R. *Dyeing and chemical technology of textile fibres*. 1984.
209. Mirabella, F.M. *Modern techniques in applied molecular spectroscopy*. Vol. 14. 1998: John Wiley & Sons.
210. Green, P. and MacDonald, L. *Colour engineering: achieving device independent colour*. Vol. 30. 2011: John Wiley & Sons.
211. Schanda, J. *Colorimetry: understanding the CIE system*. 2007: John Wiley & Sons.
212. Moulder, J.F. *Handbook of X-ray photoelectron spectroscopy*. Physical electronics, 1995: p. 230-232.
213. Okpalugo, T.I.T. et al. *High resolution XPS characterization of chemical functionalised MWCNTs and SWCNTs*. Carbon, 2005. **43**(1): p. 153-161.
214. Yang, L. et al. *A new carboxyl-copper-organic framework and its excellent selective absorbability for proteins*. Journal of Solid State Chemistry, 2014. **218**: p. 64-70.
215. Guo, X. et al. *XPS analysis for cubic boron nitride crystal synthesized under high pressure and high temperature using Li3N as catalysis*. Applied Surface Science, 2014. **321**: p. 94-97.
216. Höhne, G., Hemminger, W.F. and Flammersheim, H.J. *Differential scanning calorimetry*. 2013: Springer Science & Business Media.
217. Hunter, R.J. *Zeta Potential in Colloid Science: Principles and Applications* (New York: Academic). 1981.
218. Deb, H. et al. *Immobilization of cationic titanium dioxide (TiO₂⁺) on electrospun nanofibrous mat: synthesis, characterization, and potential environmental application*. Fibers and Polymers, 2018. **19**(8): p. 1715-1725.
219. Morshed, M.N. et al. *Stabilization of zero valent iron (Fe⁰) on plasma/dendrimer functionalized polyester fabrics for Fenton-like removal of hazardous water pollutant*. Chemical Engineering Journal, 2019. **374**: p. 658-673.
220. Connelly, N.G. and Geiger, W.E. *Chemical redox agents for organometallic chemistry*. Chemical Reviews, 1996. **96**(2): p. 877-910.
221. Li, D. et al. *Processable aqueous dispersions of graphene nanosheets*. Nature nanotechnology, 2008. **3**(2): p. 101-105.
222. He, H. and Riedl, T. *Klinowski, Solid-state NMR studies of the structure of graphite oxide, Thejournal ofPhysical Chemistry. 100 (51)(1996) 19954-19958. A Lerf, H. He, M. Forster,]. Klinowski, Structure of graphite oxide revisited. The Journal of Physical Chemistry B, 1998. 102(23): p. 4477-4482.*
223. Heggie, D., Wardman, R.H. and Luo, M.R. *A comparison of the colour differences computed using the CIE94, CMC (l: c) and BFD (l: c) formulae*. Journal of the Society of Dyers and Colourists, 1996. **112**(10): p. 264-269.
224. Luo, M.R. and Rigg, B. *Uniform Colour Space Based on the CMC (l: c) Colour-difference Formula*. Journal of the Society of Dyers and Colourists, 1986. **102**(5-6): p. 164-171.
225. Li, C. et al. *Flexible graphene electrothermal films made from electrochemically exfoliated graphite*. Journal of Materials Science, 2016. **51**(2): p. 1043-1051.
226. Yang, H. *Research on application of carbon fiber heating material in clothing*. in IOP Conference Series: Earth and Environmental Science. 2017. IOP Publishing.
227. Wang, X., Zhi, L. and Müllen, K. *Transparent, conductive graphene electrodes for dye-sensitized solar cells*. Nano Letters, 2008. **8**(1): p. 323-327.
228. Sun, Y.-P. et al. *Characterization of zero-valent iron nanoparticles*. Advances in Colloid and Interface Science, 2006. **120**(1-3): p. 47-56.
229. Cullis, C.F. and Hirschler, M.M. *The significance of thermoanalytical measurements in the assessment of polymer flammability*. Polymer, 1983. **24**(7): p. 834-840.
230. Mittal, A. et al. *Adsorption of hazardous dye crystal violet from wastewater by waste materials*. Journal of Colloid and Interface Science, 2010. **343**(2): p. 463-473.
231. Harifi, T. and Montazer, M. *In situ synthesis of iron oxide nanoparticles on polyester fabric utilizing color, magnetic, antibacterial and sono-Fenton catalytic properties*. Journal of Materials Chemistry B, 2014. **2**(3): p. 272-282.
232. Sudrajat, H. and Babel, S. *A new, cost-effective solar photoactive system N-ZnO@ polyester fabric for degradation of recalcitrant compound in a continuous flow reactor*. Materials Research Bulletin, 2016. **83**: p. 369-378.
233. Wawrzekiewicz, M. et al. *Adsorptive removal of acid, reactive and direct dyes from aqueous solutions and wastewater using mixed silica-alumina oxide*. Powder Technology, 2015. **278**: p. 306-315.



Cite this: *New J. Chem.*, 2019, 43, 6643

The role and importance of surface modification of polyester fabrics by chitosan and hexadecylpyridinium chloride for the electrical and electro-thermal performance of graphene-modified smart textiles

Milad Asadi Miankafshe, ^{*ab} Tariq Bashir ^{ac} and Nils-Krister Persson^{ab}

Graphene has the potential to create highly valuable electrical conductive textile systems with maintained pliability and psychological comfort. There have already been numerous studies regarding electrically functionalized graphene-coated textiles. However, processing development is far from being exhausted. Here we have studied electro-thermal textiles based on the most common fibers, polyester, and an industry-relevant graphene impregnation method by introducing surface pre-modification of fabrics for graphene-modified textile processing. For this purpose, polyester fabrics were treated with four different cationic agents and impregnated with graphene oxide (GO) colloidal particles. Then, direct chemical reduction of GO to an electrically conductive graphene oxide (rGO) was performed. A pristine fabric modified by rGO showed a high resistance of $27.3 \text{ k}\Omega \text{ cm}^{-1}$ without any electro-thermal activity, whilst chitosan-treated (CS) and hexadecylpyridinium chloride-treated (HDPC) fabrics had resistance values of 2.7 and $0.59 \text{ k}\Omega \text{ cm}^{-1}$ respectively, and excellent heat propagation with a good temperature distribution. The steady-state temperature of CS-treated and HDPC-treated fabrics increased from 28 °C and 33 °C to 60 °C and 120 °C, respectively, as the voltage applied increased from 10 V to 30 V. These rGO-modified fabrics also have excellent electro-mechanical performance, and are good candidates for flexible strain sensor applications.

Received 26th October 2018,
Accepted 2nd April 2019

DOI: 10.1039/c8nj05445b

rsc.li/njc

Introduction

Flexible electro-thermal heating elements have been used for a wide range of applications—for example, electrically heated garments,^{1–3} seat heaters in vehicles,⁴ thermal de-icing in aircraft and ice-prevention of structural membranes such as in wings,^{5,6} heated floor panels in aircrafts to control the cabin temperature,⁷ and continuous temperature sensing systems in construction and industrial applications.^{8,9}

These systems are mostly based on integration of metallic wires and textile fibers. Recently, textiles with electrical properties (known as e-textiles) for use in many smart applications and in heating elements, have been prepared by different methods, *e.g.* deposition of conjugated polymers onto textiles by chemical vapor deposition,¹⁰ spinning of nano-metallic filaments such as

stainless steel microfilaments with conventional staple fibers,¹¹ melt-spinning of nanoparticles and carbon products with polymers,¹² preparation of non-woven fabrics made of staple stainless steels, carbon fibers and polymers,¹³ and dip-coating of conventional textiles with graphene.¹⁴

Among these, graphene is an excellent choice for e-textiles. A single two-dimensional exfoliated graphene oxide (GO) sheet has a thickness of one or a few atoms of sp^2 -bonded carbon atoms and could be used as a colloidal dye in the textile dyeing industry,¹⁴ offering interesting optical, electrical, and thermal properties.^{15,16}

GO is produced by exfoliating graphite through a simple Harsh oxidation by Hummers' method,^{17–19} resulting in highly oxygenated graphene with hydroxyl and epoxide functional groups on the surface, and carboxyl and carbonyl groups at the edge of the sheets.²⁰ The availability of oxygen functional groups on the structure of GO gives excellent hydrophilic behavior and possible chemical bonding with textiles. Thus, an aqueous dispersion of GO could be prepared with a solubility as high as 2.0 wt% and applied as a dye to the textile. Exfoliated GO has electrical insulation properties owing to the attached

^a The Swedish School of Textile, Polymeric E-textiles, University of Borås, SE-501 90 Borås, Sweden. E-mail: milad.asadi@hb.se; Tel: +46723993664

^b Smart Textiles, University of Borås, SE-501 90 Borås, Sweden

^c Swedish Centre for Resource Recovery, University of Borås, SE-501 90 Borås, Sweden

functional groups.²¹ Consequently, reduction of exfoliated GO to graphene (rGO) is required to obtain electrical conductivity,^{14,22} and for production of covalently functionalized graphene-coated textiles.^{23–25}

The main weakness of this dyeing process in order to achieve an industrial product is that the GO nano-sheets do not adhere properly to most textiles at any pH values, probably because of electrostatic repulsion between the particles and the textile substrate since most textiles such as polyester,²⁶ as well as GO nano-sheets, have a negative surface potential (ζ) in aqueous solution^{27–29} and absorption of GO into the textile strongly rely on to the pre-modification of the fibers. It has been reported that modification of polyester fabrics with cationic agents enhances the uptake of anionic dyes by changing the surface charge of the polyester fabric.^{30,31} Thus, GO sheets could easily and uniformly aggregate in a fiber with a positively charged polyelectrolyte. When alkalinized polyester fabric is impregnated with a cationic agent, the surface charge of the fiber is positive and GO nano-sheets form hydrogen bonds and possibly undergo ionic interaction with positively charged groups on the agent that is present on the surface of fibers.²⁷

In order to better understand the role of cationic agents in adsorption and their accompanying electrical properties, it is important to determine the degree of uptake of GO by polyester through various cationic agents and their electrical, electro-mechanical, and electro-thermal properties.

The effect of hexadecylpyridinium chloride (HDPC) ($C_{21}H_{38}ClN$) on the surface charge of polyester fabrics and on the absorbency of GO has already been studied.²⁷

Poly(diallyldimethylammonium)chloride (PDDAC), ($C_8H_{16}ClN$)_n, is an important water-soluble, cationic, functional commercial polymer that is used as a cationic agent to modify the surface of polyester fabric in the textile dyeing industry,^{30,31} and also in the production of antibacterial fiber.^{32,33}

Branched polyethylenimine (PEI) $H(NHCH_2CH_2)_nNH_2$ ²⁸ has an extremely high cationic charge-to-density ratio and each amino nitrogen can be protonated since the total cationic charge of PEI increases with the acidity of the solution.³⁴ These properties make it an excellent candidate for examination as a cationic agent.

Chitosan (CS) has been used as a dispersant in GO dispersion,³⁵ in addition to layer-by-layer self-assembly of GO and CS onto the textiles for UV-blocking applications.³⁶ Bio-composite membrane with a lamellar structure of reduced graphene oxide–chitosan (rGO–CS),³⁷ and also chitosan–graphene bio-composite nanofibers, have already been studied.^{38,39} However, chitosan could also be used as a cationic agent to modify the surface charge of the fabric.³¹

In this paper, polyester fabrics were pre-modified with the cationic agents mentioned and further dip-coated with GO dispersion to identify the most relevant candidate for use in different applications. Adsorption of GO into CS-modified and HDPC-modified textiles appears promising for use in industrial applications (in both textile strain sensors and electro-thermal elements). Use of these agents as mordants not only improves the qualitative and quantitative adhesion of GO to textiles, but also considerably increases the conductivity of the fabric,

resulting in realization of a textile heater that could be electrically driven—reaching 120 °C and 60 °C at a voltage of 30 V for HDPC-modified and CS-modified textiles, respectively. To the best of our knowledge, no graphene-modified textile heater elements have yet been reported.

In addition, we investigated the surface chemical composition, the morphology, and interaction between graphene and polyester fabric, and also the manufacturing-based quality of each sample, the electrical conductivity, the electro-mechanical performance, and the electro-thermal performance.

Experimental

Materials

Sodium hydroxide (NaOH) solution (Sigma-Aldrich Co., USA) was used for alkalization of the fabrics. Chitosan (CS) (Sigma-Aldrich) solution was prepared by dissolving it in acetic acid solvent (0.1 M).⁴⁰ Poly-(diallyldimethylammonium)chloride (PDDAC) (Sigma-Aldrich), branched polyethylenimine (PEI) (Sigma-Aldrich) and hexadecylpyridinium chloride monohydrate (HDPC) (Sigma-Aldrich) aqueous solutions were prepared by dissolving them in ultrapure water.⁴¹ A commercial aqueous dispersion of graphene oxide (4 g L^{−1}) (Graphenea S.A., Spain). Later, sodium hydrosulfite ($Na_2S_2O_4$) (Sigma-Aldrich) was used as reductant in the experiment. The molecular structures of cationic agents as well as GO and rGO nano-sheets are shown in Fig. 1.

Surface charge modification of PET fabrics

A rib knitted polyester fabric (gauge 20; air-jet textured filament; dtex 167/144/1; produced in house by an OVJA 0.8 E knitting machine, Mayer & Cie CO., Germany) was prepared for the experiment. The weight of the fabric was 176.5 g m^{−2}. Fabrics were cut into 3 × 9 cm² specimens. In order to increase the

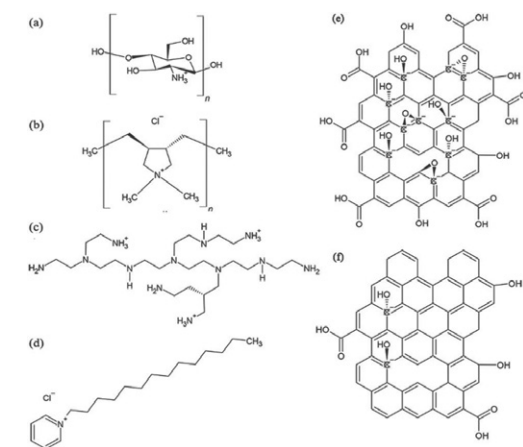


Fig. 1 Molecular structure of (a) chitosan (CS), (b) poly-(diallyldimethylammonium)chloride (PDDAC), (c) branched polyethylenimine (PEI), (d) hexadecylpyridinium chloride monohydrate (HDPC), (e) graphene oxide (GO), and (f) reduced graphene oxide (rGO).

wettability and dyeability of the fabrics, samples were alkalinized with an aqueous solution of sodium hydroxide (12 wt%) with a liquor ratio of (1 : 50) at 60 °C for 90 min.^{42,43} Further, they were washed properly with warm ultrapure water and rinsed with acetone to remove any remaining impurities. Fabrics were dried in oven at 80 °C for 10 min and the surface charge of polyester fabrics were modified by soaking in a solution of CS (4 g L^{−1} acetic acid 1 M, pH = 4), PEI (4 g L^{−1}, pH = 5) and HDPC (4 g L^{−1}, pH = 6), and a solution of PDDAC (0.8 g L^{−1}, pH = 6). All solutions were stirred at room temperature for 24 h and balanced for 2 h. The soaking process followed out for 60 minutes at 60 °C and samples were rinsed by warm ultrapure water before drying at 70 °C for 10 min.

Synthesis of rGO on modified-PET fabrics

Surface-modified samples were dyed by dipping into an aqueous dispersion of GO (0.4 wt%, pH = 3) for 30 min at 40 °C while stirring. Liquor ratio was around (1 : 100) and GO dispersion was previously sonicated for 30 min. Further GO-modified samples were dried in oven at 80 °C for 90 minutes. According to published reports,²² the highest electrical conductivity and mechanical properties are gained by using sodium hydrosulfite as the reductant due to its low electrode potential in alkaline solution. Thus, GO-modified fabrics were chemically reduced using a $Na_2S_2O_4$ aqueous solution (50 mM, L : R = 1 : 100) while stirring for 30 min at 95 °C. Then samples were rinsed by warm ultrapure water and dried at 70 °C for 90 min.

Characterization

X-ray photoelectron spectroscopy (XPS) studies of samples were carried out by a spectrophotometer (PHI 5500 ESCA, Physical Electronics INC., USA) equipped with monochromatic aluminium (Al) source (photon energy = 1486.6 eV). Owing to the insufficient conductivity, an electron neutralizer was used to do the charge compensation. The binding energy (BE) positions were aligned with reference to an adventitious carbon peak (C1s = 28.0 eV), a common surface contaminant, before data analysis. To minimize the impact of sample chemistry, argon ion sputtering was avoided during the analysis. Survey scan for the compositional evaluation (energy range of 0 to 1300 eV; step size of 0.4 eV per step), and the narrow scan for the chemical state analysis with selected range for individual element and step size of 0.05 eV per step for C1s and O1s spectra and 0.1 eV per step for N1s spectra were performed.^{44–47}

Fourier transform infrared (FTIR) spectra was recorded via a FTIR spectrometer (Nicolet iS10, Thermo Fisher Scientific Co., USA) to investigate the chemical compositions.

Electrokinetic measurements were took place to determine the zeta-potential (ζ) values of fabrics as a function of the pH values of the electrolyte solution (0.001 M KCl). The measurement was carried out using the streaming potential method, in which a liquid is forced to flow through two parallel plates contain samples and streaming potential is generated (Surpass, Anton Paar AB., Sweden). 0.01 M HCl and 0.01 M NaOH were used to adjust the pH values of the electrolyte solution.

The zeta potential values were calculated using the Helmholtz–Smoluchowski equation.⁴⁸

In order to characterize surface tension of the modified fabrics, contact angles measurement was carried out by an optical tensiometer (Attension theta, Biolin scientific Co., Sweden). The contact angle of a liquid drop on a solid surface is defined as the angle formed by the intersection of the liquid–solid and the liquid–vapor interfaces. Young's contact angle of a liquid droplet on an ideal solid surface is defined by the mechanical equilibrium of the droplet under the action of three interfacial tensions:⁴⁹

$$\gamma_{lv} \cos \theta_Y = \gamma_{sv} - \gamma_{sl} \quad (1)$$

where θ_Y is the Young contact angle, γ_{lv} , γ_{sv} , and γ_{sl} represent the liquid–vapour, solid–vapor, and solid–liquid interfacial tensions, respectively.⁵⁰

The morphology of rGO-modified samples was investigated through SEM (FEI Quanta200 ESEM, Thermo Fisher Scientific Co., USA) with an acceleration voltage of 5 and 10 kV, and 10 mm of working distance.

The reflectance spectra of samples in the visible spectral range (λ = 400–700 nm) were recorded with a Datacolor Check Pro spectrum (Datacolor Co., USA) and color strength of the wavelength with maximum absorbency (400 and 410 nm for GO-modified and rGO-modified samples) was calculated according to Kubelka–Munk theory:^{51,52}

$$\frac{K}{S} - \frac{K_0}{S_0} = \frac{(1-R)^2}{2R} - \frac{(1-R_0)^2}{2R_0} \quad (2)$$

where, K_0 and S_0 are absorption coefficient and scattering coefficient of control samples. K and S are absorption and scattering coefficient of modified samples. R and R_0 are reflectance of modified sample and control sample, respectively.

The color strength is proportional to the concentration of colloidal dye uptake by the fabric and could be written as bellow, where C is dye concentration and k is a constant:

$$\Delta \frac{K}{S} = k \Delta C \quad (3)$$

The color properties of the samples were expressed in terms of CIELab values and total color change (ΔE) of each sample was investigated exclusively. ΔE in CIE system is obtained by following equation;^{53,54}

$$\Delta E_{ab}^* = \sqrt{(L_2^* - L_1^*)^2 + (a_2^* - a_1^*)^2 + (b_2^* - b_1^*)^2} \quad (4)$$

where a^* is the coordinate responses in the green to red color range, b^* is the coordinate responses in blue to yellow color range, and L^* is responding the brightness and darkness of the color. The color range of CIELab coordinates are shown in Fig. 2(c).

Sheet resistance (R_{sh}) of samples in the unit of k Ω □^{−1} or k Ω per square was measured with a 4-probe method from direct current (DC) electrical resistance measurement according to the following equation;^{55–58}

$$R_{sh} = \frac{\rho}{t} = R \frac{W}{L} \quad (5)$$

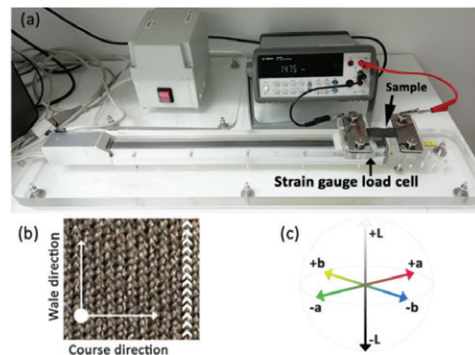


Fig. 2 (a) The electro mechanical set-up used for the experiment, (b) course and wale direction in the knitted fabric, and (c) the colors range of *a*, *b*, and *L* coordinates in CIElab system.

where, ρ is resistivity, t is the sheet thickness, R is the measured resistance, L is the distance between two probes, and W is the probe width.

The relative changes in electrical resistance of fabrics in both wale and course directions (Fig. 2(b)) at various strain levels (0–35%) were recorded by using a self-made fabric dynamic resistance machine (Fig. 2(a)), programed with ACT controller software (SMC Co., USA).

In order to investigate the electro-thermal performance of the samples, a range of voltages (5–30 V) were applied to the rGO-modified fabrics through a DC power supply. An infrared thermal camera (FLIR-E63900, FLIR System Co., Sweden) and a 3-channel thermal data-logger (SD200 Extech, FLIR System Co., Sweden) were used to characterize the surface temperature distribution.

To better understanding the thermal behavior of the modified fabrics, thermal characterization of samples was carried out with a differential scanning calorimeter (DSC Q2000, TA Instruments Co., UK) under nitrogen atmosphere.

Results and discussion

When an alkalinized PET is treated with a solution of cationic agent, hydroxyl and carboxyl groups of alkalinized fabric could make hydrogen or electrostatic bond with functional groups of

the agent. For instant, protonated amine present in CS or PE might form electrostatic bonds with PET.

After the surface modification, fabrics were immersed in GO dispersion, resulting a quick attraction between GO nano-sheets and fabric, in which oxygen functional groups of GO could form a hydrogen or electrostatic bond with hydroxyl and amino groups of modified fabrics. The possible reaction site of alkalinized polyester, protonated chitosan and GO nano-sheets are illustrated in Fig. 3.

Since the attraction between GO and a modified fabric is much stronger than a pristine fabric, GO-modified fabrics were successfully reduced with chemical reduction without losing a considerable degree of GO during the process. An overall illustration of the process is shown in Fig. 4.

In order to study the influence of each modification on fabric properties, a pristine fabric was used as a control sample. It was washed with ultrapure water and acetone, dried in oven at 80 °C for 10 min and modified with GO in the same manner. The composition of samples is summarized in Table 1.

X-ray photoelectron spectroscopy (XPS)

The atomic composition of an untreated PET, PET-CS, PET-PE, PET-HDPC, and PET-PDDAC as well as PET-GO and PET-rGO samples were evaluated by XPS. The wide scan spectra of the samples are shown in Fig. 5.

As it can be seen from Table 2, a control sample contains 75% carbon and 25% oxygen. Since Both CS and PE are rich in amino groups, by modification of fabric with CS and PE, nitrogen was detected in the surface composition, having 67% carbon, 28% oxygen, and 5% nitrogen for PET-CS; and 74% carbon, 19% oxygen and 7% nitrogen for PET-PE.

In order to investigate the chemical groups introduced on the polyester surface, high resolution spectra of the C1s, O1s and N1s peaks were investigated in details. In the N1s XPS spectrum of PET-CS (Fig. 6(a)), peaks at 397.5 eV ($-\text{C}\equiv\text{N}$) and at 399.2 eV ($-\text{NH}_2$) with corresponding proportion of 37.5 and 62.5% and in the N1s XPS spectrum of PET-PE (Fig. 6(b)), peaks at 397.2 eV ($-\text{C}\equiv\text{N}$), 399.3 eV ($-\text{NH}_2$), and 401.2 eV ($-\text{CONH}_2$) with corresponding proportion of 17, 68, and 15% were observed. However, nitrogen was not detected in the composition of PET-PDDAC and PET-HADPC.

The C1s spectrum of a pristine PET (Fig. 6(c)) can be fitted with four peaks at 283.8 eV, 285.0 eV, 286.5 eV and 289.0 eV attributed to $\text{C}=\text{C}$, $\text{C}-\text{C}$, $\text{C}-\text{O}$, and COO^- bonds, respectively.

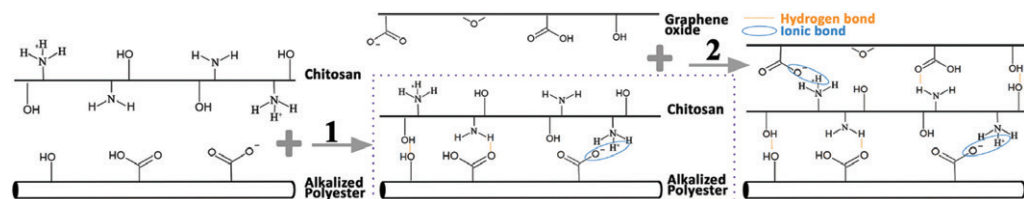


Fig. 3 Illustration of the possible reaction sites of (1) alkalinized polyester and protonated chitosan, and reaction sites of (2) GO and chitosan-modified fiber.

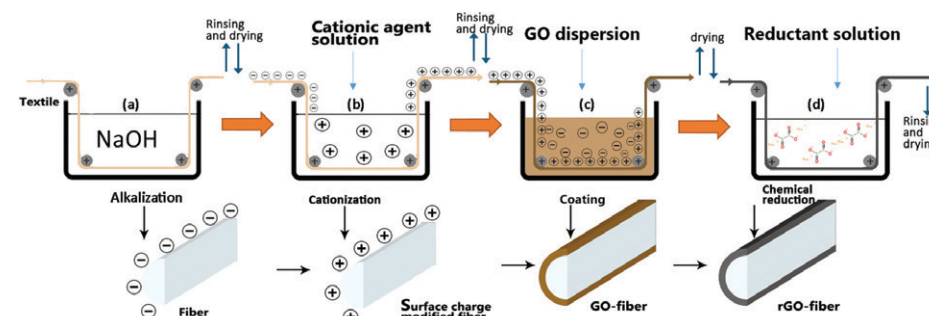


Fig. 4 Illustration of the functionalization process. (a) Alkalization of the textile, (b) surface charge modification, (c) impregnation of the modified textiles with graphene oxide (GO), and (d) chemical reduction of GO-modified textile to generate electrical conductivity.

Table 1 The composition of samples

Sample	Composition
PET-GO	Polyester, graphene oxide
PET-ALK-GO	Alkalinized polyester, graphene oxide
PET-CS-GO	Alkalinized polyester, chitosan, graphene oxide
PET-HDPC-GO	Alkalinized polyester, hexadecylpyridinium chloride, graphene oxide
PET-PE-GO	Alkalinized polyester, branched polyethylenimine, graphene oxide
PET-PDDAC-GO	Alkalinized polyester, poly(diallyl-dimethylammonium)chloride, graphene oxide
PET-rGO	Polyester, reduced graphene oxide
PET-ALK-rGO	Alkalinized polyester, reduced graphene oxide
PET-CS-rGO	Alkalinized polyester, chitosan, reduced graphene oxide
PET-HDPC-rGO	Alkalinized polyester, hexadecylpyridinium chloride, reduced graphene oxide
PET-PE-rGO	Alkalinized polyester, branched polyethylenimine, reduced graphene oxide
PET-PDDAC-rGO	Alkalinized polyester, poly(diallyl-dimethylammonium)chloride, reduced graphene oxide

The concentration of all chemical groups on the PET surface before and after modification can be calculated from the high resolution C1s peaks. The unmodified PET contain 19% $\text{C}=\text{C}$, 57% $\text{C}-\text{C}$, 15% $\text{C}-\text{O}$, and 9% COO^- groups. PET-CS contain 9% $\text{C}=\text{C}$, 49% $\text{C}-\text{C}$, 34% $\text{C}-\text{O}$, and 8% COO^- groups; PET-PDDAC contain 18% $\text{C}=\text{C}$, 51% $\text{C}-\text{C}$, 22% $\text{C}-\text{O}$, and 9% COO^- groups; PET-PE contain 32% $\text{C}=\text{C}$, 52% $\text{C}-\text{C}$, 11% $\text{C}-\text{O}$, and 5% COO^- groups. For PET-HDPC, the concentration of $\text{C}=\text{C}$ increases to 39% and the concentration of $\text{C}-\text{C}$ and COO^- decrease to 51 and 6% and a newly introduced $\text{C}-\text{OH}$ groups (287.0 eV) with concentration of 7% was detected. The presence of $-\text{OH}$ could increase the hydrophilicity of polyester by forming hydrogen bonds with water.

Further, XPS analysis for PET-GO and PET-rGO provides evidence of reduction of graphene oxide as content of oxygen decrease to 20% for PET-rGO from 25% for PET-GO and content of carbon increases from 74% for PET-GO to 80% for PET-rGO. A wide scan range XPS spectrum of PET-GO and PET-rGO is shown in Fig. 5(b).

C1s spectrum of PET-GO (Fig. 6(d)) can be fitted with two peaks at 285.0 eV, 287.0 eV, corresponding to $\text{C}-\text{C}$ and $\text{C}=\text{O}$ bonds having a concentration of 60 and 40%. While, for PET-rGO (Fig. 6(e)) the concentration of $\text{C}-\text{C}$ bonds increases to 72%, the concentration of $\text{C}=\text{O}$ bonds decrease to 21%, and a new peak at 289.0 eV attributed to COO^- with a concentration of 7% was observed.

ATR-FTIR spectroscopy

ATR-FTIR analysis was performed on alkalinized, surface-modified, GO-modified, and rGO-modified fabrics to investigate the chemical composition of the samples and their possible bonds.

All spectra were normalized by equalizing the height of adsorption peak at 1713 cm^{-1} , which represent $\text{C}=\text{O}$ stretch (ester). Peak at 725 cm^{-1} represents the aromatic $\text{sp}^2\text{ C}-\text{H}$ bend (Fig. 7). The peak at 1017 cm^{-1} indicate plane vibration of benzene ring, the peaks at 1094 and 1240 cm^{-1} represent $\text{C}-\text{O}$ stretch (ester), and absorption at 2920 cm^{-1} is due to the asymmetric $\text{C}-\text{H}$ stretching. All these peaks are identical to polyester.

Once the fabric was modified with a solution (4 g L^{-1}) of chitosan, a very low intense peak around 3400 cm^{-1} was detected on PET-CS. peaks between 1550 and 1700 such as $\text{N}-\text{H}$ bonds at 1560 and 1650 cm^{-1} might be covered by strong $\text{C}=\text{O}$ peak at 1713 cm^{-1} .

By increasing the concentration of chitosan to 8 g L^{-1} , a peak at 3425 cm^{-1} , representing $\text{N}-\text{H}$ stretching was appeared on PET-CS and it was detected on PET-CS-GO and PET-CS-rGO.

However, the results show that when the fabric is treated with 8 g L^{-1} of chitosan solution, electrical conductivity of the fabric is not satisfying, and conversely optimal electrical properties is obtained when fabric is modified with 4 g L^{-1} of chitosan solution. Fig. 7 shows the FTIR spectra of a fabric pre-modified with a solution (8 g L^{-1}) of chitosan.

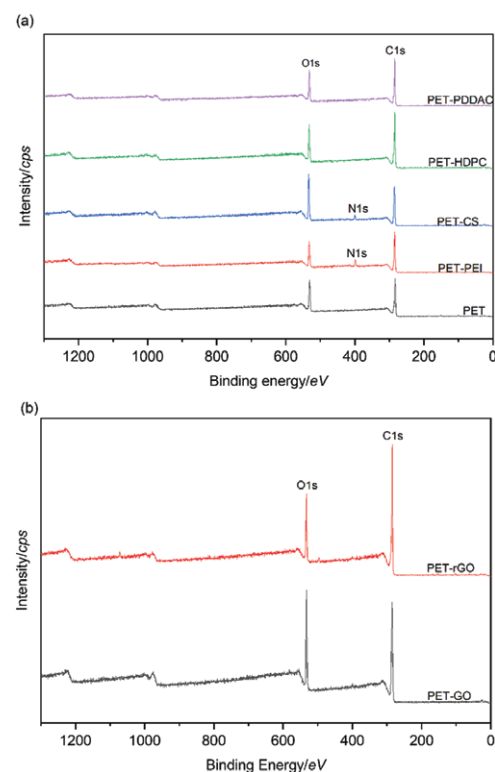


Fig. 5 Wide scan XPS spectra of (a) pristine polyester (PET), PET-PEI, PET-CS, PET-HDPC, and PET-PDDAC. (b) PET-GO and PET-rGO.

Table 2 Atomic ratio of surface chemical composition of samples

Sample	C (%)	O (%)	N (%)
PET	75	25	0
PET-CS	67	28	5
PET-HDPC	77	23	0
PET-PDDAC	76	24	0
PET-PE	74	19	7
PET-GO	74	25	1
PET-rGO	80	20	0

PET-PE sample has additional peaks at 1576 and 3427 cm^{-1} , these peaks also represent N-H bonds. After absorption of GO on modified polyesters, peak at 2920 cm^{-1} was disappeared and it is comprehensible through chemical composition of GO sheets. For rGO-coated samples due to the reduction of oxygen functional groups, peaks at 1094, 1172, and 1240 cm^{-1} are almost disappeared.

Streaming potential measurements

The isoelectric point ($\text{iep} = \text{pH}|_{\zeta=0}$) observed by electrokinetics was measured as streaming potential to determine the zeta-potential values. Polyester fabric has an isoelectric point of

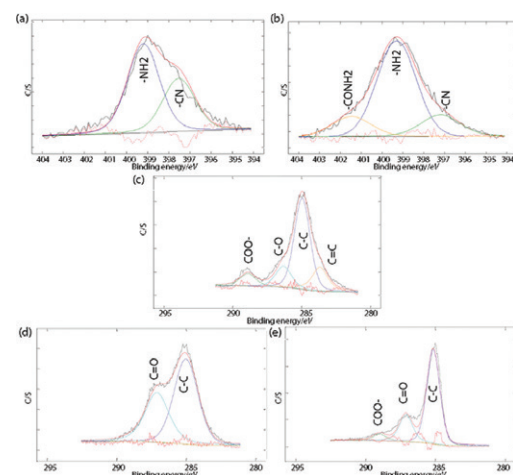


Fig. 6 N1s XPS analysis of (a) PET-CS and (b) PET-PE, and corresponding C1s spectrum of (c) PET, (d) PET-GO and (e) PET-rGO.

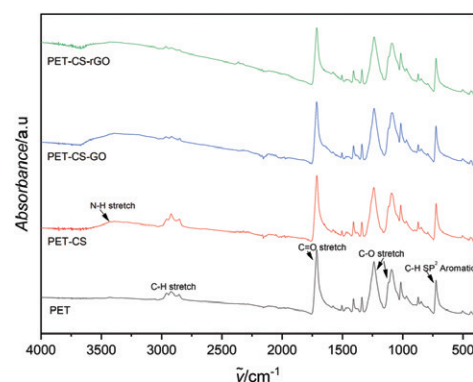


Fig. 7 ATR-FTIR spectra of a pristine fabric (PET), chitosan (8 g L⁻¹) treated fabric (PET-CS), graphene-coated fabric (PET-CS-GO), and reduced graphene-coated fabric (PET-CS-rGO).

$\text{pH} = 3.9$ which indicate that surface charge of polyester is negative for pH higher than 3.9. The negative surface charge of polyester is due to the dissociation of functional groups ($-\text{OH}$ and $-\text{COOH}$) of the polymer.

Graphene oxide carries negative surface charge in any pH, due to the ionization of oxygen-containing functional groups and it displays strong pH dependence, starting from -19 mV at pH 1.0 and increases to -49 mV at pH 8.0.^{59,60} negative surface charge of GO may lead to hindrance the attachment of the GO on the surface of a pristine polyester.

After treatment of the fabrics by cationic agents, degree of carboxylic groups decreases and positively charged functional groups are present on the surface of the textile. This results in increasing the value of isoelectric points. PET-PE carries

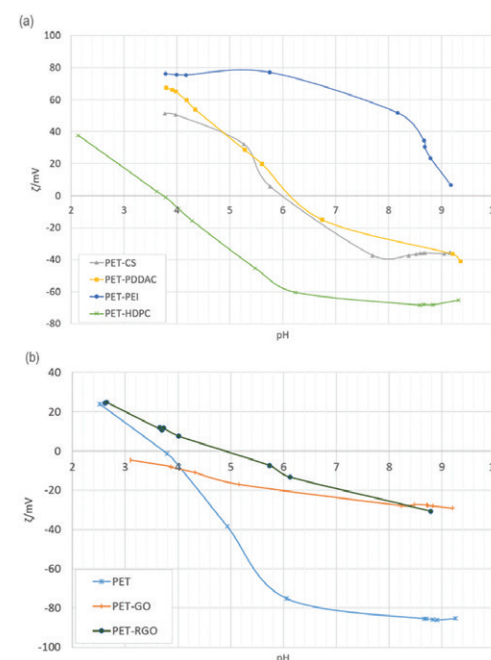


Fig. 8 Zeta potential (ζ) values determined for (a) PET-CS, PET-PDDAC, PET-PE, and PET-HDPC fabrics and (b) pristine PET fabric, PET fabric modified by graphene oxide (PET-GO), and an PET fabric modified by reduced graphene oxide (PET-rGO) in dependence on pH of an aqueous 10^{-3} mol L⁻¹ KCL solution.

positive surface charge for any range of pH. PET-PDDAC and PET-CS have isoelectric point of 6.2 and 6.0, respectively. For PET-HDPC, isoelectric point has not changed by having the same value as a pristine PET ($\text{pH}|_{\zeta=0} = 3.9$), this could be due to the increase of ($-\text{OH}$) groups of PET-HDPC samples. The zeta-potential values of surface-modified fabrics are shown in Fig. 8(a).

Further, surface charge of GO-modified and rGO-modified fabrics were recorded (Fig. 8(b)). Due to the presence of functional groups on the surface of GO-modified fabrics, it carries negative surface charge for any range of pH. However, reduction

of oxygen functional groups increases the zeta potential value and PET-rGO has an $\text{pH}|_{\zeta=0}$ of 5.

Sessile-drop goniometry

Sessile-drop goniometry was performed to measure the contact angle of samples. A deionized water droplet was placed on front side of fabrics and a camera with a display performance of 60 frame per second (fps) was used to determine the initial contact angle and the absorption time. Sessile-drop goniometry measures the static contact angle. However, for a rough surface such as textile, the liquid moves around before it settles and wetting phenomenon is more than a static state.

The effect of fabric modification with cationic agents and further functionalization of fabric with GO and rGO on the surface wettability were evaluated by image processing. A pristine polyester has a contact angle of 91° and adsorption time of 0.8 s. the wettability of fabric increases by introducing HDPC as the absorption time decreased to 0.2 s and contact angle decreased to 61° . Fig. 9 shows the image sequences of water droplet placing on pristine PET and PET-HDPC samples.

The absorption time was increased to 13 s for PET-CS. However, the contact angle is lower (79°) as compare to a pristine sample. The adsorption time for PET-PDDAC and PET-PE samples also increased to 3 and 6 s, having a contact angle of 77 and 62° , respectively.

After GO-modification of the fabric, it turned out to be more hydrophobic, having an average contact angle of 137° . However, after the reduction of functional groups on the surface of GO nano-sheets, fabrics show different contact angles depending on the pre-treatment of the fabrics. For instant, PET-rGO, PET-PDDAC-rGO and PET-HDPC-rGO have a contact angle of 138 , 132 , and 131° , which demonstrate that the hydrophobicity of the fabric decrease after treatment by PDDAC and HDPC. However, for PET-CS-rGO and PET-PE-rGO, the contact angle increase to 144 and 145° (Fig. 10). The hydrophobicity of PET-rGO fabrics is beneficial for many outdoor applications by maintaining the electrical conductivity, antistatic, and heat generation properties.

Surface morphology

Morphology of the coating layers was investigated by mean of scanning electron microscope (SEM). SEM images of the



Fig. 9 Image sequences of placing a deionized water droplet on (a) an unmodified polyester (PET), and (b) HDPC-modified polyester fabric (PET-HDPC) over time.

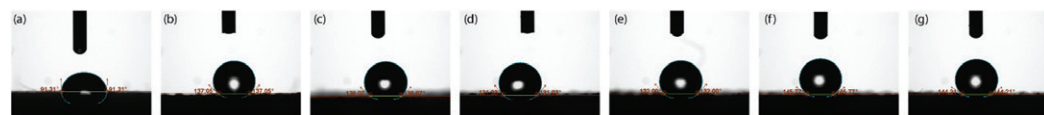


Fig. 10 Water contact angle of (a) pristine PET, (b) graphene oxide-modified polyester (PET-GO), (c) reduced graphene oxide-modified polyester fabric (PET-rGO), (d) reduced graphene oxide-HDPC modified polyester fabric (PET-HDPC-rGO), (e) reduced graphene oxide-PDDAC modified polyester fabric (PET-PDDAC-rGO), (f) reduced graphene oxide-PE modified polyester fabric (PET-PE-rGO), and (g) reduced graphene oxide-CS modified polyester fabric (PET-CS-rGO).

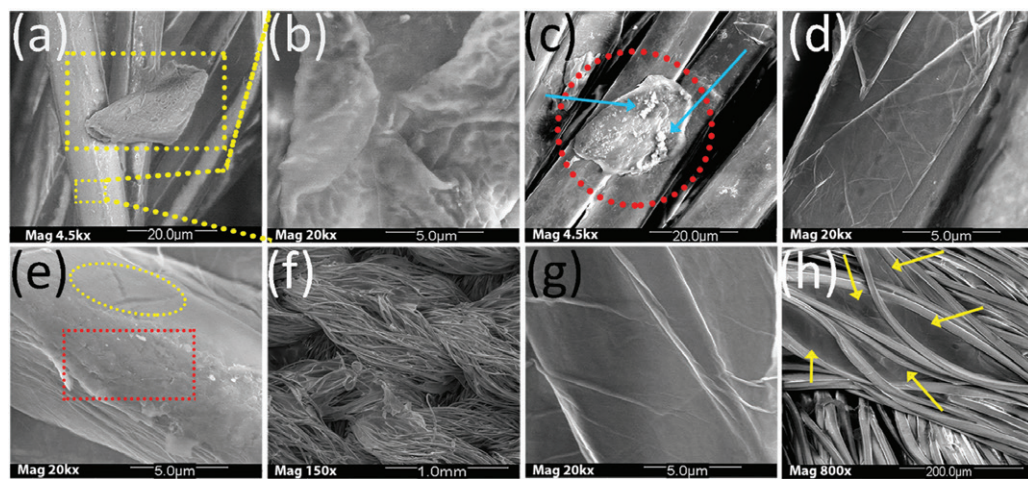


Fig. 11 SEM images of (a) PET-GO sample (4.5kx Mag.), (b) PET-GO sample (20kx Mag.), (c) PET-CS-GO sample (4.5kx Mag.), (d) PET-CS-GO sample (20kx Mag.), (e) PET-HDPC-GO sample (20kx Mag.), (f) PET-HDPC-GO sample (150x Mag.), (g) PET-PDDAC-GO sample (20kx Mag.), (h) PET-PDDAC-GO sample (800x Mag.).

control (GO-PET) and pre-modified GO-coated fabrics are shown in Fig. 11.

For the control sample (Fig. 11(a)), GO nano-sheets are not absorbed to the surface of the fibers properly and there is a barely sufficient attachment between GO nano-sheets and fibers.

It can be seen from Fig. 11(b) that for a control sample, coating layers are wrinkled and it might results in increasing the electrical resistivity. Fig. 11(c) shows the surface of a chitosan-treated fabric (PET-CS-GO) and red circle site in the image shows multilayers of GO attached to the surface of fibers. There are some particles attached to aggregated GO nano-sheets (blue arrows), which are possibly impurities from the environment. It can be seen from Fig. 11(d) that multilayer of GO nano-sheets are appropriately attached to the surface of PET-CS-GO fibers, which is possibly due to the strong bonding of carboxyl and carbonyl groups of the GO nano-sheets and hydroxyl and protonated amino groups of chitosan.

Fig. 11(e) and (f) show the surface of HDPC-modified sample (PET-HDPC-GO). Multilayers of GO nano-sheets are formed on the fiber (red rectangle) as well as the single layers (yellow ellipse). In both cases, coating layer is attached to the fiber properly. Most smooth and even coating was formed on the surface of PDDAC-modified sample (PET-PDDAC-GO) with minimum

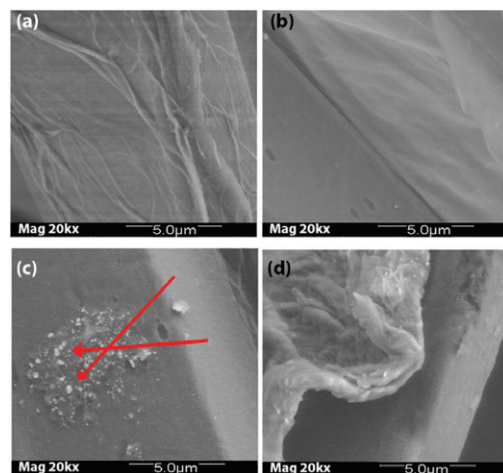


Fig. 12 SEM images of (a) PET-rGO sample (20kx Mag.), (b) PET-CS-rGO sample (20kx Mag.), (c) PET-HDPC-rGO sample (20kx Mag.), and (d) PET-PDDAC-rGO sample (20kx Mag.).

Table 3 Reflectance (R), color strength (K/S), and relative percentage difference (RPD) of color strength for GO-modified and rGO-modified fabrics

Sample	R	K/S	RPD
GO-modified samples			
PET-GO	10.29	3.90	—
PET-ALK-GO	10.86	3.65	−6.46
PET-CS-GO	7.75	5.49	40.52
PET-PE-GO	8.84	4.70	20.24
PET-HDPC-GO	8.18	5.15	31.78
PET-PDDAC-GO	8.42	4.98	27.34
rGO-modified samples			
PET-rGO	7.67	5.65	—
PET-ALK-rGO	7.66	5.72	1.24
PET-CS-rGO	5.91	7.55	33.61
PET-PE-rGO	5.99	7.54	33.43
PET-HDPC-rGO	6.03	7.45	31.66
PET-PDDAC-rGO	5.78	7.75	36.97

wrinkles of GO nano-sheets (Fig. 11(g)). In this case, GO sheets with a large surface area are formed among the mono-filaments of the fiber as well (Fig. 11(h)).

SEM images of rGO-modified samples (Fig. 12) were recorded to observe the influence of chemical reduction on

the morphology of the samples. It was observed that shrinkages through the coating layers for control sample (PET-rGO), shown in Fig. 12(a), were successfully prevented by pre-treating the fabric with chitosan (PET-CS-rGO) (Fig. 12(b)) and HDPC (PET-HDPC-rGO) (Fig. 12(c)). Aggregation of sodium was observed (red arrows) on some sites of PET-HDPC-rGO. This might be the impurities from reduction process due to interaction of sodium hydrosulfite ($\text{Na}_2\text{S}_2\text{O}_4$) with HDPC or GO. However, PDDAC-modified fabric (PET-PDDAC-rGO) does not show a uniform and smooth coating layer (Fig. 12(d)).

The color strength and an estimation of dye concentration

As it can be seen from Table 3, PET-CS up-take highest concentration of colloidal dye having a relative percentage difference (RPD) of color strength of 40.52%. However, the up-taken dye was increased for all pre-modified samples, having a RPD of 31.78, 27.34 and 20.24% for PET-HDPC-GO, PET-PDDAC-GO and PET-PE-GO, respectively. As it was expected, due to the higher repulsion between GO nano-sheets and alkalinized polyester, the color strength of alkalinized fabric (PET-ALK-GO) decreased (−6.46%).

After chemical reduction of GO nano-sheets, all pre-modified samples show higher color strength as compare to a control sample.

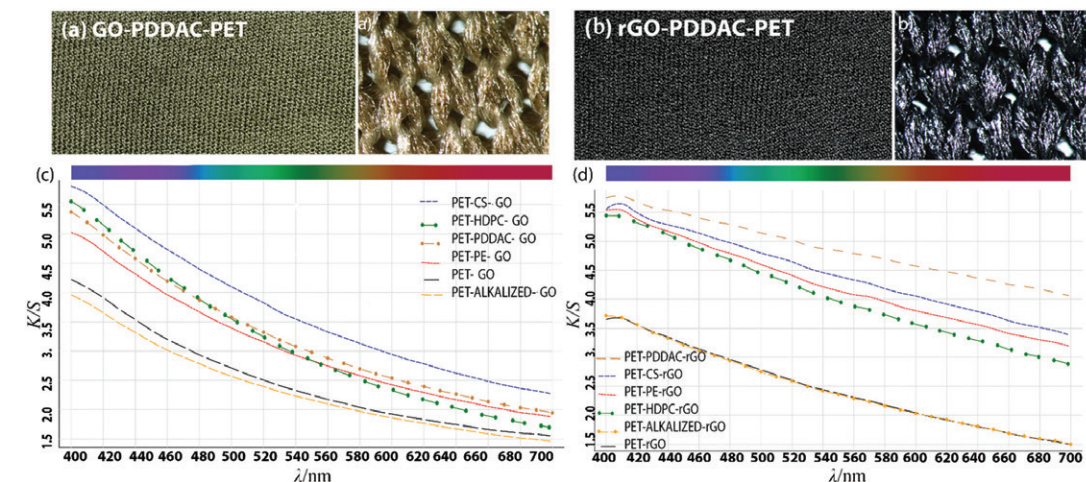


Fig. 13 A digital and microscopic images of (a) PET-PDDAC-GO and (b) PET-PDDAC-rGO. K/S values in the visible spectral range (400–700 nm) of (c) GO-modified and (d) rGO-modified samples.

Table 4 CIElab coordinates of GO-modified and rGO-modified fabrics. Color differences (ΔE) of a control and pre-treated samples in both CIE and CMC systems. L^* is the coordinate response to brightness and darkness of the surface, a^* coordinate response to green-red shade of color, and b^* coordinate response to yellow-blue shade of color

Sample	L^*	a^*	b^*	ΔE (CIE)	ΔE (CMC)	Sample	L^*	a^*	b^*	ΔE (CIE)	ΔE (CMC)
PET-GO	46.92	1.64	10.24	—	—	PET-rGO	36.86	0.96	4.49	—	—
PET-ALK-GO	47.53	1.66	9.75	0.78	0.51	PET-ALK-rGO	36.91	0.89	4.47	0.09	0.11
PET-CS-GO	40.58	2.16	8.97	6.49	3.34	PET-CS-rGO	31.43	0.71	2.84	5.69	3.49
PET-PE-GO	43.45	2.01	9.58	3.55	1.85	PET-PE-rGO	31.95	0.63	3.25	5.08	3.03
PET-HDPC-GO	43.57	2.83	11.61	3.81	2.42	PET-HDPC-rGO	32.40	0.82	3.72	4.54	2.58
PET-PDDAC-GO	42.73	2.10	9.75	4.24	2.16	PET-PDDAC-rGO	30.48	0.44	2.06	6.85	4.42

For example, PET-CS-rGO, PET-PE-rGO, PET-PDDAC-rGO, and PET-HDPC-rGO have a RPD of 33.61%, 33.43%, 36.97%, and 31.66%, respectively. The reflectance spectra of GO-coated and rGO-coated samples are shown in Fig. 13.

CIELab coordinates and total color differences (ΔE) according to CIELab and CMC (2:1) systems for GO-modified and rGO-modified fabrics are collected in Table 4. It can be seen that decrease in ΔE values of the pre-modified fabrics as compare to a control sample (PET-GO) are noticeable. These fabrics have lower value for L^* coordinate which stand for darkness-brightness of the color.

Manufacturing-based quality of modified fabrics

In order to investigate the evenness of coating layers, color difference (ΔE) of each sample was measured according to CIE and CMC systems.^{61,62} According to the standards, a ΔE of 1.0 is the smallest color difference that human eye might detect. Hence, any ΔE less than 1.0 is imperceptible and acceptable for textile industry.⁵³ As it can be seen from Fig. 14(a), a control sample has a high average ΔE of 1.66 ± 1.22 and the sample does not show a sufficient color evenness. On the contrary all surface modified samples pass the dyeing quality test, having an average ΔE less than 1.

PET-CS-rGO ($\Delta E = 0.21 \pm 0.07$) and PET-HDPC-rGO ($\Delta E = 0.3 \pm 0.16$) have the most even dye quality, which

Table 5 Sheet resistance (R_{sh}) and maximum current (I) at a voltage of 30 V for a control and rGO-modified samples

Sample	R_{sh} ($k\Omega \square^{-1}$)	I (mA)
PET-rGO	27.3 ± 2.8	—
PET-ALK-rGO	122 ± 9.8	—
PET-CS-rGO	2.7 ± 0.09	15
PET-PE-rGO	3.9 ± 0.2	5.56
PET-HDPC-rGO	0.59 ± 0.02	61.50
PET-PDDAC-rGO	38.5 ± 0.5	—

could be another reason performing better electrical activity. PET-PDDAC-rGO and PET-PE-rGO fabrics have an average ΔE of 0.55 ± 0.19 and 0.63 ± 0.25 . K/S values in the visible spectral range of a control sample, PET-CS-rGO, PET-PE-rGO, PET-PDDAC-rGO, PET-HDPC-rGO samples in $\lambda = 400$ –700 nm wavelength are shown in Fig. 14(b) and (f).

Electrical conductivity

Functional groups present on edges and surface of the GO sheets are the reason of electrically insulating properties. In order to bring electro-conductive properties to the fabrics, GO-modified samples were chemically reduced to rGO and sheet resistance (R_{sh}) of reduced samples was recorded with a 4-probe method (Fig. 17(a) and (b)).⁶³ The current-voltage

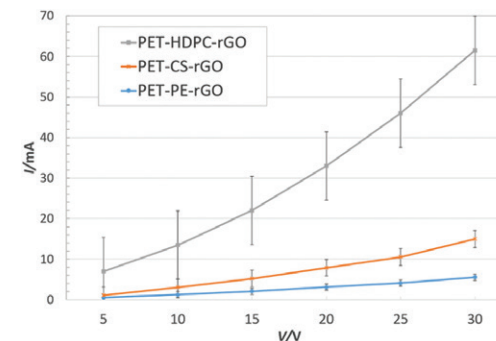


Fig. 15 Current vs. voltage profile of PET-HDPC-rGO, PET-CS-rGO, and PET-PE-rGO samples.

profile of samples was recorded in a voltage range of 5–30 V. The sheet resistance and maximum current at a voltage of 30 V are summarized in Table 5. A control fabric, without any surface modification shows a sheet resistance of $27.3 \pm 2.8 k\Omega \square^{-1}$. As it was expected, an alkalinized fabric shows higher electrical resistance, having a sheet resistance of $122 \pm 9.8 k\Omega \square^{-1}$. The sheet resistance of PET-HDPC-rGO, PET-CS-rGO, and PET-PE-rGO decrease to 0.59 ± 0.02 , 2.7 ± 0.09 , and $3.9 \pm 0.19 k\Omega \square^{-1}$ as compare to a control sample, having a value of $27.3 \pm 2.8 k\Omega \square^{-1}$. While for PET-PDDAC-rGO the value increases to $38.5 \pm 0.54 k\Omega \square^{-1}$, which is possibly due to the morphology of the surface of fabrics.

In order to having a better conductivity, smoothness and uniformity of the coating layer is more important than the amount of colloidal dye absorbed by the fabric.

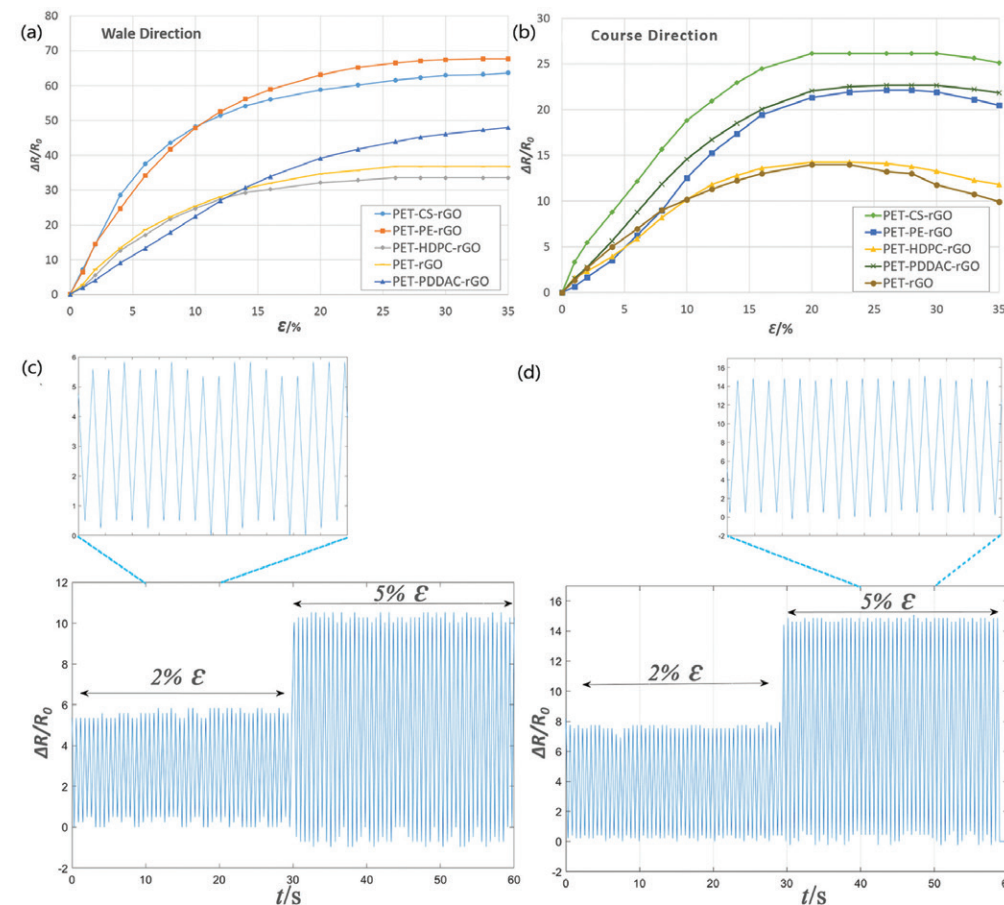


Fig. 16 The relative percent change of resistance over strain (0–35%) in (a) wale direction, and (b) course of the samples. PET-PE-rGO has the highest relative resistance change of 68% in wale direction and PET-PE-rGO having a relative resistance change of 26% in course direction. Figure (c) and (d) illustrate the relative percent of resistance change vs. time profiles of PET-HDPC-rGO and PET-CS-rGO respectively, through cyclic strain of 2 and 5% for 60 s.

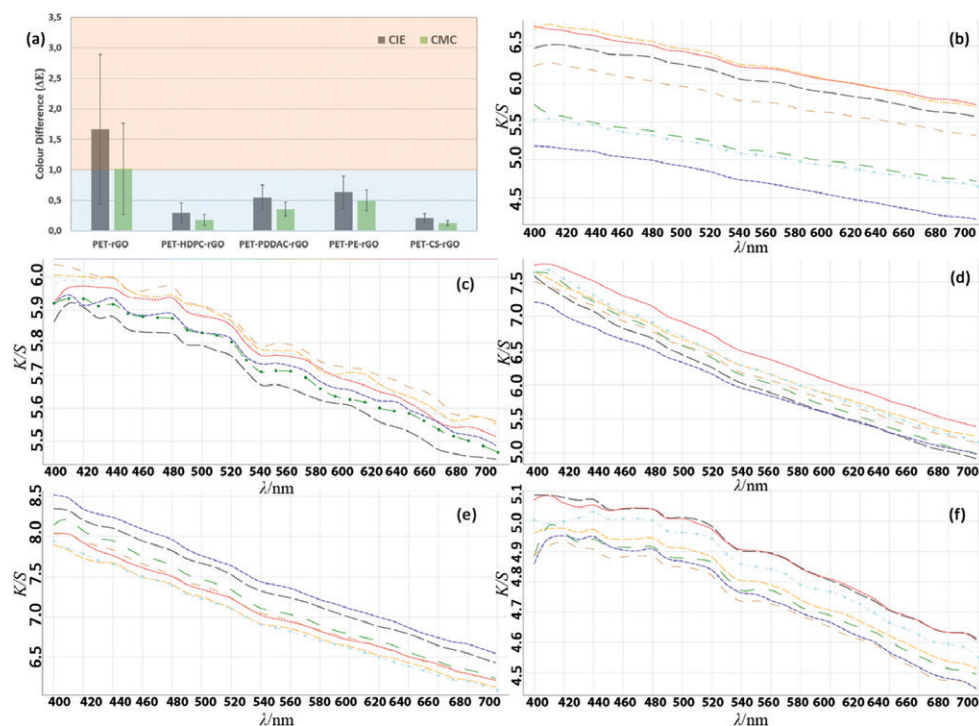


Fig. 14 (a) Color differences (ΔE) of samples according to CIE and CMC systems. K/S values in the visible spectral range (400–700 nm) of (b) a control sample, (c) PET-CS-rGO, (d) PET-PE-rGO, (e) PET-PDDAC-rGO, (f) PET-HDPC-rGO samples.

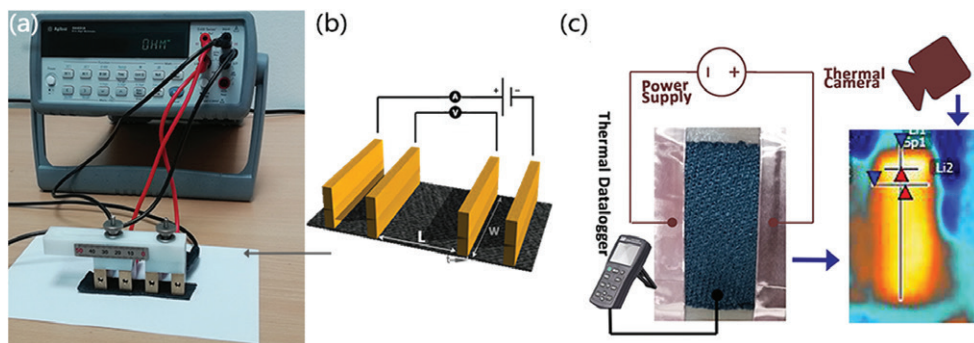


Fig. 17 (a) A build-up 4-probe measurement was used for estimating sheet resistivity of the samples. (b) Illustration of the 4-probe arrangement, the outer two probes are current carrying and the inner two probes measure the voltage drop. (c) An illustration of the set up for electro-thermal profile determination.

Although PET-PDDAC-rGO has the highest degree of GO up-taken, but surface resistance is higher than a control sample. Thus, choosing the right agent is obligatory to achieve high conductivity. PET-PDDAC-rGO does not have a homogeneous coating and free electrons are not able to move easily toward fibers.

A power supply was used to apply voltages (5 to 30 V) to the fabric and average current passing through the fabric was recorded (Fig. 15). PET-HDPC-rGO could reach to maximum current of $61.5 \pm 0.5\%$ mA at 30 V. PET-CS-rGO and PET-PE-rGO have the maximum current of $15.00 \pm 1\%$ and $5.56 \pm 0.5\%$ mA at 30 V and no current was recorded for other samples.

Electro-mechanical performances

The resistance change of the graphene-modified fabrics as a function of applied tensile strain (0–30%) was recorded and percent relative change in sheet resistance ($\Delta R/R_0$) of samples was calculated. Electro-mechanical test was carried out in both wale and course direction of the fabrics. A rib knitted fabric stretch more freely in the course direction as applying a tensile force in that direction leads to opening and stretching the loops. On the contrary, stretching in wale direction tightens the pores. It was observed that in course direction relative resistance change was lower for all samples and almost after applying 20% strain, the electrical resistance start to increase as the pores loose. While due to pores tightening in wale direction, strain sensitivity was higher and electrical resistance decreases by applying a strain up to 35%. The relative resistance change remain constant for applied strain higher than 35%.

As it can be seen from Fig. 16(a), PET-PE-rGO has the highest sensibility (68%) to 30% applied strain in wale direction, while PET-CS-rGO, PET-PDDAC-rGO, PET-HDPC-rGO, and PET-rGO has 64, 48, 34, and 37% relative resistance change for 30% applied strain. Applied strain higher than 30% in wale direction does not put either negative or positive effect on resistivity as the change in resistance remains constant. However, highest sensitivity in course direction was associated to PET-CS-rGO sample by having 27% relative change in resistance (Fig. 16(b)).

In order to investigate the conducting stability of the PET-HDPC-rGO and PET-CS-rGO, the resistance change of

the samples was measured during the consecutive stress-strain cycles. Fabrics were constantly stretched by 2% and 5% elongation for 90 s and no drift was observed. Fig. 16(c and d) illustrate the relative resistance change of PET-HDPC-rGO and PET-CS-rGO respectively through 2% and 5% applied strain in the wale direction.

Electro-thermal performances

In order to characterize the electro-thermal properties of rGO-coated fabrics, direct current (DC) power was applied (5–30 V) to the samples with valid heating area of $2 \times 1.5 \text{ cm}^2$ and electro-thermal properties was investigated under ambient condition with a thermal camera and a thermal data-logger sensor (Fig. 17(c)).

Since the electrical resistance of a control and PDDAC-modified fabrics are high and no current is passing through the fabric, there is no heat exchange to the fabrics. In this case, PET-PE-rGO also did not show any significant increase in temperature (38°C at 30 V). After supplying electrical power to PET-CS-rGO and PET-HDPC-rGO, the temperature increased monotonically over time until a steady state temperature was reached (Fig. 18).

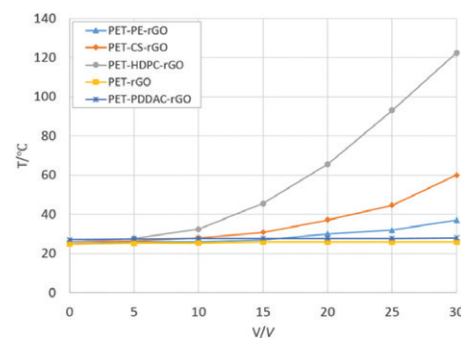


Fig. 18 The steady-state temperature (T) vs. applied voltages (V) profile of the samples.

It was observed that the steady state temperature increases by increasing voltage applied with a quadratic correlation of input voltage and temperature. The results are consistent with Joule's law;^{64,65}

$$P = \frac{U^2}{R} \quad (6)$$

where, P is power, U is applied voltage, and R is the resistance.

PET-HDPC-rGO has a higher steady state temperature at the same voltage as compare to CS-modified sample. This is attributed to the lower transduction of electrical energy into Joule heating. Heating rate curve of HDPC-treated sample at 30 V is illustrated in Fig. 19(a).

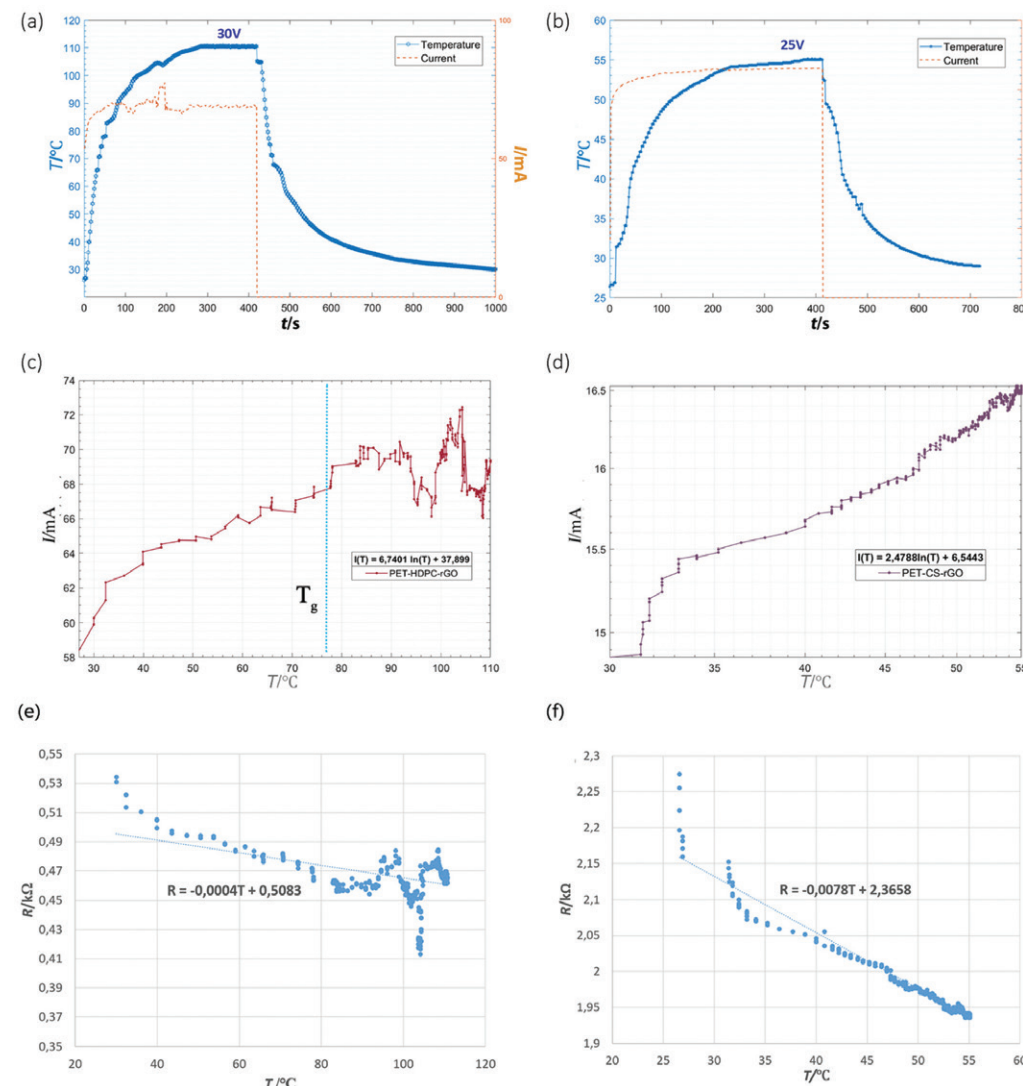


Fig. 19 Temperature and current versus time profile of the (a) PET-HDPC-rGO by having a steady state temperature of 115°C at a constant voltage of 30 V, (b) PET-CS-rGO with a steady state temperature of 55°C at a constant voltage of 25 V, response time for both fabrics are less than 120 s, the current vs. temperature profile of (c) PET-HDPC-rGO and (d) PET-CS-rGO during the electro-thermal activity with a function of $I(T) = 6.74 \ln(T) + 37.9$ and $I(T) = 2.478 \ln(T) + 6.5$, respectively. The measured resistance change vs. temperature profiles of (e) PET-HDPC-rGO with a function of $R = 0.0004T + 0.5$, and (f) PET-CS-rGO with a function of $R = 0.0078T + 2.36$.

PET-HDPC-rGO shows steady state temperature of 120 °C with a maximum heating rate of 0.5 °C s⁻¹ at a driving voltage of 30 V. Steady state temperature of 60 °C with a maximum heating rate of 0.2 °C s⁻¹ at driving voltage of 25 V was observed for CS-treated sample (Fig. 19(b)), which has higher sheet resistance as compare to PET-HDPC-rGO.

It has been reported that a thin film of graphene has a steady state temperature of 139 °C at given voltage of 30 V.⁶⁵ Considering the sheet resistance of a thin film of graphene is around 0.159 kΩ □⁻¹. Although a modified fabric has higher surface area than a film still achieving 0.59 kΩ □⁻¹ sheet resistance and 120 °C steady state temperature is a noticeable outcome.

In order to meet comfort of the human body in heating garment for cold proof applications such as outdoor service clothes, the cold storage working cloths, and submarine work clothes, the heating temperature is generally about 40 °C. In medical applications such as hot compress therapy, the temperature of the garment usually is around 55 °C.⁶⁶ Both CS and HDPC-modified fabrics fulfil the temperature requirement for such applications.

By decreasing the applied voltage from 30 to 25 V, the steady state temperature of PET-HDPC-rGO and PET-CS-rGO decrease to 93 and 54 °C, respectively. Additionally, the time required to reach 90% of the steady state temperature which called “the response time” is an important factor for heat performance evaluation and applications.^{65,67} Both samples show a response time less than 120 s. After reaching to the steady state temperature, the power supply was switched off and the temperature started to decrease immediately with a logarithmic trend line of $T = -6.27 \ln(s) + 63.7$ for PET-HDPC-rGO and $T = -17.14 \ln(s) + 133.6$ for PET-CS-rGO samples. Both samples had a temperature loss gradient of 0.137 s⁻¹.

Carbon has negative temperature coefficient (NTC) and by increasing the temperature, the resistance of graphene will decrease⁶⁸ and it results in increasing the current flow. By increasing the temperature from room temperature to 110 °C for PET-HDPC-rGO (Fig. 19(c)), the current increase from 58 to 69 mA and resistance of the fabric decreases to 0.46 Ω (Fig. 19(e)).

Further, for CS-modified sample current increases from 14.8 to 16.5 mA (Fig. 19(d)), as temperature increases to 55 °C with a gradient of 0.06. As results, electrical resistance decreases to 1.94 Ω (Fig. 19(f)). Having NTC properties makes graphene-modified fabric a good candidate for continuous temperature sensing applications.

Fig. 20 shows the infrared thermal images of PET-CS-rGO sample at its steady state temperature under an applied voltage of 25 V. As it has been reported before, Graphene has an even heat distribution.⁶⁴ And the evenness of heat distribution along a graphene coated fabric might be due to both graphene properties and the evenness of the coating.

Glass transition temperature (T_g) of PET-HDPC-rGO was recorded by DSC measurement (76.5 °C) (Fig. 21(a)). The fluctuations observed in current and resistant profile of PET-HDPC-rGO for temperatures higher than 80 °C (Fig. 19(c)), might be due to the change in crystallinity of the polymer.

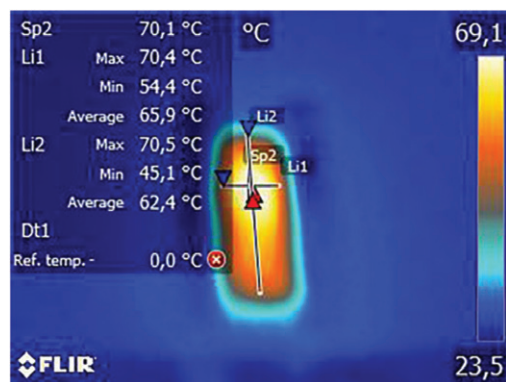


Fig. 20 Infrared image at steady state temperature of PET-CS-rGO, at an applied voltage of 25 V, reaching to average temperature of 66 °C while having a good thermal expansion through fabric surface.

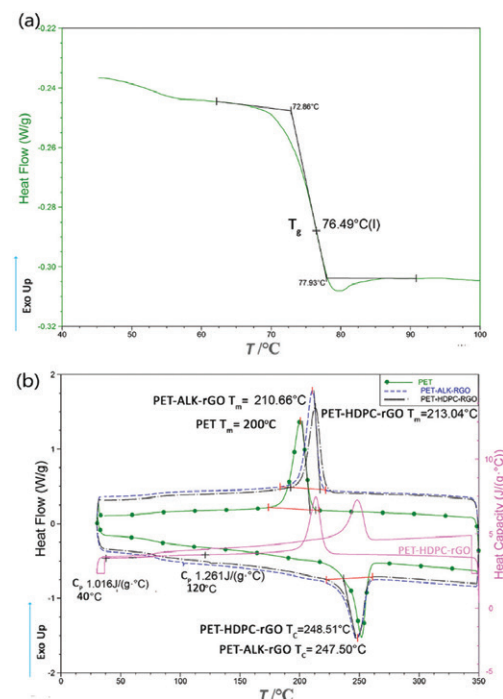


Fig. 21 (a) DSC photographs of PET-HDPC-rGO, with a glass transition (T_g) of 76.5 °C. (b) DSC photographs of a control polyester fabric (PET), a pre-alkalized polyester fabric coated by reduced graphene oxide (PET-ALK-rGO), and a HDPC-surface modified polyester fabric coated by reduced graphene oxide. Heat capacity profile of PET-HDPC-rGO. Melting temperature (T_m) of a polyester fabric with a value of 200 °C increases to 213 °C for a PET-HDPC-rGO fabric. Heat capacity at constant pressure (C_p) of the same sample at 120 °C is 1.261 J (g °C)⁻¹.

Additionally, to better understanding the thermal behavior of a graphene modified fabric, melting temperature (T_m) was measured (Fig. 21(b)).

For an unmodified fabric (PET), an alkalized fabric modified by rGO (PET-ALK-rGO), as well as a PET-HDPC-rGO fabric. T_m were 200 °C, 210 °C, and 213 °C for PET, PET-ALK-rGO, and PET-HDPC-rGO fabrics, respectively. Increase in T_m for both PET-ALK-rGO and PET-HDPC-rGO is noticeable.

Heat capacity of A PET-HDPC-rGO sample was recorded in order to further calculation of required energy in heater elements applications. PET-HDPC-rGO has a range of heat capacity of 1.016 J (g °C)⁻¹ to 1.261 J (g °C)⁻¹ form 40 to 120 °C.

Conclusions

To the best of our knowledge, due to the high electrical resistance of graphene-modified polyester fabrics, electro-thermal activity of such textiles has not yet been reported. Further, the apparent quality of these textile are typically not relevant for large scale production. We introduced a process that includes surface charge modification of the polyester fabric through chitosan and HDPC in which the surface resistance of the fabric decreases to 2.7 and 0.59 kΩ □⁻¹, respectively, as compare to a non-modified fabric having a value of 27.3 kΩ □⁻¹. It gives an adequate electrical conductivity to fabrics for electro-thermal heaters and many cold proof applications; e.g. medical and outdoor service clothes, having a high psychological comfort as conventional textiles.

In addition, the total color difference (ΔE) less than 1 unit is required to fulfill appearance quality in textile dyeing industry and fabrics prepared by our method have a ΔE lower than 0.5, are highly promising for large-scale productions.

Conflicts of interest

The authors declare no conflict of interest.

Acknowledgements

The work was carried out within the strategic innovation programme SIO Grafen, a joint initiative of Vinnova, Swedish Research Council, Formas and Swedish Energy Agency. A special thanks to Inuheat AB and the Smart Textiles initiative. Dr Li Guo and Mr Emanuel Gunnarsson are acknowledged for support with electrical measurements.

References

- J. E. Craddock, *US Pat.*, 1394810, 1921.
- S. Park and S. Jayaraman, *MRS Bull.*, 2003, **28**, 585–591.
- L. Li, W.-m. Au, F. Ding, T. Hua and K. S. Wong, *Text. Res. J.*, 2014, **84**, 477–487.
- T. Wittkowski, *US Pat.*, 0246415A1, 2014.
- M. J. Giamati, *US Pat.*, 5412181, 1995.
- R. S. Ely and I. M. Ketcham, *US Pat.*, 2496279, 1950.

- K. C. Schramm, *US Pat.*, 6834159B1, 2004.
- E. Kochman and D. Kochman, *US Pat.*, 6713733B2, 2004.
- K. Ohgushi, M. Hijiri and Z. Kitazawa, *US Pat.*, 4983814, 1991.
- T. Bashir, M. Skrifvars and N. K. Persson, *Polym. Adv. Technol.*, 2011, **22**, 2214–2221.
- P.-W. Hwang, A.-P. Chen, C.-W. Lou and J.-H. Lin, *J. Ind. Text.*, 2014, **44**, 477–494.
- S. Kumar, H. Doshi, M. Srinivasarao, J. O. Park and D. A. Schiraldi, *Polymer*, 2002, **43**, 1701–1703.
- M. S. Ozen, I. Usta, M. Yuksek, E. Sancak and N. Soin, *Fibres Text. East. Eur.*, 2018, **1**, 94–100.
- B. Fugetsu, E. Sano, H. Yu, K. Mori and T. Tanaka, *Carbon*, 2010, **48**, 3340–3345.
- M. D. Stoller, S. Park, Y. Zhu, J. An and R. S. Ruoff, *Nano Lett.*, 2008, **8**, 3498–3502.
- J. W. Suk, R. D. Piner, J. An and R. S. Ruoff, *ACS Nano*, 2010, **4**, 6557–6564.
- W. S. Hummers Jr and R. E. Offeman, *J. Am. Chem. Soc.*, 1958, **80**, 1339.
- M. Hirata, T. Gotou, S. Horiuchi, M. Fujiwara and M. Ohba, *Carbon*, 2004, **42**, 2929–2937.
- S. Park and R. S. Ruoff, *Nat. Nanotechnol.*, 2009, **4**, 217.
- A. Lerf, H. He, M. Forster and J. Klinowski, *J. Phys. Chem. B*, 1998, **102**, 4477–4482.
- S. Stankovich, R. D. Piner, X. Chen, N. Wu, S. T. Nguyen and R. S. Ruoff, *J. Mater. Chem.*, 2006, **16**, 155–158.
- M. Shateri-Khalilabad and M. E. Yazdanshenas, *Carbohydr. Polym.*, 2013, **96**, 190–195.
- S. Stankovich, D. A. Dikin, R. D. Piner, K. A. Kohlhaas, A. Kleinhammes, Y. Jia, Y. Wu, S. T. Nguyen and R. S. Ruoff, *Carbon*, 2007, **45**, 1558–1565.
- A. B. Bourlins, D. Gournis, D. Petridis, T. Szabó, A. Szeri and I. Dékány, *Langmuir*, 2003, **19**, 6050–6055.
- M. Lotya, Y. Hernandez, P. J. King, R. J. Smith, V. Nicolosi, L. S. Karlsson, F. M. Blighe, S. De, Z. Wang and I. T. McGovern, *J. Am. Chem. Soc.*, 2009, **131**, 3611–3620.
- A. M. Grancaric, A. Tarbuk and T. Pusic, *Color. Technol.*, 2005, **121**, 221–227.
- J. A. Moleon, A. Ontiveros-Ortega, E. Gimenez-Martin and I. Plaza, *Dyes Pigm.*, 2015, **122**, 310–316.
- H. Bao, Q. Chen, L. Zhang and G. Chen, *Analyst*, 2011, **136**, 5190–5196.
- I. A. Sahito, K. C. Sun, A. A. Arbab, M. B. Qadir and S. H. Jeong, *Carbohydr. Polym.*, 2015, **130**, 299–306.
- T. Salem, S. Uhlmann, M. Nitschke, A. Calvimontes, R.-D. Hund and F. Simon, *Prog. Org. Coat.*, 2011, **72**, 168–174.
- F. R. Oliveira, D. A. J. De Oliveira, F. Steffens, J. H. O. do Nascimento, K. K. O. S. e Silva and A. P. Souto, *Procedia Eng.*, 2017, **200**, 309–316.
- D. Fischer, H. Dautzenberg, K. Kunath and T. Kissel, *Int. J. Pharm.*, 2004, **280**, 253–269.
- R. Krajcik, A. Jung, A. Hirsch, W. Neuhuber and O. Zolk, *Biochem. Biophys. Res. Commun.*, 2008, **369**, 595–602.
- O. Boussif, F. Lezoualc'h, M. A. Zanta, M. D. Mergny, D. Scherman, B. Demeneix and J.-P. Behr, *Proc. Natl. Acad. Sci. U. S. A.*, 1995, **92**, 7297–7301.

- 35 M. Tian, X. Tang, L. Qu, S. Zhu, X. Guo and G. Han, *Mater. Lett.*, 2015, **145**, 340–343.
- 36 M. Tian, X. Hu, L. Qu, M. Du, S. Zhu, Y. Sun and G. Han, *Appl. Surf. Sci.*, 2016, **377**, 141–148.
- 37 W.-S. Hung, S.-M. Chang, R. L. G. Lecaros, Y.-L. Ji, Q.-F. An, C.-C. Hu, K.-R. Lee and J.-Y. Lai, *Carbon*, 2017, **117**, 112–119.
- 38 T. Kuilla, S. Bhadra, D. Yao, N. H. Kim, S. Bose and J. H. Lee, *Prog. Polym. Sci.*, 2010, **35**, 1350–1375.
- 39 Y. Liu, M. Park, H. K. Shin, B. Pant, J. Choi, Y. W. Park, J. Y. Lee, S.-J. Park and H.-Y. Kim, *J. Ind. Eng. Chem.*, 2014, **20**, 4415–4420.
- 40 M. Rinaudo, G. Pavlov and J. Desbrieres, *Polymer*, 1999, **40**, 7029–7032.
- 41 A. Jayakrishnan and D. O. Shah, *J. Polym. Sci., Polym. Chem. Ed.*, 1983, **21**, 3201–3208.
- 42 E. M. Sanders and S. H. Zeronian, *J. Appl. Polym. Sci.*, 1982, **27**, 4477–4491.
- 43 L. M. Olson and M. Wentz, *Text. Chem. Color.*, 1984, **16**, 48.
- 44 J. F. Moulder, *Physical electronics*, 1995, 230–232.
- 45 T. I. T. Okpalugo, P. Papakonstantinou, H. Murphy, J. McLaughlin and N. M. D. Brown, *Carbon*, 2005, **43**, 153–161.
- 46 L. Yang, L. Xin, W. Gu, J. Tian, S. Liao, P. Du, Y. Tong, Y. Zhang, R. Lv and J. Wang, *J. Solid State Chem.*, 2014, **218**, 64–70.
- 47 X. Guo, B. Xu, W. Zhang, Z. Cai and Z. Wen, *Appl. Surf. Sci.*, 2014, **321**, 94–97.
- 48 R. J. Hunter, *Zeta potential in colloid science: principles and applications*, Academic press, 1981, pp. 22–24.
- 49 T. Young, *Philos. Trans. R. Soc. London*, 1805, **95**, 65–87.
- 50 T. Young, *Philos. Trans. R. Soc. London*, 1805, **95**, 65–87.
- 51 E. R. Trotman and E. Russell, *Dying and chemical technology of textile fibers*, Edward Arnold, London, 6th edn, 1984, pp. 109–135.
- 52 F. M. Mirabella, *Modern techniques in applied molecular spectroscopy*, John Wiley & Sons, 1998.
- 53 P. Green and L. MacDonald, *Colour engineering: achieving device independent colour*, John Wiley & Sons, 2011.
- 54 J. Schanda, *Colorimetry: understanding the CIE system*, John Wiley & Sons, 2007.
- 55 F. M. Smits, *Bell Syst. Tech. J.*, 1958, **37**, 711–718.
- 56 I. Miccoli, F. Edler, H. Pfnür and C. Tegenkamp, *J. Phys.: Condens. Matter*, 2015, **27**, 223201.
- 57 M. Tokarska and K. Gniotek, *J. Text. Inst.*, 2015, **106**, 9–18.
- 58 L. Guo, T. Bashir, E. Bresky and N. K. Persson, *Smart Textiles and their Applications*, Elsevier, 2016, pp. 657–693.
- 59 D. Li, M. B. Müller, S. Gilje, R. B. Kaner and G. G. Wallace, *Nat. Nanotechnol.*, 2008, **3**, 101–105.
- 60 H. He and T. Riedl, *J. Phys. Chem. B*, 1998, **102**, 4477–4482.
- 61 D. Heggie, R. H. Wardman and M. R. Luo, *J. Soc. Dyers Colour.*, 1996, **112**, 264–269.
- 62 M. R. Luo and B. Rigg, *J. Soc. Dyers Colour.*, 1986, **102**, 164–171.
- 63 L. Guo, T. Bashir, E. Bresky, N. K. Persson and V. Koncar, *Smart textiles and their applications*, Woodhead Publishing Limited, Cambridge, 2016.
- 64 D. Sui, Y. Huang, L. Huang, J. Liang, Y. Ma and Y. Chen, *Small*, 2011, **7**, 3186–3192.
- 65 C. Li, Y.-T. Xu, B. Zhao, L. Jiang, S.-G. Chen, J.-B. Xu, X.-Z. Fu, R. Sun and C.-P. Wong, *J. Mater. Sci.*, 2016, **51**, 1043–1051.
- 66 H. Dai, H. Yang and J. Yin, *Climate Dynamics*, 2017, **49**, 1513–1529.
- 67 X. Wang, L. Zhi and K. Müllen, *Nano Lett.*, 2008, **8**, 323–327.
- 68 X.-Y. Fang, X.-X. Yu, H.-M. Zheng, H.-B. Jin, L. Wang and M.-S. Cao, *Phys. Lett. A*, 2015, **379**, 2245–2251.



Cite this: DOI: 10.1039/c9nj06437k

Electrostatic grafting of graphene onto polyamide 6,6 yarns for use as conductive elements in smart textile applications

Milad Asadi Miankafshe, ^{*ab} Tariq Bashir^{ac} and Nils-Krister Persson^{ab}

Electrostatic graphene-grafted conductive yarns were prepared based on a scalable manufacturing method using conventional polyamide 6,6 (PA 6,6) multifilament yarns, common in the textile industry. Graphene oxide (GO) shows negative surface charge at any pH and PA 6,6 has an isoelectric point (IEP = $\text{pH}_{\text{I}=\text{O}}$) of 3.6. When GO and a polymer have the same charge sign, the resulting electrostatic interaction is repulsive and an electrostatic attraction does not arise until the polymer backbone has an oppositely charged sign compared to the GO nanosheets. To achieve this, yarns were modified with protonated chitosan (CS) followed by dip-coating with GO, resulting in electrostatic grafting of oxygen functional groups of GO onto amino groups of CS polymer chains. This coating process provides durable electrically conductive yarns (3×10^{-2} to $4 \times 10^{-2} \text{ S m}^{-1}$) with an excellent fastness to washing. It leads to the realization of graphene-grafted yarns as building elements of smart textiles, obtaining metal-free textile sensors. These yarns are capable of supplying power to an LED light using a 9 V battery and are expected to be an excellent candidate for feeding V-bed flat-knitting, Jacquard and raschel knitting machines. To achieve this, a wearable tactile sensor was designed and prepared using a flat-knitting machine and the sensor was characterized through electrical, mechanical, and electromechanical measurements.

Received 29th December 2019,
Accepted 10th April 2020

DOI: 10.1039/c9nj06437k

rsc.li/njc

Introduction

As textiles are a unique class of fabricated materials, involved in almost every human social activity, smart textiles *i.e.* the combination of textiles and any other enabling technology such as electronics, often regarded as the key factor for obtaining smartness, are forecast to have a tremendous impact on society.^{1,2} However, the development of smart textiles runs the risk of stagnation if the prevalent paradigm of mounting the enabling technology on the surface of textiles (what has been called the integration on approach³) prevails, as it results in bulky, heavy, and non-compliant products with low comfort, which are based on inefficient production and require many non-automatic processes which need manual steps.

Instead, an alternative approach for achieving smartness is interesting. In what has been denoted as the integration in approach,³ the very yarns, or a subset thereof, are conductive and when weaved in, or knitted in, simultaneously add to the

structural cohesion as well as the function. Ultimately, the goal is to maintain textile comfort, smoothness, pliability, washability, and production infrastructure while maintaining low production costs.

Electroconductive fibers are currently attracting much attention for a range of applications from electrostatic discharge^{4–6} to health monitoring and diagnostic systems,^{7–14} supercapacitors^{15–19} and energy harvesting threads.^{20–23} Many of these are based on electrically conductive polymers or metallic conductive mechanisms. An interesting alternative is fibres based on any of the carbon allomorphs for electrical conductivity.²⁴ Among these, graphene – a system of two-dimensional nanosheets with a thickness of one or a few atoms of sp^2 -bonded carbon atoms – is presently the object of intensive study.^{25–35} This is due to the fact that (a) only small amounts are needed to achieve any effect (electrical or otherwise), and that (b) a thin layer with potentially minimal impact on the thickness of already small structures is often enough.

Graphene with electrical functionality could be introduced at many levels in the textile hierarchy (Fig. 1). Integration of graphene on the fabrics occurs *via* different methods such as dip-coating,^{36–39} pad-coating,^{40–42} knife-coating,^{43–45} inkjet printing^{46–48} and more. Among the mentioned methods, dip-coating is a cost-effective, easy to handle and readily scalable process. However, a drawback of dip-coating knitted and woven

^a The Swedish School of Textile, Polymeric E-textiles, University of Borås, SE-501 90 Borås, Sweden. E-mail: milad.asadi@hb.se; Tel: +46 729339664

^b Smart Textiles, University of Borås, SE-501 90 Borås, Sweden

^c Swedish Centre for Resource Recovery, University of Borås, SE-501 90 Borås, Sweden

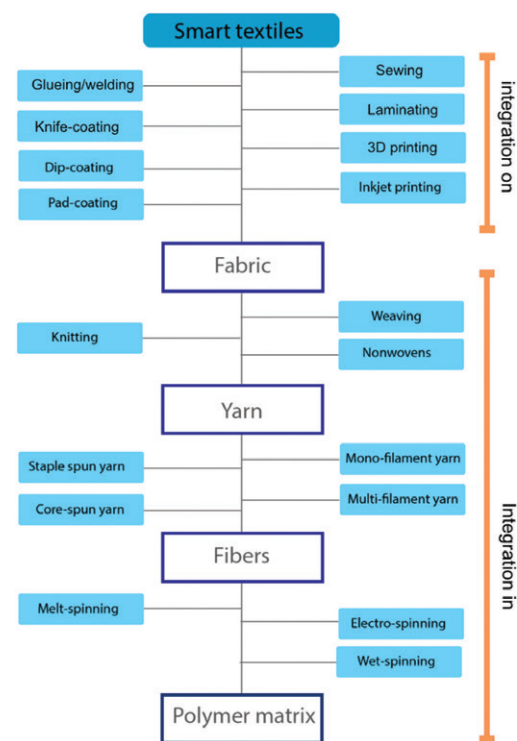


Fig. 1 A general scheme of the textile hierarchy (and the production processes) from the fibers to the final garment as well as the processes in which integration of graphene could be applied in or on the textile materials. Starting from the fabric level, all processes below and including the fabric forming process that adds functionality are denoted as integration in. Adding in the form of lamination, sewing, glueing, coating etc. to an existing fabric is denoted as integration on.

fabrics is that to produce a smart garment of any complexity, cutting and subsequent steps such as sewing, glueing, welding, laminating, or other integration techniques are required.

Another approach of making graphene containing fibres is more interesting for large production and it could be obtained by introducing graphene into the polymer matrix. Graphene-polymer composite fibers could be prepared *via* electro-spinning,^{49–55} wet-spinning^{56–60} and melt-spinning processes.^{61–70} Among these, the melt-spinning process is more commercially attractive since the other methods are less environmentally benign.⁷¹ Furthermore, the dispersion of graphene in the polymer matrix has always been very challenging in both the melt-spinning and wet-spinning processes.⁷¹

Other techniques such as chemical vapour deposition (CVD), growth of graphene along Cu wires or meshes^{72–74} and use of the dimension-confined hydrothermal method^{51,75} are limited to lab-scale production and are not useful for continuous production of textile fibers.

The ultimate approach, when it comes to reliability of a product for the textile industry, is instead conventional textile

fibres functionalized with a very thin layer of graphene. In this case, the conventional textiles receive electrical functionality without compromising physical properties of the textile and maintain high pliability, smoothness (good handle) and compliance as well as being compatible with automatic and cost-effective large-area manufacturing.

In our previous work,⁷⁶ we showed that by applying a surface charge modification step to the dip-coating process of polyester fabrics with GO dispersion, the evenness of the coating and subsequently its electrical conductivity were enhanced significantly. This is because the GO dispersion in many textiles carry negative surface charges in aqueous solutions^{77–80} and pre-treatment of polyester yarns^{81,82} with cationic agents is necessary to ensure the electrostatic attraction between the polymer backbone and GO nanosheets.

In this study, we have instead focused on the integration of graphene in individual textile polyamide yarns as the conductive element in smart textile applications, making it an accessible and cost-effective potential method for use in the textile industry. The idea is that as the material is built structurally by weaving or knitting thread by thread, (electrical) functionality and desirable patterns and circuits are simultaneously created. Weave- and knit-patterns enable the creation of electrical circuits. We developed a yarn coating process in which graphene-grafted yarns could be prepared using chitosan (CS) as the cationic agent and conventional polyamide (PA 6,6) yarn as the main substrate. PA fibers are one of the most used synthetic fibers within the textile industry, demonstrating the potential of the method. The resulting yarns are capable of supplying power to LED lights and are used for constructing a tactile sensor.

Using this method allows the production of both cheap conductive yarns and specific smart garments for different applications by applying graphene yarns in advanced knitting machines such as Stoll flat-knitting machines. There is still a lack of standard sufficient yarn functionalisation with graphene. This method could give a better understanding of developing industrial production lines.

Experimental

Materials

A flat polyamide 6,6 high tenacity multifilament yarn (Enka Nylon 444HRST, 470dtx72) was selected for the experiment. Sodium hydroxide (NaOH) solution (Sigma-Aldrich Co., USA) was used for the pre-alkalization process. Chitosan (CS) (Sigma-Aldrich Co., USA) solution was prepared by dissolving CS powders in a solvent of 0.1 M acetic acid⁸³ and an aqueous solution of hexadecylpyridinium chloride monohydrate (HDPC)⁷⁷ (Sigma-Aldrich Co., USA) was prepared using distilled water.⁸⁴ In our previous work, we demonstrated that HDPC gives the highest conductivity to graphene in polyester fabric coating. However, HDPC is toxic while CS is a sustainable bio-sourced compound. For that, here we only report CS-modified yarns in detail, while using HDPC-modified yarns as an electrical

conductivity reference. CS and HDPC solutions were stirred at room temperature for 24 h and settled for 2 h. A commercial aqueous dispersion of graphene oxide (4 g L⁻¹) (Graphenea S.A., Spain) was used for the coating and sodium hydrosulfite (Na₂S₂O₄)⁸⁵ (Sigma-Aldrich Co., USA) was applied to reduce GO (rGO) nanosheets and deliver covalently functionalized fibers.

Fabrication of the graphene-grafted yarns

To increase dyeability of the fibers,^{86,87} yarns were treated with an aqueous solution of sodium hydroxide (12 wt%; yarn to liquor ratio 1 : 50) at 60 °C for 90 min. The yarns were then washed several times in warm ultrapure water and acetone to remove any remaining impurities and dried in an oven at 80 °C for 10 min. The surface charge modification of yarns was applied by soaking them in a solution of 4 g L⁻¹ of CS or HDPC for 60 minutes at 60 °C and followed by rinsing several times in warm ultrapure water and drying at 80 °C for 10 min.

Furthermore, yarns were coated by dipping into an aqueous dispersion (0.4 wt%) of GO (pH = 3.5) with a yarn to liquor ratio of 1 : 50 (GO dispersion was sonicated for 30 min before the dip-coating process). The process starts at 45 °C decreasing with a temperature gradient of 0.5 °C min⁻¹ for 30 min. Finally, the yarns were thermally cured in an oven at 80 °C for 10 minutes. The surface modification of yarns results in electrostatic grafting of GO nanosheets onto the polymer.

In order to provide the yarns with electro-conductive properties, GO-grafted yarns were chemically reduced using a 50 mM Na₂S₂O₄ aqueous solution⁸⁵ with a yarn to liquor ratio of 1 : 100 for 30 min at 95 °C. Then, the yarns were rinsed several times in

warm ultrapure water and dried at 70 °C for 10 min. The time-temperature profile of the process is illustrated in Fig. 2.

A pristine yarn with no surface modification was prepared in the same manner as a control sample. It was observed that for such a yarn, the coating was easily separated from the yarn during the rinsing and no electrical conductivity was achieved. It demonstrates the necessity of cationic surface modification of polyamide yarns to assure the electrical functionality of the product.

Characterization

Zeta potentials (ζ) of the samples were determined using streaming potential measurements using a cylindrical cell (Surpass, Anton Paar GmbH., Austria). The zeta potential values were calculated with the Fairbrother–Mastin (FM) equation (eqn (1)) and recorded as a function of the pH of the electrolyte solution (0.001 M KCl), where the pH was adjusted with 0.01 M HCl and 0.01 M NaOH solutions.⁸⁸

$$\zeta = \frac{dE_s}{dP} \frac{\mu}{\epsilon \epsilon_0} \lambda_b \quad (1)$$

where ζ is the zeta potential, dE_s/dP is the slope of streaming potential *versus* differential pressure, μ is the electrolyte viscosity, ϵ is the dielectric constant of the electrolyte, ϵ_0 is the vacuum permittivity, and λ_b is the conductivity of the bulk electrolyte solution.

The surface morphology of GO and rGO-grafted yarns were investigated using scanning electron microscopy (SEM) (FEI Quanta200 ESEM, Thermo Fisher Scientific CO., USA) with an acceleration voltage of 10 kV, and a working distance of 10 mm. Fourier transform infrared (FTIR) spectroscopy (Nicolet iS10,

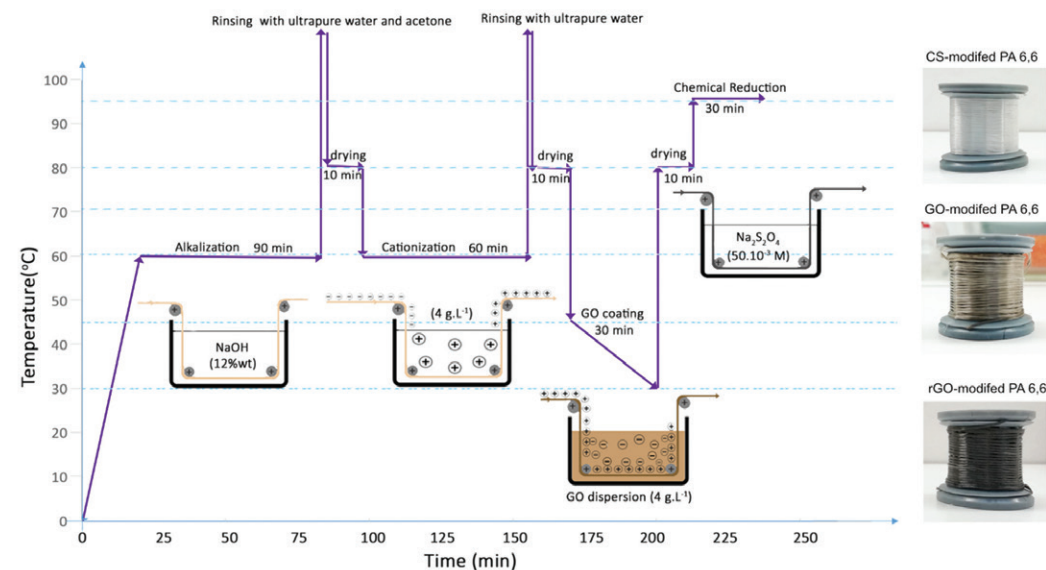


Fig. 2 The time-temperature profile of the coating process and the microscopic images of resulting fibers.

Thermo Fisher Scientific CO., USA) was used to investigate the chemical composition of the yarns. X-ray photoelectron spectroscopy (XPS) was performed using a spectrophotometer (PHI 5500 ESCA, Physical Electronics INC., USA) with monochromatic Al-K α radiation (photon energy = 1486.6 eV).

In order to determine the tensile properties of the samples and investigate whether the modification process damaged tensile properties of yarns or not, a pristine yarn as well as all modified samples were tested using a tensile tester (H10KT, Tinius Olsen Co., USA). The test was carried out as per DIN 53834 standard with a gauge length of 100 mm, load cell of 5 N and clamp speed of 200 mm min⁻¹. At least five different replicas of samples were tested and the averaged results of Young's modulus, tenacity, elongation at break, and tensile strength were recorded.

The electrical conductivity of rGO-grafted yarns was measured using a two-probe method. To demonstrate the electromechanical performances, the electrical resistance of the yarns were recorded, while the yarns were extended using a mechanical testing system and the relative changes in electrical resistance were calculated. All electrical and electromechanical tests were carried out at room temperature. Finally, a wearable tactile sensor was prepared by using a V-bed flat machine. Electrical properties and the strain and bending sensibility of the sensor were recorded.

Fastness to washing of the coating was measured to ensure the bonding strength of the rGO nanosheets with PA fibers and the durability of the product. Water washing tests were carried out by washing a functionalized PA fabric (40 × 30 mm²) in 50 ml of aqueous solution of sodium carbonate (0.5 wt%) and ECE (B) phosphate detergent (0.5 wt%) at 25 °C for 15 min followed by several rinsing with distilled water and dried at 90 °C. The surface electrical resistance and k/s values of the sensor were recorded after each washing cycle. A higher k/s value indicates a higher concentration/thickness of the coating. The intensity of reflectance on the surface of the coated yarns varies over different thicknesses of the coating layers.

A Datacolor Check Pro spectrometer (Datacolor CO., USA) was used to record the reflectance spectra of rGO-modified samples in the visible spectral range (λ = 400–700 nm) and the color strength was calculated according to the Kubelka–Munk theory (eqn (2)).^{89,90}

$$\frac{K}{S} - \frac{K_0}{S_0} = \frac{(1-R)^2}{2R} - \frac{(1-R_0)^2}{2R_0} \quad (2)$$

where K_0 and S_0 are the absorption coefficient and the scattering coefficient of the control samples. K and S are the absorption coefficient and scattering coefficient of rGO-modified samples. R and R_0 are reflectance values of the rGO-modified sample and control sample, respectively. The color strength is proportional to the thickness of the rGO layers.

Results and discussion

Streaming potential measurements

The electrokinetic properties of control yarns (PA) and surface charge modified yarns (PA-CS), as well as graphene grafted

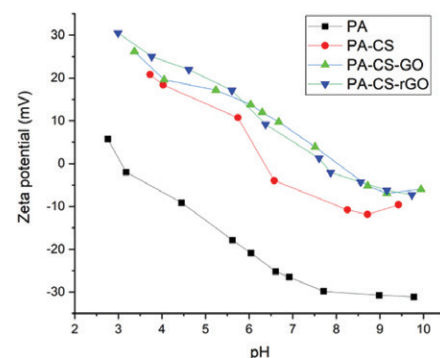


Fig. 3 The dependence of the zeta potentials of the PA yarns on the pH of an aqueous 0.001 M KCl electrolyte solution.

yarns (PA-CS-GO and PA-CS-rGO) were studied using the streaming potential method (Fig. 3). PA yarn displayed an isoelectric point (IEP = pH_{IEP}) of 3.6 and once the yarn was modified with chitosan, the IEP increased to 9.5.

As it has already been studied, because of the ionization of oxygen-containing functional groups of graphene oxide, it carries a negative surface charge in any pH and it exhibits strong pH dependence, starting from −19 mV at pH 1.0 and increasing to −49 mV at pH 8.0.⁹¹ Thus, after electrostatic grafting of GO onto the fibers, the IEP decreases to 8.2 for PA-CS-GO. Reduction of the oxygen-containing functional groups of GO resulted in increasing the IEP to 9.1 for PA-CS-rGO.

Surface morphology

The morphology of the yarns was investigated using scanning electron microscopy (SEM). As shown in Fig. 4(a), there are a few sites with wrinkled GO nanosheets randomly attached to the coating layer (white arrow) in the PA-CS-GO fiber. These nanosheets were detached in the chemical reduction process, resulting in a homogeneous coating Fig. 4(b). After chemical reduction with sodium hydrosulfite and rinsing the yarn, some impurities including sodium compounds were still observed (white arrow).

Chemical compositions

ATR-FTIR analysis was performed on pristine polyamide 6,6 yarns, and alkalized, surface modified and GO-grafted yarns to investigate the chemical composition of the samples.

The FTIR spectra of the polyamide 6,6 samples are normalized to the highest peak at 1629 cm⁻¹ corresponding to the C=O stretching vibration in the amide groups of the polyamide chain. The peak at 3296 cm⁻¹ is related to N-H stretching vibrations and the presence of the band at 1534 cm⁻¹ represents the amide II group of the polyamide chain. The peaks at 3067, 2930, 1198, and 1274 cm⁻¹ are related to C-O stretching of the amides.^{92,93}

After alkali treatment (PA-ALK), the peaks at 1105, 1707, and 1739 cm⁻¹ disappeared. Furthermore, the intensities of the

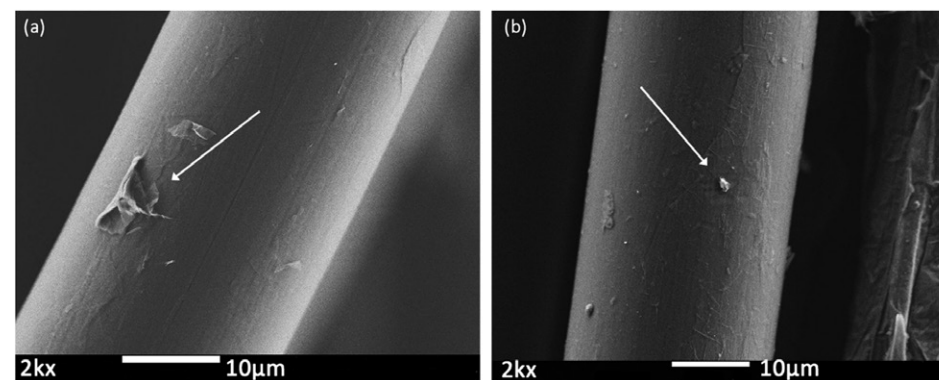


Fig. 4 SEM images of (a) (PA-CS-GO) and (b) (PA-CS-rGO) with 2k \times magnification.

bands at 1275, 1198, and 1534 cm⁻¹ increased after CS treatment (PA-CS) and the intensity of the peak at 1415 cm⁻¹ corresponding to vibrations of the CH₂ groups, decreased. The band at 1534 cm⁻¹ was downshifted to 1528 cm⁻¹ (Fig. 5) and a slight change in the intensity of the N-H stretching band at 3297 cm⁻¹ was observed. The presence of shifted, increased or decreased peaks confirm the change in the chemical structure of the amide functional groups within the polyamide chains.

After modification of the yarns with GO (PA-CS-GO), intensities of the mentioned peaks changed, the peak at 1528 cm⁻¹ was upshifted to 1535 cm⁻¹ and the intensities of the peaks at 1198, 1275, and 1532 cm⁻¹ decreased. This could confirm the chemical bonding between GO nanosheets and modified polyamide 6,6. Once the fiber is chemically reduced (PA-CS-rGO), the peaks at 932, 1174 and 1198 cm⁻¹ disappeared and the intensities of the peaks relating to the N-H stretch at 3296 and

1534 cm⁻¹, C-O stretching of amides at 3067 and 2930 cm⁻¹, and C=O stretching at 1629 cm⁻¹ decreased significantly.

The atomic composition of the surface of the fibers was evaluated using X-ray photoelectron spectroscopy (XPS). Surface chemical composition (in at%) of the PA fiber showed 75% carbon and 25% oxygen. After modification with chitosan (PA-CS), the atomic ratio of carbon increased to 79.5% and the oxygen content decreased to 20.5%. However, no nitrogen was detected on the PA-CS fiber, which could be due to the low concentration of nitrogen (<1) in the chitosan-grafted PA fibers.

Once the fiber is modified with graphene, the atomic ratio (at%) of the oxygen content increased to 25%, while the carbon content decreased to 75%. As expected, after the reduction of the functional groups of graphene oxide, the carbon proportion increased to 82.5% and the oxygen proportion decreased to 17.5%. The wide scan spectra and high-resolution C 1s spectra of the samples are shown in Fig. 6.

The chemical states of the carbon (C 1s peaks) of the samples are shown in Table 1. Once the fiber is modified with chitosan (PA-CS), the proportion of C=C bonding increased from 6% to 12%. As expected, once the fiber is modified with graphene oxide (PA-CS-GO), the intensity of oxidized COO⁻ bonding increased from 7.5% (PA-CS) to 14% (PA-CS-GO) and the proportion of C=C bonding decreased from 12% (PA-CS) to 7.5% (PA-CS-GO). After chemical reduction (PA-CS-rGO), the majority of carbon are in the C-C bond (79%) with a minor amount of oxidized C-O bonding (15.5%).

Tensile properties of the yarns

In order to ensure that chemical functionalization of PA polymer chains does not weaken the strength of the conventional PA yarns, a tensile test was carried out on all the fibers. In the tensile test, five clamped replicas of each sample were subjected to a constant elongation rate to stretch and break the filament, while tensile strength (N), elongation at break (%), modulus (N tex⁻¹), and tenacity (N tex⁻¹) were recorded.

As can be seen in Table 2, the surface modification of the polyamide 6,6 with a dilute acetic solution of CS (PA-CS) did

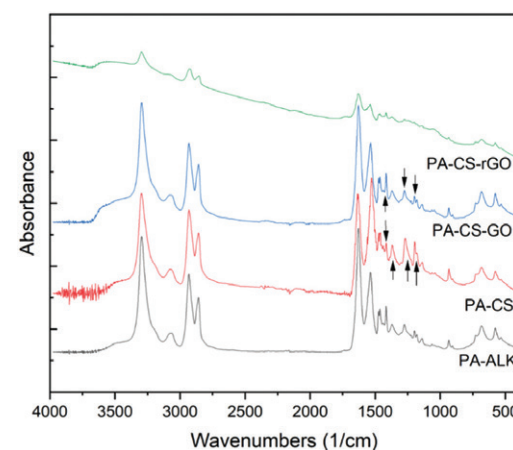


Fig. 5 FTIR spectra (400 to 4000 cm⁻¹) of alkalized polyamide 6,6 (PA-ALK), CS treated polyamide (PA-CS), graphene oxide grafted polyamide (PA-CS-GO) and reduced graphene oxide grafted polyamide (PA-CS-rGO).

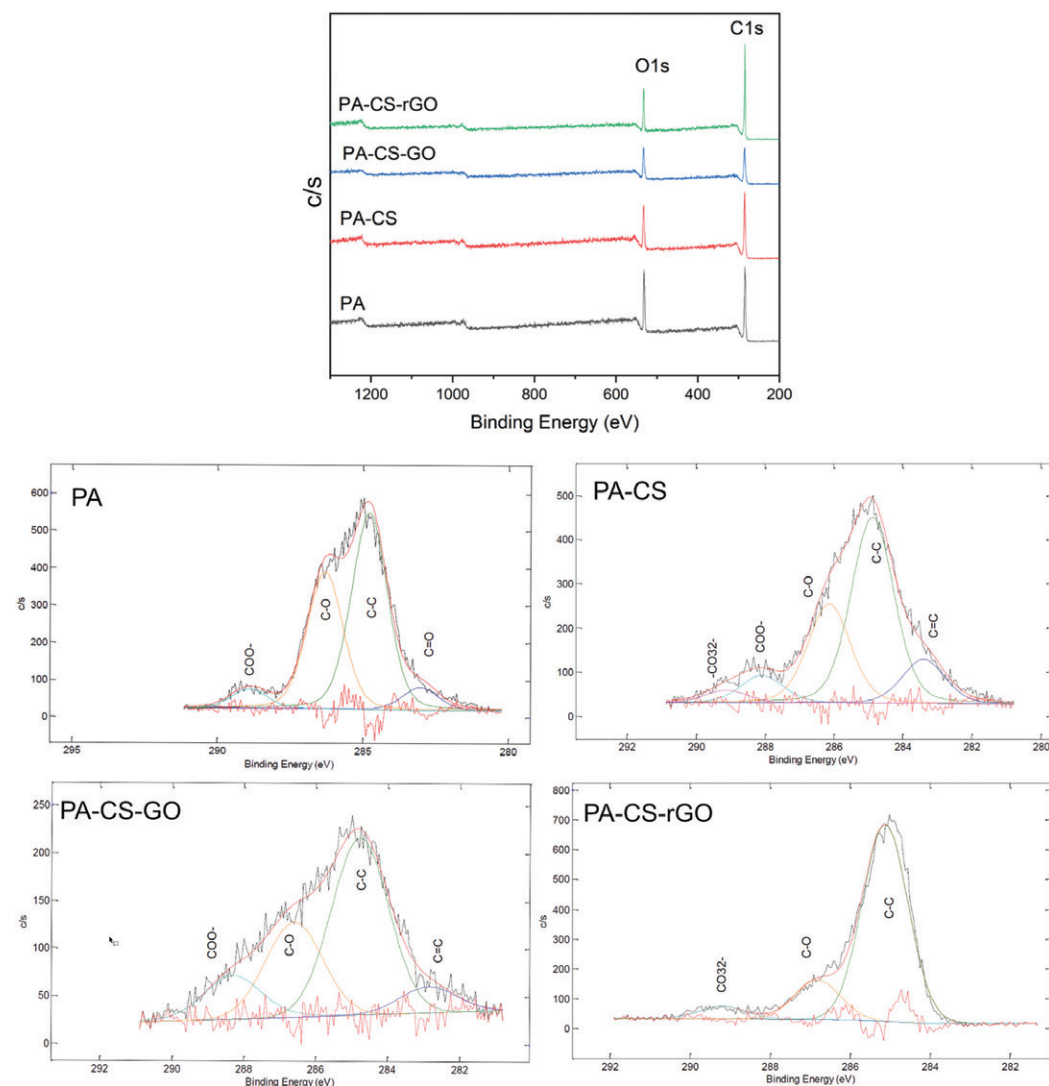


Fig. 6 (a) Wide scan XPS spectra of PA, PA-CS, PA-CS-GO, and PA-CS-rGO samples and (b) high-resolution spectra of C 1s for the samples.

Table 1 The chemical states of carbon (C 1s peaks) and the proportion of the bonds

Sample	283.8 eV (C=C)	285.0 eV (C-C)	286.5 eV (C-O)	289.0 eV (COO ⁻)	289.5 eV (CO ₃ ²⁻)
PA	6.0	53.0	36.5	4.5	—
PA-CS	12.0	50.5	27.0	7.5	3.0
PA-CS-GO	7.5	51.0	27.5	14.0	—
PA-CS-rGO	—	79	15.5	—	5.5

not downgrade the tensile properties of the yarn. For instance, the tensile strengths of pristine polyamide 6,6 and CS-modified

Table 2 Tensile properties of the pristine, surface modified and functionalized polyamide 6,6 yarns

Sample	Tensile strength (N)	Elongation at break (%)	Tenacity (N tex ⁻¹)	Modulus (N tex ⁻¹)
PA	27.82 ± 0.62	49.08 ± 2.26	0.591 ± 0.01	0.883 ± 0.033
PA-CS	27.26 ± 0.38	57.2 ± 2.33	0.58 ± 0.008	0.826 ± 0.033
PA-CS-GO	25.04 ± 0.42	51.9 ± 1.53	0.533 ± 0.009	0.787 ± 0.036
PA-CS-rGO	27.67 ± 0.64	58.9 ± 1.32	0.589 ± 0.013	0.752 ± 0.046

yarns are 27.82 and 27.26 N, and the tenacity values of the yarns are 0.59 and 0.58 N tex⁻¹, respectively. However, elongation

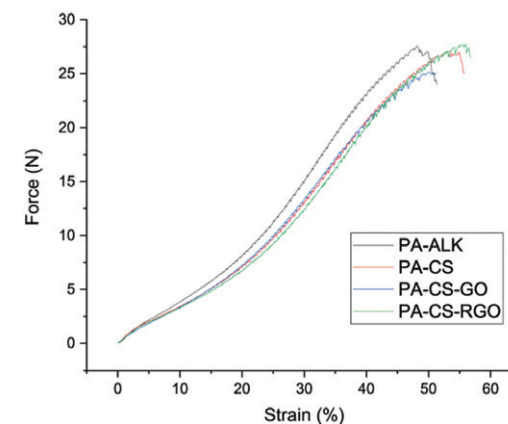


Fig. 7 Typical stress-strain curves of an alkalinized polyamide 6,6 (PA-ALK), chitosan modified (PA-CS), graphene oxide grafted (PA-CS-GO), and chemically reduced (PA-CS-rGO) yarns.

at break and modulus of the yarn change from 49% and 0.88 N tex⁻¹ to 57.2% and 0.82 N tex⁻¹, respectively, for CS-modified yarn, showing higher elasticity.

After the GO-grafting process (PA-CS-GO), an imperceptible decrease in tensile strength (25 N), tenacity (0.53 N tex⁻¹), elongation

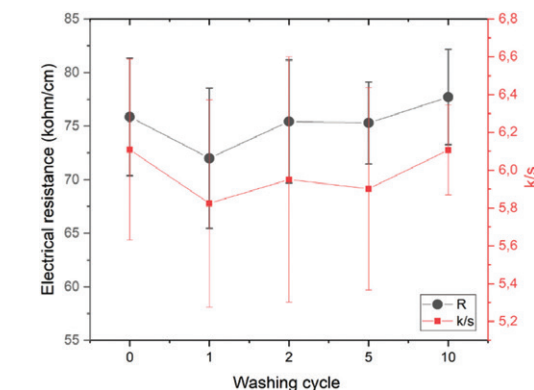


Fig. 9 Surface electrical resistance and k/s values of the fabric after different washing cycles.

at break (51.9%) and modulus (0.78 N tex⁻¹) were observed. However, the chemical reduction process (PA-CS-rGO) does not weaken the tensile strength (27.67 N tex⁻¹) and tenacity (0.58 N tex⁻¹), yet the elongation at break increased to 58.9% and modulus decreased to 0.75 N tex⁻¹. The stress-strain curves of alkalinized polyamide 6,6 (PA), CS-modified (PA-CS), GO-grafted (PA-CS-GO), and rGO-grafted (PA-CS-rGO) yarns are illustrated in Fig. 7.

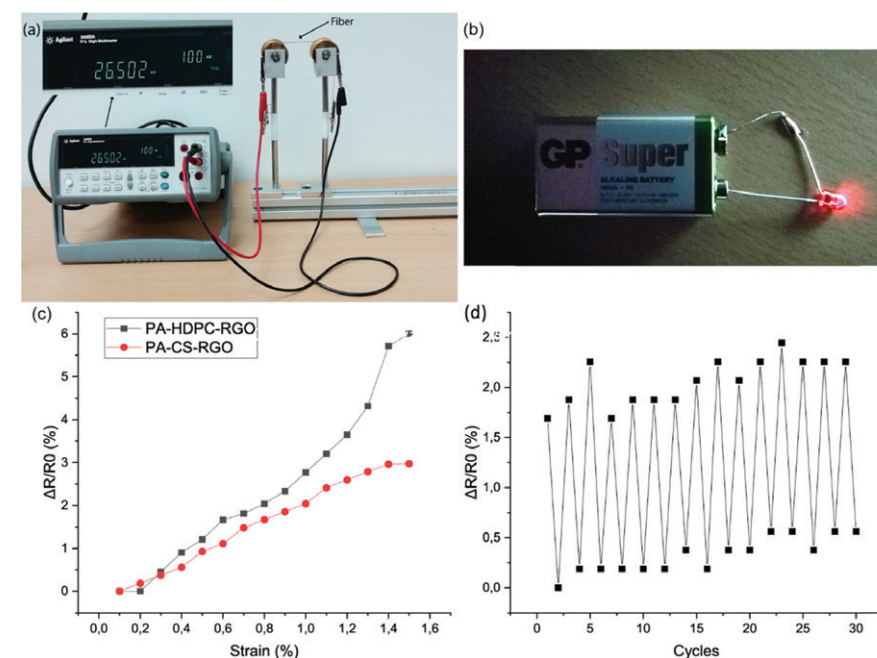


Fig. 8 (a) A two-probe setup for measuring the resistance of the yarns. (b) Emission of an LED lamp by using a conventional polyamide 6,6 yarn, modified with CS and graphene (PA-CS-rGO). (c) Relative change in resistance vs. applied strain for PA-HDPC-rGO and PA-CS-rGO yarns. (d) Relative change in resistance of the PET-CS-rGO yarn vs. cyclic strain of 1%.

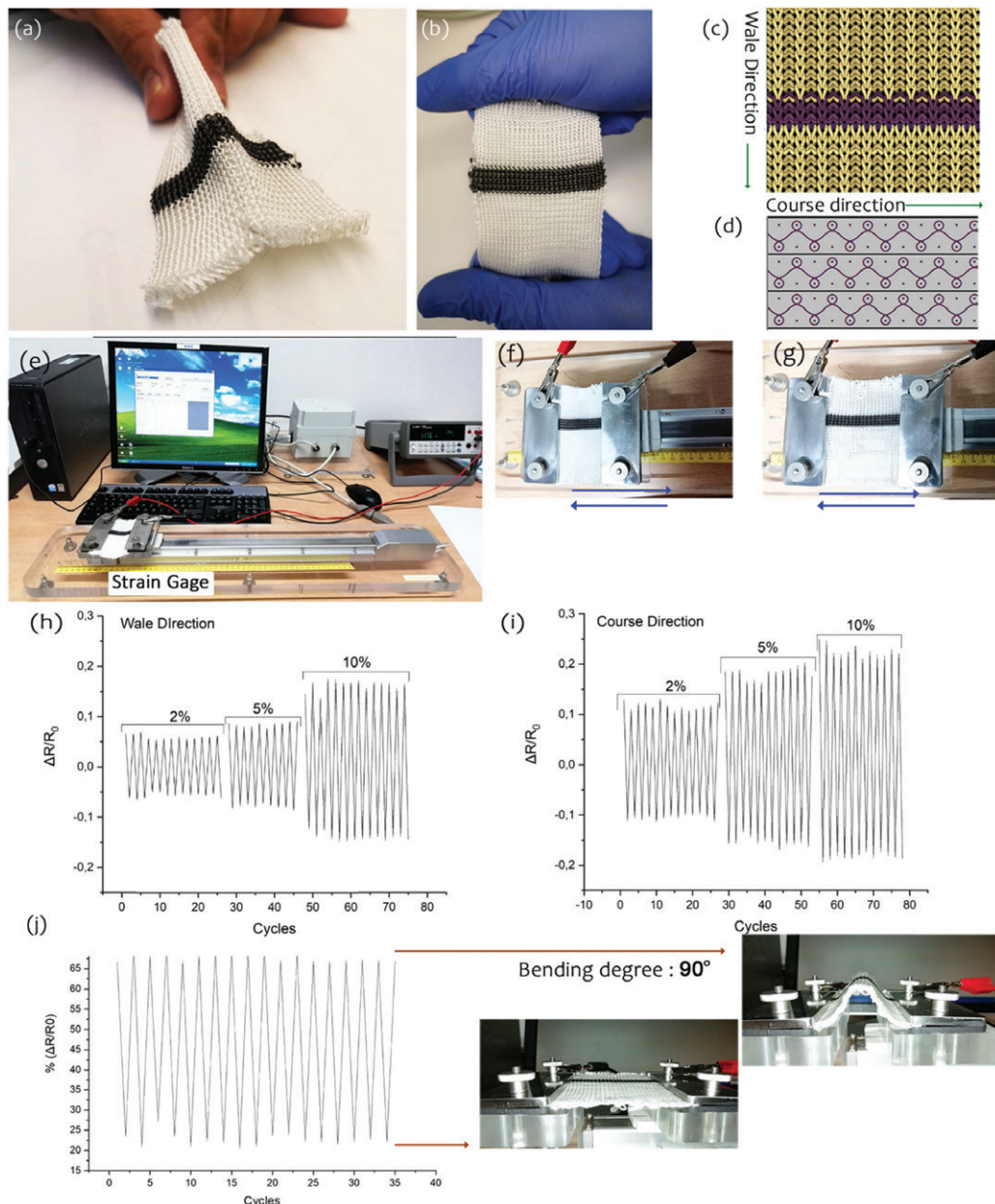


Fig. 10 (a) and (b) Rib 1 × 1 knitted wearable tactile sensor by using PA 6,6 yarn as non-conductive and graphene-grafted PA 6,6 yarn as conductive blocks. Images (c) and (d) show the fabric structure and pattern of rib 1 × 1 knitted fabric. Image (e) is the made-in-house strain gauge controlled by computer software used for the electromechanical characterization. Images (f) and (g) show the sensor in relaxed and 5% strain applied states, respectively. (h) and (i) illustrate the relative percentage change of electrical resistance, while applying a cyclic strain of 2 to 10% in both wale and course directions, respectively. (j) Demonstrates the relative percentage change of resistance at the bending degree of 90° for 20 consecutive cycles.

As the results show, all these slight changes in PA yarns are negligible, and it can be confirmed that the chemical functionalization processes do not downgrade the essential tensile properties of the yarns. This makes these yarns excellent candidates available for use in industrial production processes such as knitting and weaving.

Electrical performances

Electrical conductivity (S m^{-1}) of the rGO-grafted samples was measured via a two-probe method using direct current (DC) electrical resistance measurements (Fig. 8(a)). GO is electrically insulating due to the presence of functional groups on the edges and surface of the GO nanosheets, and chemical reduction of GO is required to exhibit conductive properties. Still, rGO grafted yarns without surface modification (PA-rGO) do not exhibit electrical conductivity, probably due to the weak interactions between GO nanosheets and the filaments of the yarn. Surface modification with CS on polyamide 6,6 (PA-CS-rGO) yarns provide electrical properties with an average conductivity of $3 \times 10^{-2} \pm 0.49 \text{ S m}^{-1}$. Modification of the yarn with HDPC also provides electrical properties, and the average electrical conductivity of HDPC-grafted polyamide 6,6 (PA-HDPC-rGO) was $4 \times 10^{-2} \pm 0.19 \text{ S m}^{-1}$. Both cationic agents show nearly alike electrical performances. The electrical conductivity of the yarns was high enough to light an LED light using a 9 V battery (Fig. 8(b)).

The variation in electrical resistance *versus* applied strain was recorded by applying up to 1.5% strain to the yarns (note that the relative resistance did not increase for an applied strain higher than 1.5%). Fig. 8(c) represents the relative change in resistance *versus* applied strain profiles of PA-CS-rGO and PA-HDPC-rGO yarns and Fig. 8(d) shows the relative change in resistance when a cyclic strain of 1% is applied to PA-CS-rGO yarns. The electromechanical behavior of the yarns strongly depends on cationic agent species and microstructure of the coating. For both polyamide 6,6 samples (PA-CS-rGO and PA-HDPC-rGO), the variation in electrical resistance increased by increasing the strain. However, chitosan shows more stable electrical conductivity below 1.5% applied strain.

Washing fastness

A washing test was applied on the knitted fabric for ten cycles following drying in an oven at 90 °C for 20 min. The electrical resistance and k/s values of the fabric were recorded after the washing cycles (Fig. 9). As shown, the surface electrical resistance of the sample decreases slightly after the first washing cycle (from 75 ± 5.4 to $72 \pm 6.5 \text{ k}\Omega \text{ cm}^{-1}$). This could be due to the removal of impurities. Then, the surface electrical resistance rebounds to 75 ± 3.8 and $77 \pm 4.8 \text{ k}\Omega \text{ cm}^{-1}$ after five and ten washing cycles, respectively. The overall results show that the coating has good fastness to washing and its electrical conductivity is not being influenced, notably, by the washing process.

The k/s value shows a slight change from 6.1 ± 0.4 to 5.82 ± 0.54 , 5.95 ± 0.64 , 5.9 ± 0.53 , and 6.1 ± 0.23 after one, two, five and ten washing cycles, respectively. It shows that the

thickness/concentration of the coating remains almost constant and that the coating has very good fastness to washing.

Preparation of the tactile sensor and the electro-mechanical performance

A hand-powered V-bed rib flat machine, gage size E12, was used to integrate the PA-CS-rGO yarn into a one-to-one rib knitting structure (Fig. 10(d)) to build a tactile sensor. The resulting tactile sensor maintains the flexibility and comfort of a conventional fabric giving it a smooth handle (Fig. 10(a and b)). This makes it an optimal choice for applications in which the fabric is in touch with the human body. The electro-mechanical sensitivity of the sensor was recorded in both the wale and course direction of the fabric (Fig. 10(c)) using a built-in-house strain gauge unit controlled with computer software (Fig. 10(e)).

The sensor shows a stable relative resistance change ($\Delta R/R_0$) of 10% for cyclic 2% strain applied, 20% for cyclic 5% strain applied and almost 28% for cyclic 10% strain applied in the wale direction, and relative resistance change ($\Delta R/R_0$) of 20% for cyclic 2% strain applied, 30% for cyclic 5% strain applied and 35% for cyclic 10% strain applied in the course direction. An one-to-one rib knitted fabric is highly elastic in the course direction, yet less elastic in the wale direction (Fig. 10(h and i)). This makes it to give different resistance-change variations in both directions having higher resistance to strain sensibility in the course direction. Furthermore, a cyclic bending test at 90° was applied to the sensor (Fig. 10(j)) to assure the functionality of the sensor for use in tactile sensor garments. The fabric shows a stable relative resistance change in a cyclic 90° bending test ($\Delta R/R_0 \approx 50\%$).

Conclusions

In this work, we demonstrate that an optimized functionalization process could be applied to conventional textile yarns to build electro-conductive textile elements. The results show that electrically conductive polyamide 6,6 yarns with a diameter as low as 0.06 mm are capable of lighting an LED light using a 9 V battery and being the active part of a tactile sensor. These yarns maintain the physical and mechanical properties of the original yarn retaining its comfort, pliability and smoothness. This makes them excellent candidates to be used together with conventional yarns in knitting and weaving industries to design the cost-effective large-scale production of complex wearable devices and smart garments for a wide range of applications, contributing to the future field of fibretronics.

Conflicts of interest

There are no conflicts to declare.

Acknowledgements

This work was carried out with financial support from the Erling Persson Foundation. A special thanks goes to TEKNO

stiftelsen, the strategic innovation program SIO Grafen, and the Smart Textiles initiative.

References

- 1 N. K. Persson, J. G. Martinez, Y. Zhong, A. Maziz and E. W. H. Jager, *Adv. Mater. Technol.*, 2018, **3**, 1700397.
- 2 A. Schwarz, L. Van langenhove, P. Guermontprez and D. Deguillemont, *Text. Prog.*, 2010, **42**, 99–180.
- 3 L. Guo, T. Bashir, E. Bresky and N. K. Persson, *Smart textiles and their applications*, Elsevier, 2016, pp. 657–693.
- 4 K. B. Cheng, T. H. Ueng and G. Dixon, *Text. Res. J.*, 2001, **71**, 732–738.
- 5 K. B. Cheng, S. Ramakrishna and K. C. Lee, *Polym. Compos.*, 2001, **22**, 185–196.
- 6 T. H. Ueng and K. B. Cheng, *Composites, Part A*, 2001, **32**, 1491–1496.
- 7 A. Lymberis and D. E. De Rossi, *Wearable ehealth systems for personalised health management: state of the art and future challenges*, IOS Press, 2004.
- 8 R. Paradiso, G. Loriga and N. Taccini, *IEEE Trans. Inf. Technol. Biomed.*, 2005, **9**, 337–344.
- 9 D. De Rossi, F. Carpi, F. Lorussi, A. Mazzoldi, R. Paradiso, E. P. Scilingo and A. Tognetti, *Autex Res. J.*, 2003, **3**, 180–185.
- 10 D. De Rossi, F. Carpi, F. Lorussi, R. Paradiso, E. P. Scilingo and A. Tognetti, *Wearable Electronics and Photonics*, 2005, pp. 59–80.
- 11 D. De Rossi, F. Carpi, N. Carbonaro, A. Tognetti and E. P. Scilingo, Electroactive polymer patches for wearable haptic interfaces, *2011 Annual International Conference of the IEEE Engineering in Medicine and Biology Society*, IEEE, 2011, pp. 8369–8372.
- 12 A. R. Bastos, L. P. Da Silva, V. P. Gomes, P. E. Lopes, L. C. Rodrigues, R. L. Reis, V. M. Correlo and A. P. Souto, *Org. Electron.*, 2019, 105401.
- 13 A. Schwarz, J. Hakuzimana and E. P. Gasana, Westbroek and L. Van Langenhove, Gold coated polyester yarn, *Advances in Science and Technology*, Trans Tech Publications Ltd., 2008, vol. 60, pp. 47–51.
- 14 T. Bashir, M. Skrifvars and N. K. Persson, *Polym. Adv. Technol.*, 2012, **23**, 611–617.
- 15 Y. Huang, H. Hu, Y. Huang, M. Zhu, W. Meng, C. Liu, Z. Pei, C. Hao, Z. Wang and C. Zhi, *ACS Nano*, 2015, **9**, 4766–4775.
- 16 J. Bae, M. K. Song, Y. J. Park, J. M. Kim, M. Liu and Z. L. Wang, *Angew. Chem., Int. Ed.*, 2011, **50**, 1683–1687.
- 17 L. Liu, Y. Yu, C. Yan, K. Li and Z. Zheng, *Nat. Commun.*, 2015, **6**, 1–9.
- 18 J. A. Lee, M. K. Shin, S. H. Kim, H. U. Cho, G. M. Spinks, G. G. Wallace, M. D. Lima, X. Lepró, M. E. Kozlov and R. H. Baughman, *Nat. Commun.*, 2013, **4**, 1–8.
- 19 K. Wang, Q. Meng, Y. Zhang, Z. Wei and M. Miao, *Adv. Mater.*, 2013, **25**, 1494–1498.
- 20 Z. Chai, N. Zhang, P. Sun, Y. Huang, C. Zhao, H. J. Fan, X. Fan and W. Mai, *ACS Nano*, 2016, **10**, 9201–9207.

- 21 X. Pu, L. Li, M. Liu, C. Jiang, C. Du, Z. Zhao, W. Hu and Z. L. Wang, *Adv. Mater.*, 2016, **28**, 98–105.
- 22 A. Lund, K. Rundqvist, E. Nilsson, L. Yu, B. Hagström and C. Müller, *npj Flexible Electron.*, 2018, **2**, 1–9.
- 23 S. H. Ji, Y.-S. Cho and J. S. Yun, *Nanomaterials*, 2019, **9**, 555.
- 24 P. Morgan, *Carbon fibers and their composites*, CRC Press, 2005.
- 25 Q. Ke and J. Wang, *J. Materiomics*, 2016, **2**, 37–54.
- 26 Z. Xu and C. Gao, *Mater. Today*, 2015, **18**, 480–492.
- 27 Y. Hu, H. Cheng, F. Zhao, N. Chen, L. Jiang, Z. Feng and L. Qu, *Nanoscale*, 2014, **6**, 6448–6451.
- 28 S. H. Aboutalebi, R. Jalili, D. Esrafilzadeh, M. Salari, Z. Gholamvand, S. Aminorroaya yamini, K. Konstantinov, R. L. Shepherd, J. Chen and S. E. Moulton, *ACS Nano*, 2014, **8**, 2456–2466.
- 29 J. Foroughi, G. M. Spinks, D. Antiohos, A. Mirabedini, S. Gambhir, G. G. Wallace, S. R. Ghorbani, G. Peleckis, M. E. Kozlov and M. D. Lima, *Adv. Funct. Mater.*, 2014, **24**, 5859–5865.
- 30 Y. J. Yun, C. S. Ah, W. G. Hong, H. J. Kim, J.-H. Shin and Y. Jun, *Nanoscale*, 2017, **9**, 11439–11445.
- 31 Y. J. Yun, W. G. Hong, W. J. Kim, Y. Jun and B. H. Kim, *Adv. Mater.*, 2013, **25**, 5701–5705.
- 32 H. Cheng, Y. Hu, F. Zhao, Z. Dong, Y. Wang, N. Chen, Z. Zhang and L. Qu, *Adv. Mater.*, 2014, **26**, 2909–2913.
- 33 X. Xiang, Z. Yang, J. Di, W. Zhang, R. Li, L. Kang, Y. Zhang, H. Zhang and Q. Li, *Nanoscale*, 2017, **9**, 11523–11529.
- 34 H. Matsumoto, S. Imaizumi, Y. Konosu, M. Ashizawa, M. Minagawa, A. Tanioka, W. Lu and J. M. Tour, *ACS Appl. Mater. Interfaces*, 2013, **5**, 6225–6231.
- 35 Y. Zhou, X. Liu, D. Sheng, C. Lin, F. Ji, L. Dong, S. Xu, H. Wu and Y. Yang, *Chem. Eng. J.*, 2018, **338**, 117–125.
- 36 B. Fugetsu, E. Sano, H. Yu, K. Mori and T. Tanaka, *Carbon*, 2010, **48**, 3340–3345.
- 37 J. Ge, H.-B. Yao, W. Hu, X.-F. Yu, Y.-X. Yan, L.-B. Mao, H.-H. Li, S.-S. Li and S.-H. Yu, *Nano Energy*, 2013, **2**, 505–513.
- 38 D. Kongahge, J. Foroughi, S. Gambhir, G. M. Spinks and G. G. Wallace, *RSC Adv.*, 2016, **6**, 73203–73209.
- 39 I. A. Sahito, K. C. Sun, A. A. Arbab, M. B. Qadir and S. H. Jeong, *Electrochim. Acta*, 2015, **173**, 164–171.
- 40 M. Shateri-khalilabad and M. E. Yazdanshenas, *Cellulose*, 2013, **20**, 963–972.
- 41 X. Hu, M. Tian, L. Qu, S. Zhu and G. Han, *Carbon*, 2015, **95**, 625–633.
- 42 K. Krishnamoorthy, U. Navaneethaiyer, R. Mohan, J. Lee and S.-J. Kim, *Appl. Nanosci.*, 2012, **2**, 119–126.
- 43 H. Kim and S. Lee, *Fibers Polym.*, 2018, **19**, 965–976.
- 44 G. Manasoglu, R. Celen, M. Kanik and Y. Ulcay, *J. Appl. Polym. Sci.*, 2019, **136**, 48024.
- 45 H. Kim and S. Lee, *J. Text. Sci. Eng.*, 2017, **54**, 315–326.
- 46 K. Chi, Z. Zhang, J. Xi, Y. Huang, F. Xiao, S. Wang and Y. Liu, *ACS Appl. Mater. Interfaces*, 2014, **6**, 16312–16319.
- 47 N. Karim, S. Afroz, A. Malandraki, S. Butterworth, C. Beach, M. Rigout, K. S. Novoselov, A. J. Casson and S. G. Yeates, *J. Mater. Chem. C*, 2017, **5**, 11640–11648.

- 48 N. Karim, S. Afroz, S. Tan, K. S. Novoselov and S. G. Yeates, *Sci. Rep.*, 2019, **9**, 1–10.
- 49 C. H. Kim, B.-H. Kim and K. S. Yang, *Carbon*, 2012, **50**, 2472–2481.
- 50 Y. Zhang, Y. Wang, J. Jia and J. Wang, *Sens. Actuators, B*, 2012, **171**, 580–587.
- 51 Z. Dong, C. Jiang, H. Cheng, Y. Zhao, G. Shi, L. Jiang and L. Qu, *Adv. Mater.*, 2012, **24**, 1856–1861.
- 52 H. R. Pant, C. H. Park, L. D. Tijing, A. Amarjargal, D.-H. Lee and C. S. Kim, *Colloids Surf., A*, 2012, **407**, 121–125.
- 53 B. Bera, D. Mandal and M. D. Sarkar, *Imp. J. Interdiscip. Res.*, 2016, **2**.
- 54 N. Promphet, P. Rattanarat, R. Rangkipan, O. Chailapakul and N. Rodthongkum, *Sens. Actuators, B*, 2015, **207**, 526–534.
- 55 A. F. De faria, F. O. Perreault, E. Shauly, L. H. Arias Chavez and M. Elimelech, *ACS Appl. Mater. Interfaces*, 2015, **7**, 12751–12759.
- 56 H.-P. Cong, X.-C. Ren, P. Wang and S.-H. Yu, *Sci. Rep.*, 2012, **2**, 1–6.
- 57 Y. He, N. Zhang, Q. Gong, H. Qiu, W. Wang, Y. Liu and J. Gao, *Carbohydr. Polym.*, 2012, **88**, 1100–1108.
- 58 Y. Li, J. Sun, Q. Du, L. Zhang, X. Yang, S. Wu, Y. Xia, Z. Wang, L. Xia and A. Cao, *Carbohydr. Polym.*, 2014, **102**, 755–761.
- 59 B. Fang, L. Peng, Z. Xu and C. Gao, *ACS Nano*, 2015, **9**, 5214–5222.
- 60 L. Chen, Y. He, S. Chai, H. Qiang, F. Chen and Q. Fu, *Nanoscale*, 2013, **5**, 5809–5815.
- 61 Z. Xu and C. Gao, *Acc. Chem. Res.*, 2014, **47**, 1267–1276.
- 62 Z. Xu and C. Gao, *Nat. Commun.*, 2011, **2**, 571.
- 63 Z. Xu, Y. Zhang, P. Li and C. Gao, *ACS Nano*, 2012, **6**, 7103–7113.
- 64 R. Jalili, S. H. Aboutalebi, D. Esrafilzadeh, R. L. Shepherd, J. Chen, S. Aminorroaya-yamini, K. Konstantinov, A. I. Minett, J. M. Razal and G. G. Wallace, *Adv. Funct. Mater.*, 2013, **23**, 5345–5354.
- 65 M. Strååt, S. Toll, A. Boldizar, M. Rigdahl and B. Hagström, *J. Appl. Polym. Sci.*, 2011, **119**, 3264–3272.
- 66 X. Zhang, P. Suresh kumar, V. Aravindan, H. H. Liu, J. Sundaramurthy, S. G. Mhaisalkar, H. M. Duong, S. Ramakrishna and S. Madhavi, *J. Phys. Chem. C*, 2012, **116**, 14780–14788.
- 67 Y. Lu, X. Xiao, Y. Liu, J. Wang, S. Qi, C. Huan, H. Liu, Y. Zhu and G. Xu, *J. Alloys Compd.*, 2020, **812**, 152144.
- 68 B. Kalantari, M. R. Mohaddes Mojtahedi, F. Sharif and R. Semnani Rahbar, *Polym. Compos.*, 2015, **36**, 367–375.
- 69 H.-H. Liu, W.-W. Peng, L.-C. Hou, X.-C. Wang and X.-X. Zhang, *Compos. Sci. Technol.*, 2013, **81**, 61–68.

- 70 F. Meng, W. Lu, Q. Li, J. H. Byun, Y. Oh and T. W. Chou, *Adv. Mater.*, 2015, **27**, 5113–5131.
- 71 X. Ji, Y. Xu, W. Zhang, L. Cui and J. Liu, *Composites, Part A*, 2016, **87**, 29–45.
- 72 C. Hu, X. Zhai, L. Liu, Y. Zhao, L. Jiang and L. Qu, *Sci. Rep.*, 2013, **3**, 2065.
- 73 X. Li, T. Zhao, K. Wang, Y. Yang, J. Wei, F. Kang, D. Wu and H. Zhu, *Langmuir*, 2011, **27**, 12164–12171.
- 74 X. Li, T. Zhao, Q. Chen, P. Li, K. Wang, M. Zhong, J. Wei, D. Wu, B. Wei and H. Zhu, *Phys. Chem. Chem. Phys.*, 2013, **15**, 17752–17757.
- 75 H. Cheng, J. Liu, Y. Zhao, C. Hu, Z. Zhang, N. Chen, L. Jiang and L. Qu, *Angew. Chem., Int. Ed.*, 2013, **52**, 10482–10486.
- 76 M. A. Miankafshe, T. Bashir and N.-K. Persson, *New J. Chem.*, 2019, **43**(17), 6643–6658.
- 77 J. A. Moleon, A. Ontiveros-ortega, E. Gimenez-martin and I. Plaza, *Dyes Pigm.*, 2015, **122**, 310–316.
- 78 H. Bao, Q. Chen, L. Zhang and G. Chen, *Analyst*, 2011, **136**, 5190–5196.
- 79 I. A. Sahito, K. C. Sun, A. A. Arbab, M. B. Qadir and S. H. Jeong, *Carbohydr. Polym.*, 2015, **130**, 299–306.
- 80 A. M. Grancaric, A. Tarbuk and T. Pusic, *Color. Technol.*, 2005, **121**, 221–227.
- 81 T.-S. Choi, Y. Shimizu, H. Shirai and K. Hamada, *Dyes Pigm.*, 2001, **48**, 217–226.
- 82 M. H. V. Baouab, H. Zghida, R. Gauthier and H. Gauthier, *J. Appl. Polym. Sci.*, 2004, **91**, 2513–2522.
- 83 M. Rinaudo, G. Pavlov and J. Desbrieres, *Polymer*, 1999, **40**, 7029–7032.
- 84 A. Jayakrishnan and D. O. Shah, *J. Polym. Sci., Polym. Chem. Ed.*, 1983, **21**, 3201–3208.
- 85 M. Shateri-khalilabad and M. E. Yazdanshenas, *Carbohydr. Polym.*, 2013, **96**, 190–195.
- 86 E. M. Sanders and S. H. Zeronian, *J. Appl. Polym. Sci.*, 1982, **27**, 4477–4491.
- 87 L. M. Olson and M. Wentz, *Text. Chem. Color.*, 1984, **16**.
- 88 S. Salgın, U. Salgın and N. Tuzlali, *Desalin. Water Treat.*, 2016, **57**, 26031–26040.
- 89 E. R. Trotman, *Dyeing and chemical technology of textile fibres*, Wiley, 1984.
- 90 F. M. Mirabella, *Modern techniques in applied molecular spectroscopy*, John Wiley & Sons, 1998.
- 91 D. Li, M. B. Müller, S. Gilje, R. B. Kaner and G. G. Wallace, *Nat. Nanotechnol.*, 2008, **3**, 101.
- 92 D. R. Brezinski, *An infrared spectroscopy atlas for the coatings industry*, Federation of Societies for Coatings Technology, 1991.
- 93 M. P. Gashti, R. Assefipour, A. Kiumarsi and M. P. Gashti, *Prep. Biochem. Biotechnol.*, 2013, **43**, 798–814.

PAPER



Cite this: *Dalton Trans.*, 2020, **49**, 17281

Development of a multifunctional graphene/
Fe-loaded polyester textile: robust electrical and
catalytic properties†

Mohammad Neaz Morshed, ^{a,b,c,d} Milad Asadi Miankafshe, ^{*e,f}
Nils-Krister Persson,^{e,f} Nemeshwaree Behary^{b,c} and Vincent A. Nierstrasz^a

A graphene/Fe loaded polyester fabric (PET) with robust electrical and catalytic properties has been successfully developed for the first time via a simple coating-incorporation method using hyperbranched poly(amidoamine) (PAMAM) dendrimer as the binder. Both graphene oxide (GO/rGO) and zerovalent iron (Fe⁰) nanoparticles were loaded on the polyester fabric surface before and after chemical grafting of PAMAM. Full characterization of fabrics before and after modifications has been performed by sessile droplet goniometry, ζ -potential, K/S coating evenness, SEM, XPS, FTIR, TGA and DSC analyses. The results showed successful and uniform coating of GO/rGO and loading of Fe⁰ on PET and also showed the correlation between the type of chemical moiety responsible for uniform GO coating, high Fe⁰ loading and their electrical and catalytic activities. Sheet resistance (R_{sh}) analysis was carried out to measure the conductivity of the samples. The lowest R_{sh} (corresponding to high conductivity) was found in PET-PAM-rGO-Fe⁰ ($0.74 \pm 0.13 \text{ k}\Omega \text{ sq}^{-1}$) followed by PET-rGO-Fe⁰ ($1.32 \pm 0.18 \text{ k}\Omega \text{ sq}^{-1}$), PET-PAM-rGO ($2.96 \pm 0.08 \text{ k}\Omega \text{ sq}^{-1}$) and PET-rGO ($3.41 \pm 0.34 \text{ k}\Omega \text{ sq}^{-1}$). Furthermore, Fe⁰-loaded samples were found to be effective in the catalytic removal of toxic water pollutants (crystal violet dye) with ~99% removal of pollutants in around one hour, as observed by UV-vis spectroscopy. The relatively high electrical conductivity and catalytic activity of PET-PAM-rGO-Fe⁰ are related to the role played by PAMAM in the uniform rGO coating and high Fe⁰ loading. These findings are of great importance as they allow envisaging the development of multifunctional textiles for combined smart and green chemistry application.

Received 21st September 2020,

Accepted 26th October 2020

DOI: 10.1039/d0dt03291c

rsc.li/dalton

1. Introduction

In recent years, functionalized textiles have emerged as tools for various applications in flexible electronics, energy storage systems, health monitoring and environmental remediation systems.^{1–5} Robustness, high elasticity, mechanical flexibility,

low cost and lightweight properties of functional textiles have made them the ideal choice for many intricate applications.⁶

However, the functionalization of technical textiles for environmental remediation application often becomes problematic. In this regard, several studies have suggested the loading of conductive and eco-friendly materials such as carbon nanotubes (CNT),⁷ graphite, graphene oxide (GO), and reduced graphene oxide (rGO)^{8–11} on the textile surface to replace metallic wires. Such an approach maintains the pliability and stability of textiles while introducing conductive surfaces.¹⁰

Among them, GO and rGO are attracting special attention due to their eco-friendliness, well-defined microenvironments, high electrical and thermal conductivity, high flexibility as well as good thermal and chemical stability.^{12–15} However, non-uniform dispersion of GO/rGO on the textile surface, low binding and fixation, as well as poor washing fastness limit the potential of GO/rGO based e-textiles. It has been reported that¹⁶ the anionic character of most textiles and GO/rGO introduces repulsive interactions between them and

^aTextile Materials Technology, Department of Textile Technology, The Swedish School of Textiles, Faculty of Textiles, Engineering and Business, University of Borås, SE-50190 Borås, Sweden

^bEcole Nationale Supérieure des Arts et Industries Textiles (ENSAT), GEMTex Laboratory, 59056 Roubaix, France

^cUniversité de Lille, Nord de France, F-59000 Lille, France

^dCollege of Textile and Clothing Engineering, Soochow University, 215006 Suzhou, China

^eThe Swedish School of Textile, Polymeric E-textiles, University of Borås, SE-501 90 Borås, Sweden. E-mail: milad.asadi@hb.se; Tel: +46763319111

^fSmart Textiles, University of Borås, SE-501 90 Borås, Sweden

† Electronic supplementary information (ESI) available. See DOI: 10.1039/d0dt03291c

causes non-uniform distribution of the latter on textiles. Our previous studies have reported that modification of polyester and polyamide fabrics with cationic agents enhances the uptake, uniformity and stability of GO due to the ionic interaction between the positively charged polyester surface and the negatively charged graphene oxide.^{11,16}

Poly(amidoamine) (PAMAM) dendrimer is an eco-friendly hyperbranched cationic polymer with explicit surface functional groups capable of forming complexes between textiles and GO/rGO *via* covalent and non-covalent interactions.¹⁷ Various studies have reported the effectiveness of PAMAM in binding functional materials on the support matrix.^{18–21} N. A. S. Omar *et al.* (2020)²² reported the presence of strong interactions between GO/rGO and PAMAM in a NH₂rGO–PAMAM nanocomposite. However, to the best of our knowledge PAMAM as a binder for GO coating on textiles has not been considered so far.

Although a uniform coating is a precondition for better conductivity in e-textile application, there is another challenge of graphene-based e-textiles that requires equal attention: reduced graphene oxide suffers from the loss of electrical conductivity due to the defects in the crystal structure and partial restoration of the sp² structure of graphene during the harsh reduction process.²³ Therefore, graphene-based e-textiles are not suitable for applications where very high electrical conductivity is required. Hence, the idea of doping metal nanoparticles in graphene coating has been introduced.²⁴ The two-dimensional honeycomb structure of GO provides a well-defined microenvironment for metal nanoparticle loading.²⁵ The addition of metal nanoparticles such as Fe⁰ to graphene-coated polyester textiles can improve the conductivity of e-textiles. Iron doped graphene-based e-textiles have been reported to have a wide range of applications in the semiconductor industry. However, catalytic application of such materials in environmental remediation has been frequently overlooked. Loading of Fe⁰ introduces additional functionality as a fibrous catalyst, which is promising for environmental remediation application as reported in the literature.^{26–29}

Here in this study reports a potential approach for the development of multifunctional technical textile with electrical and catalytic properties. Hyperbranched PAMAM dendrimer (serving as both cationic and crosslinking agent) has been used to increase the robustness of the functionality through uniform coating of graphene oxide and stable loading of Fe⁰ on a polyester fabric. This study is the first effort of such an approach. Physical and analytical characterization of the resultant materials by means of sessile droplet goniometry, ζ-potential, HR-SEM, FTIR, TGA, DSC, XPS and spectrophotometric analyses were carried out. The electrical properties of the materials were evaluated through sheet resistance (*R_{sh}*) analysis using the 4-probe method. The catalytic properties were studied through catalytic reduction of crystal violet dye in the presence of NaBH₄. The role of desired surface modification of polyester fabric with cationic PAMAM has also been discussed based on above mentioned analysis.

2. Experimental

2.1. Chemicals

Hyperbranched PAMAM dendrimer, petroleum ether, ethanol (C₂H₆O), hydrogen peroxide (H₂O₂), iron(III)-chloride-hexahydrate (FeCl₃·6H₂O), sodium tetrahydroborate (NaBH₄), sodium hydroxide (NaOH), ethanol (Et-OH) and crystal violet dye (CAS no. 548-62-9) were purchased from Sigma-Aldrich Ltd. A commercial aqueous dispersion of graphene oxide (4.0 g L⁻¹) was purchased from Graphenea S.A., Spain. All purchased chemicals used in this study were of analytical grade and used as received. The chemical structures of PAMAM dendrimer, crystal violet dye, GO and rGO nanosheets are shown in Fig. 1.

2.2. Polyester nonwoven fabric

The polyester nonwoven fabric used in this study was fabricated in the Swedish School of Textiles (the University of Borås) based on a web of cylindrical polyethylene terephthalate fibers (average diameter, 12 μm) formed by carding and consolidated by needle punching (mechanical entanglement of fibers into the nonwoven fabric by repetitive penetration of barbed needles). The physical characteristics of the fabricated nonwovens are displayed in Table S1 of ESI.†

Prior to surface activation, dirt, dust, contaminants and spinning oil in the fabricated polyester nonwoven fabrics removed by a series of cleaning steps including the Soxhlet extraction method as described elsewhere.^{24,30} The removal of impurities was performed in three (03) steps and successively assessed by comparing the surface tension of rinsed water (from a PET rinsing bath) with that of freshwater (the surface tension of freshwater is 72.6 mN m⁻¹, and if the surface tension of rinsed water is close to that of freshwater it refers to a high degree of cleanliness).³¹

2.3. Surface activation and dendrimer grafting on polyester nonwoven fabrics

A two-step surface activation and functionalization of polyester nonwoven fabrics were performed as follows:

(a) The smooth hydrophobic fiber surface of the polyester nonwoven fabric was modified into a rough hydrophilic surface (altered surface property and increased wettability) through an alkaline hydrolysis process as described in the literature.¹⁶ Typically, the nonwoven fabric was constantly stirred in an alkaline bath containing 12 wt% sodium hydroxide and distilled water (1 : 50) at 60 °C for 90 min. Here, the polyester fiber underwent a nucleophilic substitution reaction during which chain scission of PET occurred, resulting in the formation of hydroxyl and carboxylic end groups, which improve the hydrophilic properties of the surface. The modified nonwoven fabric (termed PET) was then rinsed/neutralized with distilled water, filtered and dried at 90 °C.

(b) The freshly activated polyester nonwoven fabric was further modified using hyperbranched PAMAM dendrimer which consists of an ethylenediamine core and tertiary amine branches, favorable for the incorporation of zerovalent iron

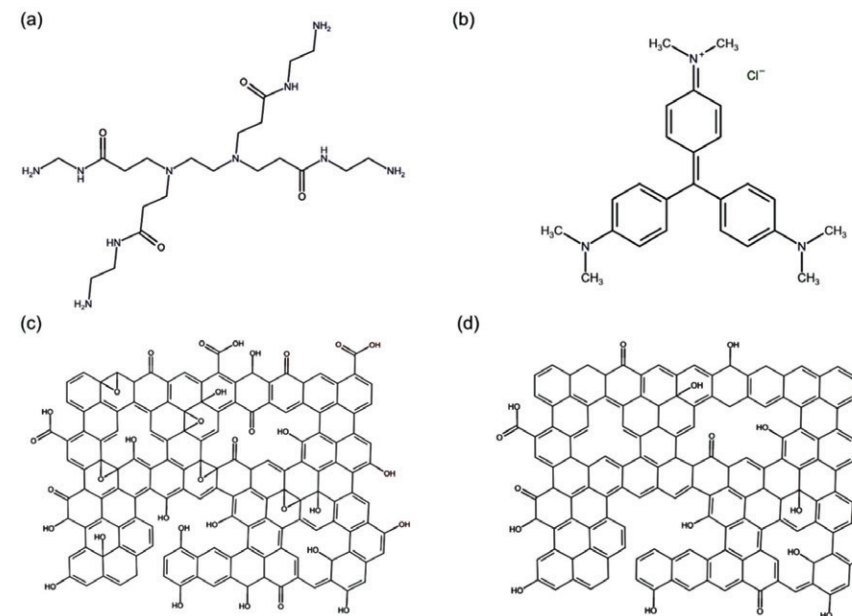


Fig. 1 Chemical structure of (a) hyperbranched PAMAM dendrimer consisting of an ethylenediamine core and tertiary amine branches; (b) crystal violet dye; (c) graphene oxide (GO) and (d) reduced graphene oxide (rGO).

nanoparticles (Fe⁰) and graphene oxide (GO/rGO) by a chemical grafting method as described in the literature.^{32–34} Typically, the PET nonwoven fabric was immersed in an ethanol/water (3 : 1 v/v) bath for 4 h at 70 °C in an atmospheric air chamber. The resultant material termed PET-PAM was then rinsed, filtered and dried at 60 °C overnight.

2.4. GO coating and Fe⁰ loading on polyester nonwoven fabrics

Scalable coating of graphene oxide (also reduced graphene oxide) and loading of zerovalent iron nanoparticles on the

polyester fabric (with or without dendrimer grafting) were achieved through dip coating and an *in situ* reduction-immobilization method (as illustrated in Fig. 2). In the first step, the PET fabric was dipped in an ultra-sonicated (for 30 min) aqueous dispersion of GO (0.4 wt%; pH = 3; L/R 1 : 100) at 45 °C for 30 min under mild stirring. The resultant PET-GO and PET-PAM-GO were oven-dried at 90 °C for 90 min. In the second step, iron particles were loaded and stabilized in the GO incorporated polyester fabric by using FeCl₃·6H₂O as the precursor.^{27,34} For that, the GO modified samples were dipped in a solution containing iron precursor (0.6 wt%), water (75%)

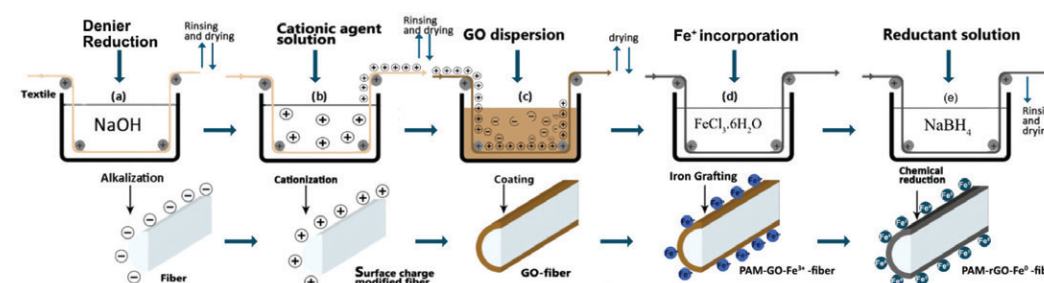
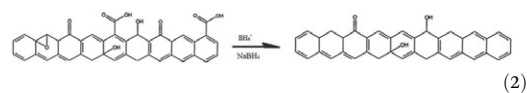
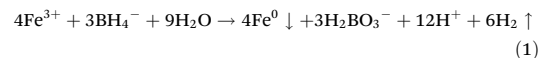


Fig. 2 Schematic illustration of (a) alkalization of polyester fibers; (b) PAMAM-grafting; (c) incorporation of GO; (d) incorporation of Fe³⁺ (e) *in situ* immobilization of rGO and Fe⁰.

and ethanol (25%) (L/R 1 : 100) for 4 h under constant magnetic stirring at room temperature. The resultant PET-GO-Fe³⁺ and PET-PAM-GO-Fe³⁺ were immediately reduced to PET-rGO-Fe⁰ and PET-PAM-rGO-Fe⁰ respectively (according to reactions (1) and (2)) by using NaBH₄ aqueous solution (5 mM, L/R 1 : 50) at 95 °C for 45 min under stirring. The resultant fabrics were then rinsed with warm ultrapure water, dried at 70 °C for 90 min, and then stored in an O₂-free desiccator.



2.5. Characterization of materials

2.5.1. Sessile droplet goniometry. In order to characterize the surface tension of the modified fabric, contact angle measurement was carried out with an optical tensiometer (Attension theta, Biolin scientific CO., Sweden). Typically, the sample was placed on the sample stage of the instrument. The stage was adjusted to the desired height as viewed using a camera, and the a mounting syringe contained distilled water. A 5 µL water droplet was dropped on the surface of the textile sample and the droplet was filmed for 10 s. The data were collected with an automatic data collection panel of a Theta Optical Tensiometer and the analysis of the water droplet was performed using the OneAttension software and the Young–Laplace equation.³⁵ The software was able to fit the Young–Laplace equation to the shape of the droplet accurately considering all of the points of the drop profile over a period of time (10 s). All experiments were performed in triplicate and the mean contact angle was taken into consideration.

2.5.2. Electrokinetic measurements. Electrokinetic measurements were carried out to determine the ζ-potential values of fabrics as a function of the pH values of the electrolyte solution (0.001 M KCl). The measurement was carried out using the streaming potential method as described in our previous report,¹⁶ in which a liquid is forced to flow through two parallel plates containing the textile samples, and a streaming potential is generated (Surpass, Anton Paar AB., Sweden). 0.01 M HCl and 0.01 M NaOH were used to adjust the pH values of the electrolyte solution. The zeta potential values were calculated using the Helmholtz–Smoluchowski equation³⁶ (eqn (1)).

$$\zeta = \frac{dl_{\text{str}}}{d\Delta p} \times \frac{\eta}{\epsilon \times \epsilon_0} \times \frac{L}{A} \quad (1)$$

where $dl_{\text{str}}/d\Delta p$ is the slope of streaming current vs. differential pressure, η is the electrolyte viscosity, ϵ represents the dielectric coefficient of the electrolyte, ϵ_0 represents the permittivity, L is the length of the streaming channel and A is the cross-section of the streaming channel.

2.5.3. Microscopic analysis. The surface morphologies of treated and pristine PET were observed by scanning electron microscopy (SEM) using a ZEISS EVO15, MEB HR ZEISS Sigma 300 electron microscope, and a digital optical microscope (OM) from Dino-Lite. Prior to SEM imaging, all samples were metalized with conductive materials (gold) using a Biorad E5200 device. The average fiber diameter and particle size of materials were investigated from HR-SEM images using image analysis software ImageJ1.40G, as described in our previous studies³⁴ and the corresponding size distribution histograms and standard deviation were obtained. In the OM, the samples were placed firmly in the sample stand. The lens distance and focus of the OM were adjusted by using a control wheel mounted on the top of the instrument prior to capturing images by using the Dino capture 2.0 software.

2.5.4. The color strength and the coating evenness measurement. A Datacolor Check Pro spectrum (Datacolor Co., USA) was used to obtain reflectance spectra in the visible spectral range ($\lambda = 400\text{--}700$ nm) and the color strength at a wavelength of maximum absorbance (420 nm) was calculated according to the Kubelka–Munk theory (eqn (2)).^{37,38}

$$\frac{K}{S} - \frac{K_0}{S_0} = \frac{(1-R)^2}{2R} - \frac{(1-R_0)^2}{2R_0} \quad (2)$$

where K_0 and S_0 are the absorption and scattering coefficients of the control sample, respectively. K and S are the absorption and scattering coefficients of the modified samples, respectively. R and R_0 are the reflectance of the modified and control samples, respectively. The color strength is proportional to colloidal dye uptake as illustrated in eqn (3).

$$\Delta \frac{K}{S} = k\Delta C \quad (3)$$

where C is the dye concentration and k is a constant.

In order to study the distribution of the coating, the color properties of the samples were expressed in terms of CIELab color space values. The total color change (ΔE) of each sample was investigated exclusively based on the CIE and CMC systems. ΔE in the CIE system is obtained using eqn (4).^{39,40}

$$\Delta E_{\text{ab}}^* = \sqrt{(L_2^* - L_1^*)^2 + (a_2^* - a_1^*)^2 + (b_2^* - b_1^*)^2} \quad (4)$$

where a^* expresses the green–red color range, b^* represents the blue–yellow color range, and L^* expresses the brightness–darkness of the color.

2.5.5. X-ray photoelectron spectroscopy (XPS). XPS study was carried out using a spectrophotometer (PHI 5500 ESCA, Physical Electronics INC., USA) equipped with a monochromatic aluminum (Al) source (photon energy = 1486.6 eV). The binding energy (BE) positions were associated with reference to an adventitious carbon peak (C 1s = 285.0 eV) before data analysis. Due to insufficient conductivity, an electron neutralizer was used to compensate for the charge. Survey scan for the compositional evaluation (energy range of 0 to 1100 eV; step size of 0.4 eV per step), and narrow scan for the chemical

state analysis with the selected range for individual elements and a step size of 0.1 eV per step were performed.^{41–44}

2.5.6. Fourier transform infrared (FTIR) spectroscopy. FTIR chemical analysis of the pristine and modified polyester nonwoven were performed using an FTIR spectrometer (Nicolet iS10, Thermo-Fisher Scientific Co., USA) to investigate the possible changes in the surface functional properties of the materials. Spectra were obtained in the wavenumber range of 400 cm^{−1} to 4000 cm^{−1}. The samples were drilled before IR analysis, and background spectra were recorded in air.

2.5.7. Thermogravimetric analysis (TGA). TGA demonstrates the thermal degradation of the studied sample by measuring the change in the mass of the sample upon heating, giving a controlled temperature gradient. Thermogravimetric curves are plotted in integral (relative mass in % of initial mass; TG) and differential (a derivative of TG curve over time; DTG curves) forms. The peak of the DTG curve represents T_{max} of the composition and the temperature corresponding to 5 wt% degradation in the TG curve is noted as T_{onset} . Approximately 10 mg of each sample was placed in a platinum crucible and the TG and DTG curves were obtained (TGA Q500, TA Instruments Co., UK) under nitrogen flow (40 cm³ min^{−1}) from 25 °C to 600 °C at a linear heating rate of 20 °C min^{−1}.

2.5.8. Differential scanning calorimetry (DSC). DSC is a key technique to correlate temperatures with the specific physical properties of substances and to directly determine the enthalpy associated with the process of interest.⁴⁵ DSC measurement (DSC Q2000, TA Instruments Co., UK) was performed under a nitrogen atmosphere on approximately 5 mg of each sample. The samples were heated from 25 to 200 °C in aluminum pans at a heating rate of 10 °C min^{−1}, held under isothermal conditions for 2 min to destroy its anisotropy and cooled down at a cooling rate of 10 °C min^{−1} to 25 °C. Then it was heated up to 200 °C at the same heating rate. All thermal parameters were calculated during the second heating scan.

2.6. Method to study the electrical properties of the polyester nonwoven fabric

The electrical conductivity of the modified polyester fabric was measured by the 4-probe method (works by bringing four equally spaced co-linear probes in contact with the material) using tungsten probes and a 34401A Digital Multimeter, 6½ Digit (Keysight Technologies Inc.). Typically, the samples were placed firmly under the probes, a direct current is applied between the two outer probes (1 and 4), and the voltage drop is measured between the two inner probes (2 and 3). The sheet resistance (R_{sh}) of the samples was calculated from direct current (DC) electrical resistance measurement using eqn (5). However, it should be noted that the most accurate measurements are taken from the centre of the sample.

$$R_{\text{sh}} = \frac{\pi}{\ln(2)} \frac{\Delta V}{I} \quad (5)$$

Here, R_{sh} is the sheet resistance, ΔV is the change in the voltage measured between the inner probes, and I is the

current applied between the outer probes. The sheet resistance is expressed in the units $\Omega \text{ sq}^{-1}$, or “ohms per square”, to differentiate it from the bulk resistance. The thickness of the measured material and sheet resistance were used in eqn (6) to calculate the resistivity of the material:

$$\rho = R_{\text{sh}} \cdot t \quad (6)$$

where ρ is the resistivity and t is the sheet thickness in cm.

2.7. Method to study the catalytic properties of the polyester nonwoven fabric

The catalytic performances of the treated and untreated polyester nonwoven fabric were studied through the catalytic removal of crystal violet dye (in aqueous solution) in the presence of NaBH₄. An UV/Visible spectrophotometer was used to monitor the removal performance. Toxicity reduction analysis was carried out through COD analysis. The recyclability and reusability of the nonwovens were also studied.

2.7.1. Color removal. The dye removal reaction was carried out in a quartz cuvette placed in a UV-visible spectrophotometer (Thermo Scientific™ Evolution 201 UV-Vis spectrophotometer) and containing 2 mL of dye solution (50 mg L^{−1}), 0 to 700 mg L^{−1} nonwoven fabric and 0.5 ml of NaBH₄ (0.1 M). The instant-to-initial absorbance ratio of crystal violet solution (A/A_0) was determined at different time intervals. Thus, the changes in A/A_0 values allowed the assessment of progress in color removal. The color removal or conversion percentage was calculated according to the concentration at predetermined time intervals by using eqn (7)⁴⁶ referring to the absorbance calibration curve of the known standard solution.

$$\text{Conversion}(\%) = \frac{C_0 - C}{C_0} \times 100 \quad (7)$$

where, C_0 = initial concentration of the colorant solution, C = concentration of the colorants at different time intervals.

2.7.2. Toxicity reduction study. The toxicity reduction of water after removal of dyes was studied through chemical oxygen demand (COD) analysis according to the ASTM D1252-06 (B) method using COD vials provided by CHEMetrics, Inc. (USA) similar to the method reported earlier.³ The result was presented as parts per million (mg L^{−1}) and calculated using the following equation (eqn (8)).

$$\text{COD (mg L}^{-1}\text{)} = (23\,010 \times \Delta_{620}) \times 3 \quad (8)$$

where, Δ_{620} represents the absorption difference (at λ_{620} nm) of the vials after digestion of the water sample at 150 °C for 2 h.

2.7.3. The recyclability and reusability study of the nonwoven catalysts. After completion of removal of crystal violet dye, the nonwovens were removed from the solution and washed with distilled water before reuse for another dye removal cycle. The samples were tested to evaluate their potential recyclability and reusability in the catalytic system under the same experimental conditions.

3. Results

Table 1 summarizes the description of the modification and terminology of the samples studied in this report. The results section has been divided into two parts: (1) evidence of surface modification of polyester nonwoven fabrics by coating of graphene oxide and loading of zerovalent iron nanoparticles and (2) analysis of the electrical and catalytic properties of the resultant polyester nonwoven fabrics.

Part 1: Evidence of surface modification of polyester nonwoven fabrics by coating of graphene oxide and loading of zerovalent iron nanoparticles

3.1. Sessile droplet goniometry analysis

The wettability of all samples was studied through sessile-drop goniometry, which hence reflects the surface chemical properties, roughness and diffusion resistance before and after respective surface modifications. Fig. 3 shows the optical image of sessile water droplets deposited on the surface of the polyester nonwoven fabric and quantitative analysis of the corresponding water contact angle. It can be seen that the water contact angle of the pristine polyester that was used in this study was as high as 138°, indicating the characteristic hydrophobic nature of the polyester fabric, which is higher than that of the single polyester fiber ($\theta_{\text{H}_2\text{O}} = 80^\circ$).

However, after alkaline hydrolysis of the nonwoven fabric, the water contact angle reduced to $\theta_{\text{H}_2\text{O}} = 0^\circ$ indicating an increase in the hydrophilic properties of the surface due to the formation of hydroxyl (–OH) and carboxylic (–COOH) end groups. A nucleophilic substitution reaction with chain scission of PET occurred. However, PAMAM dendrimer that consists an ethylenediamine core (and tertiary amine branches) tends to provide a hydrophobic surface ($\theta_{\text{H}_2\text{O}} = 126^\circ$) which is consistent with the previous literature while providing favorable surface functional groups necessary for stable GO and Fe^0 incorporation. The analysis further shows that while graphene oxide (GO) provides a surface with sufficient hydrophilic characteristics ($\theta_{\text{H}_2\text{O}}$ of PET-GO is 36° and $\theta_{\text{H}_2\text{O}}$ of PET-PAM-GO is 48°) the reduced graphene oxide leads to intensely hydrophobic surfaces ($\theta_{\text{H}_2\text{O}}$ of PET-rGO is 122° and $\theta_{\text{H}_2\text{O}}$ of PET-PAM-rGO is 126°). However, an interesting surface property was observed for Fe^0 grafted samples showing strong hydrophilic characteristics, which can be due to the presence

of iron particles in metal or oxide form. Iron particles show well established hydrophilic properties as explained in a number of previous studies.^{32,47}

3.2. Electrokinetic measurements (ζ -potential analysis)

The isoelectric point ($\text{iep} = \text{pH}|\zeta = 0$) to determine the ζ -potential values of the pristine and modified polyester fabric has been observed by electrokinetics and measured as the streaming potential. The summary of ζ -potential analysis of the samples is displayed in Fig. 4. It can be seen that the isoelectric point of pristine polyester fibers was recorded at $\text{pH} = 3.9$ which means that a negative surface charge will be observed for the polyester fibers at pH higher than 3.9. Due to further addition of –OH and –COOH groups upon alkaline hydrolysis of the PET fibers (PET), the surface charge and isoelectric point became further negative starting from -6.89 mV at $\text{pH} = 3.4$ down to -49.23 mV at $\text{pH} = 9.9$ (see Fig. 4).

Polyamidoamine (PAMAM) dendrimer which consists of an ethylenediamine core and tertiary amine branches results in a positive surface charge. Upon grafting of PAMAM on PET the surface charge increases to $+52.31$ mV at $\text{pH} = 3.7$. The isoelectric point of PET-PAM was recorded at $\text{pH} = 8.2$. This can be due to the fact that, after dendrimer grafting, the degree of –COOH and –OH groups decreases while that of $-\text{NH}_2$ surface functional groups increases. The positive charge of PAMAM grafted PET may facilitate the grafting of the negatively charged graphene compared to pristine polyester. On the other hand, although graphene oxide has been reported to demonstrate a negative surface charge at any pH due to the ionization of oxygen-containing functional groups, here (for PET-PAM-GO) the mutual presence of PAMAM and graphene oxide on the surface showed a negative surface property with an isoelectric point at $\text{pH} = 4.8$. The zeta potential value was found to be initially $+10.35$ mV at $\text{pH} = 3.2$ which reduced to -46.88 mV at $\text{pH} = 9.9$. A negative surface containing PAMAM dendrimer and graphene oxide may pose an ideal environment for robust electrostatic incorporation of cationic iron particles (Fe^{3+}) to improve the electro-catalytic properties of polyester nonwoven fabrics. Upon incorporation of Fe^{3+} and GO followed by reduction to Fe^0 and rGO respectively, the isoelectric points of PET-PAM-rGO and PET-PAM-rGO- Fe^0 shifted to $\text{pH} = 7.2$ and $\text{pH} = 7.0$ respectively signifying that an increase in the

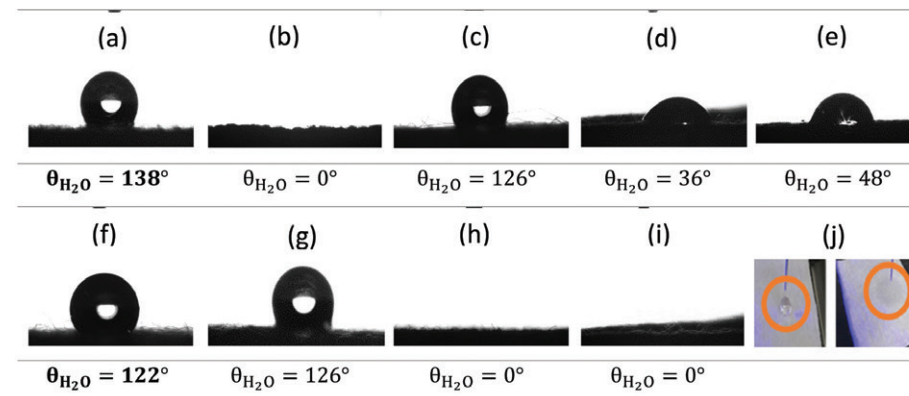


Fig. 3 Contact angle measurement analysis of (a) pristine PET, (b) PET, (c) PET-PAM, (d) PET-GO, (e) PET-PAM-GO, (f) PET-rGO, (g) PET-PAM-rGO, and (h) PET-rGO- Fe^0 , (i) PET-PAM-rGO- Fe^0 and (j) digital image representing the wettability of the nonwoven before (left) and after (right) surface activation.

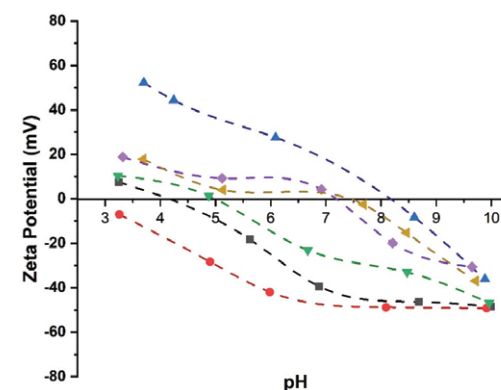


Fig. 4 ζ -potential analysis of pristine PET (■), PET (●), PET-PAM (▲), PET-PAM-GO (▼), PET-PAM-rGO (◆) and PET-PAM-rGO- Fe^0 (●) as a function of the pH values of the electrolyte solution (0.001 M KCl).

zeta potential can be due to the reduction of oxygen-containing groups during the reduction reaction.

3.3. Morphological analysis and size distribution of iron particles

The surface morphologies of the polyester nonwoven before and after coating layers of graphene oxide and iron nanoparticles were investigated using scanning electron microscope (SEM) and digital optical microscope (OM) as shown in Fig. 5 and 6. The pristine PET nonwoven (Fig. 5a) exhibits a random network of overlapped fibers and multiple connected pores with a smooth surface. Visible changes were observed after the coating of graphene oxide, indicating that the surface of both the PET and PET-PAM samples were covered with a thin layer

of graphene oxide sheet (Fig. 5b). However, in the control sample (PET) it can be seen that the GO nanosheets are non-uniformly distributed over the surface of polyester (less homogeneity and more roughness), which can be due to the electrostatic repulsive behavior of the GO and fiber surface. Besides a number of creases were found in the coating layer of PET-GO, which might result in drop of electrical conductivity. After PAMAM grafting on polyester, the GO sheets underwent strong interfacial interaction with organic layers, which improves the compatibility between the GO sheets. Fig. 5d shows the surface of a polyamidoamine-treated fabric (PET-PAM-GO) where a multilayered GO sheet with a fairly uniform distribution is observed. Few regions showed a slightly thicker layer and agglomeration can be due to the strong bonding of the carboxyl and carbonyl groups of the GO nano-sheets and protonated amino groups of PAMAM dendrimer.

After Fe^0 incorporation into the GO coated polyester fabric, the appearance of brilliant spots on the PET-rGO- Fe^0 (Fig. 5e) and PET-PAM-rGO- Fe^0 (Fig. 5f) suggests the formation of iron nanoparticles over the GO sheets. Herein, the high-density well-defined microenvironments at the GO sheet suggest Fe^0 stabilization between two sheets, resulting in entrapment within the hexagonal structure and between the sheets. This was accompanied by a more compact structure on PET-PAM-rGO- Fe^0 as compared to PET-rGO- Fe^0 , due to the strong interaction between NH_2 cross-linked GO and Fe^0 . In addition, it can be clearly seen that Fe^0 incorporation into the PET-GO and PET-PAM-GO samples produced clusters with the pronounced aggregation of smaller particles. In polyamidoamine dendrimer grafted polyester, the highly dispersed GO displayed a smoother external surface and more attenuated roughness and a uniform particle distribution (see Fig. S1, ESI†) with a diameter of 78 ± 38 nm compared to PET-rGO- Fe^0 (average particle diameter, 133 ± 56 nm). The sheet-like structure of GO is

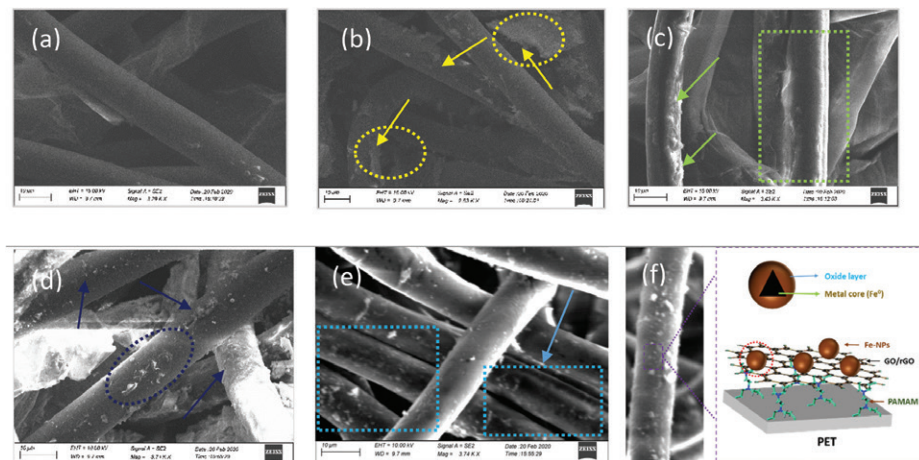


Fig. 5 SEM micrograph of (a) PET; (b) PET-GO; (c) PET-PAM-GO; (d) PET-rGO-Fe⁰; and (e) PET-PAM-rGO-Fe⁰ and (f) schematic representation of PET-PAM-rGO-Fe⁰ (scale: 10 nm).

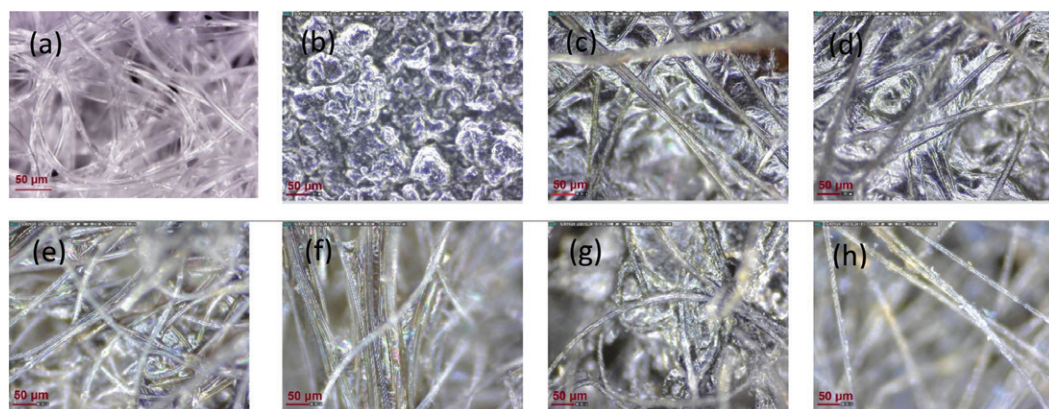


Fig. 6 Digital optical microscope images of (a) PET, (b) GO, (c) PET-GO, (d) PET-PAM-GO, (e) PET-rGO, (f) PET-PAM-rGO, (g) PET-rGO-Fe⁰ and (h) PET-PAM-rGO-Fe⁰ (scale: 50 μm).

more visible in digital micrographs (Fig. 6) than in SEM images. The dispersion of zerovalent iron nanoparticles over GO sheets is more clearly visible as well (Fig. 6g and h). This micrograph further supports the claim of uniform distribution of functional materials.

3.4. The color strength and the coating evenness analysis

The color strength test was carried out for PET-GO, PET-PAM-GO, PET-PAM-rGO, PET-PAM-rGO-Fe⁰, PET-rGO, PET-rGO-Fe⁰ samples. As can be seen from Table 2, the K/S value increased slightly from 3.94 to 4.42, when comparing the PET-GO and PET-PAM-GO samples. It is due to the higher absorbance of GO by the PET-PAM sample. As the reduction of

GO to rGO changes the brown color of the fabric to carbon color, the L^* , a^* , and b^* coordinates change from 45.44, 1.36, and 7.77 to 40.80, 1.55, and 5.75, respectively. After the fabric is incorporated with iron the L^* , a^* , and b^* coordinates change to 41.91, 2.64, and 10.59, respectively. The digital images of the samples are shown in Fig. S2 of ESI†. The color differences (ΔE) in both the CIE and CMC systems of the samples were determined by finding the mean of ten random color measurements on each specimen as illustrated in Fig. S3 of ESI†. The value less than 1 ($\Delta E < 1$) are not visible to human eyes. Thus, the values higher than 1 ($\Delta E > 1$) are not acceptable in the textile dyeing industry for commercial production. Here, we can estimate the evenness of each incorporation step by

Table 2 CIELAB color strength and the coating evenness measurement

Sample name	%R at Wl. of max abs. (420 nm)	K/S at Wl. of max abs.	L^*	a^*	b^*	ΔE (CIE)	ΔE (CMC)
PET-GO	10.22	3.94	45.44	1.36	7.77	1.38 ± 0.85	0.79 ± 0.48
PET-rGO	7.73	5.51	33.6	0.36	1.05	0.59 ± 0.4	0.36 ± 0.23
PET-rGO-Fe ⁰	4.32	10.63	26.12	0.21	1.69	0.64 ± 0.26	0.5 ± 0.16
PET-PAM-GO	9.3	4.42	40.80	1.55	5.75	0.86 ± 0.49	0.64 ± 0.37
PET-PAM-rGO	8.34	5.05	36.42	0.47	1.42	0.84 ± 0.63	0.49 ± 0.33
PET-PAM-rGO-Fe ⁰	8.33	5.08	41.91	2.64	10.59	1.81 ± 0.62	1.51 ± 0.51

Here, (%R) = reflectance, K/S = color strength, CIELab coordinates (L^* is the coordinate response to brightness and darkness of the surface, a^* coordinate response to the green-red shade of color, and b^* coordinate response to the yellow-blue shade of color), ΔE (CIE) = color differences in the CIE system and ΔE (CMC) = color differences in the CMC system.

determining the ΔE value of the specimen. PET-PAM-GO has a value of 0.86 ± 0.49 and 0.64 ± 0.37 in the CIE and CMC systems, while PET-GO has a value of 1.38 ± 0.85 and 0.79 ± 0.48 in the CIE and CMC systems, respectively. All samples except PET-PAM-rGO-Fe⁰ (1.81 ± 0.62 (CIE), 1.51 ± 0.51 (CMC)) have a ΔE value of less than 1.

3.5. ATR-FTIR spectroscopy analysis

ATR-FTIR analysis of the samples was performed to investigate the chemical composition of the samples and possible chemical bonds. All spectra were normalized by levelling the height of the adsorption peak at 1711 cm^{-1} , which indicates the C=O stretch (ester) of polyester. Other identical peaks to polyester including the aromatic sp^2 C-H bend (723 cm^{-1}), plane vibration of the benzene ring (1015 cm^{-1}), C-O stretch (ester) (1095 and 1240 cm^{-1}), and asymmetric C-H stretching (2965 cm^{-1}) were also observed. As can be seen from Fig. 7a, after the adsorption of GO on polyester (PET-GO), a peak appeared at 3433 cm^{-1} which can be attributed to the O-H stretch. After the sample was modified with iron particles (PET-rGO-Fe⁰), the intensity of the peak at 3433 cm^{-1} increased and new peaks were detected at 1054 , 970 , 684 , 662 , and 621 cm^{-1} corresponding to the C-O, O-H, and C-H stretch. After modification of the fabric with PAMAM (PET-PAM)

(Fig. 7b), a peak with low intensity was detected at 3285 cm^{-1} , and this peak indicates the presence of the N-H bond. After the fabric was modified with rGO (PET-PAM-rGO), the intensity of some peaks such as C=O and C-O stretches decreased and the peak at 3285 cm^{-1} disappeared. Furthermore, after the modification of the sample with iron (PET-PAM-rGO-Fe⁰) new peaks were detected at 3361 cm^{-1} (O-H stretch), 961 cm^{-1} (C-H bend), 677 cm^{-1} (C-H stretch), 547 cm^{-1} , and 492 cm^{-1} (C-Br stretch). The intensity of the peaks at 1905 cm^{-1} and 1240 cm^{-1} (C-O stretch) were altered.

3.6. Thermal analysis and decomposition of materials

In a combustion process materials undergo a thermal degradation and thermal oxidative degradation processes through burning and TGA measurements could be used as an indicator of polymer flammability.⁴⁸ The temperature corresponding to the maximum weight loss rate in the DTG curve is noted as T_{max} ; the temperature corresponding to 5 wt% degradation in the TGA curve is noted as T_{onset} , T_{max} , T_{onset} , residue (%) at T_{onset} and residue (%) at 600°C of all samples were calculated from the TG and DTG curves (see Fig. 8 and Fig. S5 and Table S2 of ESI†). As can be seen in Fig. S5,† the pristine fabric (PET) has a T_{max} of 447°C . Owing to the loading of functional materials it increases to 463°C as the fabric is coated with GO

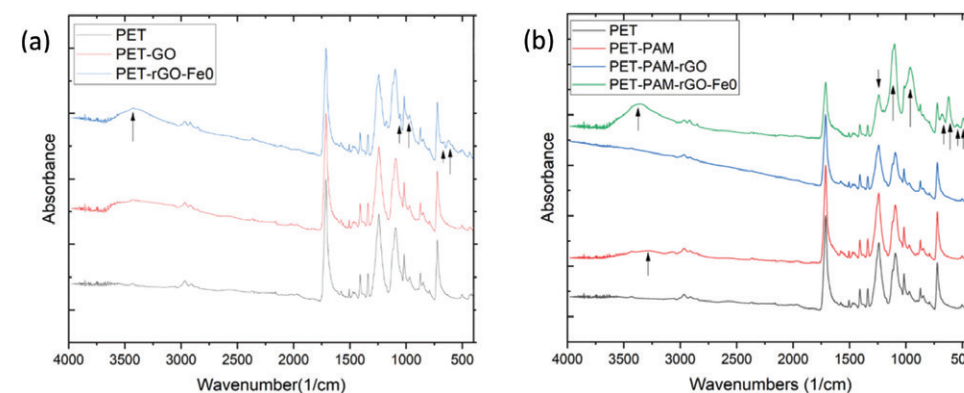


Fig. 7 ATR-FTIR spectra of PET, PET-GO, PET-rGO-Fe⁰, PET-PAM, PET-PAM-rGO and PET-PAM-rGO-Fe⁰.

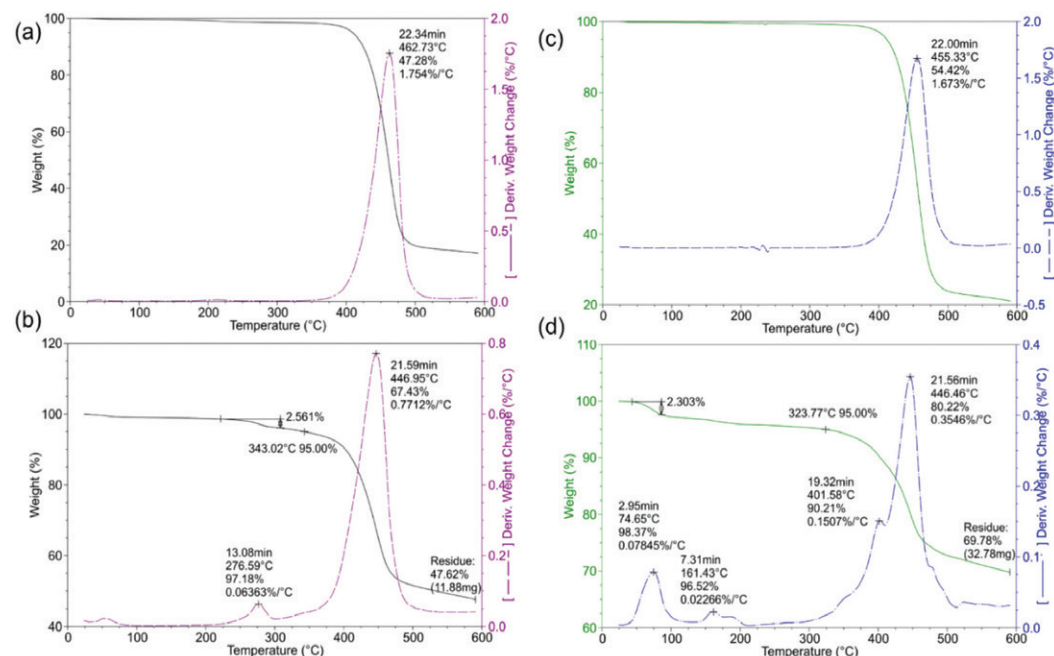


Fig. 8 TGA and DTG curves of (a) PET-GO, (b) PET-rGO-Fe⁰, (c) PET-PAM-rGO, and (d) PET-PAM-rGO-Fe⁰.

(PET-GO). After the fabric is doped with iron (PET-rGO-Fe⁰), T_{\max} decreases to 447 °C, leaving a 47.6% char residue at 600 °C. The pristine PET and PET-GO samples show almost the same residue of 17.44, and 17.52% at 600 °C, respectively. PET-PAM-rGO and PET-PAM-rGO-Fe⁰ have a T_{\max} value of 455 °C and 446 °C, respectively. The melting temperature (T_m) was obtained from the maximum endothermic melting peak of the second heating cycle of DSC analysis. The crystallization temperature (T_c) was obtained from the maximum exothermic crystallization peak of the cooling cycle. Furthermore, the heat of cold-crystallization (ΔH_c) and the heat of fusion (ΔH_f) were calculated from cooling and heating scan, respectively.

As can be seen from Fig. 8b and d, both iron-grafted samples have a small peak (PET-rGO-Fe⁰ at 276 °C, 2.82% decomposition/reduction; and PET-PAM-rGO-Fe⁰ at 161 °C, 1.85% decomposition/reduction). There is a peak at 75 °C for PET-PAM-rGO-Fe⁰ (1.63% reduction) which might be due to moisture evaporation as iron-containing functional groups tend to absorb moisture.

The melting temperature (T_m), the crystallization temperature (T_c), and the heat of cold-crystallization (ΔH_c) of the samples were obtained from DSC analyses (Table 3). T_m was obtained from the maximum of the endothermic melting peak of the second heating cycle while T_c was obtained from the maximum of the exothermic crystallization peak of the cooling cycle. It is evident from DSC analyses that the melting temp-

Table 3 DSC data from the second heating scan and cooling scan of the samples

Sample name	Melting (from the heating scan)			Crystallization (from the cooling scan)		
	T_{onset} (°C)	T_m peak (°C)	ΔH_f (J g ⁻¹)	T_{onset} (°C)	T_c peak (°C)	ΔH_c (J g ⁻¹)
Pristine PET	243	255	33.14	216	204	39.73
PET	241	254	33.67	214	201	38.44
PET-GO	232	245	28.39	207	198	34.65
PET-rGO	237	259	34.81	223	210	37.69
PET-rGO-Fe ⁰	218	240	12.17	207	188	12.64
PET-PAM	242	255	39.33	216	201	41.92
PET-PAM-GO	234	245	27.82	209	200	32.91
PET-PAM-rGO	237	249	38.19	220	208	42.38
PET-PAM-rGO-Fe ⁰	226	243	7.321	211	194	7.69

erature decreased from 255 °C for PET to 240 °C for PET-rGO-Fe⁰ and 243 °C for PET-PAM-rGO-Fe⁰. The DSC thermographs for the second heating and cooling cycles are shown in Fig. S5 of ESI† ("Melting peak width" is correlated with the distribution of crystallinity of the polymer.) T_{onset} is defined as the intersection of the tangents of the peak with the generalized baseline for polymeric materials. It can be seen that T_{onset} decreased from 243 °C for PET to 218 and 226 °C for PET-rGO-Fe⁰ and PET-PAM-rGO-Fe⁰, respectively. ΔH_f and ΔH_c of

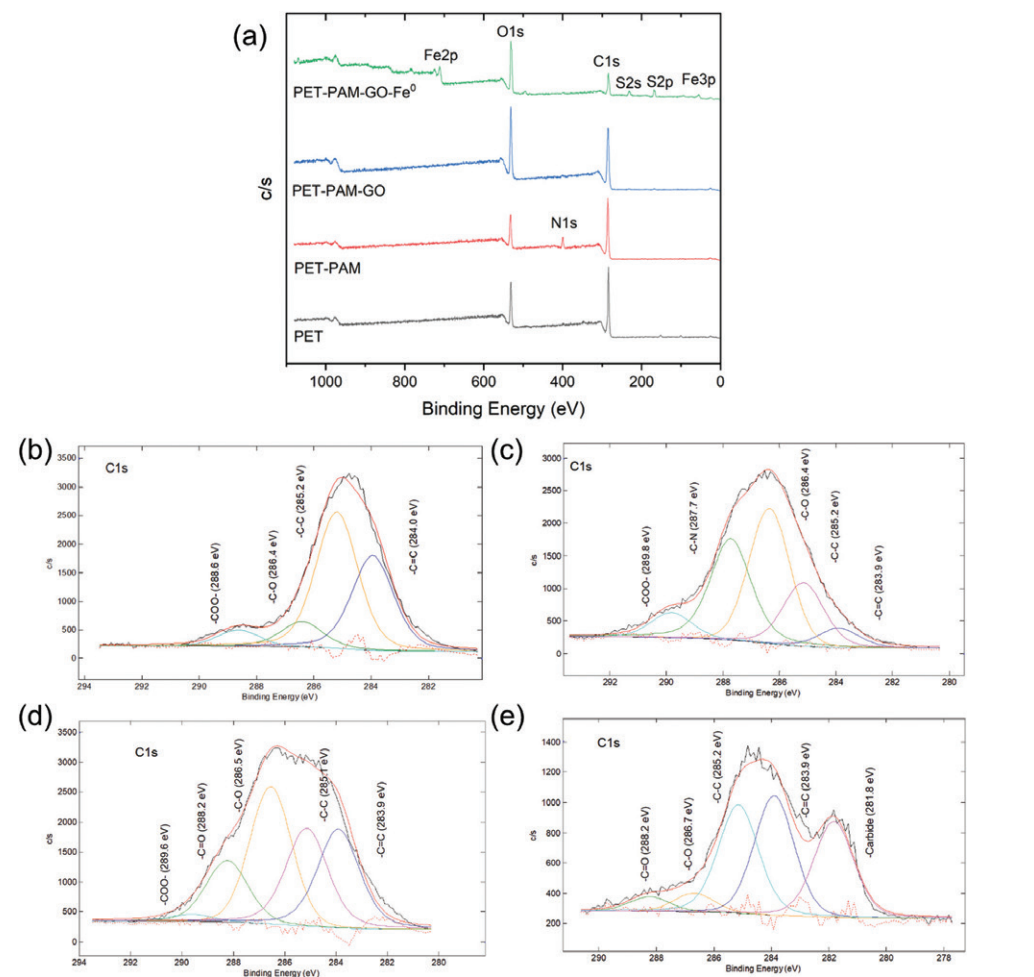


Fig. 9 Wide scan XPS spectra of (a) pristine PET, PET-PAM, PET-PAM-GO, and PET-PAM-rGO-Fe⁰ samples. C 1s XPS analysis of (b) PET, (c) PET-PAM, (d) PET-PAM-GO, and (e) PET-PAM-rGO-Fe⁰.

the sample decrease dramatically from 33.14 and 39.73 J g⁻¹ for PET to 12.17 and 12.64 J g⁻¹ for PET-rGO-Fe⁰, and it decreases to 7.32 and 7.69 J g⁻¹ for PET-PAM-rGO-Fe⁰. This might be due to the incorporation of iron into the polymer that influences the melting and crystallization processes of the polymer.

3.7. X-ray photoelectron spectroscopy (XPS) analysis

With reference to the above characterization of the materials, the PAMAM dendrimer modified samples (PET-PAM, PET-PAM-GO, and PET-PAM-GO-Fe⁰) were analyzed by XPS to identify the changes in their elemental composition and the nature of the chemical bonds due to subsequent surface modi-

fications (see Fig. 9). Pristine PET was used as the control sample. The results summarized in Table 4 show that the control sample contains 76.7 at% carbon and 21 at% oxygen. After the modification of the fabric with PAMAM (PET-PAM), nitrogen was detected in the surface composition having 74.5 at% carbon, 18 at% oxygen, and 7.45 at% nitrogen. The PET-PAM-GO sample contains 70 at% oxygen, 1.3 at% nitrogen, and 28 at% oxygen and the PET-PAM-rGO-Fe⁰ sample contains 41.6 at% carbon, 42.6 at% nitrogen, 42.5 at% oxygen and 6 at% iron.

In order to study the chemical groups on the polyester surface, the high-resolution spectra of the C 1s, O 1s, N 1s and Fe 2p peaks were investigated in detail (see Fig. 9 and Fig. S4

Table 4 Atomic proportion (at.%) of the surface chemical composition of the samples

Sample name	C 1s (at%)	O 1s (at%)	N 1s (at%)	Fe 2p (at%)
PET	76.7	21	0	0
PET-PAM	74.5	18	7.45	0
PET-PAM-GO	70	28	1.4	0
PET-PAM-rGO-Fe ⁰	41.6	42.6	1.3	6.08

of ESI[†]). In the N 1s XPS spectrum of PET-PAM (Fig. S5c of ESI[†]), the peaks at 401.1 eV (C–N) and 399.6 eV (R₂NH) with a corresponding proportion of 78 and 22% were observed. The C 1s spectrum of pristine PET (Fig. 9a) is fitted to peaks at 283.9 eV, 285.2 eV, 286.4 eV and 288.6 eV which are attributed to the C=C (35%), C–C (50%), C–O (9.6%), and COO[−] (5.4%) bonds, respectively.⁴⁹ After the modification of the fabric with PAMAM (PET-PAM) (Fig. 9b), another peak was detected at 287.7 eV corresponding to C–N, with a proportion of 6% C=C, 18.6% C–C, 36.8% C–O, 31.4% C–N and 7.2% COO[−] groups. After the modification of the fabric with GO (PET-PAM-GO) (Fig. 9c), the peak at 287.7 eV (C–N) was replaced with a peak at 288.2 eV corresponding to the C=O bonds, with a proportion of 26, 25.5, 32, 15, and 1.5% for C=C, C–C, C–O, C=O, and COO[−], respectively. This shows that the introduction of GO enriches the C–C and C–O bond types. The PET-PAM-rGO-Fe⁰ sample (Fig. 9d) had the peaks at 281.8, 283.9, 285.2, 286.7, and 288.2 eV corresponding to carbide (27.5%), C=C (32.5%), C–C (31%), C–O (5%), and C=O (4%). The Fe 2p spectra of PET-PAM-rGO-Fe⁰ (Fig. S5f of ESI[†]) indicate the binding energy of iron [Fe³⁺] in the peaks at 724.4 eV (Fe 2p) and 711.0 eV (Fe 2p) with a proportion of 33.3 and 66.7%, respectively.

Part 2: Analysis of electrical and catalytic properties of polyester nonwoven fabrics

3.8. Sheet resistance (R_{sh}) analysis of nonwoven fabrics (electrical conductivity)

The electrical conductivity of modified polyester nonwoven fabrics studied through sheet resistance analysis that are

shown in Fig. 10. GO is electrically insulating due to the number of functional groups of the GO nanosheets. Thus, the GO modified samples do not show any electrical conductivity. In order to bring electro-conductive properties to the nonwoven fabric, the GO modified samples were chemically reduced to rGO and the sheet resistance (R_{sh}) of reduced samples were measured. The sheet resistance (R_{sh}) of PET-rGO decreased slightly from 3.41 ± 0.34 to $2.96 \pm 0.08 \text{ k}\Omega \text{ sq}^{-1}$ by grafting GO with PAMAM (PET-PAM-rGO). A further reduction in the sheet resistance was observed upon incorporation of Fe⁰ (R_{sh} of 1.32 ± 0.18 and $0.74 \pm 0.13 \text{ k}\Omega \text{ sq}^{-1}$ for PET-rGO-Fe⁰ and PET-PAM-rGO-Fe⁰, respectively).

A close comparative study among conductive fabrics shows that rGO and/or Fe⁰ incorporated into PAMAM grafted nonwovens (PET-PAM-rGO and PET-PAM-rGO-Fe⁰) show lower sheet resistance (that translates to high conductivity) than that incorporated into alkaline activated polyester fabric. This provides evidence for the role of PAMAM dendrimer in increasing the conductivity of the resultant nonwoven fabric with reference to the presence of a higher and uniform distribution of conductive materials (rGO and Fe⁰) on the fiber surface as established in the previous section.

3.9. Analysis of the catalytic properties of polyester nonwoven fabrics

3.9.1. Color removal. The catalytic performance of surface-modified polyester fabric containing iron nanoparticles on the graphene-coated surface has been studied briefly by their effectiveness towards the removal of toxic colorants (crystal violet) from water. A cubic cuvette in which the dye solution and nonwoven fabric were brought into contact in the presence of a reducing agent was placed in a UV-vis spectrophotometer, as explained in section 2.7.1. The degradation of pollutants was started at once due to the formation of higher oxidation potential hydroxyl radicals ($\cdot\text{OH}$) due to the interaction between iron particles and NaBH₄ as well as adsorption of pollutants by graphene oxides. The removal of crystal violet with respect to time was recorded (real-time *in situ*) and plotted as shown in

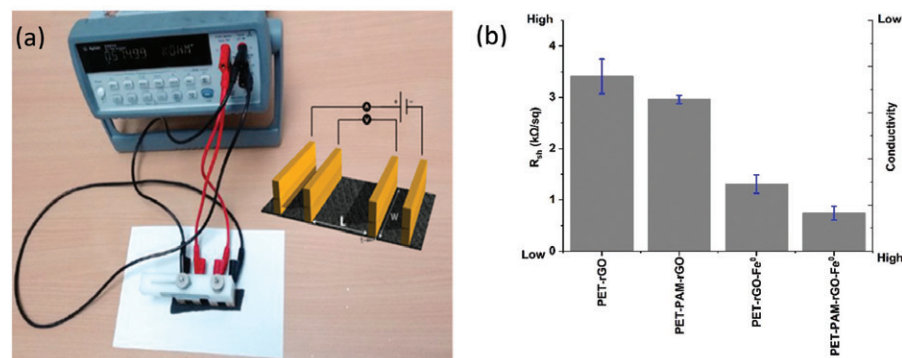
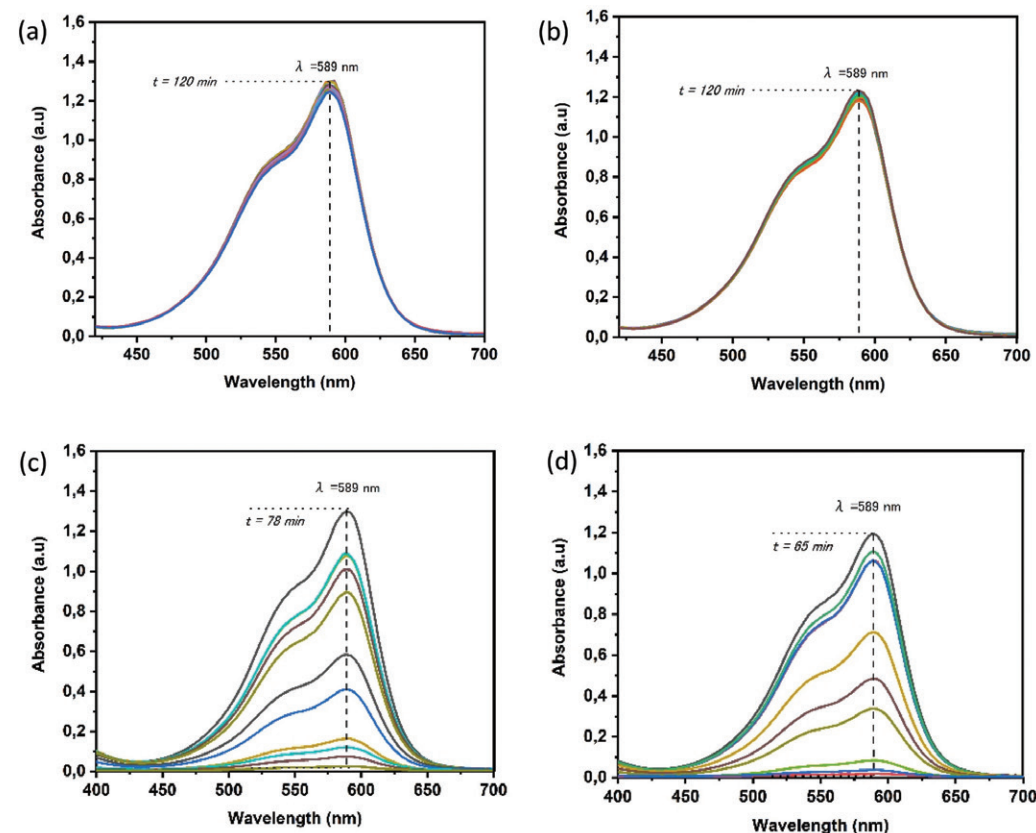
**Fig. 10** (a) 4-Probe measurement of the electrical resistance. (b) Sheet resistance (R_{sh}) analysis of the samples.**Fig. 11** UV-visible spectroscopy of catalytic removal of crystal violet dye using (a) PET-GO, (b) PET-PAM-GO, (c) PET-rGO-Fe⁰, and (d) PET-PAM-rGO-Fe⁰. [Conditions: Crystal violet = 50 mg L^{-1} , nonwoven fabric = 700 mg L^{-1} , NaBH₄ = 0.1 M , pH = 5.]

Fig. 11. The characteristic absorption peak observed at $\lambda_{590 \text{ nm}}$ is attributed to the intensity of crystal violet.⁵⁰ The removal reactions of crystal violet dyes using different nonwoven fabrics (PET-GO, PET-rGO, PET-PAM-GO, PET-PAM-rGO, PET-rGO-Fe⁰ and PET-PAM-rGO-Fe⁰) were carried out under the same experimental conditions. [Conditions: Crystal violet = 50 mg L^{-1} , nonwoven fabric = 1 cm^2 (700 mg L^{-1}), NaBH₄ = 0.1 M , pH = 5.] As shown in Fig. 11a and b, there was no significant decrease in the intensity of the dye during 120 min of exposure for PET-GO and PET-PAM-GO, except for the characteristic absorption intensity of the dye in the presence of graphene. However, many studies have reported that graphene oxide shows a higher catalytic activity in a photocatalytic environment. The control polyester fabric does not interfere with the removal of the dye as also reported in various studies.^{30,51,52}

However, a significant reduction in the intensity of the absorbance at $\lambda_{590 \text{ nm}}$ has been observed when exposed to non-

woven catalysts containing both graphene oxide and iron (PET-rGO-Fe⁰ and PET-PAM-rGO-Fe⁰), suggesting the decoloration of crystal violet. Both nonwoven catalysts showed a significantly rapid removal performance (see Fig. 11c and d). Specifically, the removal rate reached 99.04% in 65 min for PET-PAM-rGO-Fe⁰ and 97.68% in 78 min for PET-rGO-Fe⁰. Fast removal of crystal violet might be attributed to the stability, disparity and amount of functional material (iron) loaded on each nonwoven fabric, ensuring the maximum exposure of reagent and producing striking hydroxyl radicals for decoloration. Although the results indicate that graphene oxide has a fairly poor direct contribution to the removal of dyes, the hexagonal microstructures of graphene oxide facilitated the loading of zerovalent iron nanoparticles on the polyester surface towards high precision of stability, a disparity which later contributed to the removal of pollutants.

3.9.2. Kinetics of color removal using PET-rGO-Fe⁰ and PET-PAM-rGO-Fe⁰. Among all samples studied, only PET-

rGO-Fe⁰ and PET-PAM-rGO-Fe⁰ showed catalytic properties towards the removal of crystal violet dye, and so their kinetics were considered for further study in this section. For that, the [instant/initial] absorbance ratio of the crystal violet dye at $\lambda_{590\text{ nm}}$ (A/A_0) during the reduction reaction was determined, and it accounts for the corresponding concentration ratio (C/C_0) and allows plotting of $\ln(C/C_0)$ as a function of time according to eqn (9), as shown in Fig. 12a and b.

$$\ln \frac{C}{C_0} = \ln \frac{A}{A_0} = -k \cdot t \quad (9)$$

Model validation of first-order reaction kinetics for crystal violet color removal with the nonwoven fabric is performed by linear evolution of $\ln(C/C_0)$ in time as supported by R^2 values of 98.83 and 99.04 for PET-rGO-Fe⁰ and PET-PAM-rGO-Fe⁰ respectively (see Table 5). The results hence provide evidence that good linear relationships of $\ln(C/C_0)$ versus reaction time for both PET-rGO-Fe⁰ and PET-PAM-rGO-Fe⁰ follow first order

and pseudo-first-order reaction kinetics with respect to crystal violet dye removal.

By comparing the rate of reaction for both catalysts, it can be seen that PET-PAM-rGO-Fe⁰ exhibited faster (0.07384 min⁻¹) removal than PET-rGO-Fe⁰ (0.05873 min⁻¹), and this can be due to the higher quantity of Fe⁰ and better stability of the catalyst as supported by TGA analysis. On the other hand, the conversion percentage of PET-GO, PET-rGO-Fe⁰ and PET-PAM-rGO-Fe⁰ reached 4.98% in 120 min, 98.83% in 78 min, and 99.04% in 65 min, respectively (see Fig. 12c). Such a high conversion and rapid kinetics in catalytic degradation might be attributed to good stability of zero-valent iron particles and the characteristic adsorption property of GO.

3.9.3. Toxicity reduction analysis. Toxicity reduction is an important parameter in any effluent treatment process. The relative COD reduction of PET-GO, PET-rGO-Fe⁰ and PET-PAM-rGO-Fe⁰ treated solution in reference to untreated

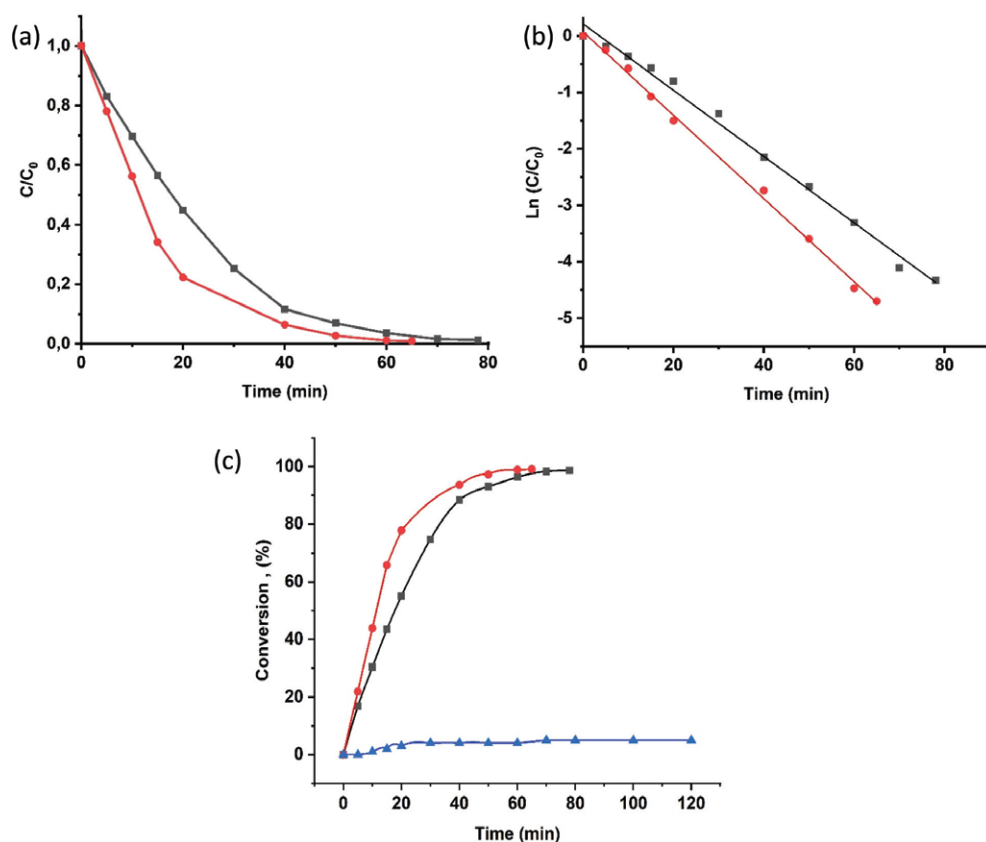


Fig. 12 Evolution of (a) C/C_0 , (b) $\ln(C/C_0)$ and (c) the conversion (%) yield in time at room temperature for removal of crystal violet dyes using PET-GO (▲), PET-rGO-Fe⁰ (■) and PET-PAM-rGO-Fe⁰ (●). [Conditions: Crystal violet = 50 mg L⁻¹, nonwoven fabric = 700 mg L⁻¹, NaBH₄ = 0.1 M, pH = 5].

Table 5 A comparison of the reaction kinetics for the removal of crystal violet dye using PET-GO, PET-rGO-Fe⁰ and PET-PAM-rGO-Fe⁰

Sample name	Conc. of pollutants	Time ^a (min)	Rate constant, k^b (min ⁻¹)	Correlation coefficient, R^{2c}	Conversion, (%)
PET-GO	50 mg L ⁻¹	120	0.00091	31.94	04.98
PET-rGO-Fe ⁰	50 mg L ⁻¹	78	0.05873	99.33	98.83
PET-PAM-rGO-Fe ⁰	50 mg L ⁻¹	65	0.07384	99.77	99.04

^a Reaction time required for complete color removal. ^b k : Rate constant for the 1st order kinetics, and is expressed in min⁻¹. ^c R^2 : Correlation coefficient of the linear regression.

solution were studied according to the method explained in section 2.7.2. The COD of the untreated solution was considered to be 100%. The results indicated a relative reduction in COD after treatment from 100% to 62.08% and 46.37% for PET-rGO-Fe⁰ and PET-PAM-rGO-Fe⁰ respectively (see Fig. S6 of ESI†). The main reason for this tendency may be due to the decreasing number of dye molecules and their intermediates, particularly with the process of oxidizing crystal violet dyes substantially mineralized into water and carbon dioxide. However, although the reduction in COD is more than 50%, even higher detoxification efficiency is a precondition for the industrial prospects of this process. Complete reduction of COD can be achieved by proposing an experimental design that involves continuous treatment of the wastewater after complete color removal, which will allow the available reactive species to react with leuco-compounds (and/or reaction intermediates) as a subsequent step for complete detoxification.

3.9.4. Analysis of recyclability and reusability. To support the practical applications of the resultant nonwoven fabric, the recyclability of PET-rGO-Fe⁰ and PET-PAM-rGO-Fe⁰ were studied under the conditions explained in section 2.7.3. The results show that the nonwoven fabric can be recycled up to five times with slight reduction in its catalytic activity as observed after the catalytic removal of crystal violet dye in constant time (see Fig. 13). It is worth mentioning that PET-PAM-rGO-Fe⁰ exhibited 91.5% of its initial activity in the fifth crystal violet removal cycle. However, the removal percentage of PET-rGO-Fe⁰ reduced to 81.3% after five-cycle application.

This may be explained by the possible variations in Fe⁰ re-aggregation and contact surface decay between the two catalysts, which remains to be elucidated through further investigation. These overall finding provides substantial ground for the improvement of a fiber-based catalytic wastewater treatment system over conventional solutions.

3.9.5. The effect of concentration of PET-rGO-Fe⁰ and PET-PAM-rGO-Fe⁰ on dye removal. The concentration of catalysts in the catalytic removal reaction is one of the most important parameters affecting the removal process of pollutants.⁵³ Therefore, the effect of the concentration of catalysts on the reduction and degradation activities has been studied. For a comparative reason, the concentration of both catalysts was changed in the same manner and the dye removal setup was identical.

The results showed the same trend for both catalysts in the removal of crystal violet dyes. The catalytic activity increased as the concentration of catalysts increased until the equilibrium concentration (see Fig. 14). It is clear that at an increasing catalyst concentration, the catalytic capacity was higher, which can be explained by the participation of a higher amount of Fe⁰ towards generating reactive species that stimulate the removal process. However, at the equilibrium concentration, although a number of iron particles are present in the reaction, the reducing agent (NaBH₄) becomes saturated and cannot produce further reactive species, resulting in a plateau effect. It is to be noted that for both catalysts (PET-rGO-Fe⁰ and PET-PAM-rGO-Fe⁰) a decrease in the concentration from

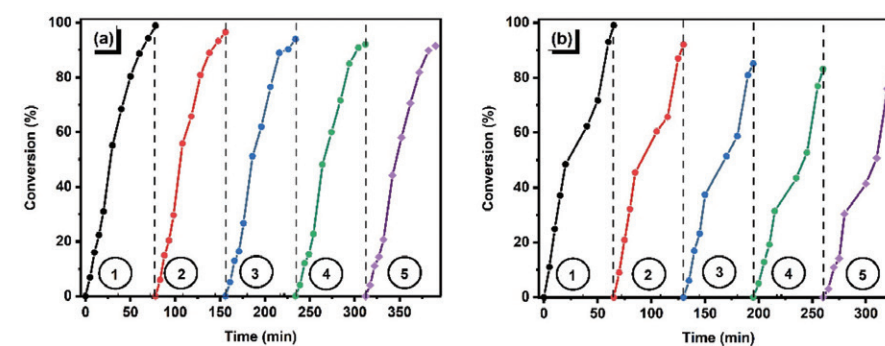


Fig. 13 Recyclability and reusability of (a) PET-rGO-Fe⁰ and (b) PET-PAM-rGO-Fe⁰ in catalytic removal of crystal violet dye. [Conditions: Crystal violet = 50 mg L⁻¹, nonwoven fabric = 700 mg L⁻¹, NaBH₄ = 0.1 M, pH = 5].

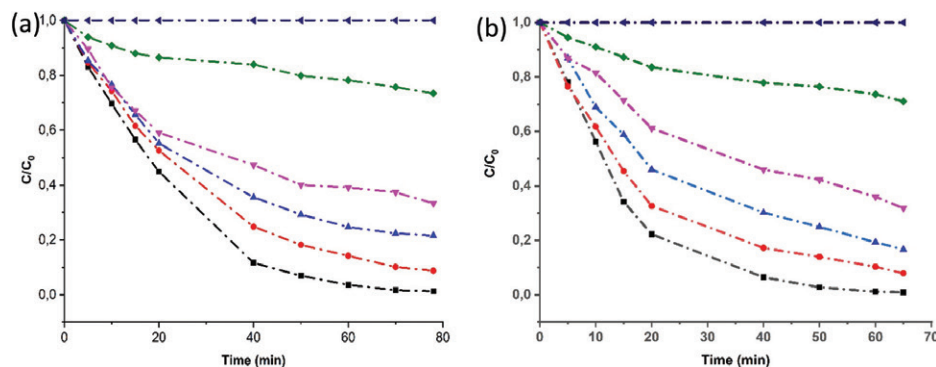


Fig. 14 Effect of the catalyst concentration [0 mg L⁻¹ (●), 50 mg L⁻¹ (▲), 100 mg L⁻¹ (▼), 300 mg L⁻¹ (▲), 500 mg L⁻¹ (●), and 700 mg L⁻¹ (■)] on the removal of crystal violet dye (a) PET-rGO-Fe⁰ and (b) PET-PAM-rGO-Fe⁰. [Conditions: Crystal violet = 50 mg L⁻¹, NaBH₄ = 0.1 M, pH = 5.]

700 mg L⁻¹ to 300 mg L⁻¹ does not significantly reduce the catalytic activity indicating that even a small quantity of the catalysts can provide a good catalytic activity.

3.9.6. The postulated mechanism for the catalytic removal of crystal violet dye using PET-rGO-Fe⁰ and PET-PAM-rGO-Fe⁰.

According to the above results, the mechanism for the catalytic removal of dye has been postulated. As seen in color removal (see section 3.9.1), the loading of metal nanoparticles on the surface of polyester nonwovens leads to catalytic behavior in nonwoven fabrics in the presence of NaBH₄. The resultant catalysts designed in this study showed complete removal of dyes over a short period of time. This robust catalytic activity of the nonwovens is attributed to the synergistic effect of Fe and NaBH₄ as explained by N. Bouazizi *et al.* (2019).³²

The pathways of this typical reduction reaction of crystal violet dye are supposed to involve the dissociation of NaBH₄ into BH₄⁻ in aqueous solution and adsorption of crystal violet dye and/or BH₄⁻ onto the Fe⁰ nanoparticles incorporated into the nonwoven fabrics, thereby favoring the transfer of H⁺ ions and electrons on their surface.⁵⁴ Reactant:Fe⁰ interactions generate a vacant region in the metal surface leading to an electron-enriched layer as illustrated in Fig. 15. The latter is supposed to impose electron transfer to the crystal violet which should behave as an electron-acceptor, thereby triggering the reduction reaction of crystal violet dye to reaction intermediates and then to nontoxic substances as evidenced by COD reduction.

In such a reaction pathway, GO oxide is expected to have a certain contribution, thus explaining the increased activity of the catalyst. On the other side, a comparative study between two prepared nonwovens (PET-rGO-Fe⁰ and PET-PAM-rGO-Fe⁰) shows that Fe incorporated in PAMAM grafted samples showed better and faster dye removability than that without PAMAM. The higher catalytic activity of PET-PAM-rGO-Fe⁰ corresponds to the presence of a higher number of uniformly distributed iron nanoparticles in the presence of PAMAM dendrimer. (Since a continuous flux of electrons due to excess amount of

Fe⁰ should favor the quick reduction of the adsorbed crystal violet.)

3.10. The role of PAMAM and hydrophilic characteristic in electro-catalytic performance

Deeper insights into surface modification of polyester nonwoven fabric using PAMAM dendrimer demonstrate a key role of -NH₂ groups in the coating of graphene oxide and iron nanoparticle fixation. The uniform coating of GO and stable grafting of Fe⁰, as well as molecular adsorption on the surface of nonwoven fabrics, boosted the electro-catalytic performance. As explained in sections 3.8 and 3.9, improvement of electrical and/or catalytic properties has been observed in PAMAM mediated modified samples (PET-PAM-rGO and PET-PAM-rGO-Fe⁰) compared to the others (PET-rGO and PET-rGO-Fe⁰). These improvements can translate to the key role exhibited by -NH₂ from PAMAM during incorporation of functional materials (GO and Fe⁰) into the nonwoven fabric.

Robust and uniform coating of graphene oxide leads to uniform conductivity of materials as discussed in section 3.8. On the other and, the difference in their removal performance has supported the claim (discussed in section 3.9) that may be ascribed to the gradual protonation of the amine group and thus improve the catalytic removal of crystal violet. In addition, from the contact angle measurements, the results obtained herein show that alkaline hydrolysis of the polyester fabric before PAMAM grafting markedly increased the hydrophilic character (-OH and -COOH), as supported by the electrokinetic measurements (ζ-potential analysis in section 3.2), and also had a significant role in the good stability of the materials, as supported by the TGA results. Herein, the wettability of the fibers appeared to be developed uniformly for all connected fibers. Comparative analysis of the average water contact angles before and after surface modification demonstrates that fibers were transformed from hydrophobic to hydrophilic character based on the anticipated surface property, which was responsible for the superior coating and incor-

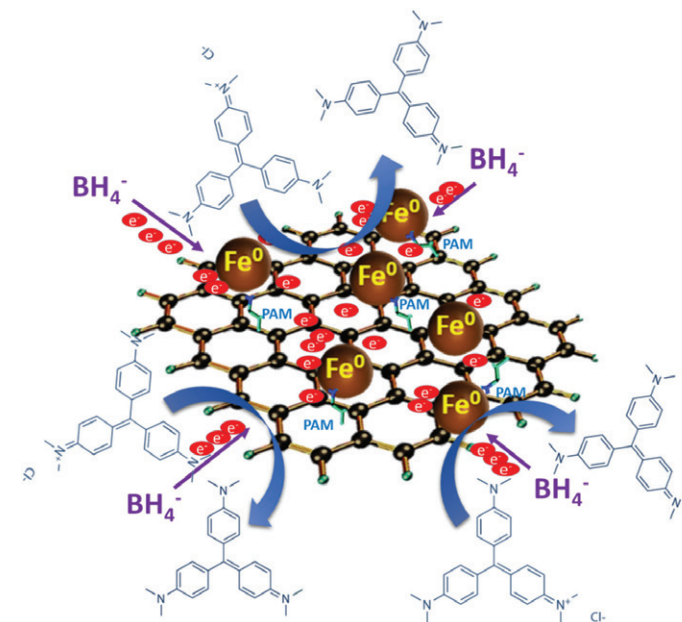


Fig. 15 The postulated mechanism for catalytic removal of crystal violet dye using the Fe⁰ incorporated polyester nonwoven fabric.

poration of the functional materials. These results are of great importance because they clearly demonstrate that the modification steps produce an exchangeable anion, which plays a key role in the electrical conductivity of materials and removal of dyes.

4. Conclusions

The newly developed multifunctional polyester fabric exhibited robust electrical conductivity and catalytic properties as observed from sheet resistance (R_{sh}) analysis, and catalytic removal of crystal violet dye. The overall finding of the study is summarized below:

- A graphene/Fe loaded polyester fabric with multifunctional properties has been successfully developed for the first time. Physical and analytical analysis supports the successful chemical grafting of PAMAM dendrimer followed by robust coating of GO (GO/rGO) and loading of Fe on polyester fabrics.
- Both coating of rGO and loading of Fe⁰ nanoparticles improved the electrical conductivity of the polyester nonwoven fabric. The sample modified with both rGO and Fe⁰ (PET-PAM-rGO-Fe⁰) showed a higher conductivity due to the characteristic conductive behavior of uniformly distributed reduced graphene oxide and metallic Fe⁰ nanoparticles.
- A multifunctional graphene/Fe loaded polyester fabric has been found to have catalytic activity towards the removal of crystal violet dye. Fastest degradation was recorded for

PET-PAM-rGO-Fe⁰ with 99.04% of pollutant removed in 65 min, a rate constant of 0.07384 min⁻¹ following a pseudo-first-order reaction, and first-order reaction kinetics obtained by linear evolution in time of $\ln(C/C_0)$ as supported by an R^2 value over 97.77.

d. Cycle reusability of the catalysts for 5 cycles without any significant reduction in their activity proved the robustness of functionalization and potential scaling up opportunity.

Here, this study has focused on the fundamental progress and aspects of multifunctional textiles while detailed study and influences of various stimuli are yet to be explored. Due to both the electrical and catalytic properties of the resultant material, an electro-Fenton-like system for effective removal of persistent and pathogenic contaminants from water can be explored. Herein the findings of this work are of great importance and allow the development of a multifunctional textile-based material for potential smart, environmental and green chemistry application.

Author contributions

M. N. M and M. A. M. contributed equally to the design of the hypothesis and collection of experimental data. N. K. P., N. B. and V. A. N. participated in analyzing and interpreting data. All authors were involved in writing and revising the manuscript.

Conflicts of interest

The authors declare no conflict of interest.

Acknowledgements

This work has been carried out in the framework of Erasmus Mundus Joint Doctorate Project—Sustainable Management and Design for Textiles (SMDTex), which is financed by the European Commission (Grant No. 532704-EM-5-2017-1-FR-ERA). Special thanks to the Erling Persson Foundation and the Smart Textiles initiative. The authors would like to thank Haike Hilke from the Department of Textile Technology at the University of Borås, Sweden for her support during experimental works.

References

- M. Stoppa and A. Chiolerio, Wearable electronics and smart textiles: a critical review, *Sensors*, 2014, **14**, 11957–11992.
- W. Zeng, L. Shu, Q. Li, S. Chen, F. Wang and X. M. Tao, Fiber-based wearable electronics: a review of materials, fabrication, devices, and applications, *Adv. Mater.*, 2014, **26**, 5310–5336.
- B. Nabil, M. N. Morshed, B. Nemeshwaree, C. Christine, V. Julien, T. Olivier and A. Abdelkrim, Development of new multifunctional filter based nonwovens for organics pollutants reduction and detoxification: High catalytic and antibacterial activities, *Chem. Eng. J.*, 2019, **356**, 702–716.
- B. Nabil, C. Christine, V. Julien and A. Abdelkrim, Polyfunctional cotton fabrics with catalytic activity and antibacterial capacity, *Chem. Eng. J.*, 2018, **351**, 328–339.
- M. N. Pervaz, G. K. Stylios, Y. Liang, F. Ouyang and Y. Cai, Low-temperature synthesis of novel polyvinylalcohol (PVA) nanofibrous membranes for catalytic dye degradation, *J. Cleaner Prod.*, 2020, 121301.
- Q. Li, Y. Wang, S. Jiang, T. Li, X. Ding, X. Tao and X. Wang, Investigation into tensile hysteresis of polyurethane-containing textile substrates for coated strain sensors, *Mater. Des.*, 2020, **188**, 108451.
- G. Cai, M. Yang, J. Pan, D. Cheng, Z. Xia, X. Wang and B. Tang, Large-scale production of highly stretchable CNT/cotton/spandex composite yarn for wearable applications, *ACS Appl. Mater. Interfaces*, 2018, **10**, 32726–32735.
- N. Karim, S. Afroj, A. Malandraki, S. Butterworth, C. Beach, M. Rigout, K. S. Novoselov, A. J. Casson and S. G. Yeates, All inkjet-printed graphene-based conductive patterns for wearable e-textile applications, *J. Mater. Chem. C*, 2017, **5**, 11640–11648.
- X. Hu, T. Huang, Z. Liu, G. Wang, D. Chen, Q. Guo, S. Yang, Z. Jin, J.-M. Lee and G. Ding, Conductive graphene-based E-textile for highly sensitive, breathable, and water-resistant multimodal gesture-distinguishable sensors, *J. Mater. Chem. A*, 2020, **8**, 14778–14787.
- M. A. Shathi, C. Minzhi, N. A. Khoso, T. Rahman and B. Bidhan, Graphene coated textile based highly flexible and washable sports bra for human health monitoring, *Mater. Des.*, 2020, 108792.
- M. A. Miankafshe, T. Bashir and N.-K. Persson, Electrostatic grafting of graphene onto polyamide 6, 6 yarns for use as conductive elements in smart textile applications, *New J. Chem.*, 2020, **44**, 7591–7601.
- K. S. Novoselov, A. K. Geim, S. V. Morozov, D. Jiang, Y. Zhang, S. V. Dubonos, I. V. Grigorieva and A. A. Firsov, Electric field effect in atomically thin carbon films, *Science*, 2004, **306**, 666–669.
- Y. Zhang, Y.-W. Tan, H. L. Stormer and P. Kim, Experimental observation of the quantum Hall effect and Berry's phase in graphene, *Nature*, 2005, **438**, 201–204.
- A. K. Geim and K. S. Novoselov, The rise of graphene, in *Nanoscience and technology: a collection of reviews from nature journals*, World Scientific, 2010, pp. 11–19.
- K. Nomura and A. H. MacDonald, Quantum transport of massless Dirac fermions, *Phys. Rev. Lett.*, 2007, **98**, 076602.
- M. A. Miankafshe, T. Bashir and N.-K. Persson, The role and importance of surface modification of polyester fabrics by chitosan and hexadecylpyridinium chloride for the electrical and electro-thermal performance of graphene-modified smart textiles, *New J. Chem.*, 2019, **43**, 6643–6658.
- A. C. Perinotto, L. Caseli, C. O. Hayasaka, A. Riul Jr., O. N. Oliveira Jr. and V. Zucolotto, Dendrimer-assisted immobilization of alcohol dehydrogenase in nanostructured films for biosensing: Ethanol detection using electrical capacitance measurements, *Thin Solid Films*, 2008, **516**, 9002–9005.
- P. Bhattacharya, M. I. Nandasiri, D. Lv, A. M. Schwarz, J. T. Darsell, W. A. Henderson, D. A. Tomalia, J. Liu, J.-G. Zhang and J. Xiao, Polyamidoamine dendrimer-based binders for high-loading lithium–sulfur battery cathodes, *Nano Energy*, 2016, **19**, 176–186.
- G. Li, S. Yu, W. Xue, D. Ma and W. Zhang, Chitosan-graft-PAMAM loading nitric oxide for efficient antibacterial application, *Chem. Eng. J.*, 2018, **347**, 923–931.
- Y. Peng, R. Yao and W. Yang, A poly (amidoamine) nanoparticle cross-linked two-dimensional metal–organic framework nanosheet membrane for water purification, *Chem. Commun.*, 2019, **55**, 3935–3938.
- M. N. Morshed, N. Behary, N. Bouazizi, J. Guan, G. Chen and V. Nierstrasz, Surface modification of polyester fabric using plasma-dendrimer for robust immobilization of glucose oxidase enzyme, *Sci. Rep.*, 2019, **9**, 1–16.
- N. A. S. Omar, Y. W. Fen, J. Abdullah, Y. M. Kamil, W. M. E. M. M. Daniyal, A. R. Sadrolhosseini and M. A. Mahdi, Sensitive Detection of Dengue Virus Type 2 E-Proteins Signals Using Self-Assembled Monolayers/Reduced Graphene Oxide-PAMAM Dendrimer Thin Film-SPR Optical Sensor, *Sci. Rep.*, 2020, **10**, 1–15.
- S. Pei and H.-M. Cheng, The reduction of graphene oxide, *Carbon*, 2012, **50**, 3210–3228.
- J.-P. Jegal, K.-C. Kim, M. S. Kim and K.-B. Kim, A lithium iron phosphate/nitrogen-doped reduced graphene oxide nanocomposite as a cathode material for high-power lithium ion batteries, *J. Mater. Chem. A*, 2014, **2**, 9594–9599.
- D. R. Dreyer, S. Park, C. W. Bielawski and R. S. Ruoff, The chemistry of graphene oxide, *Chem. Soc. Rev.*, 2010, **39**, 228–240.
- X.-Q. Li, D. W. Elliott and W.-X. Zhang, Zero-valent iron nanoparticles for abatement of environmental pollutants: materials and engineering aspects, *Crit. Rev. Solid State Mater. Sci.*, 2006, **31**, 111–122.
- M. N. Morshed, N. Bouazizi, N. Behary, J. Guan and V. Nierstrasz, Stabilization of zero valent iron (Fe⁰) on plasma/dendrimer functionalized polyester fabrics for Fenton-like removal of hazardous water pollutants, *Chem. Eng. J.*, 2019, **374**, 658–673.
- C. D. Raman and S. Kanmani, Textile dye degradation using nano zero valent iron: a review, *J. Environ. Manage.*, 2016, **177**, 341–355.
- M. N. Morshed, M. N. Pervaz, N. Behary, N. Bouazizi, J. Guan and V. A. Nierstrasz, Statistical modeling and optimization of heterogeneous Fenton-like removal of organic pollutant using fibrous catalysts: a full factorial design, *Sci. Rep.*, 2020, **10**, 1–14.
- M. N. Morshed, N. Bouazizi, N. Behary, J. Vieillard, O. Thoumire, V. Nierstrasz and A. Azzouz, Iron-loaded amine/thiol functionalized polyester fibers with high catalytic activities: a comparative study, *Dalton Trans.*, 2019, **48**, 8384–8399.
- A. Mohamed, B. Nemeshwaree, M. Brigitte, P. Anne, B. Kalim, D. Pascal, M. Anne-Sophie and F. Renato, Activity of enzymes immobilized on plasma treated polyester, *J. Mol. Catal. B: Enzym.*, 2016, **134**, 261–272.
- N. Bouazizi, J. Vieillard, R. Bargougui, N. Couvrat, O. Thoumire, S. Morin, G. Ladam, N. Mofaddel, N. Brun and A. Azzouz, Entrapment and stabilization of iron nanoparticles within APTES modified graphene oxide sheets for catalytic activity improvement, *J. Alloys Compd.*, 2019, **771**, 1090–1102.
- S. Xiao, H. Ma, M. Shen, S. Wang, Q. Huang and X. Shi, Excellent copper(II) removal using zero-valent iron nanoparticle-immobilized hybrid electrospun polymer nanofibrous mats, *Colloids Surf., A*, 2011, **381**, 48–54.
- H. Deb, M. N. Morshed, S. Xiao, S. Al Azad, Z. Cai and A. Ahmed, Design and development of TiO₂-Fe⁰ nanoparticle-immobilized nanofibrous mat for photocatalytic degradation of hazardous water pollutants, *J. Mater. Sci.: Mater. Electron.*, 2019, **30**, 4842–4854.
- H. A. Wege, J. A. Aguilar, M. Á. Rodríguez-Valverde, M. Toledano, R. Osorio and M. Á. Cabrerizo-Vilchez, Dynamic contact angle and spreading rate measurements for the characterization of the effect of dentin surface treatments, *J. Colloid Interface Sci.*, 2003, **263**, 162–169.
- A. Sze, D. Erickson, L. Ren and D. Li, Zeta-potential measurement using the Smoluchowski equation and the slope of the current–time relationship in electroosmotic flow, *J. Colloid Interface Sci.*, 2003, **261**, 402–410.
- E. R. Trotman, *Dyeing and chemical technology of textile fibres*, 1984.
- F. M. Mirabella, *Modern techniques in applied molecular spectroscopy*, John Wiley & Sons, 1998.
- P. Green and L. MacDonald, *Colour engineering: achieving device independent colour*, John Wiley & Sons, 2011.
- J. Schanda, *Colorimetry: understanding the CIE system*, John Wiley & Sons, 2007.
- J. F. Moulder, *Handbook of X-ray photoelectron spectroscopy*, Physical Electronics, 1995, pp. 230–232.
- T. I. T. Okpalugo, P. Papakonstantinou, H. Murphy, J. McLaughlin and N. M. D. Brown, High resolution XPS characterization of chemical functionalised MWCNTs and SWCNTs, *Carbon*, 2005, **43**, 153–161.
- L. Yang, L. Xin, W. Gu, J. Tian, S. Liao, P. Du, Y. Tong, Y. Zhang, R. Lv and J. Wang, A new carboxyl-copper-organic framework and its excellent selective absorbability for proteins, *J. Solid State Chem.*, 2014, **218**, 64–70.
- X. Guo, B. Xu, W. Zhang, Z. Cai and Z. Wen, XPS analysis for cubic boron nitride crystal synthesized under high pressure and high temperature using Li₃N as catalysis, *Appl. Surf. Sci.*, 2014, **321**, 94–97.
- G. Höhne, W. F. Hemminger and H. J. Flammersheim, *Differential scanning calorimetry*, Springer Science & Business Media, 2013.
- H. Deb, S. Xiao, M. N. Morshed and S. Al Azad, Immobilization of Cationic Titanium Dioxide (TiO₂⁺) on Electrospun Nanofibrous Mat: Synthesis, Characterization, and Potential Environmental Application, *Fibers Polym.*, 2018, **19**, 1715–1725.
- Y.-P. Sun, X.-Q. Li, J. Cao, W.-X. Zhang and H. P. Wang, Characterization of zero-valent iron nanoparticles, *Adv. Colloid Interface Sci.*, 2006, **120**, 47–56.
- C. F. Cullis and M. M. Hirschler, The significance of thermoanalytical measurements in the assessment of polymer flammability, *Polymer*, 1983, **24**, 834–840.
- C. Zhang and K. Fang, Surface modification of polyester fabrics for inkjet printing with atmospheric-pressure air/Ar plasma, *Surf. Coat. Technol.*, 2009, **203**, 2058–2063.
- A. Mittal, J. Mittal, A. Malviya, D. Kaur and V. K. Gupta, Adsorption of hazardous dye crystal violet from wastewater by waste materials, *J. Colloid Interface Sci.*, 2010, **343**, 463–473.
- T. Harifi and M. Montazer, In situ synthesis of iron oxide nanoparticles on polyester fabric utilizing color, magnetic, antibacterial and sono-Fenton catalytic properties, *J. Mater. Chem. B*, 2014, **2**, 272–282.
- H. Sudrajat and S. Babel, A new, cost-effective solar photoactive system N-ZnO@ polyester fabric for degradation of recalcitrant compound in a continuous flow reactor, *Mater. Res. Bull.*, 2016, **83**, 369–378.

- 53 M. Wawrzekiewicz, M. Wiśniewska, V. M. Gun'ko and V. I. Zarko, Adsorptive removal of acid, reactive and direct dyes from aqueous solutions and wastewater using mixed silica–alumina oxide, *Powder Technol.*, 2015, **278**, 306–315.
- 54 S. Wunder, F. Polzer, Y. Lu, Y. Mei and M. Ballauff, Kinetic analysis of catalytic reduction of 4-nitrophenol by metallic nanoparticles immobilized in spherical polyelectrolyte brushes, *J. Phys. Chem. C*, 2010, **114**, 8814–8820.